



Rayleigh–Taylor and Richtmyer–Meshkov instability induced flow, turbulence, and mixing. I

Ye Zhou

Lawrence Livermore National Laboratory, Livermore, CA 94550, USA



ARTICLE INFO

Article history:

Available online 6 September 2017

Editor: R. Redmer

Keywords:

Rayleigh–Taylor instability
Richtmyer–Meshkov instability
Kelvin–Helmholtz instability
Shock waves
Transition
Turbulence
Mixing
Astrophysical fluid dynamics
SuperNovae
Inertial confinement fusion (ICF)
High energy density physics (HEDP)
Direct numerical simulations (DNS)
Large-eddy simulations (LES)

ABSTRACT

Rayleigh–Taylor (RT) and Richtmyer–Meshkov (RM) instabilities play an important role in a wide range of engineering, geophysical, and astrophysical flows. They represent a triggering event that, in many cases, leads to large-scale turbulent mixing. Much effort has been expended over the past 140 years, beginning with the seminal work of Lord Rayleigh, to predict the evolution of the instabilities and of the instability-induced mixing layers. The objective of Part I of this review is to provide the basic properties of the flow, turbulence, and mixing induced by RT, RM, and Kelvin–Helmholtz (KH) instabilities. Historical efforts to study these instabilities are briefly reviewed, and the significance of these instabilities is discussed for a variety of flows, particularly for astrophysical flows and for the case of inertial confinement fusion. Early experimental efforts are described, and analytical attempts to model the linear, and nonlinear regimes of these mixing layers are examined. These analytical efforts include models for both single-mode and multi-mode initial conditions, as well as multi-scale models to describe the evolution. Comparisons of these models and theories to experimental and simulation studies are then presented. Next, attention is paid to the issue of the influence of stabilizing mechanisms (e.g., viscosity, surface tension, and diffuse interface) on the evolution of these instabilities, as well as the limitations and successes of numerical methods. Efforts to study these instabilities and mixing layers using group-theoretic ideas, as well as more formal notions of turbulence cascade processes during the later stages of the induced mixing layers, are inspected. A key element of the review is the discussion of the late-time self-similar scaling for the RT and RM growth factors, α and θ . These parameters are influenced by the initial conditions and much of the observed variation can be explained by this. In some cases, these instabilities induced flows can transition to turbulence. Both the spatial and temporal criteria to achieve the transition to turbulence have been examined. Finally, a description of the energy-containing scales in the mixing layers, including energy “injection” and cascade processes are presented in greater detail. Part II of this review is designed to provide a much broader and in-depth understanding of this critical area of research (Zhou, 2017. *Physics Reports*, 723–725, 1–160).

© 2017 Elsevier B.V. All rights reserved.

Contents

1. Introduction.....	3
1.1. Motivation and objectives	3
1.2. Overview	3
1.3. Supernovae	10
1.4. Inertial confinement fusion	13

E-mail address: yezhou@llnl.gov.

2.	1.5. Synopsis	20
2.	Linear arguments and single modes instabilities	22
2.1.	Basic linear stability arguments	22
2.1.1.	RT linear growth rate	22
2.1.2.	RM linear growth rate	23
2.1.3.	Kelvin–Helmholtz linear growth	26
2.2.	Early experiments	26
2.3.	Single-mode RTI and RMI experiments/simulations with 2D initial perturbations	27
2.3.1.	Rayleigh–Taylor flows with initial 2D perturbations	28
2.3.2.	RMI: 2D initial conditions with drop tower	29
2.3.3.	RMI: Shock tube 2D membrane free initial conditions	30
2.3.4.	Shock tube experiments with stereolithographed interfaces	33
2.3.5.	Shock proximity effects on RMI growth	36
2.4.	Single-mode experiments with 3D initial perturbations	38
2.4.1.	RTI: Weight and pulley	38
2.4.2.	RMI: Drop tower	39
2.4.3.	RMI: Shock tube	39
3.	Single-scale nonlinear models	44
3.1.	Potential flow models	44
3.1.1.	The Layzer model	44
3.1.2.	The Goncharov model	46
3.1.3.	The Sohn model	48
3.1.4.	The Abarzhi, Nishihara and Glimm model	48
3.1.5.	The Zhang and Guo potential flow model	48
3.1.6.	The asymptotic case of high density contrast	50
3.2.	Heuristic/interpolation models	52
3.2.1.	The Mikaelian model	52
3.2.2.	The Sadot et al. model	53
3.3.	Padé approximation approaches and compressibility effects	53
3.3.1.	The Zhang–Sohn model (single-point Padé approximant)	53
3.3.2.	The Zhang–Deng–Guo model (two-point Padé approximant)	54
3.3.3.	Compressibility effects	55
3.4.	Vortex and vortex Sheet models	55
3.4.1.	Vortex models	55
3.4.2.	The vortex sheet model of Matsuoka–Nishihara–Fukuda	55
4.	Multi-scale nonlinear models and assessment of models	56
4.1.	Perturbation models	56
4.1.1.	Haan's second order analysis and saturation model	56
4.1.2.	Third order nonlinearity	56
4.1.3.	The Vandenboomgaerde–Gauthier–Müller model	57
4.2.	Competition models	57
4.3.	Evaluation of nonlinear models with RTI experiments and simulations	58
4.4.	Evaluation of nonlinear models with RMI experiments and simulations	60
4.4.1.	The drop tower	60
4.4.2.	Shock tube experiments with membrane	60
4.4.3.	Shock tube experiments with stereolithographed interfaces	61
4.4.4.	Shock Tube without membrane	63
5.	Stabilizing mechanisms	66
5.1.	Viscosity	66
5.2.	Surface tension	69
5.3.	Surface tension and viscosity	71
5.4.	Diffuse interface	72
6.	Similarity, scaling, minimum state of the transition to turbulence	74
6.1.	Late-time RTI similarities	74
6.2.	Late-time RMI similarities	83
6.3.	Lie group analysis	84
6.4.	Phenomenological theory and inertial range spectra	86
6.5.	Hydrodynamic scaling	91
6.6.	Minimum state and transition to turbulence	92
6.6.1.	Spatial criterion	93
6.6.2.	Temporal criterion	94
6.7.	Numerical turbulence	96
7.	Energy injection and transfer process	98
7.1.	The nature of the energy injection in RTI	98
7.2.	The vorticity and energy deposited for RMI	99
7.3.	Basic governing and energy budget equations	103

7.4. RTI energy transfer	107
7.5. RMI energy transfer	108
8. Summary, reflections, and outlook	110
Acknowledgments	111
References	112

1. Introduction

1.1. Motivation and objectives

The current perspective of Rayleigh–Taylor (RT) and Richtmyer–Meshkov (RM) instabilities induced flows is reviewed. Understanding the physics of flows due to hydrodynamic instabilities is of importance to astrophysical fluid dynamics as well to the inertial confinement fusion (ICF) effort, which has a goal of making fusion energy a viable alternative energy source. Characterizing the structure and the evolution of the flows induced by hydrodynamic instabilities is also important to other aspects, ranging from Crab Nebula as the remnant of the historical supernova of 1054 AD, “accidental painting” technique developed by well-known Mexican muralist David Alfaro Siqueiros in the 1930s, to the induced mixing enhancement in the scramjet combustor. While the initial perturbations, such as the surface roughness of the ICF target capsule, might be small, the understanding and modeling of the flows generated by RT and RM instabilities is a formidable challenge. The flows induced by these instabilities experience linear and nonlinear development, followed by a time-dependent transition to turbulence. The greatest impact of the turbulent mixing occurs at later time. Yet, these significant issues have not adequately covered in the existing reviews, and far more significantly, some major developments were simply impossible until recently, with the rapid advancement of the supercomputing power and the diagnostics tools developed for the experiments. The high-energy-density-physics (HEDP) platforms, with their ability to fabricate precision initial conditions, have offered unparalleled opportunities for dedicated experiments at high temperature and pressure regimes. Therefore, after several decades of effort, theory, computation, and experiment have reached a certain level of maturity. This review brings these together, showing how the analytical treatments, observations from both the experimental measurements and simulations of data, as well as the phenomenological and engineering models, have been synthesized for describing the physics of the flows and mixing process. The purpose of this review is to provide a self-contained, comprehensive as well as up-to-date survey of relevant work and reference tool to this subject with a balanced discussion of the various facets of this highly multidisciplinary field. The readers with a variety of background could get either the basics or a more in-depth picture of the field.

1.2. Overview

Lord Rayleigh, his interest spurred by observations on cirrus cloud formation ([Jevons, 1857](#)), derived the properties of an interface instability that occurs when a dense fluid is supported by a lighter one ([Rayleigh, 1883, 1990](#)).¹ Rayleigh's challenge has endured ([Petrasso, 1994](#)) and found wide range of scientific and engineering applications and in natural environments throughout the universe.

The classical work of Lord Rayleigh on hydrodynamic instability, along with its modern development by Sir G.I. [Taylor \(1950\)](#), is known as the Rayleigh–Taylor instability (RTI).² At first glance, the RTI is deceptively simple: invert a glass of water and this instability occurs ([Petrasso, 1994](#)) – when dense water falls out even though the air pressure is more than sufficient to support the water in a carefully prepared experiment ([Lewis, 1950](#)). No matter how carefully the water layer was prepared to begin with, it will deviate from planarity by some small amount ([Sharp, 1984](#)).

Taylor looked at accelerated interfaces rather than unstable stratification in a gravitational field as in Rayleigh's paper. There is of course equivalence between gravity and acceleration which Taylor recognized. The combination of a perturbed interface between the heavy and light fluid and the acceleration pointing from light to heavy initiates the growth of the RT instability.³ Just such a mechanism has occurred to the cirrus clouds ([Fig. 1.1](#)), where the characteristic mushroom shapes of RT instabilities form a beautiful structure along the lower edge of the cloud.

RTI plays important roles in many areas of scientific research such as the following: interstellar medium and galaxy clusters ([Nittmann et al., 1982; Zweibel, 1991; Robinson et al., 2004; Jones and De Young, 2005; Ruszkowski et al., 2007; Scannapieco and Brüggen, 2008; Novak et al., 2011; Caproni et al., 2015](#)), inner edge of an astrophysical disc around a central back hole ([Contopoulos et al., 2016](#)), accretion onto the magnetospheres of neutron stars ([Wang and Nepveu, 1983; Wang et al., 1984](#)), Jupiter's and Saturn's magnetospheres ([Ma et al., 2016](#)), filamentary structure on the Sun ([Isobe et al., 2005](#),

¹ Lord Rayleigh's ideas on the development of hydrodynamic similarity theory and applications had great impact to the fluid mechanics community during his lifetime and beyond (see [Rott, 1992](#)).

² Professor Sir G.I. [Taylor \(1974\)](#) commented the kind of inter play which he had used between mathematics and experiment. It should not be surprising that his landmark paper ([Taylor, 1950](#)) was accompanied by the experimental work of [Lewis \(1950\)](#).

³ It is really the pressure gradient that drives the instability. In both cases, the flow is unstable if the pressure gradient points from heavy to light (as detailed in [2.1.1](#)).



Fig. 1.1. Rayleigh-Taylor cirrus clouds.

Source: Photograph courtesy of Prof. David Jewitt, University of California at Los Angeles.

2006; Berger et al., 2010), interaction between the shocked solar wind plasma and the tenuous magnetospheric plasma at the Earth (Matsumoto and Hoshino, 2004), solar atmosphere (Ruderman, 2017), Earth's ionosphere (Keskinen et al., 1981; Sazonov, 1991; Sultan, 1996; Tang and Mahalov, 2013; Mahalov and Moustaoi, 2014; Mahalov, 2014), lightning return stroke, a violent natural discharge in the lower atmosphere (Hill et al., 1980; Hill, 1991; Picone et al., 1981; Chen et al., 2015), mixing, volatile loss and compositional change during impact-driven accretion of the Earth (Halliday, 2004), geophysical formations of volcanic islands/salt domes (Selig and Wermund, 1966; Marsh, 1979; DiPrima and Swinney, 1981; Wilcock and Whitehead, 1991; Mazariegos et al., 1996), convective thinning of the lithosphere (Houseman and Molnar, 1997), non-linear interaction between surface loads and internal planetary dynamics (Plag and Jüttner, 1995), batholiths (Pons et al., 1992), salt tectonics (Podladchikov et al., 1993), weather inversions (Schultz et al., 2006), coastal upwelling which occurs near the eastern boundary of oceans (Cui and Street, 2004), oceanography (Debnath, 1994), climate dynamics (Adkins et al., 2002; Wunsch and Ferrari, 2004), magnetically confined plasma (Curzon et al., 1960; Finn, 1993), dusty plasma (d'angelo, 1993; Birk, 2002; Veerasha et al., 2005; Sen et al., 2010), quantum plasma (Bychkov et al., 2008; Modestov et al., 2009; Momeni, 2013), heavy-nuclei collision (Moretto et al., 1992), sonoluminescence (Brenner et al., 1995; Hao and Prosperetti, 1999; Lin et al., 2002),⁴ and even the sound generated by the snapping shrimp when the cavitating bubble is destroyed through a RTI (Versluis et al., 2000).

RTI has found industrial applications such as premixed combustion (Veynante et al., 1997; Veynante and Vervisch, 2002; Petchenko et al., 2006; Chertkov et al., 2009), non-premix, reactive systems (Almarcha et al., 2010; Bratsun and De Wit, 2011; Lemaigre et al., 2013), heat exchangers and sprays in internal combustors (Beale and Reitz, 1999; Thomas, 2003; Marmottant and Villermaux, 2004), industrial coating with thin liquid films (Livescu, Roy, and Schwartz, 2011), radiation pressure acceleration of heavy ions from laser-irradiated ultrathin foils (Shen et al., 2017), buoyancy-driven mixing (Turner, 1973) such as occurs in the discharge from stacks and pollutant dispersion (Whitehead and Luther, 1975; Lawrence et al., 1991; Britter and Hanna, 2003), aerosol (Hinds et al., 2002) and sediment (Chou and Shao, 2016) transport, mixing enhancement by expanding waves in supersonic flows (Li et al., 1991), underwater explosions (Penney and Price, 1942; Cole, 1948; Menon and Lal, 1998; Geers and Hunter, 2002), the detonation of a chemical explosive into dilute aluminum particle clouds (Balakrishnan and Menon, 2010); of aluminum plates driven by detonation (He et al., 2010); and by a sudden release of a compressed gas encased in a finite-sided cylindrical container (Annamalai et al., 2014). RT flow in the elastic-plastic media

⁴ See a related treatment on the buoyancy instability of imploding ideal gases (Johnson, 2015).

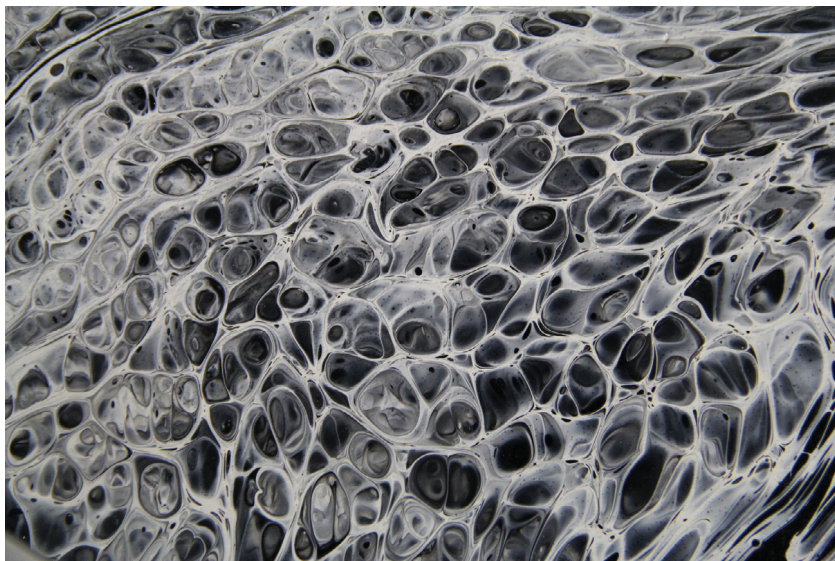


Fig. 1.2a. Pattern created using then “accidental painting” technique developed by Siqueiros in the 1930s. It is the result of a RTI of a viscous layer.
Source: From Fig. 1 of de la Calleja et al., *Phys. Fluids*, with the permission of AIP Publishing.

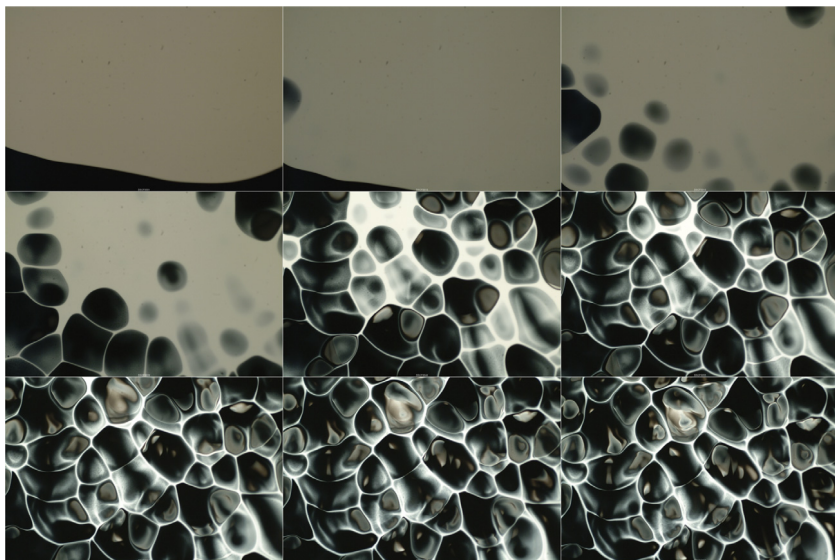


Fig. 1.2b. Image sequence, white over black paint.
Source: From Fig. 5, (Zetina et al., 2015), PLOS ONE
with permission.

and solids (Barnes et al., 1974, 1980; López cela et al., 2005, 2006; Piriz et al., 2005, 2007; Terrones, 2005; Maimouni et al., 2016; Riccobelli and Ciarletta, 2017) has been an active research area. Recently, a set of high explosive driven RT strength experiments for beryllium has produced data to distinguish predictions by various strength models (Henry de Frahan et al., 2015).

Very little scientific research could be related to the creative world of art so we should not miss this opportunity to discuss some of these topics. In two very interesting papers, de la Calleja et al. (2014) and Zetina et al. (2015) studied in detail the paintings by David Alfaro Siqueiros, a well-known Mexican muralist (White, 2009). The authors found that the pattern created using the so-called “accidental painting” technique (Fig. 1.2a) developed by Siqueiros in the 1930s can be viewed as the result of RTI of a viscous layer (Fermigier et al., 1992; Elgowainy and Ashgriz, 1997). As an illustration, they poured two layers of paints on top of each other onto a horizontal surface; white on top of black paints (Fig. 1.2b). Since the white paint is denser than the black one, the layer becomes unstable. After the instability appears, in a matter of minutes the

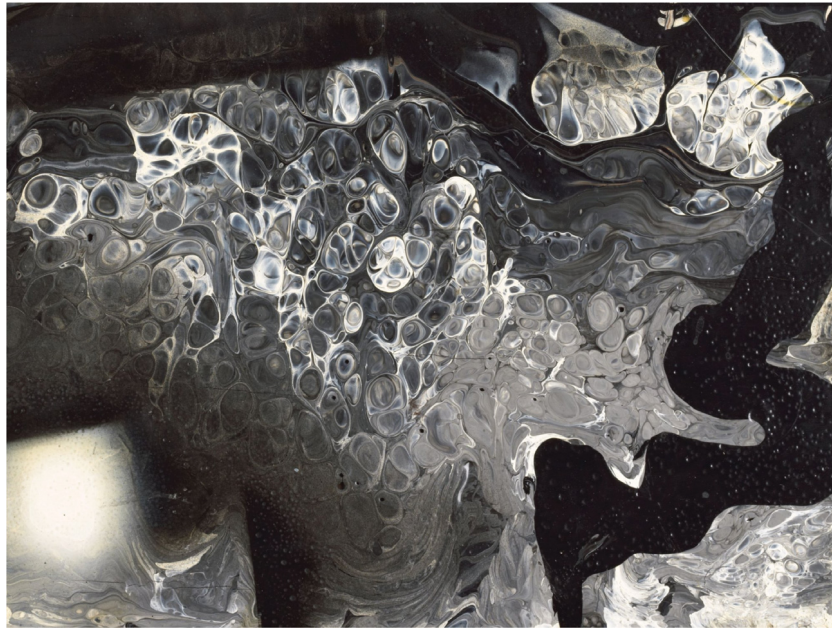


Fig. 1.2c. An example of the experimental painting technique of Siqueiros.
Source: Adopted from Fig. 1, (Zetina et al., 2015), PLOS ONE with permission.

paint begins to dry, “freezing” the “provocative” pattern as shown in Fig. 1.2c. Siqueiros’ exquisite work, *Collective Suicide*, depicts the vast army of invading seventeenth-century Spanish conquistadors on horseback (lower right) and Chichimec Indians leaping to their deaths to avoid subjugation (left) (Fig. 1.3).

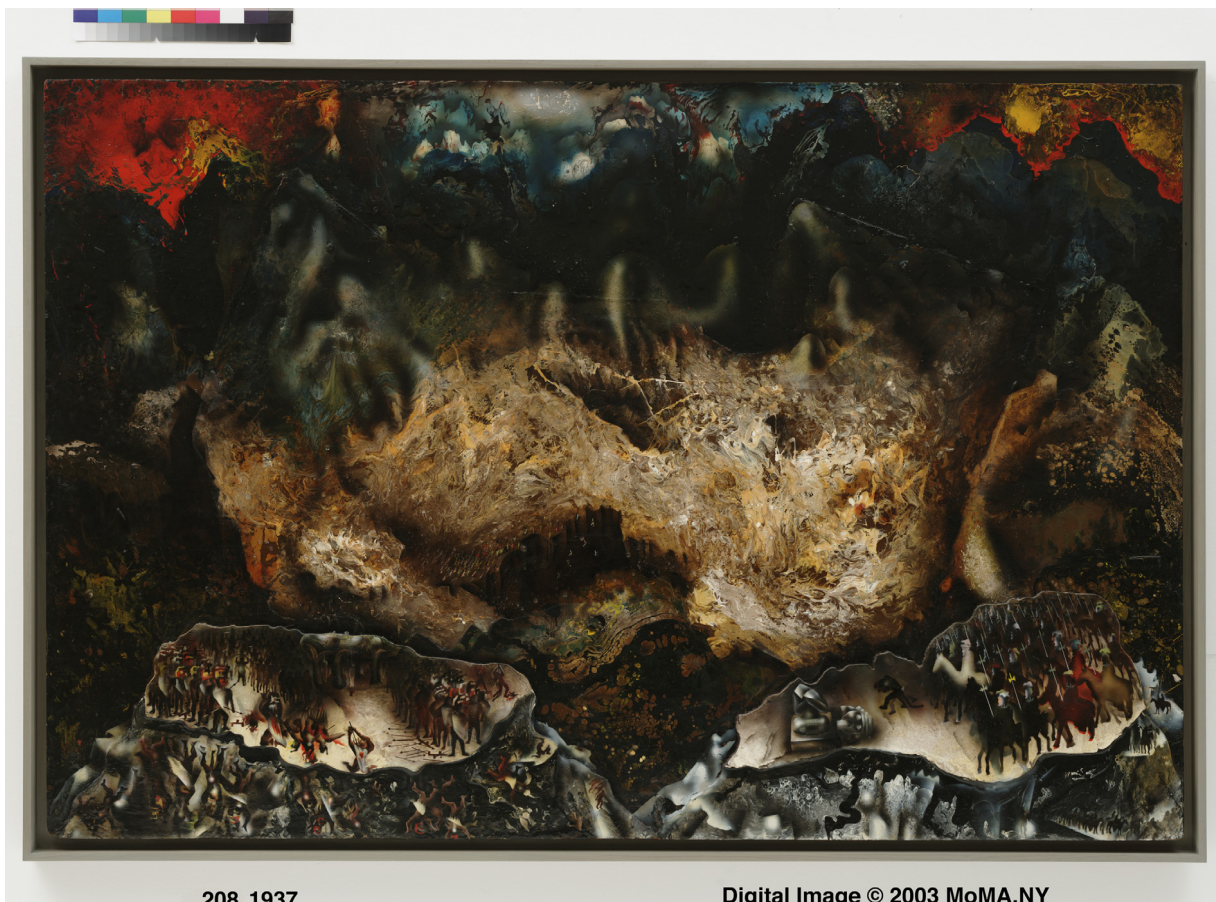
While not generated by famous artists, the images observed in nature due to RTI could be equally, if not more, provocative. Fig. 1.4 shows a composite *Hubble Space Telescope* image of the Crab Nebula, the remnant of the historical supernova of 1054 AD. As pointed out by Hester (2008), the filament structure is shaped by RTI.

Richtmyer–Meshkov (RM) instability (RMI) (Richtmyer, 1960; Meshkov, 1969) is viewed as the impulsive counterpart of Rayleigh–Taylor instability. RMI arises when a shock passes through an interface between two fluids, but with two important distinctions with RTI. First, the RMI can occur when the acceleration is toward either side of the interface, whereas for the Rayleigh–Taylor case one has instability only for acceleration in the direction of the lighter fluid. Second, the RMI evolution occurs largely during a time where the external forcing is zero since the driving is impulsive.

RMI occurs in nature in the situation of shock–magnetosphere interactions (Wu and Roberts, 1999; Wu, 2000). It has also found practical applications in enhancing the mixing in supersonic flows (Marble et al., 1987; Yang et al., 1993; Waitz et al., 1993; Yang et al., 2014), the interaction of a shock wave and a premixed flame (Khokhlov et al., 1999a,b), (Massa and Jha, 2012; Jiang et al., 2016; Chen et al., 2017a), non-premixed reactive flows (Billet and Abgrall, 2003; Billet, 2005; Billet et al., 2008; Attal et al., 2015), laser–material interactions with microfluid dynamics (Fukumoto and Lugomer, 2003; Zabusky et al., 2005; Lugomer, 2007), micron-scale fragment ejection (Asay et al., 1976; Zellner and Buttler, 2008; Zellner et al., 2007; Dimonte et al., 2013; Buttler et al., 2014). Recently, RMI in solid/liquid and solid/solid media (Samulyak and Prykarpatskyy, 2004; Mikaelian, 2005, 2013; Plohr and Plohr, 2005; Piriz et al., 2006, 2008; Buttler et al., 2012; López Ortega et al., 2014; Cherne et al., 2015; Williams, 2016; Subramaniam et al., 2017) has attracted significant attention. Based on the solid yield strength inferred from induced RM instabilities by a single steady shock wave, a new technique was proposed as a tool for experimentally evaluating the material strength of solids under high pressures (Mikaelian, 2005; Piriz et al., 2009; Dimonte et al., 2011; Buttler et al., 2012; Prime et al., 2014, 2017; Jensen et al., 2015).

The shock–bubble interaction (SBI) has been considered as a finite-mass, high-interface-curvature analog to the classical RMI (Markstein, 1957a,b; Rudinger, 1958; Rudinger and Somers, 1960; Sturtevant and Kulkarny, 1976; Abd-El-Fattah et al., 1976; Abd-El-Fattah and Henderson, 1978a, b), (Bryson and Gross, 1961; Catherasoo and Sturtevant, 1983; Picone and Boris, 1986; Picone et al., 1986; Haas and Sturtevant, 1987; Layes et al., 2003, 2005, 2009; Layes and Le Métayer, 2007; Ranjan et al., 2011). A single-shocked (see for example Ranjan et al., 2005, 2007, 2008a,b) or a twice-shocked (Haehn et al., 2010, 2011) spherical gas inhomogeneity has been studied extensively with both the shock tube experiments and numerical simulations.

Of particular interest, depending on the shock strength, the SBI may lead to ignition of the chemically reactive gases inside the bubble (Haehn et al., 2012; Haehn, 2012). The reacting shock–bubble interaction (RSBI) allows one to study the interaction between the RMI and the reaction waves inside the bubble that are initiated by the shock (Diegelmann et al.,



208.1937

Digital Image © 2003 MoMA, NY

Fig. 1.3. Collective Suicide, David Alfaro Siqueiros, 1936. Museum of Modern Art, New York.
© 2016, Copyright: 2016 Artists Rights Society (ARS), New York/SOMAAP, Mexico City.

2016a). Haehn et al. (2012) and Haehn (2012) performed first-of-its-kind RSBI experiments for a range of Mach numbers. Shock focusing leads to an ignition of the bubble gas. The numerical work of Diegelmann et al. (2016a, b, 2017) nicely complements those of Haehn et al. These investigations, quite innovative in that they include chemical reactions, have established an experimental database and a numerical framework for further studies.

Non-premixed combustion is an application where both the chemically reacting RT and RM instabilities occur. As noted recent in Attal and Ramaprabhu (2015), in the absence of an incident shock, burning results in the formation of so-called combustion waves, which spontaneously trigger RM- and RT-like instability growth of the interface. When additionally an incident shock is present, the aforementioned combustion waves and shock wave interact, resulting in significant non-planar distortions of each from a combined RTI and RMI actions. When the unstable interface is reshocked, the mixing, combustion efficiency, and combustion product formation are all significantly enhanced.

The blast wave created by the detonation of a spherical TNT charge was first calculated by Brode (1957); in his case he computed the one dimensional laminar solution. However, in three dimensions it becomes turbulent, a flow that is rich in RTI and RMI mechanisms (e.g. Balakrishnan et al., 2010; Saurel et al., 2012). Fig. 1.5a showed the cross-sectional views of the evolution of the temperature field created by the detonation of a 1-g spherical TNT charge or Aluminum-powder in air in an unconfined space (Kuhl et al., 2013). The computations were performed with a three-dimensional (3D), high-order Godunov Adaptive Mesh Refinement code (Bell et al., 1989, 1994). A spherical TNT charge was ignited at the charge center, producing a constant-velocity detonation wave that consumed the charge. The structure of the detonation wave was modeled by a similarity solution, using thermodynamic properties of TNT as specified by the Cheetah code (Kuhl et al., 2011; Kuhl, 2015). The fireball interface is impulsively accelerated when the detonation wave reaches the edge of the charge. In the physical experiment, perturbations arise either from granular irregularities on the charge surface or from molecular fluctuations, but originate in the computation from discretization errors (Boris, 1989). As detailed in Kuhl (1996), the interface is first subjected to impulsive accelerations that can lead to RMI. As the fireball expands, the shock-compressed air decelerates it, and it is thus subject to RTI. These structures are drawn inward by a backward facing shock (first predicted by Brode) that

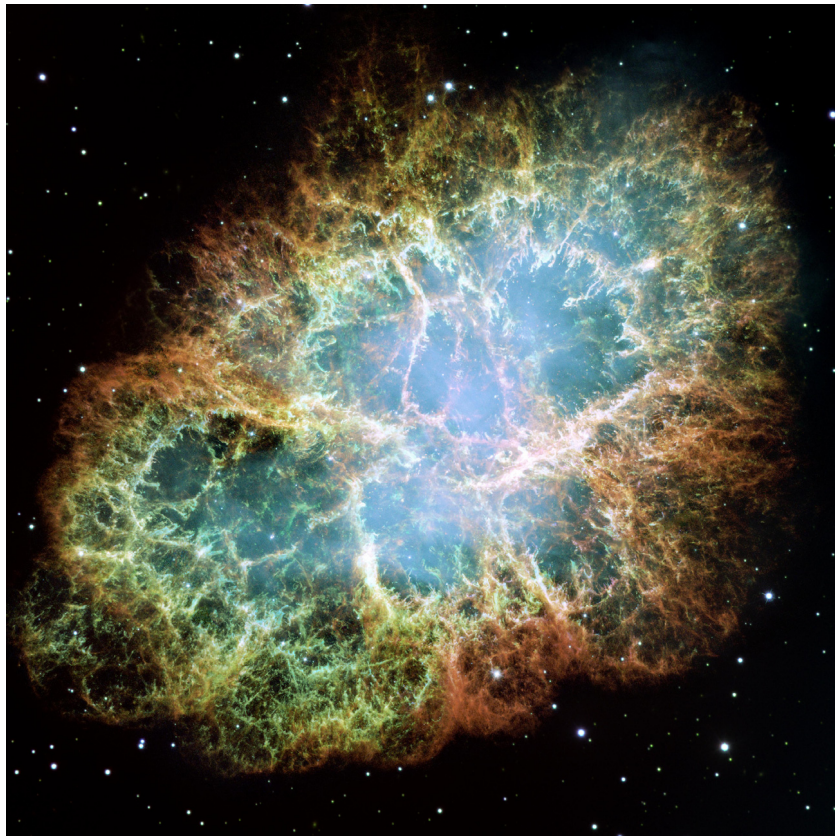


Fig. 1.4. A composite Hubble Space Telescope image of the Crab Nebula.
Source: From http://www.nasa.gov/sites/default/files/images/430453main_crabmosaic_hst_big_full.jpg, with permission from Space Telescope Science Institute, Baltimore, Maryland, USA.

implodes at the center and rebounds as a spherical blast wave. This deposits more vorticity, which intensifies the mixing. By 100 μ s, the perturbations have evolved into mushroom-shaped structures characteristic of RM- and RT- driven mixing layers. These structures rapidly evolve into the nonlinear regime. By 410 μ s, they have generated new fine structures through a nonlinear cascade process and Kelvin–Helmholtz (KH) instability (Lord Kelvin, 1871; Helmholtz, 1868) has developed due to shear flow along the walls of the bubbles (also called a Taylor cavity). Perturbations on the fireball interface cause a misalignment of pressure and density gradient that creates vorticity by the inviscid baroclinic mechanism. This leads to a self-induced production of the vorticity in the mixing region. The TNT detonation products are very fuel rich; when they come into contact with air, they form combustion products. Since this is a non-premixed system, combustion occurs in thin flame sheets (as illustrated in Fig. 1.5b, left panel). A blowup cross-section shows a mushroom-shaped structure wrapped in a thin flame sheet (Fig. 1.5b, right panel).

Balick and Frank (2002) discuss the kinematics of ejecta in astrophysical planetary nebulae. These ejecta result from stellar wind interactions late in the life of intermediate mass stars, when the stars are subject to substantial mass loss rates, and evolve rapidly through alternate phases where the stellar winds are slow, cool and dense, or fast, hot and diffuse. The internal collisions between these successive outflows give rise to shocks, and RT and RM instability within the ejecta. Spectroscopic observations and proper motion studies show that the stellar ejecta often have a linear relation between position and velocity, which is strongly suggestive of kinematical expansion from specific source events. Other dynamical instabilities are also often considered in astrophysics, beyond the usual cases of RT, RM and KH instability. For example, the nonlinear thin shell instability (Vishniac, 1983) occurs when a thin shell of matter is swept up around a hot bubble of material. If the shell advances in a particular region more than in its surroundings, then material will be diverted away from this region, reducing the column density of the shell and allowing it to accelerate yet further.

Other examples that both RTI and RMI instabilities must be considered together are at the interface between the relativistic jets and the surrounding medium (Matsumoto and Masada, 2013), the early stage of acceleration of an elastic-plastic solid (Piriz et al., 2015a) and for the energy loss due to drag (so called head loss) of straight pipeline system (Xia et al., 2015).

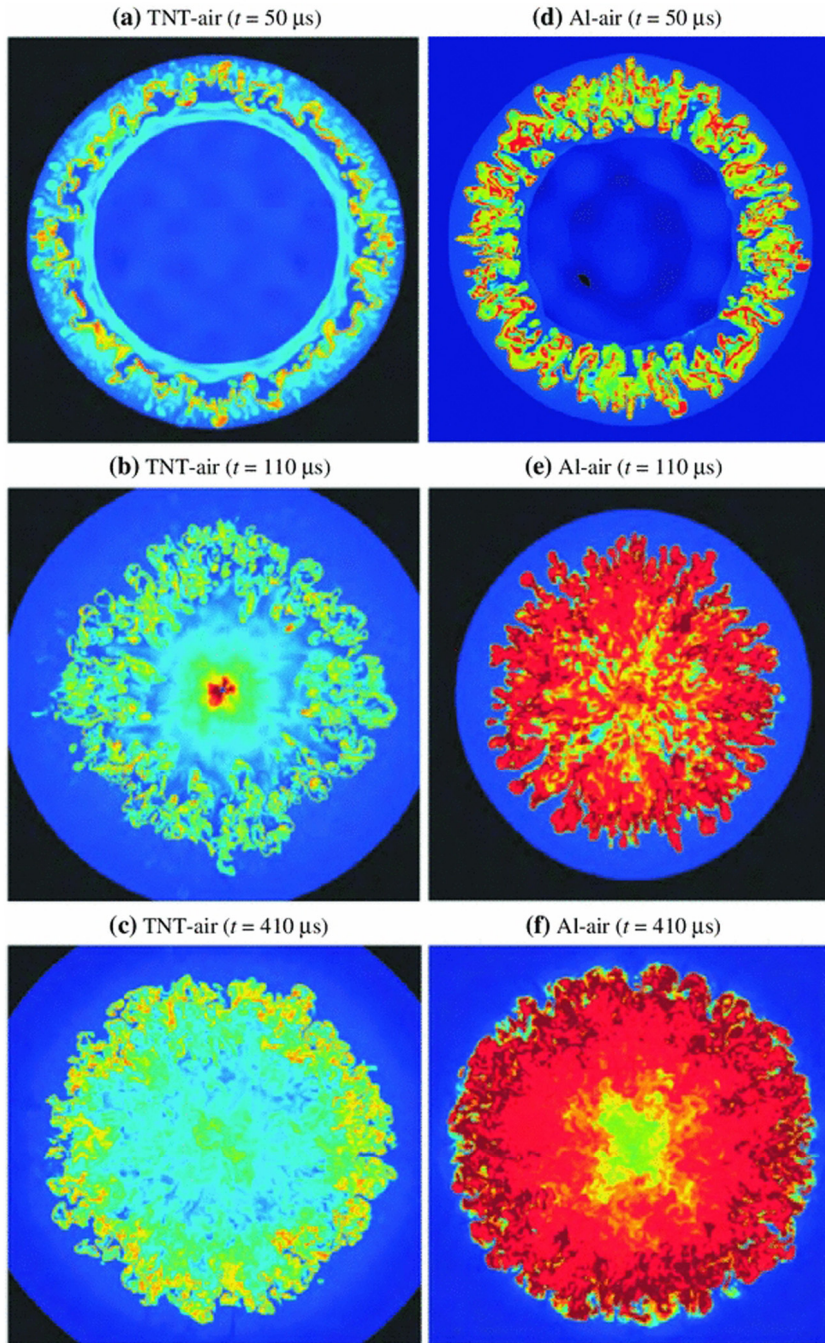


Fig. 1.5a. Cross-sectional view of the temperature field of spherical combustion clouds: frames a-c illustrate TNT-air combustion, while frames d-f depict Al-air combustion (colors denote temperature –red $3000 < T < 4000$ K; yellow: $T = 2,000$ K; turquoise: $T = 1000$ K).
Source: Fig. 2 of [Kuhl et al. \(2013\)](#), with permission from *Shock Waves*.

Up to this point, we have not mentioned two prominent RTI and RMI applications: inertial confinement fusion (ICF) and Supernovae. In these cases, one frequently studies the subject with either RTI or RMI individually in order for the problem to be analytically, computationally, or experimentally tractable. Yet, both instabilities often have to be taken into account together in order to mimic the practical applications ([Lindl, 1995, 1998](#); [Remington et al., 2000, 2006](#); [Atzeni and Meyerter-Vehn, 2004](#); [Drake, 2006, 2009](#)). The ICF and Supernovae applications are obviously extremely important and demand more detailed discussion. As a result, they will be the subjects of next two subsections.

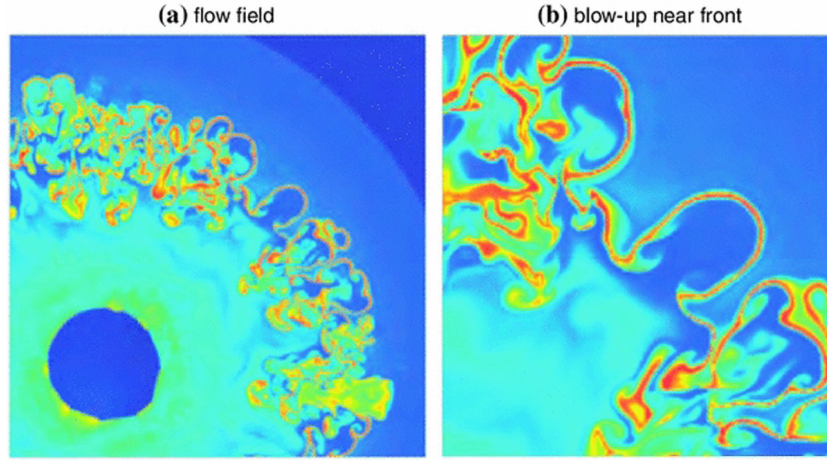


Fig. 1.5b. Exothermic flame sheet in the TNT-air fireball ($t = 100 \mu\text{s}$).
Source: Fig. 3 of Kuhl et al. (2013), with permission from Shock Waves.

1.3. Supernovae

Supernovae (SNe) were recorded as “guest stars” that suddenly appeared in the sky as early as the second century A.D. by Chinese astronomers and were visible for a year or longer (Clark and Stephenson, 1977; Murdin and Murdin, 1985; Bethe, 1990). The Crab Nebula is the remnant of a supernova explosion (Woltjer, 1972) witnessed on July 4, 1054 A.D. Even at a distance of ~ 2 kpc (Trimble, 1968), the Chinese astronomer Yei-Te Wang reported that the “guest star” was visible during the daytime for three weeks and was visible at night for 22 months (Clark and Stephenson, 1977; Hester, 2008).

Supernova 1987A was discovered in Chile, February 23.316UTC, 1987 (Arnett et al., 1989; Hillebrandt and Höflich, 1989), when light and neutrinos from the brightest supernova arrived at Earth. The circumstances of SN 1987A are nearly ideal for studying supernovae (Arnett et al., 1989). As a result, SN 1987A has become one of the most thoroughly studied objects outside the solar system and triggered a burst of publications in the scientific literature and popular press (McCray, 1998).

Supernovae are believed to explode by two distinct mechanisms: thermonuclear explosion in small stars below eight solar masses at birth and collapse of the core in more massive stars. On the one hand, Woosley and Weaver (1986) stated that Type Ia SNe are a likely outcome of an accreting white dwarf (carbon–oxygen) that is provoked into thermonuclear instability by the accumulation of a critical mass. Type I SNe are divided into three subsets: Ia, Ib, and Ic (Fig. 1.6, reproduced from Fig. 1.1 of Harkness and Wheeler (1990), all of which lack H in their spectra. See also, Wheeler and Harkness, 1990 for more details). The basic supernova classification scheme is based on early- and late-time spectra and other features. The Type II and Types Ibc SNe, on the other hand, are believed to be the consequence of gravitational collapse in massive stars. In the case of Types Ibc, the star may have shed its H envelope via winds.

In addition to producing many intermediate-mass elements, Type Ia SNe serve as standard candles for measuring the rate of expansion of the universe (see, for example Branch and Tammann, 1992). Awarded the 2011 Nobel Prize in Physics, Perlmutter et al. (1997, 1999) and Riess et al. (1998) simultaneously discovered that not only was the Universe's expansion not slowing down, it was speeding up, contrary to previous cosmological theories.

In any case, Type Ia SNe begin as carbon–oxygen white dwarfs, which accrete mass from a companion star. When the mass of the white dwarf reaches the Chandrasekhar limit (Chandrasekhar, 1931) of 1.4 solar masses, ignition occurs near the center, thus generating a thermonuclear flame front (Woosley and Weaver, 1986; Hillebrandt and Niemeyer, 2000). The expansion of ash behind the front causes the flame to become Rayleigh–Taylor unstable as it propagates outwards (Khokhlov, 1995; Reinecke et al., 2002; Gamezo et al., 2003; Zingale et al., 2005a,b; Plewa, 2007).

One of the key pieces of physics of Type Ia SNe is the propagation of the nuclear “flame” from the ignition point, specifically, the stability of the flame (Hicks, 2015) and the transition from a subsonic burn (deflagration) to a supersonic detonation (Drake, 1999). For instance, in the RT instability, growth on scales smaller than the flame thickness itself is responsible for this transition (Aspden et al., 2008a). Bell et al. (2004) concluded that a deflagration-to-detonation transition was unlikely based on their two-dimensional (2D) simulation results. Indeed, one of the interesting issues arising from these studies is whether the hydrodynamic instabilities induced in two- and three-dimensions are the same or not. Dolence et al. (2013) showed that the morphology of 2D and 3D simulations can differ dramatically owing to the direction of the turbulent energy cascade⁵: from small scales to large in 2D and the opposite in 3D. They showed that this can lead to enhanced axial

⁵ See, for example, Kolmogorov (1941), Kraichnan (1967, 1971), Batchelor (1969), Leith (1968), Kraichnan and Montgomery (1980).

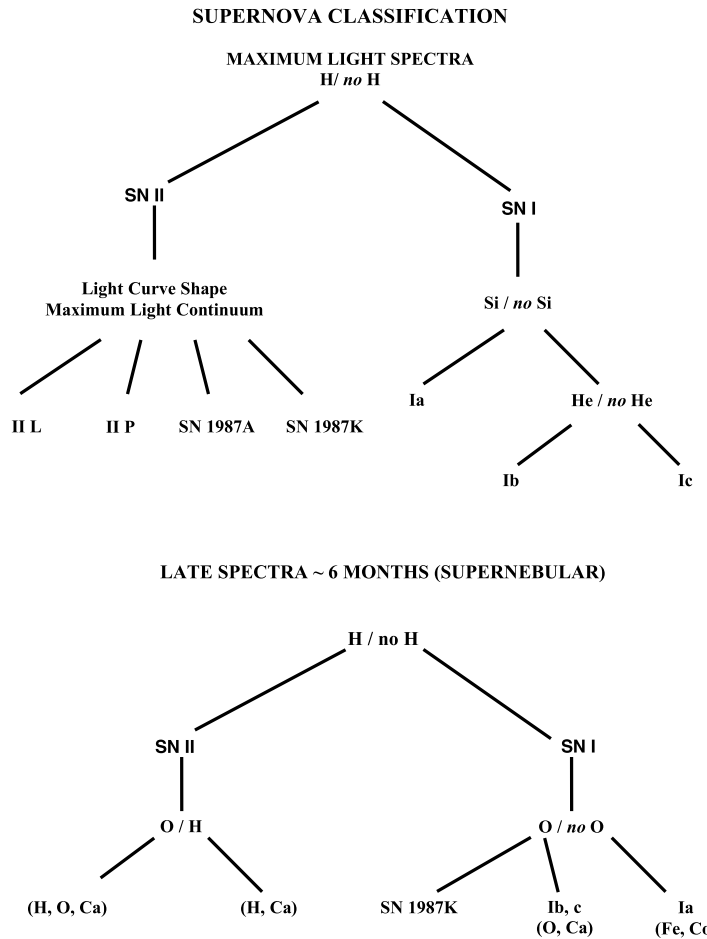


Fig. 1.6. Supernova classification based on the early- and late-time spectra and other features.
Source: From Fig. 1.1 of [Harkness and Wheeler \(1990\)](#) with permission from Springer.

sloshing – what others may have mis-attributed to the standing accretion shock instability (SASI) – which is typically missing or understated in 3D simulations. Furthermore, [Skinner et al. \(2016\)](#) showed that the traditional algorithmic simplification of solving the neutrino transport along individual radial rays in 1D – the so-called ray-by-ray approximation – can artificially enhance this sloshing motion, leading to qualitatively different outcomes compared to full, multi-dimensional transport.

Type 1b/1c SNe have been suggested to be the explosion of Wolf-Rayet stars⁶ ([Wheeler and Harkness, 1990](#)). [Hachisu et al. \(1991\)](#) found a mass dependence of the RTI. The result from 2D simulations suggests that the RTI induces more extensive mixing for smaller-mass helium stars. For those smaller than ~ 5 solar masses, mixing between the core and the envelope and the formation of clumps takes place. In contrast, almost no mixing or clump formation takes place in more massive stars. For smaller-mass stars, the mass ratio between the helium envelope and the heavy element mantle is larger, which leads to larger deceleration of the core.⁷

It is believed that the progenitor star, just before the SNe explosion, had a layered “onion-skin” structure (iron, silicon, carbon and oxygen, helium, hydrogen), with the dense core surrounded by layers of helium and hydrogen ([Shigeyama and Nomoto, 1990; Arnett, 1996](#)). Type II SNe are thought to occur as the result of a gravitational collapse and neutronization of the iron core of the star ([Bethe, 1990](#)). Their formation is accompanied by the generation of a short but very intense burst of

⁶ Wolf-Rayet (WR) stars represent the ultimate, short-lived (< 1 Myr) evolutionary phase of massive, luminous stars whose spectra indicate the presence of enhanced abundance of heavy metals and weak or absent H lines. Typically, these stars lose their outer H (and possibly also He) envelopes through strong stellar winds. As a result, when their core collapses to produce SNe, their spectra lack H (and possibly He) lines. Thus, WR stars are believed to be the primary progenitors of Type Ibc SNe, though the current evidence is inconclusive ([Crowther, 2007](#)). As summarized by [Rosslowe and Crowther \(2015\)](#), through their powerful winds and likely fate as Type Ibc SNe, WR stars are important sources of nuclear processed material to the interstellar medium ([Esteban and Peimbert, 1995; Dray et al., 2003](#)), and are capable of influencing further episodes of star formation on galactic ([Hopkins et al., 2011](#)) and local ([Shetty and Ostriker, 2008; Kendrew et al., 2012](#)) scales.

⁷ As will be made clear later, the enhanced RT instability will result because of larger core deceleration.

neutrinos (carrying away some 99% of the released energy). Neutrinos form a blast wave near the center of the progenitor star, which ultimately, and by a mechanism still not fully understood, blows it apart and gives rise to a tremendous increase in luminosity (Remington et al., 2006).

Within approximately one second, the core of a star that may have lived for ten million years, cooking its hydrogen into progressively heavier elements, implodes from something the size of our planet to something the size of a city (Burrows, 2000), achieving densities in excess of that of the atomic nucleus and velocities one-fourth the speed of light. At nuclear densities $\sim 10^{13}$ times that of tungsten, matter is barely compressible. As described vividly by Burrows (2000), the core bounces, rebounding into the infalling inner mantle and, like a piston, generates a strong shock front that overcomes the confining tamp of imploding mantle mass in order to launch a supernova explosion (Fig. 1.7, from Fig. 1 of Burrows). Fig. 1.8 shows the entropy slices in the z-y-plane at 80 ms, 200 ms, 300 ms, and 400 ms after bounce for the perturbed 3D progenitor model s18-3D using the CoCoNuT-GMT code (Müller and Janka, 2015). The evolution through several hundred ms after core bounce demonstrate one possible mechanism for shock revival, namely, vigorous non-spherical motions that push the shock out to larger radii, thereby enhancing the efficiency of neutrino heating of the post-shock material, leading eventually to explosion (Müller et al., 2017). A core-collapse SNe is driven by an extremely powerful shock, and strong shocks are the breeding ground of the RT and RM instabilities (Remington et al., 2000).

The observational data obtained since then from SN 1987A has unambiguously demonstrated that the envelope of the progenitor star had substantially fragmented during the explosion (Shigeyama et al., 1988; Fryxell et al., 1991; Kifonidis et al., 2003). The main process leading to mixing of different elements in supernovae is the RTI (Smarr et al., 1981; Arnett, 2000; Fryxell et al., 1991; Kifonidis et al., 2000). More specifically, in core-collapse supernovae, the acceleration at the material interfaces is due to a positive pressure gradient that results from the acceleration and deceleration phases of the supernova shock's motion. As discussed in Gawryszczak et al. (2010), the supernova shock experiences two major deceleration episodes during its propagation inside the envelope (and one more deceleration phase after it leaves the star and sweeps through the wind). Each deceleration phase creates a positive pressure gradient in layers with a negative density gradient (i.e., conditions suitable for RTI). Kifonidis et al. (2006) showed the growth and outward propagation of the RT mushrooms from the former Si/O and O/He interfaces of the star (Fig. 1.9a). Here a few of the RT clumps have actually reached the He/H interface before this reverse shock has managed to form.

Following the core collapse (Bethe, 1990; Janka et al., 2007; Smarr, 2009; Burrows, 2013), there is also significant RM mixing between stratified outer gas layers (Burrows et al., 1995; Guzman and Plewa, 2009). Kifonidis et al. (2006) remarked, however, that the importance of the RMI for the observational appearance of core-collapse supernova explosions has not been widely recognized in previous modeling (see however Kane et al., 1997, 2000). The RMI is provided by the supernova shock (and also a series of reverse shocks sweeping through the ejecta). Fig. 1.9b illustrates the onset of the RMI at the He/H interface (the deformed discontinuity just behind the supernova shock in the plots for $t = 99$ s and $t = 299$ s). Note also the huge hydrogen pockets that are created by the RMI.

Hammer et al. (2010) made a careful comparison of the growth of mixing instabilities at the composition interfaces of the exploding star in 3D and 2D calculations. According to the authors, in 3D RMI distortions can be seen at the (C+O)/He interface and are likely to contribute to the turbulent mixing of the metal core with the helium shell of the exploding star. At the He/H interface, however, where the shock is very close to being spherical, no clear RMI activity becomes visible before it is penetrated by fast, metal-carrying clumps that have been able to pass through the helium layer with still high velocities.

Acting on perturbations within the star before the supernova, the uneven shape of the supernova remnant (SNR) can be shown to result from the combined influence of RM and RT instabilities (Aschenbach et al., 1995; Almgren et al., 2006). Also, the extremely fast acceleration of cosmic rays in a SNR observed in Chandra X-ray images (Uchiyama et al., 2007; Uchiyama and Aharonian, 2008) may be accounted for with a magnetic field amplification mechanism, which is thought to be caused by turbulent mixing of plasmas via the RMI (Inoue et al., 2009; Sano et al., 2012; Kuramitsu et al., 2016).

The rapidly expanding ejecta from the supernova drives a shock forward into the surrounding medium, and a reverse shock forms where the ejecta are decelerated by the accumulating, shocked matter (Reynolds, 2008). The place where the ejecta and ambient medium meet, called the contact discontinuity, becomes hydrodynamically unstable (Remington et al., 2000). Indeed, RT instabilities are expected (e.g., Gull, 1973; Shirkey, 1978; Dickel et al., 1989; Chevalier et al., 1992; Jun and Norman, 1996a,b, c; Wang and Chevalier, 2001; Wongwathanarat et al., 2015), which results in fingers of dense gas ejecta protruding into, and mixing with, the shocked circumstellar material. These instabilities are relevant to remnants from both Type Ia and Type II explosions (Blondin and Ellison, 2001).

Hubble Space Telescope observations of the Crab Nebula (Fig. 1.4) show filamentary structures that appear to originate from the RTI operating on the supernova ejecta accelerated by the pulsar-driven wind (Hester et al., 1996). Pulsars are rapidly rotating magnetized neutron stars that usually form as the result of a supernova explosion. The interface between the synchrotron nebula and the swept-up shell of ejecta has been thought to be RT unstable (Davidson and Fesen, 1985). In order to understand the origin and formation of the filaments in the Crab Nebula, Jun (1998) studied the interaction of a pulsar wind with the uniformly expanding supernova remnant by means of numerical simulation. Bucciantini et al. (2004) extended this line of research by incorporating the nebular magnetic field. These simulations produce structures that bear a strong resemblance to observations of the filaments in the Crab Nebula (Hester, 2008).

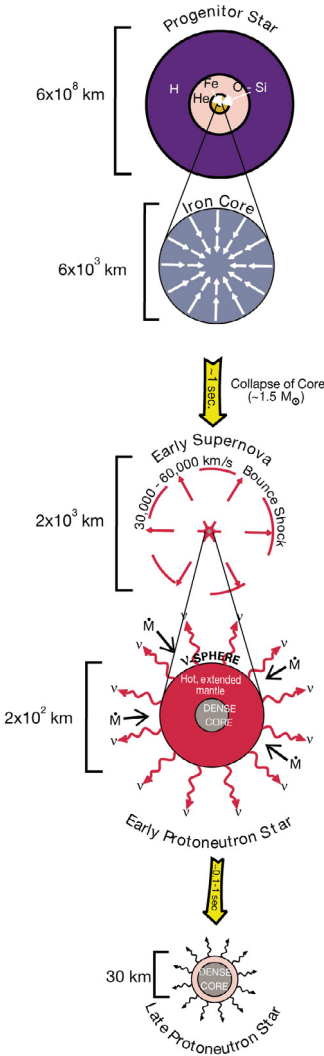


Fig. 1.7. The sequence of events in the collapse of a stellar core to a nascent neutron star (This figure is not to scale). It begins with a massive star with an ‘onion-skin’ structure, goes through white-dwarf core implosion, to core bounce and shock-wave formation, to the protoneutron-star stage before explosion, and finally to the cooling and isolated-neutron-star stage after explosion.

Source: From Burrows, 2001 with permission from *Nature*.

1.4. Inertial confinement fusion

Inertial confinement fusion (ICF) is an approach to fusion that relies on the inertia of the fuel mass to provide confinement (Nuckolls et al., 1972; Brueckner and Jorna, 1974; Nakai and Takabe, 1996; Lindl, 1998; Atzeni and Meyer-ter-Vehn, 2004). The route toward inertial fusion has been investigated either through the indirect or direct drive scheme (Lindl, 1995; Craxton et al., 2015; Betti and Hurricane, 2016). Mima (2004), Tassart (2004), and Garanin (2011) offered their perspectives on the ICF development in Asia, Europe, and Russia, respectively. In the United States, a number of intense laser based platforms with increased capabilities have been built over the years, including most recently Nova (Hunt and Speck, 1989), Nike (Obenschain et al., 1996), Omega (Boehly et al., 1997; McCrory, 2004), and the National Ignition Facility (NIF) (Hurricane and Herrmann, 2017; Hogan et al., 2001; Miller et al., 2004a,b; Moses and Wuest, 2003; Moses et al., 2009). The French Laser MégaJoule (LMJ), under construction near Bordeaux, France (Andre, 1999; Tassart, 2004; Fleurot et al., 2005; Bourgade et al., 2008; Casner et al., 2015a), is very similar to NIF.⁸ Very large facilities such as NIF and LMJ provide better opportunities in the effort to achieve ignition, a necessary step to make fusion energy a feasible alternative energy source (Edwards et al., 2013).

⁸ The coffee at LMJ is richer than NIF’s, however, as science reporter Daniel Clery (2015) quipped.

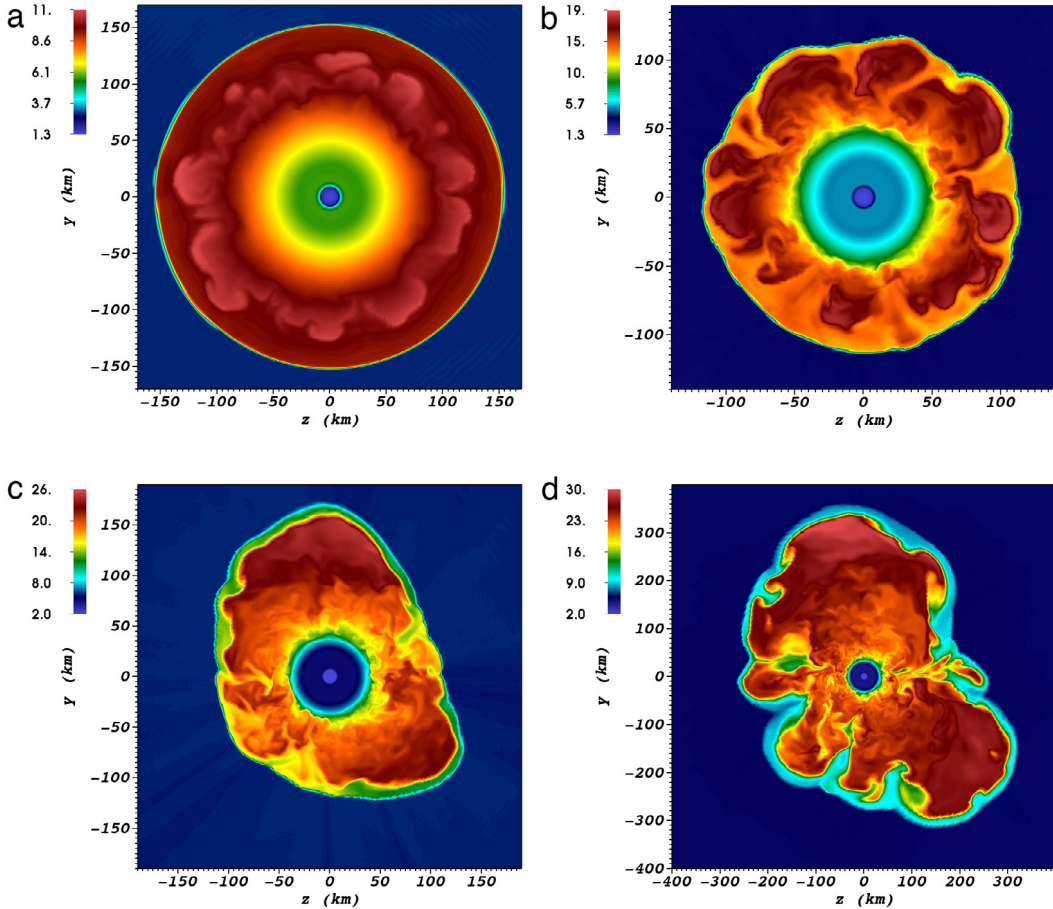


Fig. 1.8. Entropy slices in the z-y-plane at (a) 80 ms, (b) 200 ms, (c) 300 ms, and (d) 400 ms for the perturbed 3D progenitor model s18-3D using the CoCoNuT-GMT code (Müller and Janka, 2015). At 80 ms, the model begins to exhibit signs of neutrino-driven convection. At 200 ms, infalling perturbations begin to interact with large-scale oscillations, and at 300 ms, the shock front begins to deform due to increasingly strong oscillations, pushing the shock out in radius and enhancing the neutrino heating of the post-shock material. At 400 ms, the shock is deformed even more strongly and is likely on its way to shock revival and eventual explosion. Note the changing scale of the figures.

Source: Fig. 5 of Müller et al. (2017), with permission.

© 2017, B. Müller et al. (2017), *Monthly Notices of the Royal Astronomical Society*, with permission.

In the United Kingdom, the Vulcan Petawatt laser at the Rutherford-Appleton Laboratory have been used to carry out interesting experimental work on RTI (Palmer et al., 2012) and on developed turbulence and nonlinear amplification of magnetic fields (Meinecke et al., 2015; Gregori et al., 2015). Hopps et al. (2013, 2015) described in detail the Orion laser facility at the Atomic Weapons Establishment (AWE), which has been operational since April 2013, fielding experiments that require both its long and short pulse capability. For the ICF research in Russia, the main facility is ISKRA-5 at the Russian Federal Nuclear Center ‘All-Russian Scientific Research Institute of Experimental Physics’ in Sarov (Bel’kov et al., 1999; Abzaev et al., 1998; Annenkov et al., 1991, 2006; Bondarenko et al., 2007). More recently, He and Zhang (2007), Wu et al. (2014), He et al. (2016), Xie et al. (2016) and Yuan et al. (2016) reported on the development and experiments carried out at the ShengGuang-II and III laser facility in China.

Separately, the Z-pinchers, with the most powerful one built in Sandia National Laboratory (Spielman et al., 1998), is designed based on converting the stored electrical energy in a pulsed-power accelerator into X-rays (Matzen, 1997; Ryutov et al., 2000).⁹ Traditional Z-pinch implosions are known to be susceptible to the RTI (Curzon et al., 1960; Harris, 1962; Douglas et al., 1997). Some related RTI and RMI studies can be found, such as Peterson et al. (1996), De Groot et al. (1997), Velikovich et al. (1996, 2000), Zhigalin et al. (2015), and Piriz et al. (2015b). Outside United States, Z-pinch experiments have been performed on the mega-ampere generator for plasma implosion experiments (MAGPIE) pulsed power facility at

⁹ While much attention is focused on Z pinches with an implosion time in the range of tens of nanoseconds (Ryutov et al., 2000), there exist devices in which the implosion time is as long as hundreds of nanoseconds to microseconds as the imploding objects are relatively heavy metal shells (Baker et al., 1978; Degnan et al., 1995).

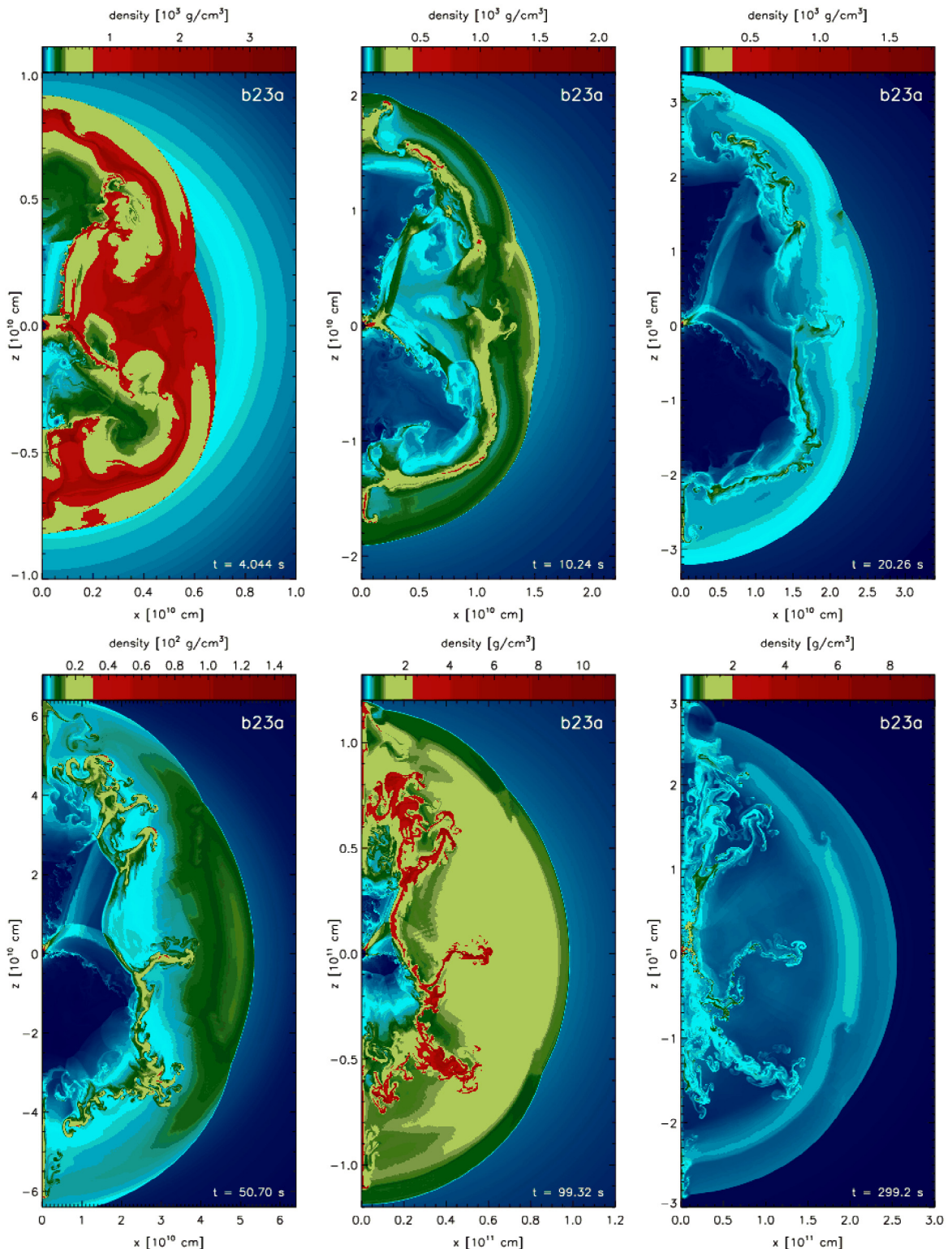


Fig. 1.9a. Snapshots of the density distribution of model b23a for several times. From top left to bottom right (a) $t = 4 \text{ s}$, (b) $t = 10 \text{ s}$, (c) $t = 20 \text{ s}$, (d) $t = 50 \text{ s}$, (e) $t = 99 \text{ s}$, and (f) $t = 299 \text{ s}$. Note the change of the radial scale. Note also the growth and outward propagation of the RT mushrooms from the former Si/O and O/He interfaces of the star, and the onset of the RMI at the He/H interface (the deformed discontinuity just behind the supernova shock in the plots for $t = 99 \text{ s}$ and $t = 299 \text{ s}$).

Source: From Fig. 2 of Kifonidis et al. (2006) from *Astron. Astrophys.* with permission.

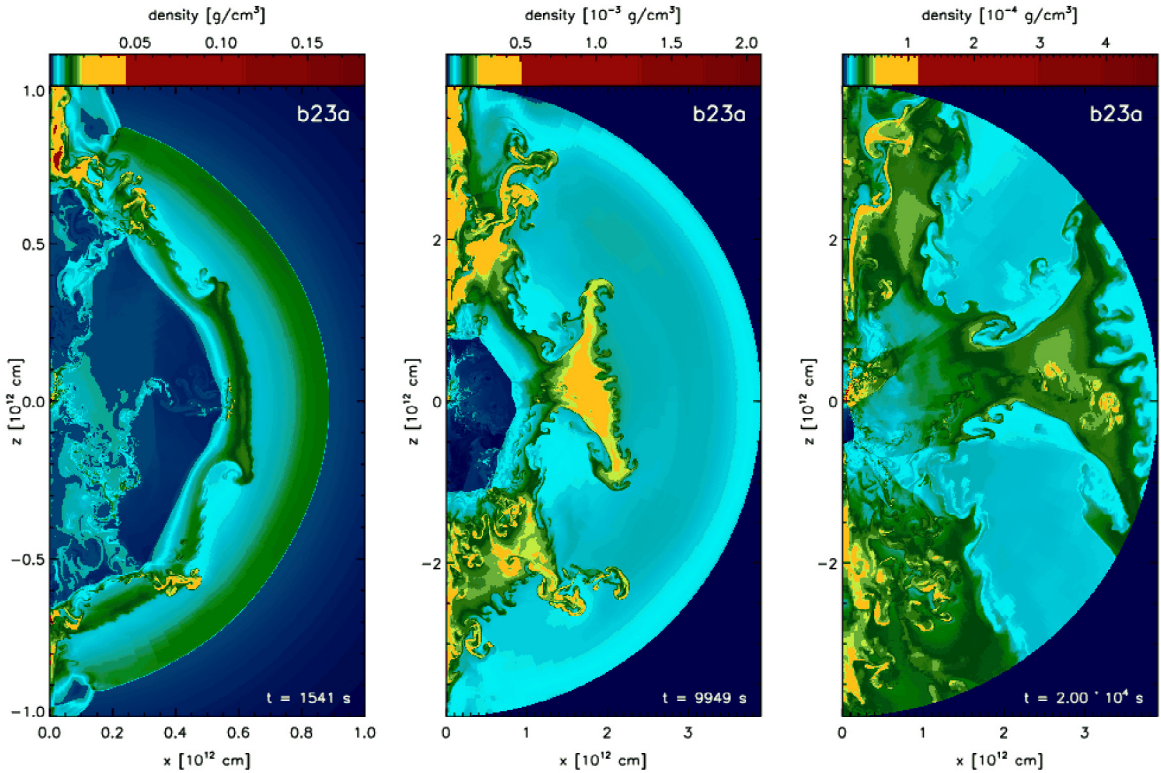


Fig. 1.9b. Snapshots of the density distribution for selected late instants in time. From left to right (a) $t \approx 1500 \text{ s}$, (b) $t \approx 10\,000 \text{ s}$, and (c) $t \approx 20\,000 \text{ s}$.
Source: From Fig. 3 of Kifonidis et al. (2006), *Astron. Astrophys.* with permission.

Imperial College, London (Lebedev et al., 2001, 2005; Mitchell et al., 1996) and in the Angara-5 facility in Russia (Grabovskii et al., 2004; Al'bikov et al., 1990; Aleksandrov et al., 2012, 2016).

At Los Alamos National Laboratory (LANL), the Plasma Liner Experiment (PLX) is a facility for studying spherically imploding plasma liners via multiple merging plasma jets (Hsu et al., 2012). For fundamental High-Energy-Density-physics (HEDP) studies (Drake, 2006), PLX is envisioned to provide an economic means for forming inertially confined cm-, μs -, and Mbar-scale plasmas (Hsu et al., 2015). It has been used to observe the Rayleigh-Taylor-instability evolution in a plasma with magnetic and viscous effects (Adams et al., 2015).

In a pioneer paper, Nuckolls et al. (1972) first noted the extreme density and pressure at astrophysical settings. Indeed, the matter in the cores of white dwarf is believed exist at more than $10^5 \text{ g}/\text{cm}^3$ and at pressures greater than 10^{15} atmospheres (Chandrasekhar, 1938). Hydrogen is believed to exist at more than one thousand times liquid density and at pressure greater than 10^{11} atmospheres (temperature $\sim 1\text{--}2 \text{ KeV}$) in the center of the Sun (Schwartzschild, 1965). Nuckolls et al. pointed out that hydrogen may be compressed to more than 10,000 times liquid density by an implosion system energized by a high energy density laser.

The books by Lindl (1998) and Atzeni and Meyer-Ter-Vehn (2004) provide a comprehensive treatment of the ICF. Here, a basic description of the ICF concept is given for completeness, adopted from that provided in Lindl (1995). To achieve conditions under which inertial confinement is sufficient for efficient thermonuclear burn, high-gain ICF targets have features similar to those shown in Fig. 1.10 (Betti and Hurricane, 2016). A capsule generally is a spherical shell filled with low-density gas. The shell is composed of an outer region, which forms the ablator, and an inner region of frozen or liquid deuterium-tritium (DT), which forms the main fuel. Energy from a driver is delivered rapidly to the ablator, which heats up and expands. As the ablator expands outward, the rest of the shell is forced inward to conserve momentum. The capsule behaves as a spherical, ablation-driven rocket. The work that can be done on the imploding fuel is the product of the pressure generated by the ablation process times the volume enclosed by the shell. The peak achievable implosion velocity determines the minimum energy (and mass) required for ignition of the fusion fuel in the shell.

The RTI is an important issue in the design of targets for laser fusion (ICF). The mechanism by which RT growth degrades capsule performance has been documented in many publications, and it can be concisely summarized as follows (Dittrich et al., 1994). As the ablation phase of the implosion proceeds, surface imperfections grow via the RT instability as low density ablated material pushes on the high-density shell. This growth causes the imploding shock to deviate from spherical, carrying the perturbation information through the shell and rippling the interface between pusher and fuel. Later in time when the

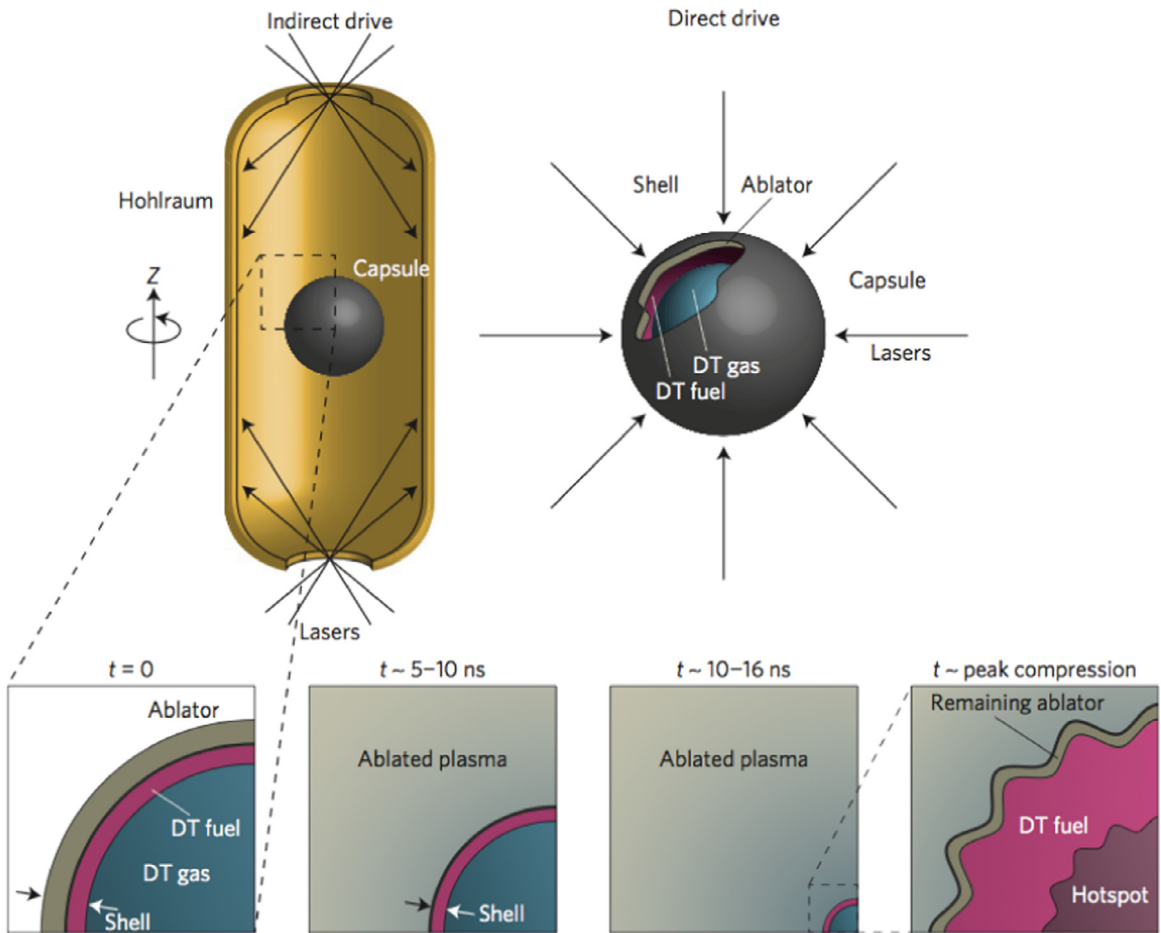


Fig. 1.10. Schematics of indirect- and direct-drive ICF. Typical targets used in laser-driven ICF are indirectly driven (upper left) or directly driven (upper right). In either case, a spherical capsule is prepared at $t = 0$ with a layer of DT fuel on its inside surface. As the capsule surface absorbs energy and ablates, pressure accelerates the shell of remaining ablator and DT fuel inwards—an implosion. By the time the shell is at approximately one-fifth of its initial radius it is traveling at a speed of many hundreds of kilometers per second. By the time the implosion reaches minimum radius, a hotspot of DT has formed, surrounded by colder and denser DT fuel.

Source: Fig. 1 of Betti and Hurricane, *Nature Physics*, 2016, with permission.

fuel is compressed, the pusher/fuel interface becomes RT unstable, which causes this rippling to grow and produce a region of mixed pusher and fuel material. Increasing the initial outer surface perturbation increases the degree of pusher–fuel mixing.

ICF implosions are subject to RT and RM instabilities during several phases of the implosion: During the initial shock and acceleration phase as the shell is brought up to its peak implosion velocity, RM instabilities at the various interfaces is followed by ablation front RT growth as the low-density blowoff plasma accelerates the dense shell of solid ablator and fuel. During the later acceleration phase, RT instability is also possible between the ablation shell and DT fuel if the Atwood number at that interface increases to put that interface in an unstable configuration (Hammel et al., 2010; Clark et al., 2011). Finally, during deceleration, multiple shock reflections occur between the implosion center and the in-flying dense shell as the implosion stagnates causing further RM instability around the forming hot spot and finally deceleration RT as well (Haan et al., 1995; Herrmann et al., 2001; Lobatchev and Betti, 2000).

More specifically, ICF depends on the formation of a central hot spot with sufficient temperature and areal density for ignition (Lindl et al., 2004; Glenzer et al., 2010). Radiative and conductive losses from the hot spot will be increased by hydrodynamic instabilities (Haan et al., 2011). For example, for the Rev. 5 ignition design, the Richtmyer–Meshkov and Rayleigh–Taylor hydrodynamic instabilities seeded by high-mode ($50 < l < 200$) ablator-surface mass perturbations from intrinsic surface roughness, the fill tube, or microscopic dust particles are predicted to mix ablator material into the interior of the shell at the end of the acceleration phase and into the hot spot as it forms (i.e., hot-spot mix). This produces enhanced hot spot X-ray emission (Hammel et al., 2010, 2011). Ablator mass mixed deep into the hot spot at ignition time greatly enhances the radiative and conductive losses of the hot spot (Regan et al., 2012).

RT and RM instabilities can cause breakup of the capsule shell and prevent ignition in ICF implosions (Haan et al., 2011; Thomas and Kares, 2012; Smalyuk et al., 2014a; Raman et al., 2014; Casey et al., 2015a). Ignition can be quenched either by

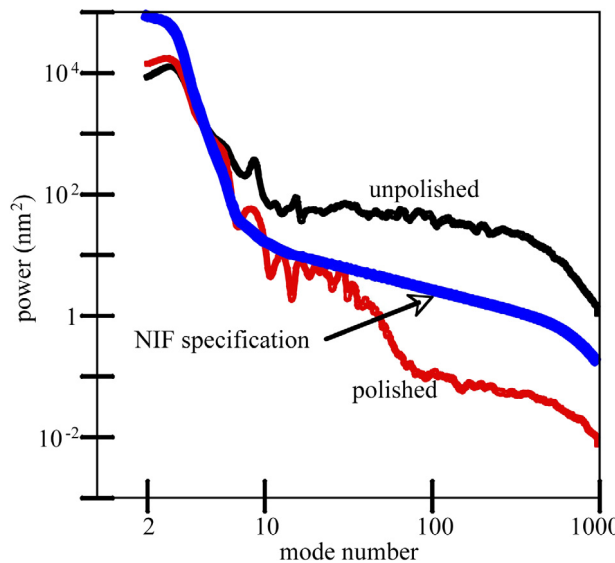


Fig. 1.11. Shown is an example of the effect of polishing on the outer surface power spectra.
Source: From, Fig. 2, (Cook et al., 2008), *Laser and Particle Beams*, with permission.

aneurysms in the density imploded shell leading to a loss of confinement or due to entrainment and mix of ablator material deep into the hot spot during the fusion fuel (Smalyuk et al., 2014b; Ma et al., 2013, 2017; Clark et al., 2016).¹⁰

The flows induced by RT and RM instabilities are time dependent and undergo both the linear and nonlinear phases of growth.¹¹ In some cases, this can result in a transition to turbulence, thought this is not believed to occur in current DT-layered ICF implosions (Weber et al., 2014a). The Kelvin–Helmholtz instability (KHI) plays a critical role for the time-dependent transition process (Zhou et al., 2003a,b; Zhou, 2007). KHI is induced from an unstable perturbed interface between fluids subject to a parallel shear flow and is one of the classical problems in fluid dynamics (Chandrasekhar, 1961; Drazin and Reid, 1981). The development of KHI often constitutes the critical step toward the onset of turbulent mixing observed both in the atmosphere and in oceans (Peltier and Caulfield, 2003; Woods, 1968). Also, the KH instability is the reason for the evolution of the mushroom structures during the RT and RM nonlinear process (Yabe et al., 1991; Zabusky, 1999; Collins and Jacobs, 2002). Hereafter, RTI, RMI, and KHI will be collectively referred to as hydrodynamic instabilities.

Three-dimensional numerical simulations and experimental data showed that the neutron yield of an ICF target capsule varies as the surface roughness of the inner shell of the capsule varies, because the level of mix that is induced during the implosion phase varies (Marinak et al., 1996). Clark et al. (2013) included the surface roughness in their detailed implosion modeling of deuterium–tritium layer experiments on the NIF. Clearly, reduction of this seed or its subsequent growth is important to the ultimate success of ICF (Watt et al., 1998). Recent years have seen significant progress in NIF capsule fabrication, including large improvements in the capsule surface smoothness (Nobile et al., 2006; Cook et al., 2008; Simakov et al., 2014). This is illustrated by black and red lines in Fig. 1.11 (reproduced from Fig. 2 of Cook et al.), which correspond to surface roughness measurements from fabricated NIF capsules.

Double-shell targets have been suggested as an alternative design for demonstrating and exploring ignition on the NIF (Amendt et al., 2002, 2007, 2010; Canaud et al., 2011), as the volumetric ('PdV') ignition in double shells is fundamentally different from the conventional "hot spot" ignition approach. Double-shells consist of a low-Z ablator outer shell that impacts a high-Z inner shell filled with high-density DT gas at room temperature instead of cryogenic preparation below the triple point of DT (≈ 19 K) (see Fig. 1.12). The outer shell acts as an efficient absorber of hohlraum-generated X-rays; it magnifies and transfers the acquired energy density when it spherically converges and collides with the inner shell. The main function of the high-Z inner shell is to limit radiative losses from the igniting fuel and to provide added inertia for delaying fuel disassembly.

Amendt et al. (2002) stressed that an important concern for double-shell stability is the feed-through of outer-surface perturbations on the inner shell to the inner surface. At the time of shell collision, an impulsive-like acceleration will be

¹⁰ Nagel et al. (2015) used X-ray area-backlit imaging to assess in-flight low mode 2D asymmetries of the shell, with a focus on the effect of the shell mounting membrane on both the radiographs and hot spot self emission images. Tommasini et al. (2015) reported on the first analysis of the perturbations induced by the tents on the in-flight areal density profiles and symmetry. The authors show that the areal density perturbations increase with the increase in tent thickness and a clear correlation exists between the modulations imposed on the areal density and the measured neutron yield.

¹¹ Goncharov (1999) differentiates the normal RM instability from the RMI which occurs at the ablation front during the shock transit (he calls it ablative RM instability).

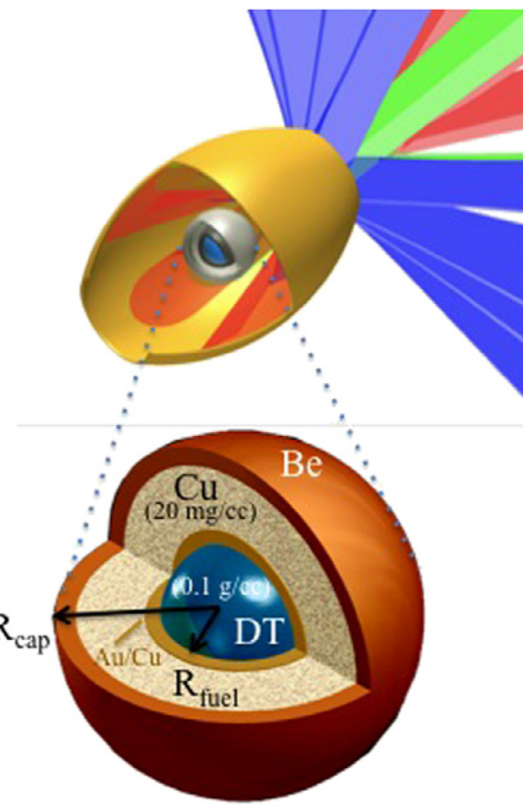


Fig. 1.12. Schematic of double-shell target design in a hohlraum. The nominal DT fuel density is 0.1 g cm^{-3} and the intra-shell Cu foam density is 20 mg cm^{-3} .

Source: Fig. 1 of Amendt et al. (2010), with permission from *Nucl. Fusion*, International Atomic Energy Agency.

delivered to the outer surface of the inner shell, promoting the RMI. The subsequently induced RT instabilities will also demand careful considerations in such design. Welser-Sherrill et al. (2008) applied the concepts of the fall-line (Amendt et al., 2002, 2005) to compute the mix-degraded yield. They have also evaluated an interface penetration fraction model developed by Amendt et al. (2002). Li et al. (2013) presented an analysis of the preheat by radiative shock in the double-shell target and illustrated the role of the preheat in mitigating the hydrodynamic instabilities.¹²

It is clear from the intensive efforts devoted to the ICF research that hydrodynamic instabilities are a critical issue. The reader is referred to the following publications and references cited: Aglitskiy et al. (2001, 2002, 2010, 2012), Barnes et al. (2002), Betti et al. (1996, 1998, 2001, 2010, 2002), Bradley et al. (2012), Bychkov et al. (1994), Casey et al. (2015a, b), Chen et al. (1994), Dahlburg et al. (1993, 1995), Gardner et al. (1991), Hager et al. (2013), Hinkel et al. (2006), Hurricane et al. (2012), Lanier et al. (2003), Ma et al. (2013, 2017), Marocchino et al. (2010), Radha et al. (2002), Roberts et al. (1980), Smalyuk et al. (1999, 2002, 2014a, b, 2017), Takabe (2004), Takabe et al. (1983, 1985, 1988), Thomas and Kares (2012), Wilson et al. (2003, 2004). The technical issues are obviously very complicated and present different challenges for a given capsule design. It is beyond the scope of this review to provide a comprehensive survey of this subject and this list only represented an incomplete collection of publications on this important subject.¹³

¹² As summarized succinctly by Di Stefano et al. (2017), the phenomenon of preheating of components is primarily due to X rays or energetic particles produced by laser–material interactions in laser-driven HEDP systems (Yaakobi et al., 1976; Lindl, 1998; Shu et al., 2014). This preheat can cause instability-like growth of structure at interfaces present in the system, which in turn alters the initial conditions and therefore complicates the analysis of processes that depend on those initial conditions. The authors found that if the amount of preheat is low (or the amount of time the system has to preheat is short), the longer wavelengths in the system, at approximately their initial amplitudes, will dominate as the main seed for instability. On the other hand, if the system is allowed to preheat for a longer time, then the influence of the shorter wavelengths will become stronger due to their faster initial growth.

¹³ Hydrodynamic instabilities in ICF is a major area of concern for alternative approaches to fusion as well. Slutz et al. (2010) noted that the magneto-Rayleigh–Taylor instability poses the greatest threat to so-called Magnetized Liner Inertial Fusion (MagLIF). Gomez et al. (2014) showed that magneto-RTI would not preclude successful integrated experiment in their testing of this concept on the Z facility. Attempting to sidestep these issues, Ren et al. (2017) proposed a new laser-driven spherically convergent plasma fusion (SCPF) scheme and demonstrated its principle experimentally at the ShengGuang III-prototype facility.

Finally, we will direct the reader's attention to some discussion in Section 15, Part II (Zhou, 2017) on the role of hydrodynamic instabilities relevant to some exciting experiments carried out at NIF (Dittrich et al., 2014; Hurricane et al., 2014a,b; Park et al., 2014).

1.5. Synopsis

Every year, there are significant numbers of publications on the subject matters related to RT and RM instabilities and many graduate students enter this exciting field. Unfortunately, many years have been passed since the publication of the review articles: D.H. Sharp, "An overview of Rayleigh–Taylor instability", *Physica D*, 12 (1984) p. 3, H.J. Kull, "Theory of the Rayleigh–Taylor instability", *Phys. Reports*, 206, (1991), p. 197, and M. Brouillette, "The Richtmyer–Meshkov Instability", *Annual Review of Fluid Mechanics*, 34, (2002) p. 445. The need for an updated, thorough review is especially acute because the topic presented is one of exceptional practical and fundamental importance. Not only were the significant issues not adequately covered in these existing reviews, but also that some major progress was simply impossible until recently, with the advancement of the supercomputing power as well as sophisticated diagnostics tools for the laser and laboratory experiments. The goal of this review article is to fill this gap by providing a much-needed comprehensive survey. All updated theoretical, computational, and experimental results will be incorporated.

The challenge confronting researchers is significant in many ways. One can start by noting that multiple instabilities might exist simultaneously and interact with each other. Oblique shocks generate all three instabilities: RT, RM, and KH (Mikaelian, 1994b). Using the results of acetylene shock tube experiments, Meshkov and his colleagues (Meshkov, 1995; Vlasov et al., 1996; Dudin et al., 1997; Bazarov et al., 2007) studied the features of turbulent mixing zone development at an interface accelerated by a non-stationary shock wave (Fig. 1.13). In this case of coupled RT and RM instabilities, the authors found that these instabilities suppress each other in some situations (Meshkov, 2013). Furthermore, both RT and RM instabilities might be involved simultaneously in the deceleration phase of ICF implosions, which has been investigated, for example, by Bradley (2014) with a hydrodynamics code to examine the amount of shock-induced RMI mixing versus RTI mixing. For linear and nonlinear phases, analytical models have been developed. An emphasis will be placed on these models that have been compared with laboratory experiments.

The mix induced by hydrodynamic instabilities is also a transitional problem. For high energy density physics applications, such as experiments on both lasers and Z pinch platforms, flows start from rest at $t = 0$, but most impact of the turbulent mixing occurs at the later time. It should be noted that transition is a major fluid dynamics field on its own right (see for instance Saric et al., 2003; Mullin, 2011). Dimotakis (2000, 2005) suggested the basic requirement for mixing transition to occur. For astrophysical flows and ICF applications, however, the flows must meet both the spatial and temporal criterions in order to achieve the transition to turbulence (Zhou et al., 2003a,b, 2009; Robey et al., 2003; Zhou, 2007). The so-called Zhou–Robey hypothesis is shown to explain the onset of turbulence in several specific cases (Drake et al., 2008).

There is significant evidence that the flows due to hydrodynamic instabilities might be initial condition dependent, while a few contrary studies have also been reported. The possible parameter space for the initial condition is extremely large. The first variable is the ratio between the initial amplitudes and wavelength. As one can appreciate, characterization of these values from the flow fields could be rather nontrivial in traditional fluid dynamics or shock tube experiments. Nevertheless, major progress has been made on this front. In this matter, there are two distinctive approaches that do start with well-defined initial perturbations. First, the unique properties of magnetic fluids offered a precise and arbitrary control of the initial interface shape, including but not limited to the ferrofluids (Pacitto et al., 2000), paramagnetic fluids (Carlès et al., 2006; Huang et al., 2007; Renault et al., 2011, 2013, 2015; Tsiklashvili et al., 2012; Adkins et al., 2017), and magnetorheological fluids (White et al., 2010). Second, the experiments performed on a high-energy-density physics (HEDP) platform have a natural advantage as the perturbations can be machined precisely as the target is built from solid-state materials.¹⁴

There is considerable freedom in setting up a hydrodynamic instability induced flow. The mixing layer due to RMI, for instance, could be rather sensitive to the strength of the shock (denoted by the Mach number), if the direction of the shock is from heavy to light or light to heavy fluids, and whether it results from a single or multiple shocks. The Atwood, Mach, and Reynolds numbers may be used *a priori* to characterize RM experiments or simulations (Motl et al., 2009; Gallis et al., 2015). Furthermore, numerical results of Ward and Pullin (2010, 2011) for RMI in fluids with Mie–Grüneisen equations of state¹⁵ revealed several noteworthy differences from the results with perfect gas (Kennard, 1938) under nondimensionally matched

¹⁴ In a case study, Spindloe et al. (2015) documented the fabrication of a suite of laser targets for the first academic-access experiment on the Orion laser facility at Atomic Weapons Establishment (AWE). This experiment, part of the POLAR project (Falize et al., 2011a; Busschaert et al., 2013), studied conditions relevant to the radiation-hydrodynamic processes occurring in a class of astrophysical star systems known as magnetic cataclysmic variables. It is also interesting that 3D printing might be of benefit to the target fabrication community. Klein et al. (2016) found that 3D printing alone was not feasible for the scale of targets that are used in the experiments. However, combining 3D printing with traditional machining, the University of Michigan team was able to take advantage of the very best part of both aspects of manufacturing.

¹⁵ Mie–Grüneisen equations of state were derived from a linear shock-particle speed Hugoniot relationship (Burshtein, 2008; Jeanloz, 1989; Mcqueen et al., 1970; Menikoff and Plohr, 1989; Roberts and Miller, 1954; Zeldovich and Raizer, 1966).

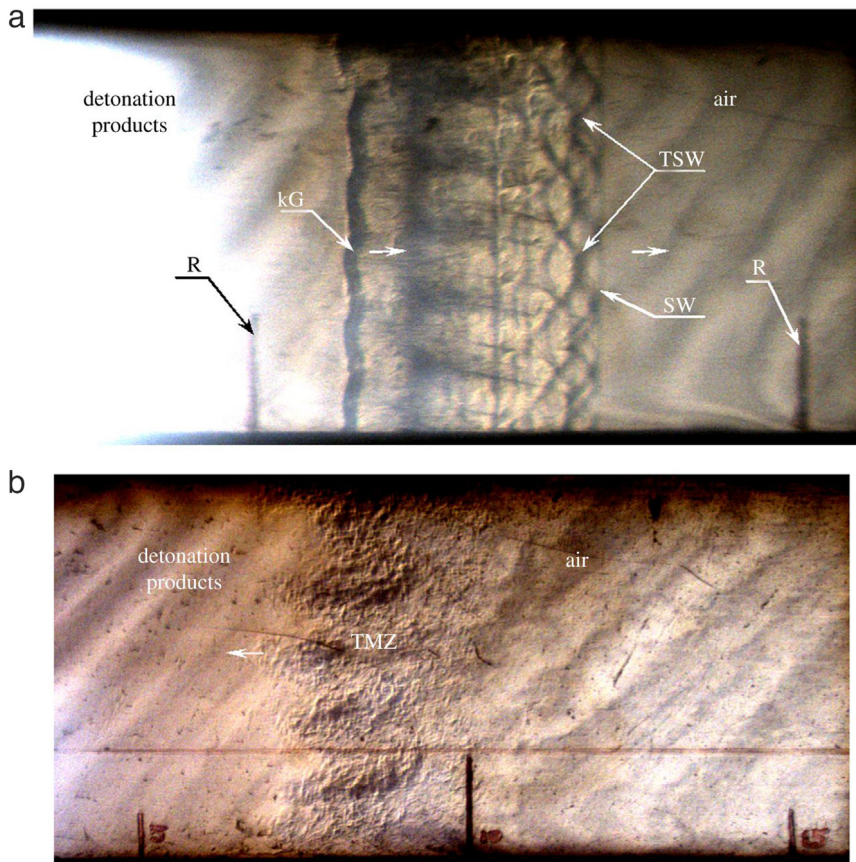


Fig. 1.13. The flow pattern in the acetylene shock tube for various times: (a) 100 μs ; (b) 700 μs . The time is counted from the time of initiation of the acetylene–oxygen mix layer; SW, shockwave; TSW, transverse shockwave system; kG, detonation products–air interface; TMZ, turbulent mixing zone; R, reference. Arrows show flow direction. Fig. 1.13a illustrates a complicated and regular flow structure behind the shock wave front at the initial times in the shock tube. The observed pattern represents the flow behind the shock wave front with three-dimensional periodic perturbation. Fig. 1.13b shows that the turbulent mixing zone develops quickly after the reflected wave.

Source: Fig. 11 of Meshkov (2013), *Philosophical Transactions of the Royal Society A*, with permission.

initial conditions at room temperature and pressure.¹⁶ For both RTI and RMI, one might be interested in the disparity between the densities of the interfacial materials (Atwood numbers), the existence of the viscosity, surface tension, and diffuse interface, as well as whether the geometry is planar, cylindrical, or spherical.

The problem becomes even more difficult after the flow induced by instabilities pass the linear, nonlinear regimes and eventually transition to turbulence. According to Hunt and Kevlahan (1993), turbulence is rather like certain diseases, which are defined by a collection of symptoms called a syndrome. These ‘symptoms’ include “randomness with a finite probability density function, strong vorticity, a complex highly three-dimensional velocity field, motion over a large and continuous range of length scales.” Renowned physicist Richard Feynman pointed out that the turbulence problem is still referred to as the last unresolved classical physics problem (Feynman et al., 1964). The presence of strong nonlinear interactions makes turbulence a truly multiple scale problem. In many problems in fundamental physics, one must simultaneously deal with uncertainty in the underlying equations of motion and with uncertainty in our ability to solve them. In turbulence, we have only the latter (Nelkin, 1994).

The scope of this review is to provide a comprehensive analysis of physics processes involved with RT and RM instability induced flow, turbulence, and mixing within a unified framework. Aimed to render the article accessible to a broad audience in the community, a significant effort is devoted to structure the review in a self-contained and pedagogical fashion.

¹⁶ The Equation of State (EOS) of matter is of great importance for accurate modeling of matter. As an example, a Mie–Grüneisen equation of state (Swegle and Robinson, 1989; Bakharakh et al., 1997) has been used in numerical simulations of RTI (López cela et al., 2006) or in analytical modeling of RMI (Piriz et al., 2006) in elastic solids. It is interesting that HEDP platforms have been developed to measure the material properties, such as EOSs, at high pressures and high densities (Kritcher et al., 2014; Remington et al., 2015), driven partly by a desire to understand the properties and structures of core-collapse supernovae, compact stars, compact star mergers (Oertel et al., 2017), highly evolved stars (Fortov, 2011), gas-giant planets (Seager et al., 2007; Stixrude, 2012), or the Earth (Dziewonski and Anderson, 1981; Buffett, 2000; Wang et al., 2013).

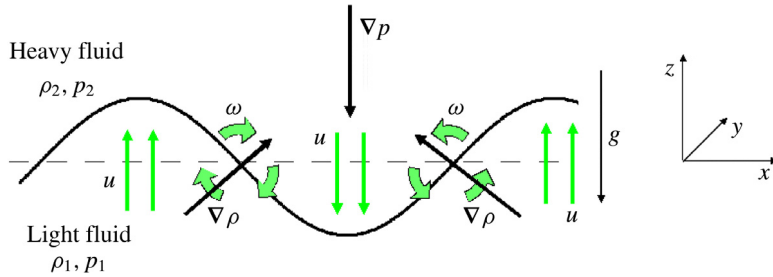


Fig. 2.1. Visualization of an unstable RT configuration baroclinic torque at the interface creates vorticity and induced a velocity field that increases the baroclinic torque.

Source: Fig. 1 of [Roberts and Jacobs \(2016\)](#), *J. Fluid Mech.* with permission.

2. Linear arguments and single modes instabilities

2.1. Basic linear stability arguments

In this section, we consider the single-mode RT and RM induced flows. The initial interface perturbation can be described by a single sine function of known amplitude (a) and wavelength (λ). The following linear theory is fully general due to the principle of superposition. Here, any perturbation at a plane boundary can be represented as a sum of Fourier modes, $e^{i(k_x x + k_y y)}$, and the theory applies to a mode of wavelength λ where the total wavenumber is $k = \sqrt{k_x^2 + k_y^2} = 2\pi/\lambda$.

Single-mode RT or RM instability is a rather special case. In the long term, small irregularities will inevitably grow and break the repetitive symmetry of the initial conditions. Indeed, surfaces with regular grooves are a common result of machining processes. The asymptotic behavior of instabilities growing from such regular surfaces may still be a useful guide to behaviors which may be found in experimental studies at intermediate times.

2.1.1. RT linear growth rate

[Fig. 2.1](#) is shown to provide the reader a visual aid for the onset of the RTI. Here g is gravity, p is the pressure, ρ is the density, and ω is the vorticity.¹⁷ The thick circular arrow represents the velocity field created by vortex. The interface becomes RT unstable if $\rho_2 > \rho_1$ and an acceleration is applied in the direction toward the denser fluids. As simply put by [Sharp \(1984\)](#), if the heavy fluid pushes the light fluid, the interface is stable; if the light fluid pushes the heavy fluid, the interface is unstable.

RTI is induced when there is a mismatch between the density gradient and pressure ([Taylor, 1950](#))

$$\nabla\rho \cdot \nabla p < 0. \quad (2.1)$$

More specifically, the RTI can be viewed to be the result of baroclinic torque created by such misalignment, as given by the inviscid 2D vorticity equation ([Cohen and Kundu, 2004](#))

$$\frac{D\omega}{Dt} = \frac{1}{\rho^2} \nabla\rho \times \nabla p, \quad (2.2)$$

As described by [Roberts and Jacobs \(2016\)](#), the dominant pressure results from the acceleration. In the unstable configuration, the torque on the interface creates vorticity as a result of a particular harmonic component of the initial perturbation. This will tend to generate additional misalignment of the gradient vectors, and in turn, creating additional vorticity and further misalignment ([Fig. 2.1](#)). The right hand side of Eq. (2.2), the baroclinic term, is the source by which vorticity is generated ([Holton, 1992](#)).

Using a linear stability analysis ([Rayleigh, 1883](#); [Taylor, 1950](#); [Drazin and Reid, 1981](#)), the growth of the amplitude, a , of small single-mode perturbation on a discontinuous interface is given by

$$\frac{d^2a}{dt^2} = gkAa \quad (2.3)$$

where $k = 2\pi/\lambda$ is the wavenumber, and A is the Atwood number,¹⁸

$$A = \frac{\rho_2 - \rho_1}{\rho_2 + \rho_1}. \quad (2.4)$$

¹⁷ The vorticity vector is given by the components of the curl of the velocity vector (see for example [Dryden et al., 1956](#)).

¹⁸ [Mohseni et al. \(2014\)](#) have introduced the relativistic Atwood number, Ar , which is typically smaller than the nonrelativistic one, A , for the same value of the density ratio. They have also shown that relativistic effects weaken the RM instability.

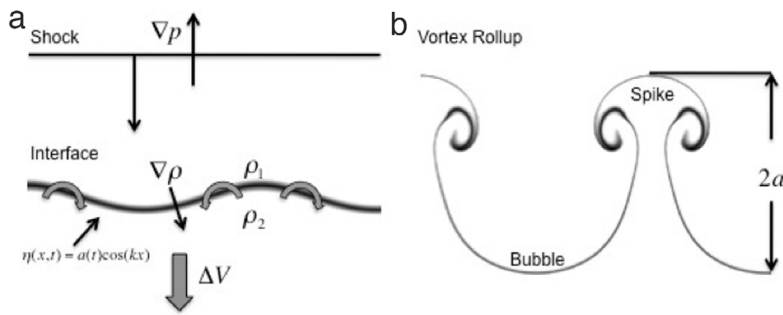


Fig. 2.2. Explanation of the deposition of baroclinic vorticity on the interface. (a) The shock wave travels downward toward the interface and applies a pressure gradient across the density gradient which generates baroclinic vorticity on the interface. (b) This baroclinic vorticity rolls up into spikes of heavy fluid separating bubbles of light fluid as the interface travels down the shock tube with the mean post-shock flow. Note that the interface velocity jump, in Richtmyer's formalism, is denoted as ΔV here.

Source: Fig. 1 of Morgan et al. (2012), J. Fluid Mech. with permission.

The growth rate, γ , is given by

$$\gamma = \pm(gkA)^{1/2}. \quad (2.5)$$

The formulae for linear growth rate were in both the Rayleigh (1883) and Taylor (1950) papers.¹⁹

The linear phase of RTI will eventually transition to a nonlinear regime. To preserve continuity in amplitude and growth rate, the nonlinear transition may occur when the linear velocity equals the terminal velocity (attributed to Enrico Fermi, see Layzer, 1955) and this occurs near saturated modes of intrinsic scales when the growth rate is classical \sqrt{gkA} (see also Dimonte, 2004). The “terminal bubble velocity”, varies as \sqrt{gkA} , was first measured in Lewis' 1950 paper. In the early research it was assumed that bubbles reached a terminal velocity and spikes grew as $\frac{1}{2}gt^2$. This picture of single mode behavior at $A = 1$ is origin of the use of the terms “bubble” and “spike” that we still use today.

To clarify specific features of RTI in 2D and 3D geometries, Kuchugov et al. (2014) presented results from their theoretical analysis and numerical simulations. For single-mode perturbations, the authors found that there are practically no differences in the development of 2D and 3D perturbations up to the end of the linear stage. Then, 3D perturbations start to grow faster than 2D ones, in agreement with the authors' previous arguments (Kuchugov et al., 2012) and early simulation of Tryggvason and Uverdi (1990). Anuchina et al. (2004) also studied the 2D and 3D evolution of single-mode interface RT perturbations both at the linear and nonlinear stages. Using their MAH-3 code, the authors found their 2D bubble velocity is consistent with the classical result of Daly (1967) and slower than the corresponding 3D value (see also Liang et al., 2016). Finally, Lee and Kim (2013) found that the three-dimensional Rayleigh–Taylor instability exhibits a stronger dependence on the density ratio than on the Reynolds number. They observed the two-layer roll-up phenomenon of the heavy fluid, which does not occur in the 2D case.

Some explanation of what is meant by 2D and 3D is given here. In these references the perturbations used are $\cos(k_2x)$ for 2D and $\cos(k_3x)\cos(k_3y)$ for 3D. The 3D mode is the sum of two Fourier modes with total wavenumber $\sqrt{2}k_3$ which is chosen equal to k_2 . This ensures the linear growth is identical. In the non-linear phase the bubbles develop into archways (2D), near-cylindrical bubbles (3D) and this is very similar to the 2D/3D behavior described in the Layzer equation (see Section 3.1). Note also that other researchers have used a $\cos(kx) + \cos(ky)$ perturbation for the 3D case.

2.1.2. RM linear growth rate

RM instability occurs when the density gradient and pressure gradient are misaligned (the incident shock wave propagates from a light to a heavy fluid ($\nabla\rho \cdot \nabla p < 0$) or from a heavy to a light fluid ($\nabla\rho \cdot \nabla p > 0$), see Lombardini et al., 2011). Fig. 2.2, adopted from Morgan et al. (2012), helps to explain the deposition of baroclinic vorticity on the interface. The shock wave travels downward in the interface and applies a pressure gradient across the density gradient which generates baroclinic vorticity on the interface. Another perspective to interpret the occurrence and development of the RMI is the pressure disturbance mechanism, which is related to the formation, focus and interaction of shock waves (Haas and Sturtevant, 1987).

In the weak shock limit, the RM instability may be viewed as a version of Rayleigh–Taylor instability in which the gravitational force is impulsive. Richtmyer (1960) recognized this connection with RTI very early. He applied the linear theory of Taylor (1950), but now modeled the shock interaction with an interface as the impulsive acceleration of two

¹⁹ The RT linear theory (Eq. (2.5)) is just the theory for waves at a stable interface with the sign of g reversed – if V_W is the wave speed (with $kV_W = \pm\sqrt{gkA}$, see Lamb, 1932).

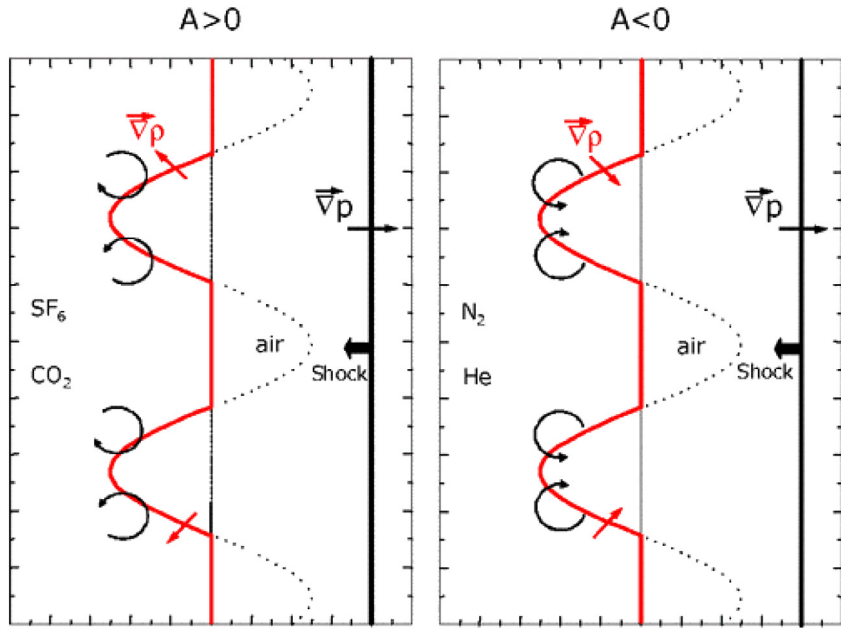


Fig. 2.3. Scheme of the present initial perturbations showing the deposition of vorticity in light/heavy and heavy/light cases (labels of the curves: --- effective, ... imaginary).

Source: Fig. 1 of Jourdan and Houas (2005), *Physical Review Letters* with permission.

incompressible fluids. Using Dirac delta function, $g = \Delta V \delta(t)$, the growth rate of the RM (modeled as the impulsively accelerated) instability takes the form

$$\frac{d^2a}{dt^2} = kA\Delta V \delta(t) a_0, \quad (2.6)$$

where $\delta(t)$ is the Dirac delta function, ΔV denotes the interface velocity jump, and a_0 is the initial amplitude. To agree with his numerical solutions to the compressible, linearized Euler equations Richtmyer proposed using post-shock Atwood numbers and amplitudes, i.e.

$$da/dt = kA^+ \Delta V a_0^+. \quad (2.7)$$

In this review, the subscript $-$ and $+$ denote the pre- and post- shock quantities, respectively. Motl et al. (2009), among others, illustrated the growth of the impulsive model against several experimental data. It should be noted that linear theory is derived assuming $|ka| \ll 1$.

Unlike the RTI, RMI can be induced regardless of the direction of the fluid accelerations. The first configuration, of course, has the similar orientation as that producing RTI. Here, the shock traveling from the light to the heavy gas (see Fig. 2.3, left figure) would result in a direct amplification of the initial perturbations at the interface. Most of the studies undertaken in this field focus on the light/heavy case because it is directly concerned with the ICF (Jourdan and Houas, 2005).

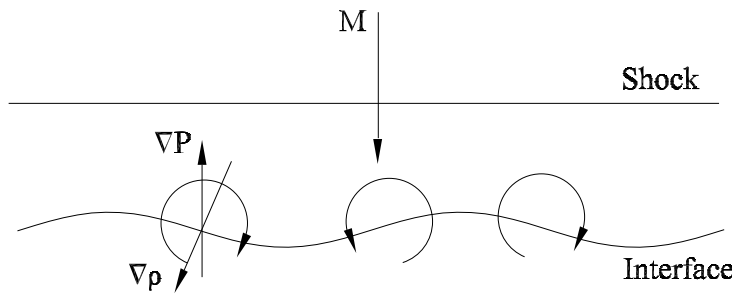
In the case of a shock traveling from the heavy to the light gas (see Fig. 2.3, right figure), a reversal phase of the initial perturbations is observed, and they continue growing in time thereafter, maintaining the changed phase (Jourdan and Houas, 2005). Fig. 2.4, adopted from Fig. 10 of Puranik et al. (2004), showed how the RM shock causes a phase inversion for the heavy/light configuration. It also illustrated that the sense of vorticity (clockwise or counterclockwise) depends upon the direction of shock propagation.

Richtmyer only considered the light-to-heavy configuration. In this case, both transmitted and reflected waves are shocks. The analysis for the heavy-to-light configuration, in which the reflected wave is a rarefaction wave, can be found in Yang et al. (1994). Meshkov (1969) pointed out the applicability of the impulsive model of Richtmyer to the both configurations and ran shock tube experiments with the acceleration direction from both sides (Collins and Jacobs, 2002). Meyer and Blewett (1972) carried out a 2D Lagrangian simulation of the single-mode RM flow to model Meshkov's experiments. These authors found that an improved agreement with simulated data can be achieved by letting

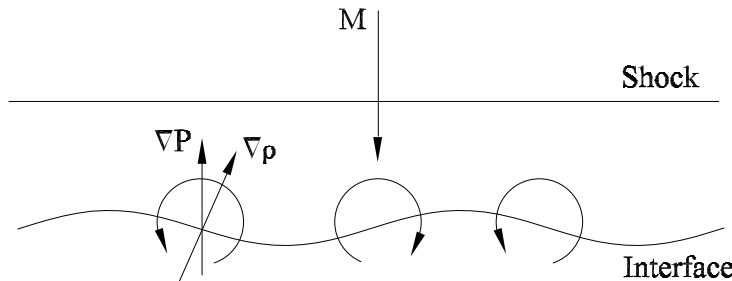
$$\frac{da}{dt} = kA^+ \Delta V (a_0^+ + a_0^-)/2. \quad (2.8)$$

Heuristically, Vandenboomgaerde et al. (1998) proposed another modified Richtmyer model,

$$\frac{da}{dt} = k\Delta V \{ [(A^+ a_0^+ + A^- a_0^-)/2] - [(A^+ - A^-)(a_0^+ - a_0^-)/6] \}. \quad (2.9)$$



Shock traveling from light to heavy fluid: no phase reversal.



Shock traveling from heavy to light fluid: phase reversal.

Fig. 2.4. Schematic showing the shock-interface interaction for the case of a shock traveling from a light to a heavy gas and vice versa, illustrating whether or not the deposition of vorticity results in phase reversal.

Source: From Fig. 10 of [Puranik et al. \(2004\)](#), with permission from *Shock Waves*.

The second part of the right-hand side is dropped, as it appears to be very small in most cases tested. Vandenboomgaerde, Mügler, and Gauthier (1998) validated the following formula

$$\frac{da}{dt} = k \Delta V \left[(A^+ a_0^+ + A^- a_0^-) / 2 \right]. \quad (2.10)$$

This expression may be reduced to the Richtmyer or the Meyer–Blewett formulas in particular cases.

Several additional works have discussed the linear phase of the RM instability ([Fraley, 1986](#); [Mikaelian, 1994a](#); [Yang et al., 1994](#); [Nishihara et al., 2010](#); [Wouchuk, 2001a,b](#); [Wouchuk and Nishihara, 1996, 1997](#); [Cobos Campos and Wouchuk, 2014](#); [Cobos Campos and Wouchuk, 2016, 2017](#); [Wouchuk and Cobos Campos, 2017](#)). Fraley's analysis reveals the complexities of shock/ interface interactions even in the linear regime. [Yang et al. \(1994\)](#) formulated and numerically solved the equations of the linear theory and compared systematically with Richtmyer's formula. [Li and Zhang \(1997\)](#) proposed a similar model and performed a comparative numerical study in two and three dimensions.²⁰ [Fraley \(1986\)](#) performed Laplace transforms and solved the linearized compressible perturbation equations,

$$\frac{da}{dt} = k \Delta V a_0^- \left[A^- + \left(\frac{\tilde{p}^+ - \tilde{p}^-}{\tilde{p}^+} \right) \frac{\tilde{F}}{\tilde{s}} \right] \quad (2.11)$$

where $(\tilde{p}^+ - \tilde{p}^-)/\tilde{p}^+$ is the shock strength. The function \tilde{F} is obtained explicitly in the first order of the shock strength (a misprint in Fraley's equation was noted by [Mikaelian, 1994a](#)). [Mikaelian \(1994a\)](#) compared the Fraley model with that of Richtmyer and determined that they agree reasonably well in most cases.

[Velikovich \(1996\)](#) determines that the RMI is related to the growth of initial transverse velocity perturbations at the interface, which may be either present initially as in symmetrical Riemann problem, or be induced by a shock passing through a corrugated interface. Because it is not caused by the instant normal acceleration of the interface, he argued that RMI is not a type of Rayleigh–Taylor instability. More recently, [Krechetnikov \(2009\)](#) found some particulars missing in Richtmyer's

²⁰ Note what is meant here by 2D and 3D simulations: 2D perturbation, $\cos(kx)$; 3D perturbation, $\cos(kx) + \cos(ky)$.

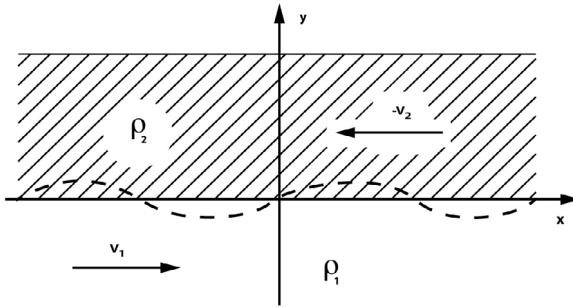


Fig. 2.5. Instability of a plane contact discontinuity. Surface perturbation can also grow by the KH instability if V_1 does not equal to V_2 .
Source: Fig. 2 of Kull (1991), *Phys. Reports.*

original treatment, including the effects of reference frames and initial velocity field perturbations. He clarified the interfacial curvature effects on the development of the RT and RM instabilities.

Kramer et al. (2010) investigated the single-mode RMI using a first-order perturbation of the two-dimensional Navier-Stokes equations in a one-dimensional unsteady shock-resolved base flow. Results from the simulations show that for weak and intermediate strength shocks, the impulsive model is adequate for prediction of the asymptotic growth rate of the perturbation. For strong shocks, the model from Wouchuk (2001a) accurately predicts the asymptotic growth rate. Lombardini and Pullin (2009) used a modified version of the impulsive theory to characterize the start-up process of the RM instability. Kramer et al. (2010) verified the characteristic start-up time proposed as a good estimate of the time for the instability to enter the linear growth regime.

Using an initial setup comparable to that of existing experimental work, Probyn et al. (2014) investigated non-linear growth rate of 2D and 3D single-mode RMI. Subsequently the code is used to evaluate the growth rate for a range of different initial conditions.

2.1.3. Kelvin-Helmholtz linear growth

As pointed already, the RTI or RMI causes the interface to roll up into the well-known mushroom-shaped structures (Inogamov, 1999). The shear layer at the interface of the fluids becomes KH unstable if there is a jump in the tangential component of the velocity across the interface. The growth rate of KHI is provided by (Drazin and Reid, 1981)

$$\gamma = \pm \left\{ gkA + \rho_1 \rho_2 k^2 \left[\frac{V_1 - V_2}{\rho_1 + \rho} \right]^2 \right\}^{1/2} - ik \left\{ \frac{\rho_1 V_1 + \rho_2 V_2}{\rho_1 + \rho_2} \right\}. \quad (2.12)$$

Fig. 2.5 provides a simple illustration for the onset of the KHI. Pertaining to the KHI, the counter-propagating velocities are given by the notations, \mathbf{V}_1 and \mathbf{V}_2 . Adopted from Kull (1991), it shows two infinitely extended fluids of different densities in a plane geometry. Surface perturbations can grow by the KHI if $\mathbf{V}_1 \neq \mathbf{V}_2$. If the nonlinearity is strong enough, then the layer will rapidly become fully turbulent due to the actions of these instabilities.

2.2. Early experiments

Lewis (1950) reported his RTI experiment along with the publication of Taylor's landmark paper. An approximately sinusoidal initial perturbation to the interface was obtained by oscillating the blade of a small paddle positioned near the interface. The instability was generated by accelerating liquids down a vertical tube using air pressure. The range of accelerations was 3–140 g (where g is the gravity). A number of combinations of fluids were employed, including the water/air, water/benzene, glycerin/air, and carbon tetrachloride/water. High-speed photography was used to view the growth of the instability. There were two important conclusions from Lewis' paper: (1) the experimental data was found to agree with linear stability theory, until the interface amplitude reached ~ 0.4 of its initial wavelength, and (2) a constant late time bubble velocity $\propto \sqrt{g}$ was attained.

Emmons et al. (1960) improved the experiments of Lewis by using a thin tank that was constrained by guide rails and accelerated using stretched rubber tubing. Here, a liquid (carbon tetrachloride or methanol) and air interface was considered. Cole and Tankin (1973) used similar experimental setup as that of Emmons et al., but with a double-ended air cylinder driven by compressed air to propel a tank containing air and water. The authors found that the measurement of the initial disturbance is difficult because of its small amplitude. Yet, the growth rate was still measured without the necessity of measuring the amplitude of the initial disturbance.

In the experimental measurements of Duff et al. (1962), a 0.007-in steel diaphragm was used to divide the tank into two parts which the desired gases could be loaded. Instability was studied by observing the flow that developed when the

slide was withdrawn by an oil-damped pneumatic piston. The process of withdrawing the diaphragm produced an initial perturbation of the interface, the cause for this being related to shear instability, mechanical vibration of the diaphragm, or a combination of these. In particular, the authors found that when the diaphragm was removed at excessively high speed, the perturbations from its motion grew much more rapidly, manifested by strong departure from sinusoidal shape, and were not negligible during the time of interest. It is shown that approximate inclusion of diffusion effects allows calculation of all features of early perturbation growth accurately to within experimental error. The Duff, Harlow and Hirt paper was the only very early paper on experiments with miscible fluids.²¹

For the RMI experiments, the interface could also be formed in the same fashion by withdrawing a thin plate that separates the fluids (Brouillette and Sturtevant, 1994; Bonazza and Sturtevant, 1996; Cavailler et al., 1990). During its withdrawal, the plate drags along a volume of fluid, due to the no-slip boundary condition on its surface. Bonazza and Sturtevant (1996) observed that once the plate completes its motion out of the test section, the dragged fluid flows back toward the opposite wall and forms surface gravity waves. The waves so generated are principally two-dimensional, but some three-dimensional disturbances may be present. This technique generates relatively thick (>1 cm) diffuse interfaces, which can significantly reduce the instability growth rate (Mikaelian, 1991; Jones and Jacobs, 1997; Morgan et al., 2016).

Puranik et al. (2004) used a thin, sinusoidal plate that initially separates the driven gas (CO_2) from the test gas (air). Fig. 2.6 shows a picture of the sinusoidal plate and the frame in which it slides when in the interface section.²² After the plate is withdrawn from the shock tube, a shock wave accelerates the interface into the test section where it is imaged. The same issue with the retraction of the plate, however, was identified because a wake was generated and a small amount of fluid was dragged with the plate. Furthermore, Puranik et al. found that as the plate begins to retract, the two gases come in contact in the region between the wall of the shock tube containing the test section window and the edge of the plate and the RT instability begins to develop immediately.

Meshkov (1969, 1970) was the first use of thin nitrocellulose membranes. Specifically, Meshkov and his co-workers (Aleshin et al., 1988; Vassilenko et al., 1992; Andronov et al., 1995) utilized a thin membrane that was pre-shaped into a sinusoid to provide the initial perturbation. The membrane was shattered by the incident shock wave. However, the broken membrane fragments, which were not destroyed, must be carried with the flow (Jones and Jacobs, 1997). Prasad et al. (2000) discussed in detail the effect of using the membrane and wires to initially form the interface for studies of the RM instability. The thin plastic membrane tends to suppress mixing by isolating the two test gases from each other and by retarding motions, owing to its inertia and the viscous no-slip condition. On the other hand, the mesh of parallel wires that initially supports the membrane enhances the mixing.

Yosef-Hai et al. (2003) investigated the dimensionality dependence using two different types of membrane-carrying frames. The “3D frame” creates a pyramid-like perturbation and initial perturbation on the interface, while the “2D frame” creates a saw-tooth-shaped membrane.

In their experiments, Houas and Chemouni (1996) and Jourdan et al. (1996) also separated the gases initially by a thin plastic or nitrocellulose membrane, which constituted the material interface. The evolution in time of the turbulent mixing zone thickness offered a tentative picture, when the measured results fall between the predictions of the linear and the $t^{2/3}$ scalings, with a tendency toward the latter one. Following an assessment of the diagnostic techniques, Houas and Chemouni carefully discussed the main experimental difficulties as the presence of membrane fragments and the disturbances induced by the wall boundary layers. As a result, for the horizontal (membrane interface) or vertical (membraneless but diffusive interface) shock tube experiments, the initial interfacial conditions are rarely accurately measured (Meshkov, 1992; Puranik et al., 2004; Sadot et al., 1998; Jourdan and Houas, 1996; Collins and Jacobs, 2002; Motl et al., 2009; Holder et al., 2003), but extrapolated backwards in time.

Many workers have also discussed consequences of the generation of the fragments from the membrane after the passage of the incident shock wave (Meshkov, 1992; Brouillette and Sturtevant, 1993; Abakumov et al., 1996; Houas and Chemouni, 1996; Erez et al., 2000). Bouzgarrou et al. (2014) attempted to clarify the influence of these fragments on the statistical determination of the velocity field and stressed that the fragments are likely to corrupt the optical measurements and to interact with the flow. Also, Collins and Jacobs (2002) pointed out that the presence of the membrane fragments in the flow also impedes the use of advanced visualization techniques such as particle image velocimetry (Prestridge et al., 2000a,b; Aure and Jacobs, 2008), planar laser Rayleigh scattering (Budzinski et al., 1994), and planar laser-induced fluorescence (PLIF) (Jacobs et al., 1993; Rightley et al., 1999).

2.3. Single-mode RTI and RMI experiments/simulations with 2D initial perturbations

The single-mode RTI and RMI induced flows are natural starting point as they are manageable in analytical modeling development. Daly (1967) carried out the first 2D RTI simulations and showed KH roll-up of the spike at $\rho_2/\rho_1 = 1.1, 2$, but not at $\rho_2/\rho_1 = 10$. With improved numerics, Youngs (1984) showed the roll-up of the spike at $\rho_2/\rho_1 = 20$. This was run to show that use of the “free-fall line” (Birkhoff, 1955; Fermi and von Neumann, 1955)²³ was not valid, except for the

²¹ Popil and Curzon (1980) highlighted one of the problems with experiments using immiscible fluids – the edge effects due to the meniscus.

²² According to Puranik et al. (2004), only the central 70% of the plate width could be shaped into a sinusoid due to manufacturing limitations. However, this has no adverse effect on the experiments since the behavior of the central (sinusoidal) portion of the interface is unaffected by the neighboring fluid.

²³ The original documents collected in Fermi and von Neumann (1955) were written in 1951 and 1953, respectively.

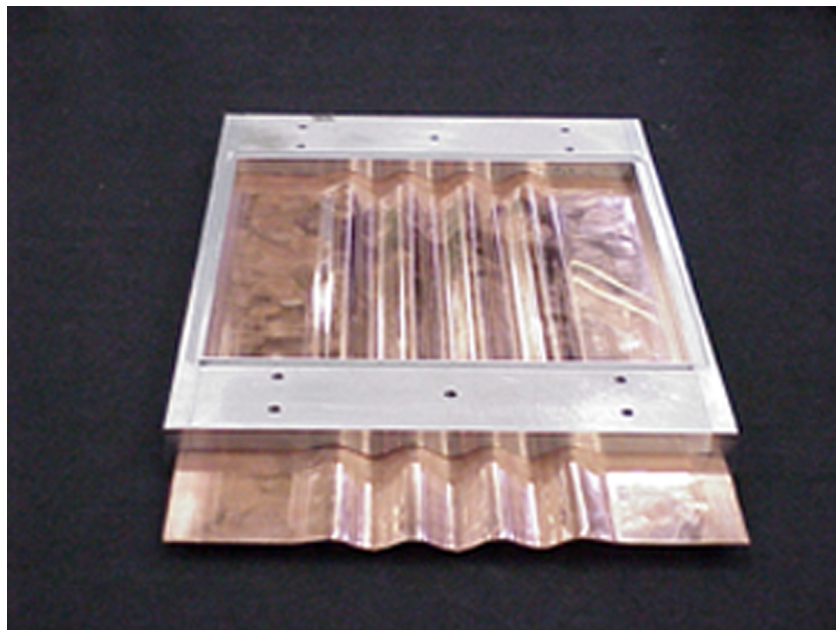


Fig. 2.6. Sinusoidally shaped copper plate and support frame.
Source: From Fig. 1 of Puranik et al. (2004), with permission from Shock Waves.

Atwood number very close to unity.²⁴ The single-mode RT, for example, continues to be the focus of research both in the experimental (for example Waddell et al., 2001; White et al., 2010; Wilkinson and Jacobs, 2007; Renoult et al., 2015) or numerical (Glimm et al., 2002; He et al., 1999a,b; Lee et al., 2011; Ramaprabhu and Dimonte, 2005; Ramaprabhu et al., 2006, 2012; Wei and Livescu, 2012; Shadloo et al., 2013) studies.

Allred and Blount (1953) and Ratafia (1973) performed early experiments of the single-mode RTI instability. Allred and Blount (1953) used an apparatus similar to that of Lewis (1950). Ratafia (1973) studied fluids of similar densities octyl alcohol/water, using bungee cords to accelerate a thin tank containing the fluids down a rail system. The rolling up of the interface was observed for the first time in these experiments. Understandably, these studies suffered from shortcomings in both the flow visualization and initial perturbation generation.

The experiments reviewed below improved these shortcomings significantly. Very symmetric, sinusoidal initial interface perturbations are obtained by gently oscillating the fluid filled container at the precise appropriate frequency. The development of the mixing zones from the 2D initial perturbations will be the focus of this subsection and the fluids system subject to 3D initial perturbation will be deferred to the next subsection. Here, we will first study the RT and RM induced mixing layers with the same low Atwood number with a similar apparatus. We will then look at the high Atwood number RM flow generated from a different experimental setup.

2.3.1. Rayleigh–Taylor flows with initial 2D perturbations

Waddell et al. (2001) used the experimental apparatus consists of a test sled, a guide rail assembly, an accelerator assembly, and a hoisting system. The test sled carries a Plexiglas tank containing the fluids under investigation, as well as the diagnostic instruments. The accelerator assembly is used to pull the test sled downward at a prescribed constant acceleration, thereby producing the body forces necessary to drive the RT instability (Fig. 2.7, reproduced from Waddell's Fig. 1). The RT induced mixing layer is observed using planer laser-induced fluorescence.

Fig. 2.8, reproduced from Fig. 4 of Waddell et al. (2001), shows the development of a RTI induced mixing layer. The two miscible fluids system, a nearly saturated calcium nitrate/water solution and a 70% isopropyl alcohol/water solution, have an Atwood number of 0.15. A sinusoidal perturbation with 2.5 wavelengths within the container was developed quickly after the release of the test sled. The experiment is accelerated at 0.74 g. In this relatively low Atwood number instability, the bubble profiles are mirror images of the spike profiles. Measurements of the initial growth rate are found to agree well with linear stability theory (Fig. 2.9).

²⁴ Youngs (1984) showed that the spike penetration fell a long way short of the free-fall line $h_S = (1/2)gt^2$. In the $A = 1$ RTI case, the single mode or multimode spike front in free-fall, $h_S = (1/2)gt^2$, exhibits the same late time behavior as the multimode bubble front, but with a different coefficient (see also Sharp, 1984; Alon et al., 1995).

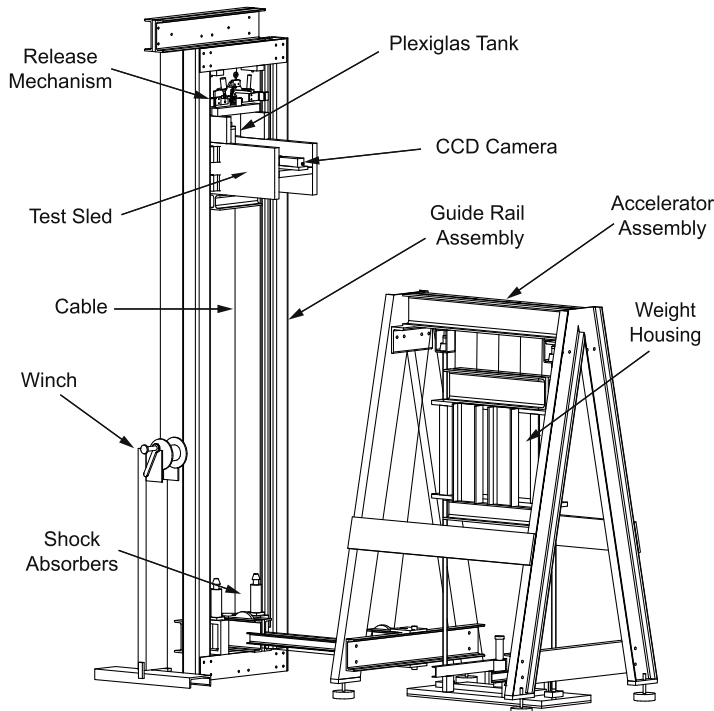


Fig. 2.7. Drawing of the experimental apparatus.
Source: Fig. 1, [Waddell et al. \(2001\)](#), *Phys. Fluids*, with the permission of AIP Publishing.

As noted in Section 1, it is important that the initial perturbation shape can be described accurately. In the traditional laboratory setting, the properties of magnetic liquids have also been studied. As an example, [White et al. \(2010\)](#) examined the nonlinear growth phase of the 2D single-mode RT instability using a magnetorheological fluid and obtained the terminal velocities of spikes and bubbles. They reported that the rate of change of the amplitude of the spikes in the $A = 1$ system is not saturating at late times (Fig. 2.10), in agreement with the Layzer-type potential theory models (e.g., the model of [Zhang, 1998](#), see next section).

Using Direct Numerical Simulations (DNS), [Wei and Livescu \(2012\)](#) investigated at the growth of the two-dimensional single-mode RTI at low Atwood number ($A = 0.04$). The effect of the initial perturbation shape is demonstrated in Fig. 2.11. The perturbation amplitude is 1/5 for both cases IC-B and IC-C and 1/25 for case IC-A. While case IC-D has the same perturbation amplitude as that of IC-B, but the diffusion layer thickness is five times larger. (Note that a good approximation for the linear stage growth rate which accounts for diffusive effects is given by [Duff et al. \(1962\)](#) for RTI. See Section 5.4 for details.)

Moreover, [Wei and Livescu \(2012\)](#) concluded that, at long times and sufficiently high Reynolds numbers (the growth stage termed *chaotic development* (CD) by the authors), the bubble acceleration becomes stationary, indicating a period of mean quadratic growth. The authors also determined that the growth coefficient, α_b , has the approximate value 0.035 for the bubble height computed based on 1% density level (see Section 6.1 for an extensive discussion on the late-time RTI similarity issues). Also, the results for late-time bubble velocity (Fig. 11 of [Wei and Livescu, 2012](#)) are similar to those obtained from three-dimensional single-mode numerical simulations (shown in Section 4.3), which also show late-time bubble reacceleration.

2.3.2. RMI: 2D initial conditions with drop tower

The single-mode RM experiments with 2D initial conditions (ICs) described here use the so-called drop tower method developed by [Jacobs and Sheeley \(1996\)](#). Note that the apparatus used in this study was used in a modified form for RT experiments ([Waddell et al., 2001](#)). According to [Niederhaus and Jacobs \(2003\)](#), a Plexiglas tank containing two unequal density liquids is mounted to a linear rail system constraining its main motion to the vertical direction. The tank is gently oscillated horizontally to produce a controlled 2D initial fluid interface shape. The sled is then released from an initial height and allowed to fall until it bounces off a fixed spring, which imparts an impulsive acceleration in the upward direction. After bouncing, the tank travels upward and then downward on the rail system while the instability develops (the spring is retracted so the sled is able to pass by it and travel down the trails until it impacts the shock absorber at the bottom of

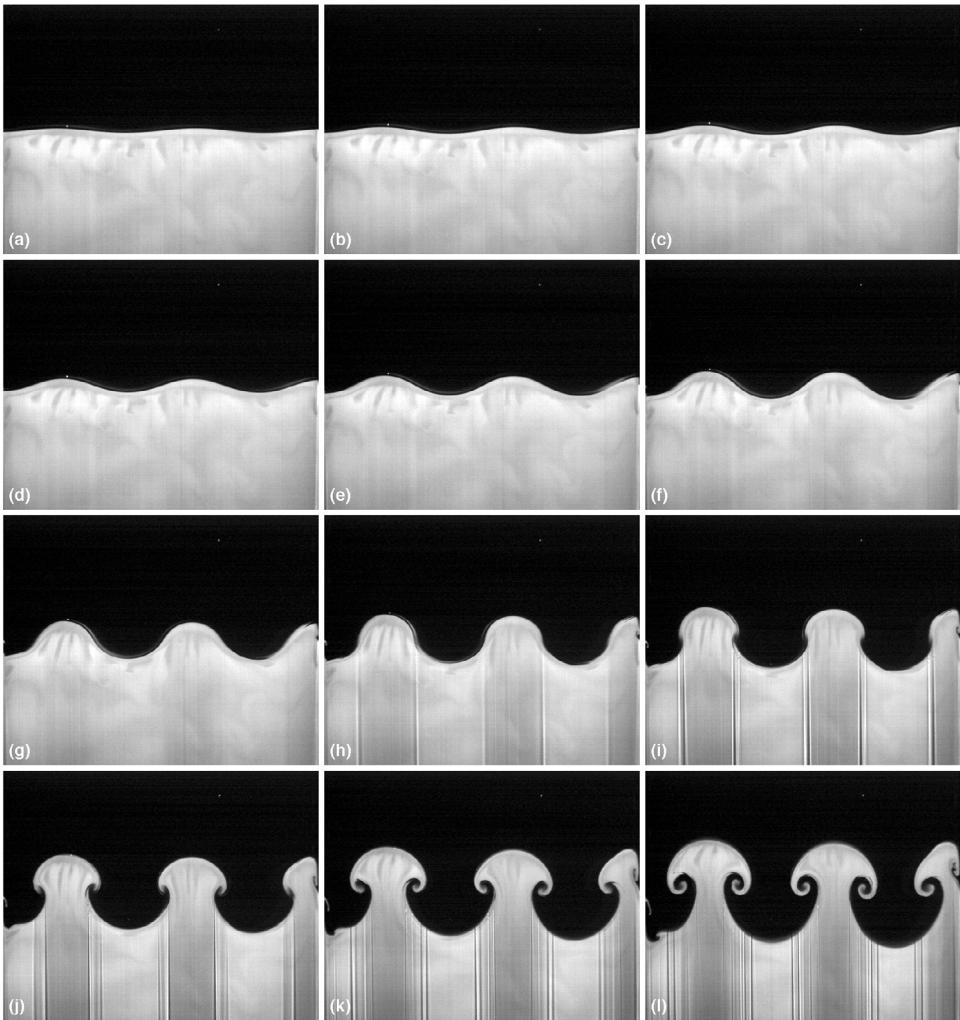


Fig. 2.8. A sequence of PLIF images showing the development of a miscible system with $A = 0.155$ accelerated at 0.74 g with an initial perturbation wavelength of 54 mm . The first frame (a) was taken immediately after the test sled was released and there is a 0.033 s increment between each subsequent image.

Source: From Fig. 4, Waddell et al., 2001, *Phys. Fluids*, with the permission of AIP Publishing.

the rails). Fig. 2 of Niederhaus and Jacobs (2003) showed a sequence of images of the sled traveling on the rail system (not shown).

Fig. 2.12 is a sequence of PLIF images showing the evolution of a RM induced mixing layer with drop tower apparatus (from Fig. 6 of Niederhaus and Jacobs (2003)). This illustrative case is resulted from a small-amplitude single-mode sinusoidal initial perturbation on a sharp interface. The Atwood number of the fluid system, a 70% isopropyl alcohol/water solution, is again low at 0.155. The perturbation with 2.5 waves is the same as that of the RTI flows previously shown in Fig. 2.8.

Vorticity is deposited along the interface by the baroclinic production mechanism during the acceleration. The impulsive acceleration causes the initial perturbation to invert (i.e. decrease and pass through zero) before growing in amplitude. Immediately after inversion, the interface retains a sinusoidal shape, but the interface begins to become non-sinusoidal. Niederhaus and Jacobs (2003) found that the linear stability theory gives excellent agreement with the measured initial growth rate for single-mode perturbations. Up to a non-dimensional time 0.7, the predicted amplitudes differing by less than 10% from experimental measurements (Fig. 2.13).²⁵

2.3.3. RMI: Shock tube 2D membrane free initial conditions

The RM instability is typically produced by the passage of a shock wave over the interface. The previous subsection (Section 2.2) mentioned several methods for generating RM instability in the shock tubes by creating an initial boundary

²⁵ The non-dimensional time, t^* , is defined as $k a_0 t$, where k is the wavenumber, a_0 is the initial amplitude.

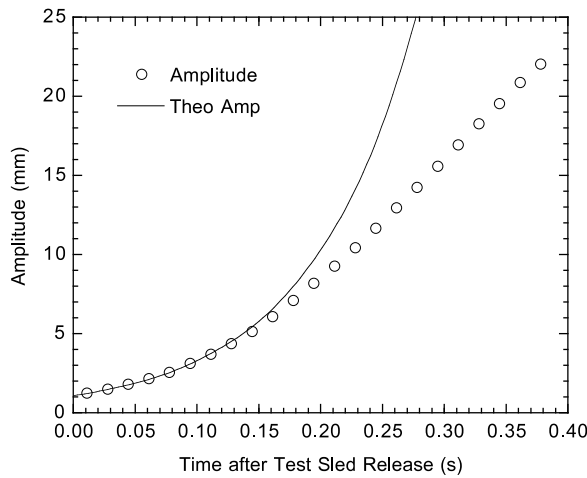


Fig. 2.9. Plot of measured amplitude versus time for a typical experiment. The solid line is the theoretical amplitude.
Source: Waddell et al., 2001, Fig. 8, *Phys. Fluids*, with the permission of AIP Publishing.

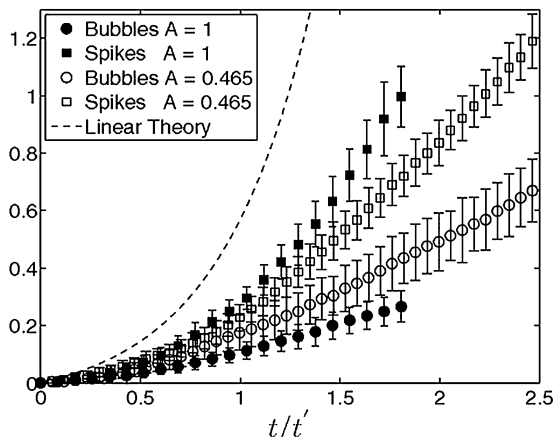


Fig. 2.10. Experimentally measured bubble and spike amplitudes as a function of time.
Source: Fig. 6 of White et al. (2010), with permission from *Physical Review E*.

between two gases in a shock tube, but this subsubsection will focus on an innovative membrane free approach devised by Jones and Jacobs (1997). Here, a vertical shock tube was manufactured with small horizontal slots located on two opposite walls. The gases entered the shock tube from opposite ends of the driven section and exited through the slots, forming a stagnation point flow at the interface location (Collins and Jacobs, 2002). A reproducible perturbation was then given to the interface by gently oscillating the shock tube at the appropriate frequency, generating a standing wave. An interface is formed with the heavy gas, SF₆, that flows upward in the shocktube and the light gas, air, flows downward (Fig. 2.14, reproduced from Collins and Jacobs, 2002, Fig. 1).

Jacobs and Krivets (2005) utilized the experimental apparatus and visualization methods of the earlier study of Collins and Jacobs (2002), but employs stronger shocks and initial perturbations with shorter wavelengths to obtain much later-time images of the single-mode instability. Fig. 2.15, reproduced from Fig. 6 of Jacobs and Krivets (2005), shows a much more evolved flow at the later times. In particular, one can observe the complete disintegration of the vortex core structures into what appears to be a fully turbulent flow.

Comparing the results between those from the drop tower and shock tube, the Atwood number effect for a single mode RM flow becomes apparent. The Atwood number of the SF₆/air fluid system is 0.6, much higher than that in the drop tower experiments. The asymmetry of the bubbles and spikes here is due to the relatively large Atwood number (Collins and Jacobs, 2002). In addition, the late time images illustrated the separation of the mushroom caps from the rest of the interface accompanied by the pronounced thinning of the mushroom stems. Jacobs and Krivets (2005) pointed out that the breaking away of the turbulent vortex row from the rest of the interface is a direct result of the large Atwood number of these experiments producing nonuniformity in the vortex spacing.

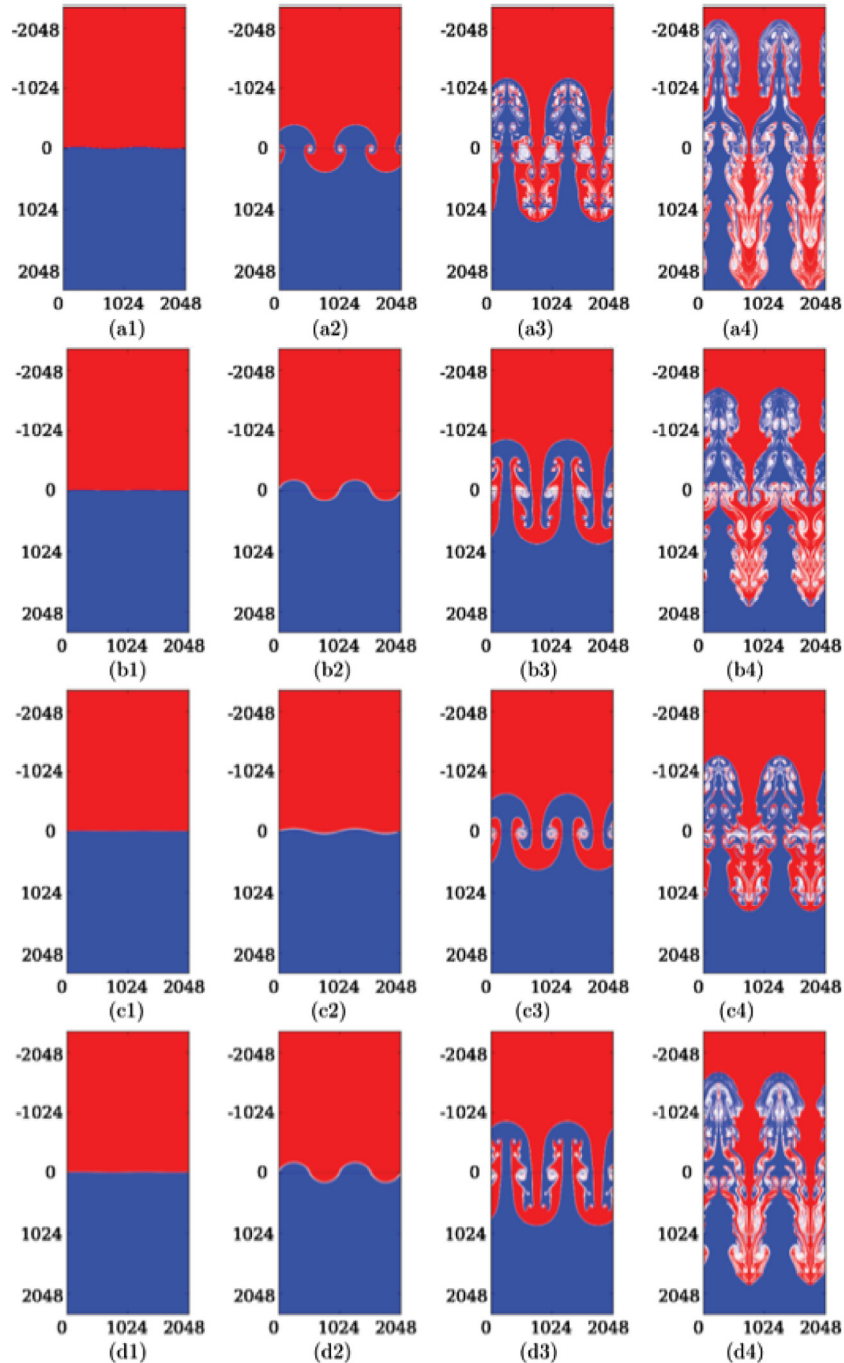


Fig. 2.11. The effects of initial conditions on the density contours in single-mode RTI at high Re ($\approx 20\,000$). a-d: IC-A, IC-B, IC-C, and IC-D. The grid size in all four simulations is $2048 \times 12\,800$.

Source: Fig. 7 of Wei and Livescu, with permission from *Physical Review E*.

The class of high-order finite difference weighted essentially nonoscillatory (WENO) Schemes, coupled with total variation diminishing TVD high-order Runge-Kutta time discretizations (Shu and Osher, 1988; Shu, 1999) was developed in Jiang and Shu (1996) for the fifth-order accurate version and in Balsara and Shu (2000) for the higher-order versions, including the ninth order version that was used in Zhang et al. (2003, 2006) for the high Reynolds number Navier-Stokes calculations. Latini et al. (2007a, b) applied the fifth- and ninth-order WENO shock-capturing method to the 2D single-mode RMI. The initial conditions and computational domain approximated the Mach 1.21 air-acetone/SF₆ shock tube experiment of Collins and Jacobs. As shown in Fig. 2.16, the simulation density and the experimental PLIF images from the experiment

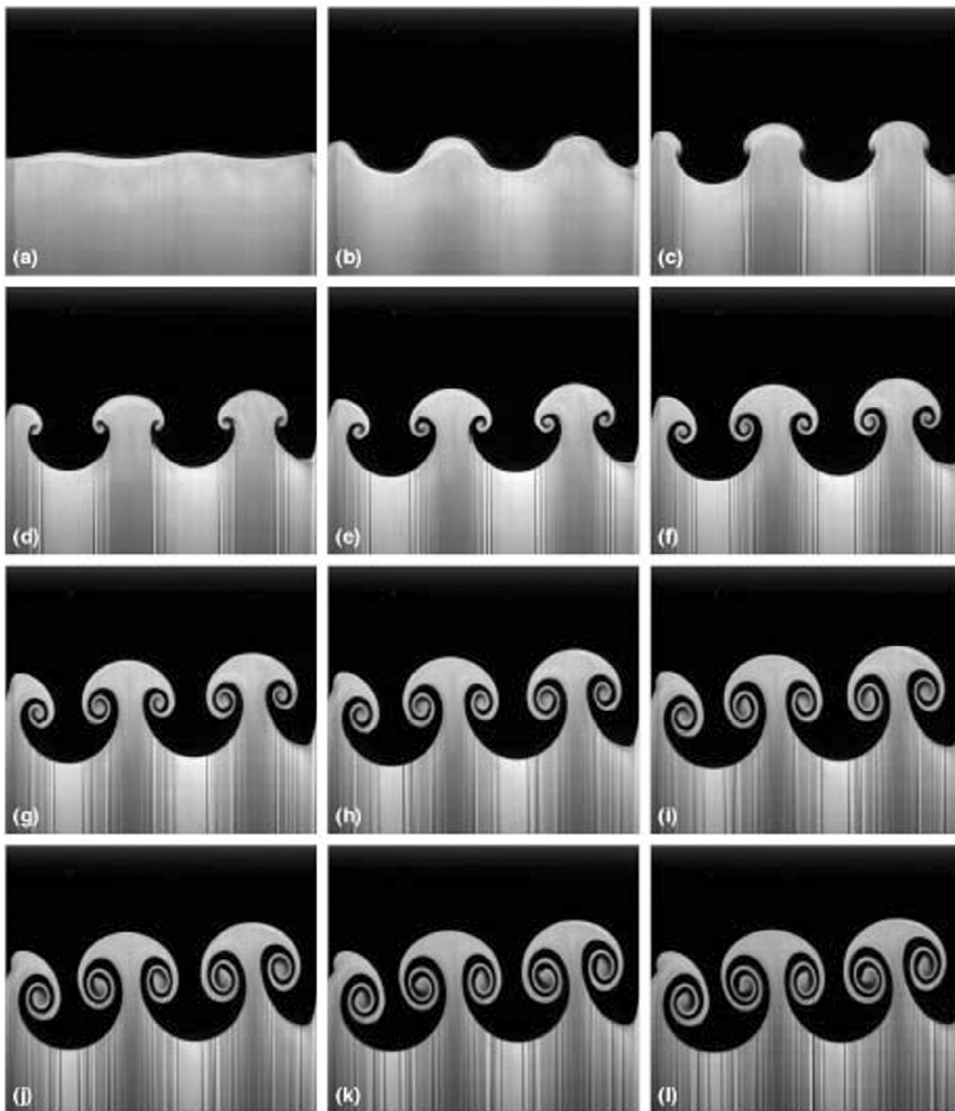


Fig. 2.12. A sequence of images from an experiment with $2\frac{1}{2}$ waves and $ka = 0.16$.
Source: From Niederhaus and Jacobs (2003), *J. Fluid Mech.* with permission.

were in good qualitative agreement (up to the time at which the driver-based expansion affects the experimental amplitude growth and before reshock).²⁶ With decreased numerical dissipation and diffusion, the higher-order reconstruction also better captures the fine-scale structures of the secondary instabilities. Latini et al. (2007b) also computed mixing layer widths, circulations, molecular mixing parameters, statistics, probability density functions (PDFs), and spectra and showed that these quantities are highly sensitive to grid resolutions and orders.

2.3.4. Shock tube experiments with stereolithographed interfaces

The characterization of the initial interface can hardly be questioned for shock tube experiments with stereolithographed interfaces. In this approach, a thin nitrocellulosic membrane ($0.5 \mu\text{m}$ thick) is deposited on a stereolithographed grid support, and constructed with chosen shape and dimensions using computer-aided design (Mariani et al., 2008). The RMI growth can be investigated to high accuracy since the 2D single mode sinusoidal perturbations at a gaseous interface is known (Incident shock Mach numbers are 1.15 and 1.4). The experiments were performed in a horizontal shock tube with a 20 cm squared cross-section (Houas et al., 2003; Jourdan and Houas, 2005).

²⁶ For discussion on the later time of this experiment after the reshock, see Part II (Zhou, 2017).

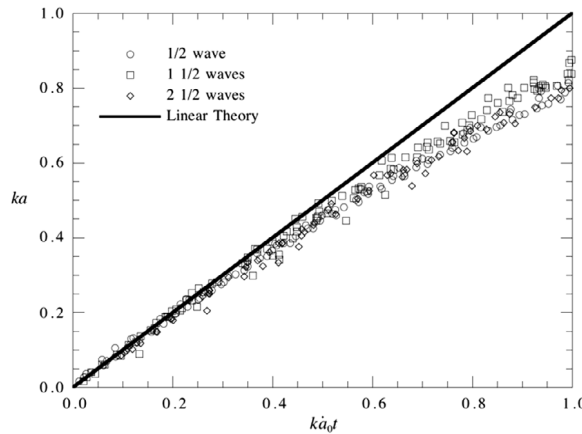


Fig. 2.13. A plot of early-time non-dimensional amplitude versus time along with a line corresponding to linear stability theory.
Source: Fig. 9, Niederhaus and Jacobs, *J. Fluid Mech.* with permission.

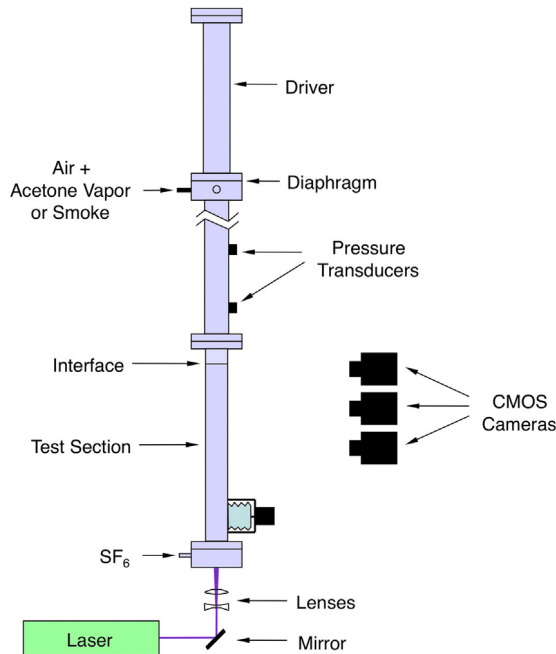


Fig. 2.14. The shock tube and PLIF system. SF_6 and an air-acetone mixture flow into the shock tube from plenums located below and above the test section. The stagnation point flow at the slot location creates the interface (b), which is given a sinusoidal perturbation by rocking the shock tube using a stepper motor and crank mechanism.

Source: From Collins and Jacobs (2002), *J. Fluid Mech.*, Fig. 1, with permission.

Fig. 2.17 shows the visualizations of both heavy-light and light-heavy sinusoidal interfaces obtained with laser sheet diagnostics (Mariani et al., 2008). The uncertainty is about $\pm 5\%$. As described by the authors, Grid 1 perturbation represents a single-period ($\lambda = 12$ cm) sinusoidal bump whereas Grid 2 perturbation has a two-period sinusoidal shape ($\lambda = 8$ cm). These stereolithographed interfaces shapes are described by the following functions: $a(y, 0) = a_0(1 - \cos ky)$ for $y \in [y_M, 200 - y_M]$ and $a(y, 0) = 0$ elsewhere. $a(y, t)$ is the amplitude of the perturbation, y the transverse dimension (in mm) of the shock tube, $k = 2\pi/\lambda$ the wave number, and (a_0, y_M) (in mm) equal to $(6.89, 40)$ and $(3.06, 20)$ for Grids 1 and 2, respectively. It should be noted that the heavy-light interface reverses after the shock passage (illustrated in Figs. 2.3 and 2.4). Experiments are in very good agreement with theory and simulations for the heavy-light case (Section 4.4), but probably due to the membrane effects, quickly deviate from them in the light-heavy configuration.

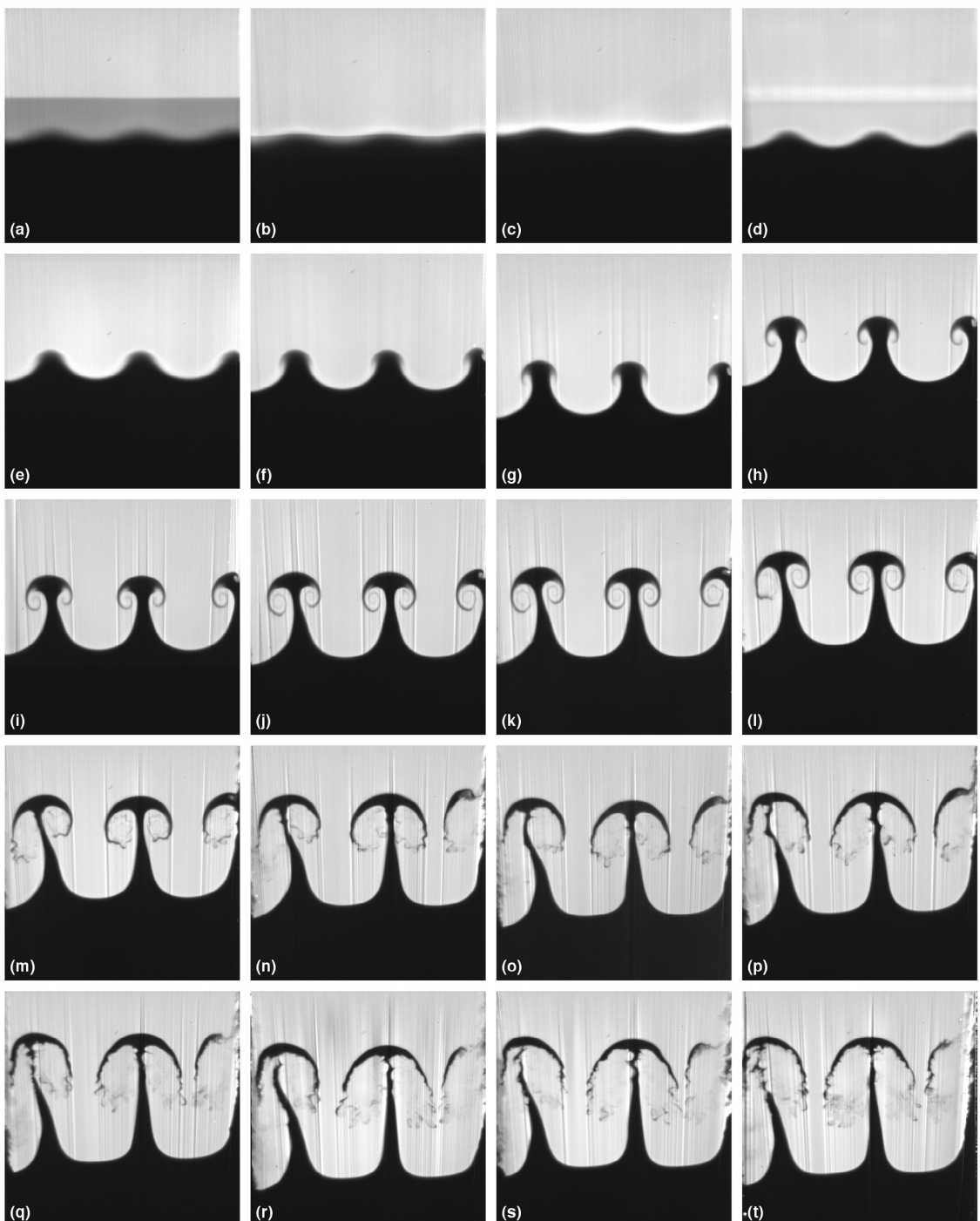


Fig. 2.15. PLIF images from 20 experiments with $M_s = 1.27$ and $\lambda = 36$ mm assembled to form a time sequence. Times relative to the shock wave arrival are (a) -0.03 ms, (b) 0.00 ms, (c) 0.01 ms, (d) 0.23 ms, (e) 0.53 ms, (f) 0.83 ms, (g) 1.23 ms, (h) 1.63 ms, (i) 2.13 ms, (j) 2.53 ms, (k) 2.93 ms, (l) 3.23 ms, (m) 3.63 ms, (n) 4.33 ms, (o) 4.63 ms, (p) 5.03 ms, (q) 5.33 ms, (r) 5.73 ms, (s) 5.93 ms, and (t) 6.13 ms.

Source: Fig. 6 of Jacobs and Krivets, *Phys. Fluids*, 2005, with the permission of AIP Publishing.

Vandenboomgaerde et al. (2014) apparently have overcome this difficulty and achieved good agreement among experimental, numerical, and theoretical results. Fig. 2.18 offered a view of their manufactured grids with their nitro-cellulosic films. Now, with a $Mach = 1.45$ shock wave, the membrane remnants have no deleterious effects on the macroscopic growth of a long wave perturbation, a result already noted by Erez et al. (2000), Fontaine et al. (2009) and Bai et al. (2010).

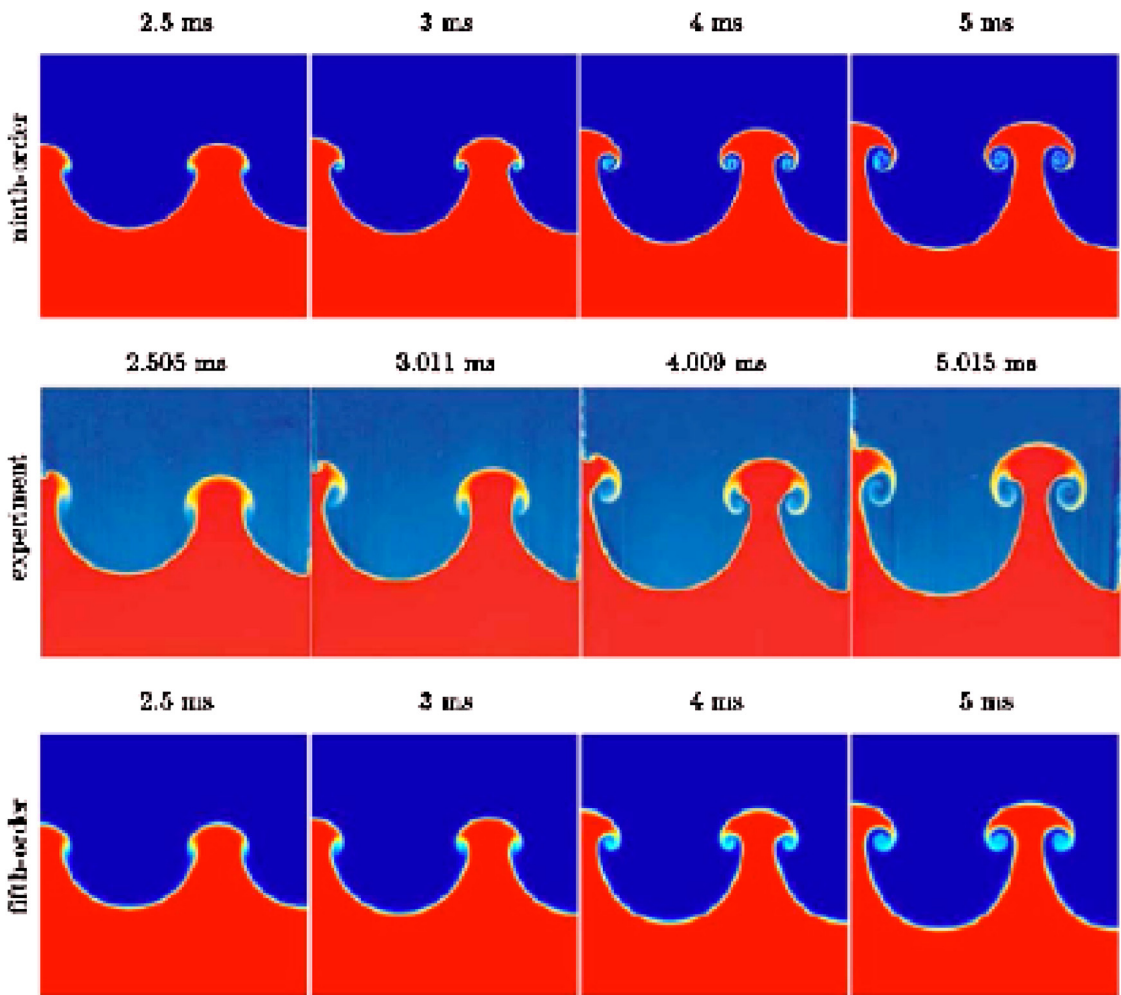


Fig. 2.16. Comparison of corrected PLIF images from the [Collins and Jacobs \(2002\)](#) experiment middle row with the density from the ninth-order WENO simulation top row and from the fifth-order WENO simulation bottom row at selected times before reshock. The gases are air-acetone (top) and SF₆ (bottom). The simulation times differ slightly from the experimental times by 0.005–0.015 ms. The experimental images are taken from Fig. 6 of Collins and Jacobs.

Source: Fig. 1 of Latini et al., *Phys. Fluids*, 2007a, with the permission of AIP Publishing.

To inspect the effect of the initial condition, [Vandenboomgaerde et al. \(2014\)](#) utilized a single-mode macroscopic perturbation with two distinct values of initial amplitudes, while kept other parameters the same ($Mach = 1.45$, pre-shock Atwood number $A = 0.679$, initial wavelength = 8 cm). For the first case, the growth rate in the linear phase agrees with the theoretical value (starts with a small $ka_0 = 0.17$, where k is the wave number of the perturbation). With a significantly increased initial value ($ka_0 = 0.52$), however, the growth computed with the asymptotic value clearly over-estimates the experimental growth (Fig. 2.19).

2.3.5. Shock proximity effects on RMI growth

When a strong shock reaches an interface between two densities, the high compression will result in a transmitted shock that recedes slowly from the interface. The Nova laser experimental measurements of [Dimonte and Remington \(1993\)](#), [Dimonte et al. \(1996b\)](#) and [Farley et al. \(1999\)](#) showed reduced growth rates compared with incompressible predictions, qualitatively in agreement with the models of [Holmes et al. \(1999\)](#) and [Hurricane et al. \(2000\)](#). Indeed, the shock will represent an impenetrable boundary, reducing the growth rate.

[Glendinning et al. \(2003\)](#) performed a high Mach number shock instability experiment, not complicated by very large initial amplitude or by significant RT growth. Experiments conducted on the Omega laser showed reduced RM growth rates in a strongly shocked system with initial amplitudes $ka_0 \leq 0.9$. The growth rate at early time is less than half the impulsive model prediction, rising at later time to near the impulsive prediction. Because incompressible models of [Meyer and Blewett \(1972\)](#) and [Sadot et al. \(1998\)](#) predict an initial perturbation growth rate that exceeds the shock recession velocity, they

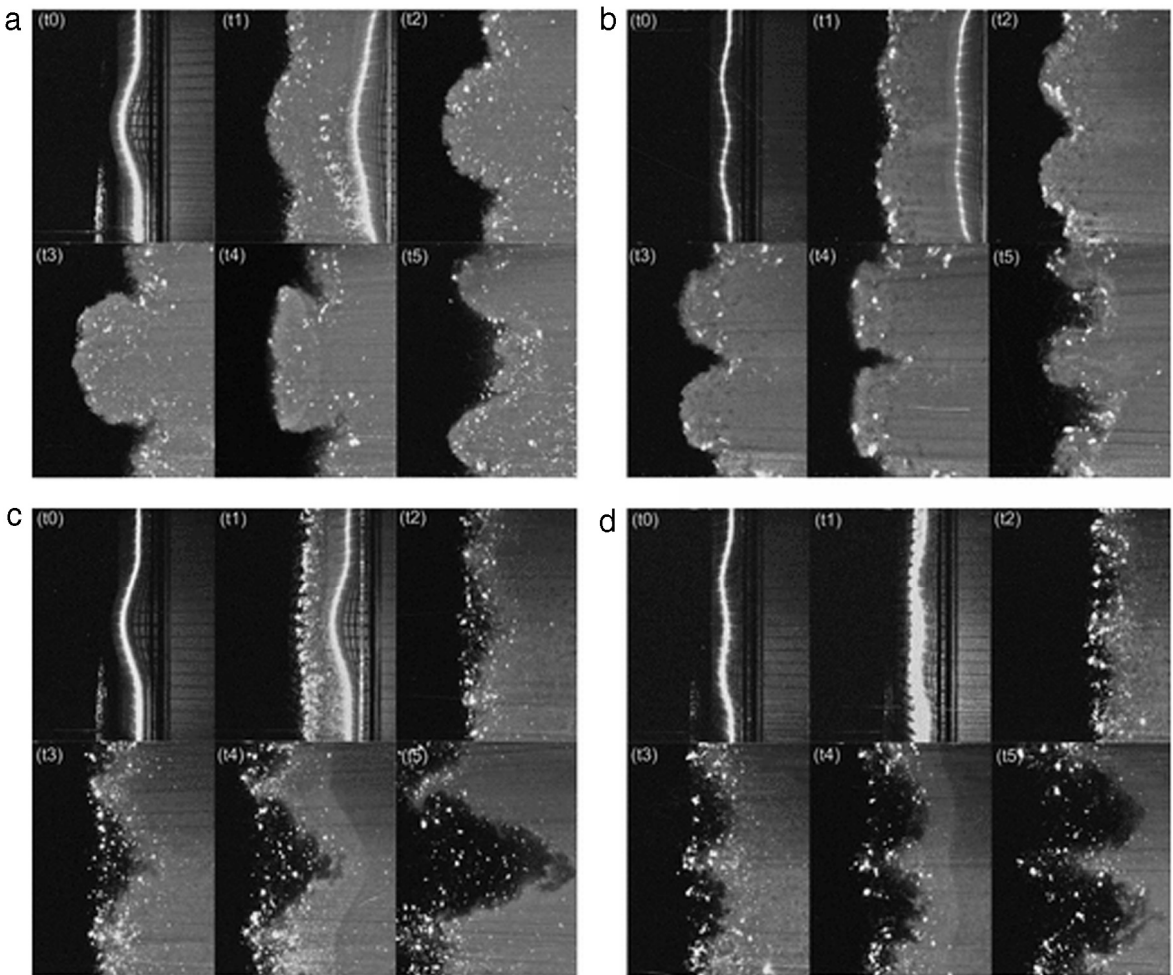


Fig. 2.17. Laser sheet pictures showing the interaction of a shock wave (moving from right to left) with a stereolithographed single mode interface for the light-heavy (air/SF₆) case with Grid 1 (a) and 2 (b) perturbations, and the heavy-light (air/He) case with Grid 1 (c) and 2 (d) perturbations. (a), (b), (c), and (d) are from runs 126, 120, 125, and 123, respectively, with a shock wave Mach number of about 1.4. Time between frames is approximately 300 and 800 μ s for the air/He and air/SF₆ experiments, and the compression of the interface by the reflected shock wave happens 1100 and 3200 μ s after the initial shock acceleration, respectively.

Source: Fig. 1 of Mariani et al. (2008), *Phys. Rev. Lett.* with permission.

do not correctly predict the observed growth. Linear compressible theory of Yang et al. (1994) does not account for the nonlinear evolution of the perturbation growth. Although the models, such as those of Holmes et al. and Hurricane et al., which reduced the initial growth rate and assumed a monotonically decreasing growth rate thereafter, correctly predicted the average growth, but they did not correctly predict the growth rate as a function of time.

Sadot et al. (1998, 2003) and Rikanati et al. (2003) performed *Mach 1.2* shock-tube experiments with sawtooth initial perturbations. Numerical simulations with Mach numbers ranging from 1.2 to 15.3 were performed to characterize the experiments of Aleshin et al. (1997) and Dimonte et al. (1996b). Both small and large amplitudes were considered in order to distinguish the effects of large amplitudes from those of compressibility (i.e., proximity of the shock wave to the perturbed interface). Recall that the Mach numbers ranged from 2.5–4.5 in the shock tube experiments (Aleshin et al., 1997) and reached up to 15.3 using the Nova laser (Dimonte et al., 1996b, see related simulations by Holmes et al., 1999).

Rikanati et al. (2003) and Glendinning et al. (2003) found that the model of Zhang and Sohn (1997a) as well as the models based on vortex evolution appropriate for accounting for the behavior observed. Sadot et al. (2003) also found good agreement between the shock-tube experiment predictions and the vorticity deposition model at *Mach* = 1.2. The vorticity deposition model was also helpful for Rikanati et al. (2003) when producing a curve for the reduction factor of the initial velocity. Fig. 2.20 shows the experimental results of Aleshin et al. (1990), Dimonte et al. (1996b) and Sadot et al. (2003) for moderate and high Mach number experiments. As can be seen from Fig. 2.20, the reduction in all of the experiments fit a single curve.

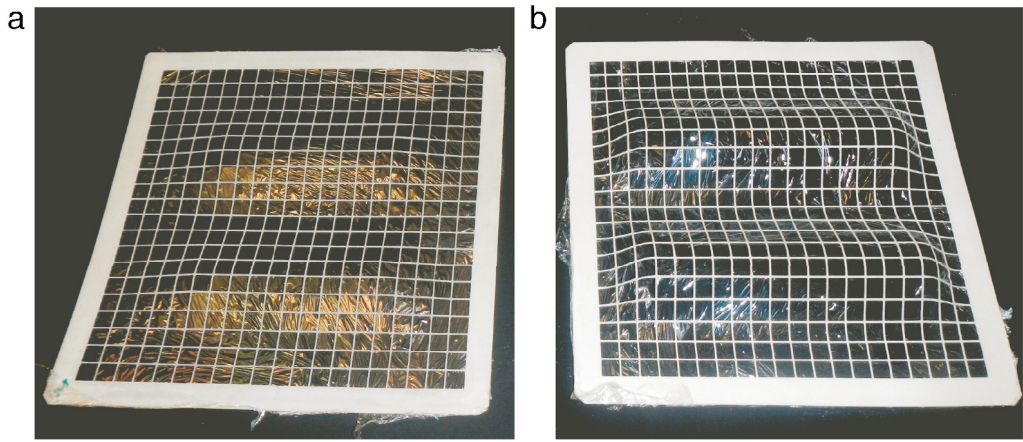


Fig. 2.18. Pictures of the grids ($\lambda = 8$ cm) with a nitrocellulose membrane. (a) Grid 1: $a_0 = 0.306$ cm, (b) Grid 2: $a_0 = 0.918$ cm. Source: Fig. 2 of Vandenboomgaerde et al. (2014), *Phys. Fluids*, with the permission of AIP Publishing.

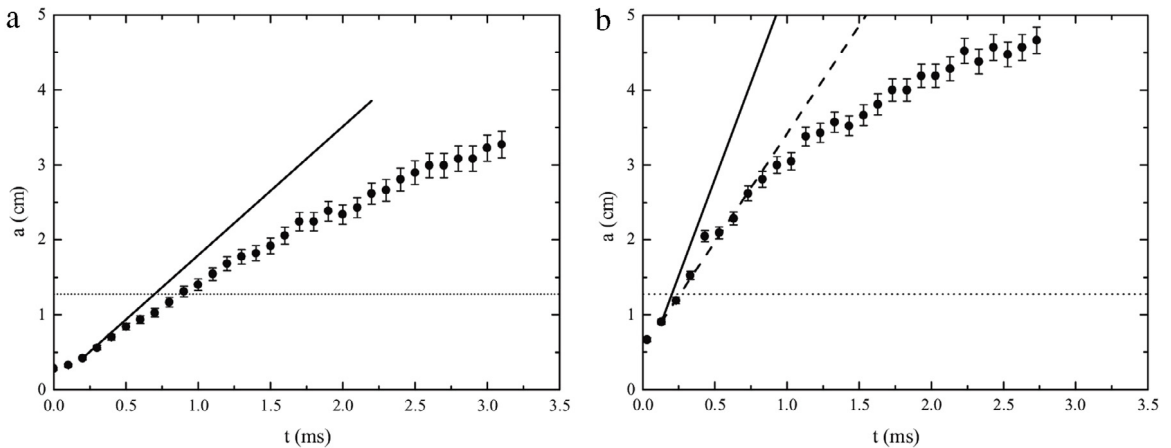


Fig. 2.19. Experimental temporal evolutions of the half peak-to-valley amplitude, $a(t)$, and theoretical growth rates. The solid lines represent the classical linear growth. For the dashed line, the growth takes into account the high initial amplitude effect and the transient phase. The dotted horizontal line represents $ak = 1$. (a) Case 1. (b) Case 2. Source: Fig. 5 of Vandenboomgaerde et al. (2014), *Phys. Fluids*, with the permission of AIP Publishing.

2.4. Single-mode experiments with 3D initial perturbations

2.4.1. RTI: Weight and pulley

Using the apparatus of Waddell et al. (2001), Wilkinson and Jacobs (2007) studied the three-dimensional RTI in a miscible fluid system. The experimental fluids are the same miscible liquid combination as used by Waddell et al. at a low Atwood number $A = 0.15$.

The three-dimensional initial perturbation, generated by an oscillation along the tank diagonal (x direction), has a surface deflection of the form $a_0 \sin(kx) \sin(ky)$, where the x and y axes are oriented along the tank diagonals. Fig. 2.21 (reproduced from Fig. 5 of Wilkinson and Jacobs) shows an example of this type of perturbation (with 2.5 wavelengths) across the diagonal. PLIF is again the method used for visualization of the fluid interface.

In Fig. 2.21, the image sequences showed that the early stage of the instability evolution is quite similar to its counterpart with a 2D initial perturbation for the same wavenumber. In a sharp contrast to the 2D case, the 3D instability eventually developed two vortices per wavelength instead of the single one found in the 2D case. Indeed, one would expect that a lower Atwood number flow would possess more symmetric features, such as the double ring configuration (Long et al., 2009). According to Wilkinson and Jacobs (2007), this symmetric topology suggested a vorticity pattern in the form of an array of vortex rings, alternatively traveling upward and downward. During the early-time period of the experiments, the amplitudes measured from these experiments show relatively good agreement with linear instability analysis (Fig. 2.22).

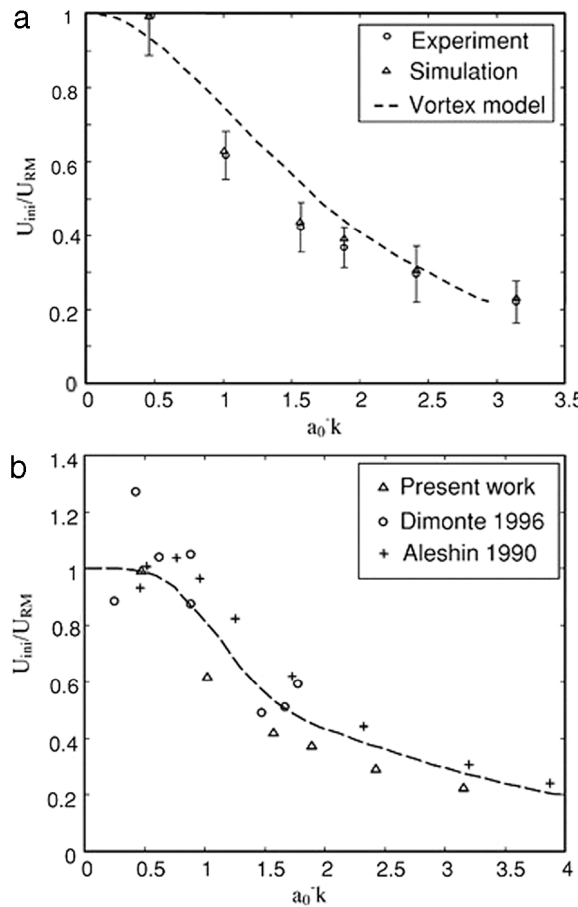


Fig. 2.20. (a) Comparison of the reduction factor between the vorticity deposition model and the shock-tube experiment at $Mach = 1.2$. (b) Comparison of the results from the Sadot et al. (2003) (“present work” in the legend) at low Mach number and Dimonte and Schneider (1996) and Aleshin et al. (1990) at moderate and high Mach number.

Source: Fig. 3 of Sadot et al. *Laser and Particle Beams* 2003 with permission.

Also, the experiments with 1 1/2 wavelengths across the diagonal showed the same two vortices in the late-time behavior (Fig. 4 of Wilkinson and Jacobs, not shown).

2.4.2. RMI: Drop tower

Chapman and Jacobs (2006) inspected the three-dimensional RMI of incompressible, miscible liquids with a 3D single-mode initial perturbation. They use the apparatus of the 2D initial perturbation experiments of Niederhaus and Jacobs (2003). In particular, the study uses a tank with a square cross section allowing the generation of a square-mode 3D initial perturbation by lateral oscillation along the tank's diagonal. Again, the two fluids system, a nearly saturated calcium nitrate/water solution and a 70% isopropyl alcohol/water solution, has a low Atwood number (0.15). The instability is generated by impulsively accelerating a tank containing the two liquids, in the same manner as that of Niederhaus and Jacobs (2003). The impulsive acceleration in these experiments is directed from the heavier fluid into the lighter one.

Fig. 2.23, reproduced from Fig. 4 of Chapman and Jacobs (2006), illustrates the evolution of a single-mode 3D RM instability. Once again, images obtained from these experiments revealed the development of a vorticity pattern in the form of an array of vortex rings, alternatively traveling upward and downward. The amplitude measured showed that good agreement with linear stability theory is attained up until $k a_0 t = 1$, which is significantly later than has been observed in the 2D experiments that showed good agreement only until $k a_0 t = 0.7$.

Fig. 11 of Chapman and Jacobs (not shown) suggested that both the 2D and 3D measurements exhibited the same general shape at late time in the non-linear regime. However, the 3D amplitudes exhibited significantly increased nonlinear growth.

2.4.3. RMI: Shock tube

Long et al. (2009) utilized the same basic apparatus and techniques as those of previous 2D initial perturbation RM investigations (Jones and Jacobs, 1997; Collins and Jacobs, 2002; Jacobs and Krivets, 2005). The vertical oscillation results in

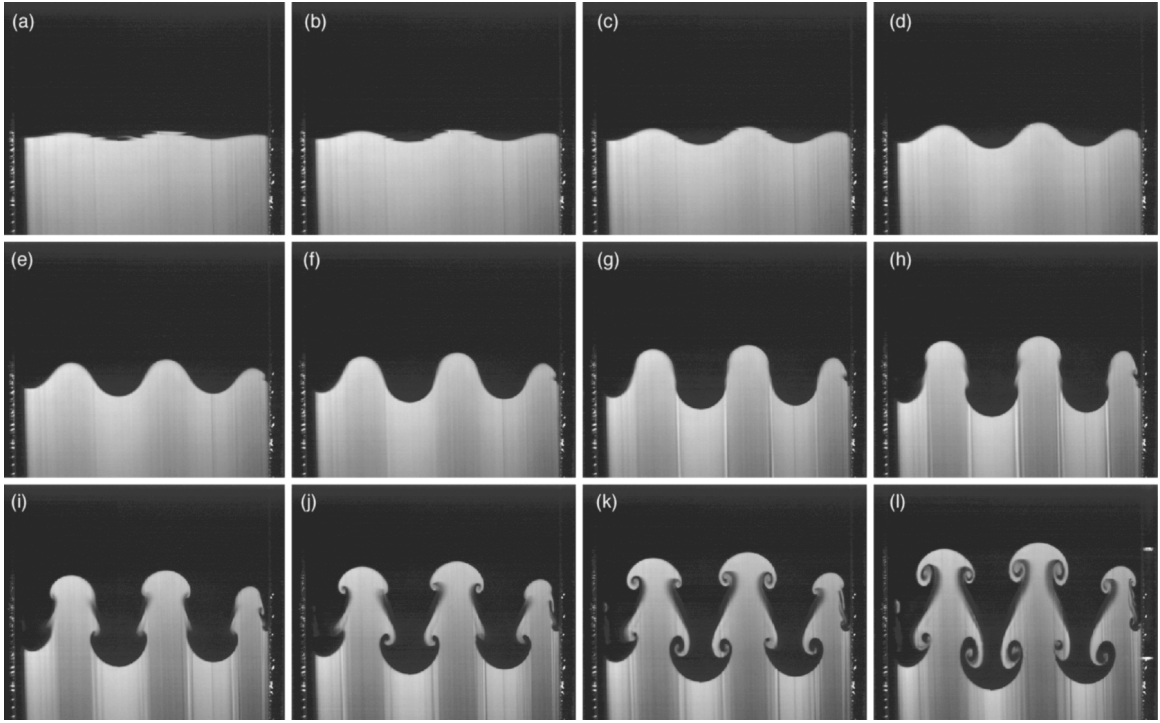


Fig. 2.21. A sequence of PLIF images from an experiment with 2 1/2 waves across the diagonal. Times relative to the beginning of acceleration are (a) 46.7 ms, (b) 80 ms, (c) 113.3 ms, (d) 146.6 ms, (e) 179.9 ms, (f) 213.2 ms, (g) 246.5 ms, (h) 279.8 ms, (i) 313.1 ms, (j) 346.4 ms, (k) 379.7 ms, and (l) 413 ms.
Source: Fig. 5 of Wilkinson and Jacobs (2007) *Phys. Fluids*, with the permission of AIP Publishing.

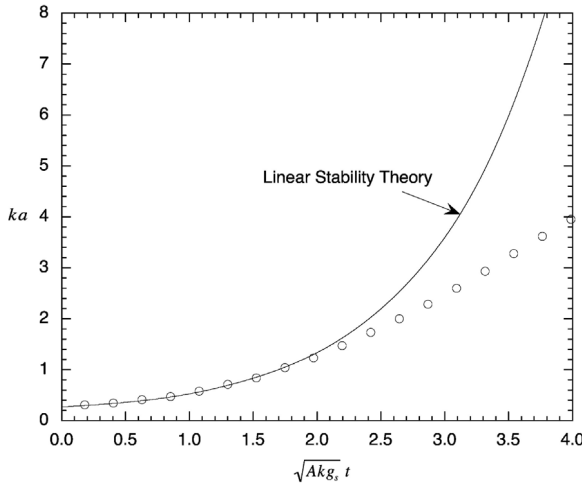


Fig. 2.22. Typical plot of the comparison between the solution of a linear stability theory and amplitude measurements showing the extent of agreement with linear stability theory. In this case, measured amplitude agrees with the linear theory up to $ka \sim 1$.
Source: From Fig. 13 of Wilkinson and Jacobs, *Phys. Fluids*, 2007, with the permission of AIP Publishing.

a square, single-mode 3D perturbation of the form $a_0 \cos(kx) \cos(ky)$, where the x and y axes are directed through the tank diagonals. In addition to PLIF, another method of visualization, Mie scattering images, was introduced. The shock tube experiments utilize SF₆ for heavy gas and air for the light gas, producing a higher Atwood number; $A = 0.65$.

Fig. 2.24, reproduced from Fig. 3 of Long et al. (2009), showed a comparison of experimental PLIF (left) and Mie scattering (center) images. These images are drastically different from those obtained in the drop tower (Chapman and Jacobs, 2006). Long et al. (2009) reasoned that this difference in topology is the Atwood number effect, since the instability will lose its symmetry with a higher Atwood number. Increasing an Atwood number caused the vortex ring surrounding the spike to

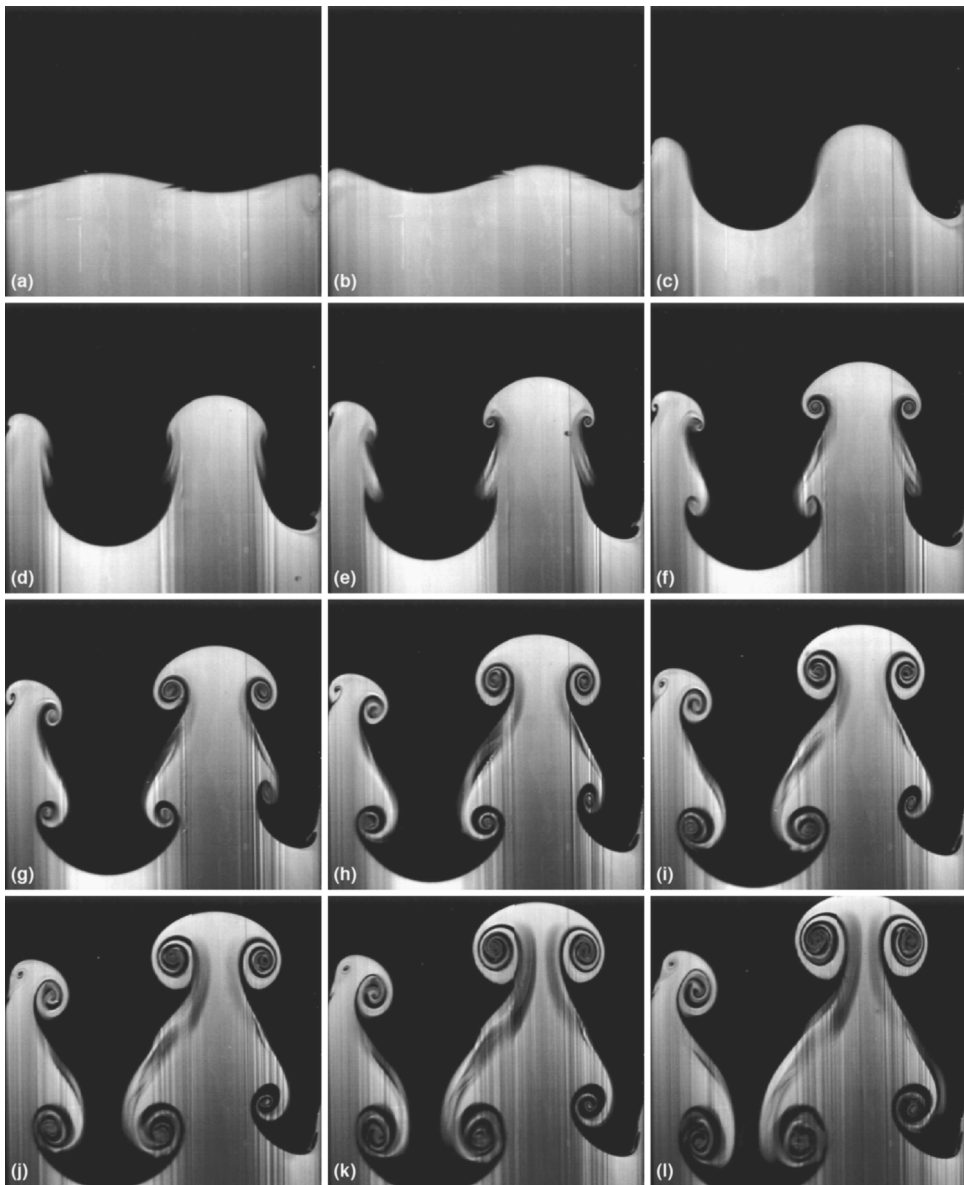


Fig. 2.23. A sequence of images from an experiment with 1 1/2 waves across the diagonal giving $ka_i = 0.38$. Times relative to the midpoint of spring impact are: (a) –33 ms, (b) 33 ms, (c) 100 ms, (d) 167 ms, (e) 233 ms, (f) 300 ms, (g) 367 ms, (h) 433 ms, (i) 500 ms, (j) 567 ms, (k) 633 ms, and (l) 700 ms.
Source: From Fig. 4, Chapman and Jacobs, *Phys. Fluids*, with the permission of AIP Publishing.

increase in strength at the expense of that surrounding the bubble and the stronger ring stretched the weaker one into the configuration.

Hence, the sequences of images showed a development that is similar in many ways to the single mode 2D instability instead. Nevertheless, Long et al. (2009) noted two important differences: First, the vortices remain very compact in the 3D experiments and simulation throughout their development. Second, the spike remains relatively thick compared to the 2D counterpart.

Long et al. also found good agreement between the experiments and a three-dimensional numerical simulation of this experiment utilizing the Eulerian adaptive mesh refinement code, RAPTOR (Figs. 2.45 and 2.25). The amplitude measured and simulated showed that the linear stability theory is fairly accurate until the time reached 1.5 ms. Both the experiments and simulation indicated a $t^{-0.54}$ late time scaling for the overall growth rate.

Continuing their previous shock tube studies (Zhai et al., 2011; Si et al., 2012), Luo et al. (2013) developed a method to create a discontinuous gaseous interface with a minimum-surface feature with the soap film technique. This interface has a zero-mean curvature (Isenberg, 1992), which is different from the interface used by Yosef-Hai et al. (2003), Chapman and

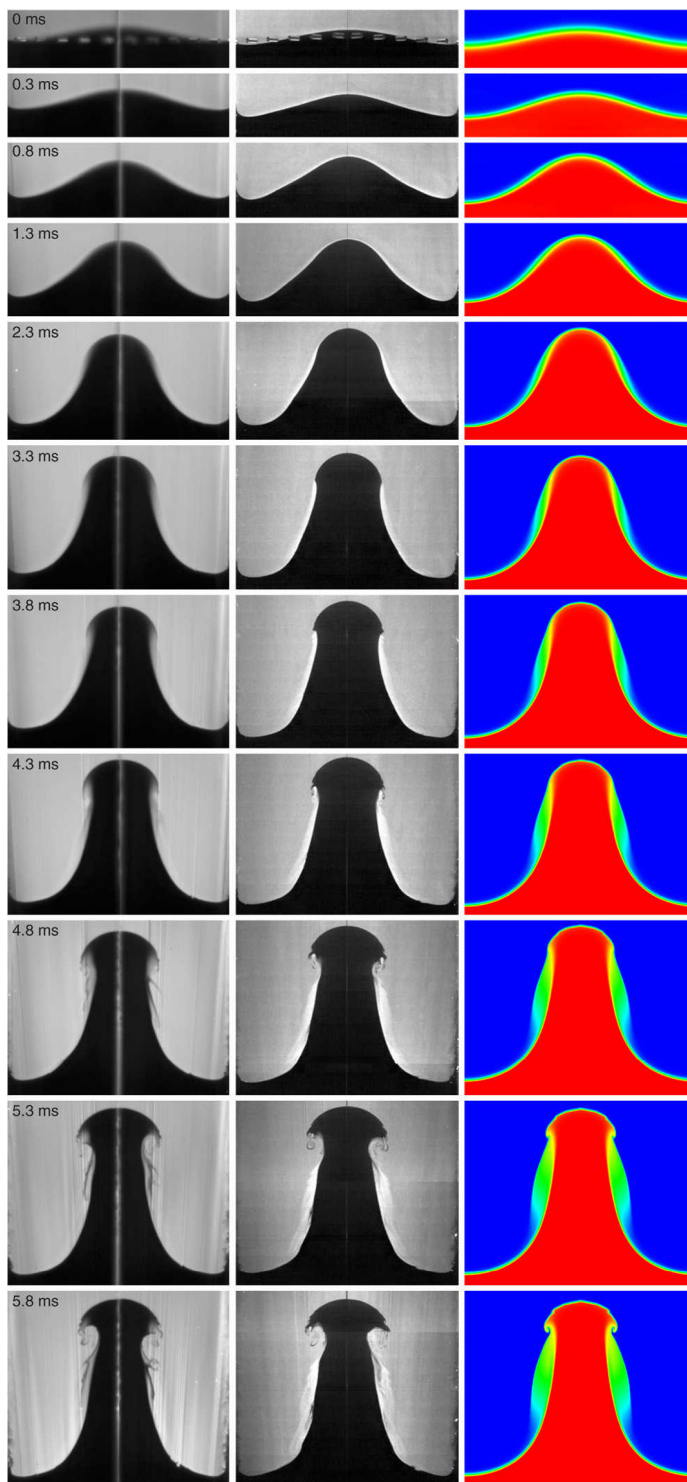


Fig. 2.24. Image sequences from the PLIF (left) and Mie scattering (center) experiments compared with that of the numerical simulation (right). Source: Fig. 3, Long et al., *Phys. Fluids*, with the permission of AIP Publishing.

Jacobs (2006), and Long et al. (2009). The initial condition can be controlled since the interface formed is free of supporting mesh or pins. Five interfaces with different amplitude are realized in the shock-tube experiments. The initial amplitude of the boundary varies from 3 to 7 mm (with fixed wavelength of 35 mm). Fig. 2.26 shows Schlieren sequences of the interface evolution in the experiments.

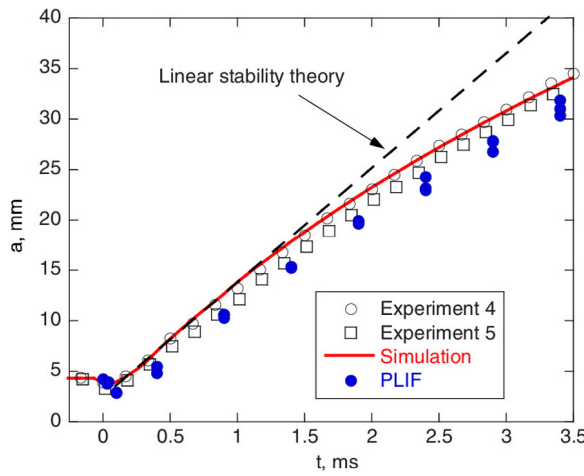


Fig. 2.25. A comparison with early time amplitude measurements with linear stability theory, i.e., Richtmyer's impulsive model.
Source: From Fig. 9, Long et al., *Phys. Fluids*, with the permission of AIP Publishing.

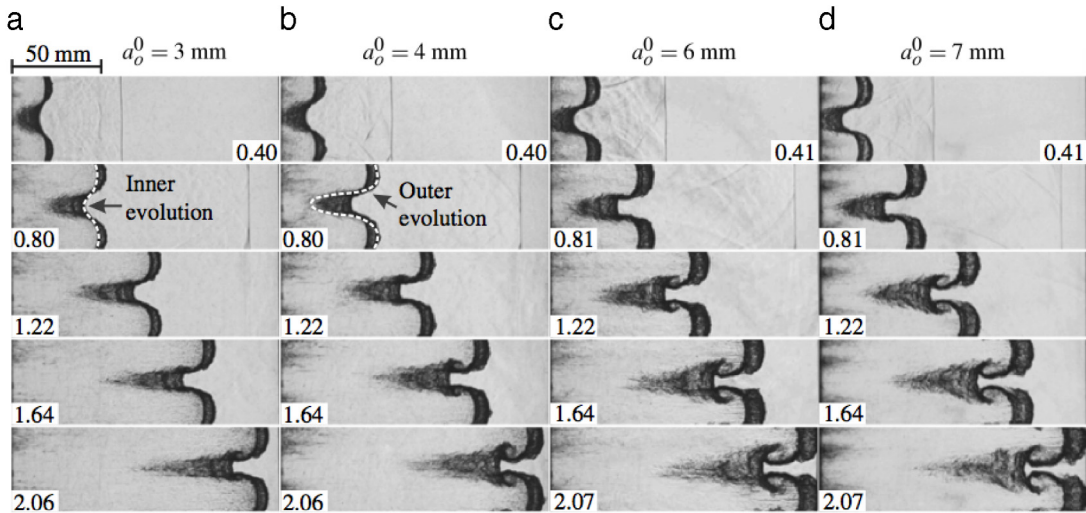


Fig. 2.26. Schlieren sequences showing the evolution of shocked air(left)/SF₆(right) interface for initial amplitudes varying from 3 to 7 mm. The shock propagates from left to right. Inserted numbers indicate the time in ms.
Source: Luo et al., Fig. 2, *J. Fluid Mech.*, 2013 with permission.

The dimensionless growth of the overall amplitude in the symmetry plane is significantly lower than those from the experimental results of the 2D single-mode (Niederhaus and Jacobs, 2003) and 3D single-mode case (Chapman and Jacobs, 2006) (Fig. 2.27). The significant differences of the Atwood number, 0.67 of Luo et al. and 0.15 used by Chapman & Jacobs and Niederhaus & Jacobs, should be noted. Using an appropriate constant, the experimental results agree well with a nonlinear model of Mikaelian (2003). These results on the curvature effect are consistent with the theoretical assertion of Krechetnikov (2009).

Numerically, Luo et al. (2016b) and Guan et al. (2017) studied the 2D and 3D single-mode interfaces, both identical and opposite principal curvatures of the interfaces. The authors considered five types of 3D interfaces and compared with the 2D interface and the 3D minimum-surface featured interface.

In a non-standard RMI experiments, Zou et al. (2017) created a *flat* interface (N₂/SF₆) by a membraneless technique and produced a *nonplanar* incident shock wave. Specifically, a rippled shock with three different segments separated by triple points is formed by the incident planar shock diffracting around the rigid cylinder (Fig. 2.28). For the rippled shock wave, the initial amplitude and width can be extracted from the Schlieren images (without considering the reflected shock). The total height and extent of the rippled shock could be defined in the same fashion as a perturbed single-mode interface in standard RMI. Quantitative shapes of the nonplanar incident shock front depend on a non-dimensional parameter, η , the ratio of spacing from cylinder to interface over cylinder diameter (Fig. 2.29 and Table 2.1). Fig. 2.30 illustrates that as η increases, the

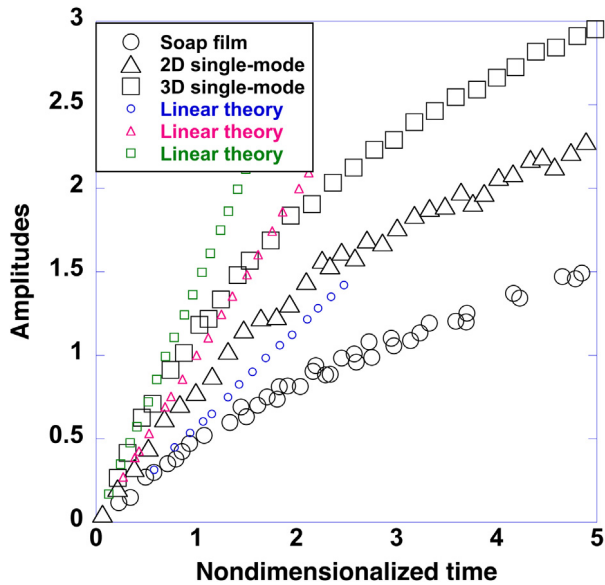


Fig. 2.27. The dimensionless growth of the overall amplitude in the symmetry plane is compared with the experimental results of the 2D single-mode (Niederhaus and Jacobs, 2003) and 3D single-mode (Chapman and Jacobs, 2006).

Source: Luo et al., Fig. 5a, *J. Fluid Mech.*, 2013 with permission.

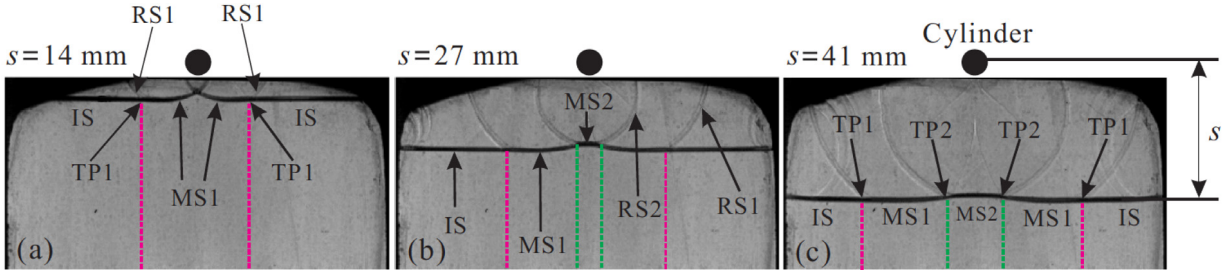


Fig. 2.28. Schlieren pictures displaying the wave pattern after the planar shock wave diffracts around a 10-mm-diameter rigid cylinder. The initial shock propagates from top to bottom, and s denotes the distance from the cylinder to the planar incident shock front. IS, incident shock; RS, reflected shock; TP, triple point; MS, Mach stem.

Source: Fig. 3 of Zou et al. (2017) with permission from *Phys. Rev. E*.

penetration depth of the cavity decreases while the area of the cavity increases. Thus, the growth rate of this non-standard RMI instability is much smaller than that of the standard RM one (Table 2.1).

3. Single-scale nonlinear models

There are a number of distinctive approaches to extend the linear stability analysis into the nonlinear regime.²⁷ The asymptotic case of high density contrast will also be considered for the RMI flows in real materials.

Note that several models first give nonlinear results for a single-mode perturbation and then go on to consider the case multi-mode initial perturbations.²⁸ The discussion of multi-mode initial perturbations will be deferred to the next section.

3.1. Potential flow models

3.1.1. The Layzer model

The potential flow modeling approach, pioneered by Layzer (1955) for RT instability, attempts a solution to the governing equations in the form of a local expansion near the bubble tip. The theory of Davies and Taylor (1950) was also based on the

²⁷ Latini et al. (2007a) and Latini (2007) provided a concise summary of single-scale nonlinear models available at the time. Also, see Bai et al. (2017) for a related numerical study.

²⁸ Of course, one needs to study nonlinear models because in the linear regime each mode by definition evolves independently of the other modes.

Table 2.1

Experimental parameters, amplitude and wavelength of incidental non-planar shock, and the comparison of the growth rate of the interface amplitude between predicted value from the Richtmyer's theory and experimental values. The values of the Mach number and velocity jumps are approximately (1.22, 1.21, 1.23), (76.1 m/s, 73.0 m/s, 79.3 m/s), respectively. The values of the Atwood numbers are 0.68 for all cases. This table is based on the data provided in Table II and Table III of Zou et al. (2017).

η	Amplitude of nonplanar incidental shock (a_0) (mm)	Wavelength of nonplanar incidental shock (λ_0) (mm)	$\frac{a_0}{\lambda_0}$	Standard RMI growth rate (theory) (m/s)	Non-standard RMI growth rate (measured) (m/s)
2.0	2.8	52.8	0.05	16.25	4.68
3.3	1.6	39.3	0.04	12.47	2.94
4.0	1.5	79.6	0.02	6.77	2.25

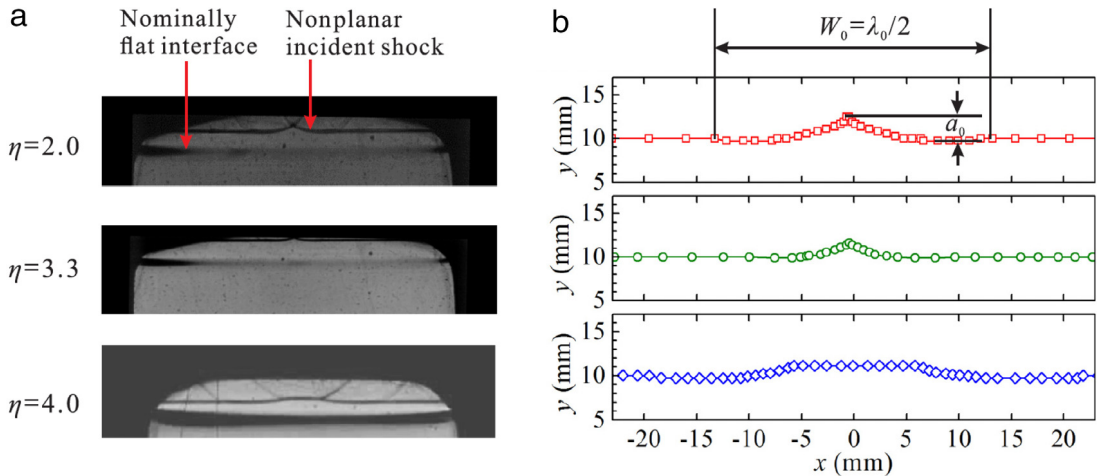


Fig. 2.29. (a) Schlieren pictures showing the shapes of the rippled incident shock and the interface. (b) Quantitative shape of the incident shock front extracted from the Schlieren images. a_0 , initial amplitude of rippled shock; W_0 , initial width of rippled shock; λ_0 , initial wavelength of rippled shock.

Source: Fig. 4 of Zou et al. (2017) with permission from *Phys. Rev. E*.

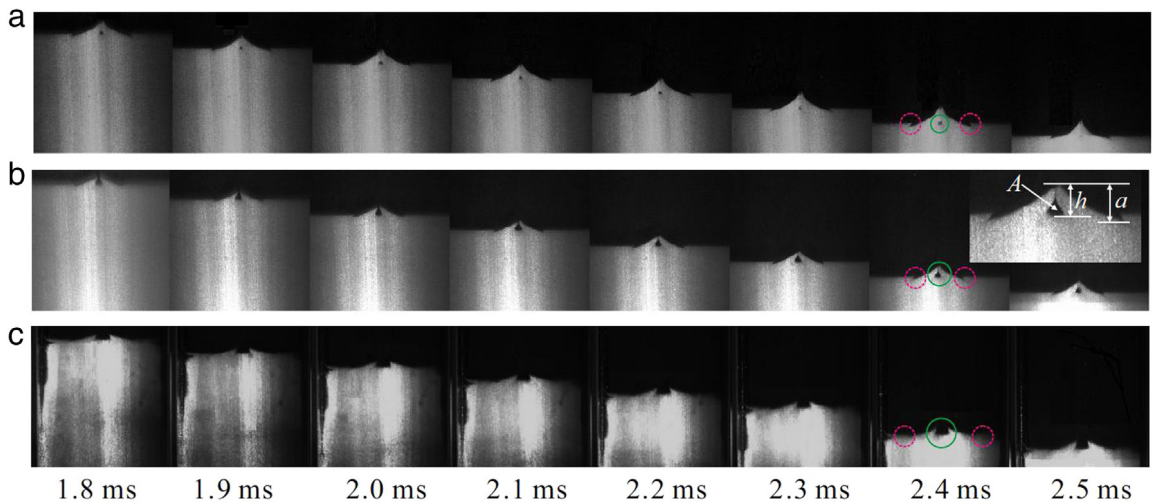


Fig. 2.30. Fog visualization sequences showing the evolution of the planar interface impacted by the rippled shock for $\eta = 2.0$ (a), $\eta = 3.3$ (b), and $\eta = 4.0$ (c). Solid circles indicate the N_2 cavity and dashed circles indicate the steps. a : amplitude from top to bottom of the interface; h : height from top of the interface to bottom of the cavity; A : area of the cavity.

Source: Fig. 5 of Zou et al. (2017) with permission from *Phys. Rev. E*.

idea of approximately satisfying the equations of motion in the neighborhood of the vertex of the bubble (Zufiria, 1988a). The nonlinear boundary value problem for the Euler equations was simplified to a set of ordinary differential equations. This model is appropriate only to the fluid–vacuum interfaces (Atwood number $A = 1$). The solution demands knowledge of the

velocity field, which Layzer assumed to be available by a single Fourier mode, and is consistent with the results of Rayleigh and Taylor at the short and long times, respectively.

Layzer considered two cases at $A = 1$: 2D bubbles in the form of archways (Fourier mode) and 3D bubbles rising in a cylindrical tube (Bessel function mode).²⁹ The limiting bubble velocities were

$$2D : v = \sqrt{\frac{g\lambda}{6\pi}} \quad 3D : v = \sqrt{\frac{gD}{2\beta_1}} \quad (3.1)$$

where λ is the wavelength, D is the diameter and $\beta_1 = 3.83171$ is the first zero of the Bessel function $J_0(r)$.

Layzer's simple model has been shown to agree with more accurate solutions that require numerical integration (Birkhoff and Carter, 1957). Both Birkhoff and Carter (1957) and Garabedian (1957) considered the two-dimensional flow of an incompressible fluid past a gas bubble in an infinitely long tube between parallel walls. Using an improved scheme of the procedure proposed by Birkhoff and Carter, Vanden-Broeck (1984) computed the shape of a bubble-rise at a constant velocity and confirmed Garabedian's finding. Hecht et al. (1994) extended the Layzer's model to the RM flows and obtained an analytic expression for the asymptotic bubble growth rate.

It is interesting that there is a reference earlier than Davies and Taylor (1950) giving the limiting velocity for a bubble rising in a cylindrical tube (Dumitrescu, 1943). This paper gives $v = 0.351\sqrt{gD}$ compared to $v = 0.361\sqrt{gD}$ for the Layzer model (Eq. (3.1)).

Zufiria (1988a) followed the ideas of Davies and Taylor (1950) and Layzer (1955), but now allowed the possibility of the bubbles changing their basic sizes. The values obtained for the acceleration of the front were in very good agreement (Zufiria, 1988b) with experimental results of Read (1984). Zufiria model was also extended to multiple-bubble evolution of RT instability of finite density ratio (Sohn, 2007, 2008). The key difference between the Layzer and Zufiria models is that the velocity potential in the former model is an analytical function of sinusoidal form, while in the latter has a point source (Sohn, 2008). These two approaches have certain similarities, such as approximating the shape of the finger near the tip as a parabolic form, and using a set of ordinary differential equations for the growth rate of the fingers. These two methodologies give qualitatively the same but quantitatively different predictions as shown in Sohn and Zhang (2001).

More work on various aspects of the Layzer model can be found, for instance, in Cameron and Pike (1965), Ott (1972), Hazak (1996), Zhang (1998), Mikaelian (1998), Abarzhi (1998, 2000), Clavin and Williams (2005), Goncharov and Li (2005), Clark and Tabak (2005, 2006), Inogamov and Abarzhi (1995), Herrmann et al. (2008) and Sohn (2009). Zhang's model for spikes, valid for $A = 1$ only, appears to be quite reasonable (Mikaelian, 2008) for both 2D and 3D simulations. In the RTI and RMI work by Krechetnikov (2009), the analysis of the stability of curved interfaces led to the rigorous generalization of the classical idea of Layzer (1955) on approximating the potential function in free-boundary problems with curved base-state interfaces. This new stability analysis, based on operator and boundary perturbation theories, also delineated the validity of the original Richtmyer growth rate equation as well as its dependence on the frame of reference. Banerjee et al. (2013) considered the development of RT and RM instability within a finite upper and lower boundary. In RTI, the growth and growth rate of bubble tip and spike tip are significantly reduced for small height and depth compared with infinite fluid. In RM instability the same features as RT are observed; however, the process is very slow compared to RT and for small time scale it behaves like an infinite fluid.

Layzer's method suggests a fundamental difference between two- and three-dimensional motions (Inogamov and Oparin, 1999). The spectral decomposition of the velocity potential can be carried out in a series of rectangular, square, and triangular arrays. While the vortices are rectilinear in planar geometry and ring-shaped in axisymmetric geometry in the case of the 2D motion, the vortices are found to be very complicated in the 3D case.

The Layzer model and subsequent developments by Goncharov, Sohn and other researchers, all assume that the perturbed surface height is singled-valued which is not valid when vortex roll-up begins. This restriction has important consequences for very late stage behavior. It should be noted that the heuristic, two-point Padé approximant, vortex models overcome this restriction.

3.1.2. The Goncharov model

Goncharov (2002) extended the Layzer's model to arbitrary Atwood numbers. In this important work, he obtained an accurate approximation of conservation equations (valid at the tip of the bubble) in the form of a convergent Fourier series. The governing equation for the velocity potential, ϕ , obeys the Laplace equation and the jump conditions at the fluid interface $y = \eta(x, t)$. He writes the velocity potential near the bubble tip as

$$\begin{aligned} \phi^h &= \tilde{a}_1(t) \cos(kx) e^{-k(y-a_0)} \\ \phi^L &= \tilde{b}_1(t) \cos(kx) e^{k(y-a_0)} + \tilde{b}_2(t)y \end{aligned} \quad (3.2)$$

where a_0 is the initial amplitude. Again, the interface amplitude, a , is expanded near the tip of the bubble, $\{x, y\} = (0, a(0, t))$,

$$a = a_0(t) + a_2(t)x^2. \quad (3.3)$$

²⁹ There is a close connection to the 2D/3D behavior discussed in Section 2.1.

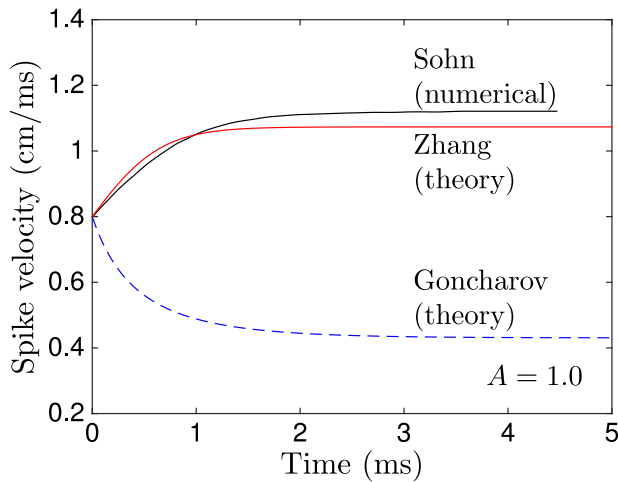


Fig. 3.1. The spike velocity from theoretical predictions of Goncharov (2002) and Zhang (1998) and the numerical data from Sohn (2004).

Therefore, five ordinary differential equations are solved for the functions, $a_0(t), a_2(t), \tilde{a}_1(t), \tilde{b}_1(t), \tilde{b}_2(t)$. This model provides a continuous bubble evolution from the earlier exponential growth to the nonlinear regime when the RTI bubble velocity saturates at

$$v_b = \begin{cases} \sqrt{2Ag}/[(1+A)(3k)], & \text{for 2D} \\ \sqrt{2Ag}/[(1+A)k], & \text{for 3D} \end{cases} \quad (3.4a)$$

and the asymptotic RMI bubble velocity becomes

$$v_b = \begin{cases} (3+A)/[3(1+A)kt], & \text{for 2D} \\ 2/[(1+A)kt], & \text{for 3D} \end{cases} \quad (3.4b)$$

where k is the perturbation wavenumber given by

$$2D : k = \frac{2\pi}{\lambda} (\lambda = \text{wavelength})$$

$$3D : k = \frac{2\beta_1}{D} (D = \text{diameter}). \quad (3.4c)$$

Note again that Fourier mode (2D case) and Bessel function (3D case) expansions were used.

Potential flow models such as those of Goncharov assume a simple parabolic shape for the bubble and solve for the flow immediately around the bubble tip. From their numerical simulation, Ramaprabhu et al. (2006) confirmed that the potential flow models are accurate in the regime that they are applicable, namely, for Atwood number $A \sim 1$. However, as A decreases, they lose accuracy at late times due to the onset of vortical motion which complicates the bubble shape. Liang et al. (2016) performed a Lattice Boltzmann (Chen and Doolen, 1998) simulation of three-dimensional RTI flows, the preliminary results of which have been reported in Liang et al. (2014). At Atwood number = 0.15, the authors compared the simulation results with the predictions of the potential flow theory (Goncharov, 2002), modified potential theory (Banerjee et al., 2011) and extended Layzer model (Sohn, 2009).

Goncharov recognized the shortcoming of his model for the RTI spike. Specifically, Mikaelian (2008) determined that this model underestimated the RTI spike and RMI spike with large a_0 , but overestimated RMI spike with small a_0 (see also, Mikaelian, 2009a). As an example, the results from numerical simulations show that the growth rate of spikes increases initially for systems with large density ratios (Sohn, 2004, see the $A = 1.0$ spike velocity curve, Fig. 11, right panel). To illustrate the difference, Fig. 3.1 presents a comparison between Goncharov's model (2002), Zhang's model (1998), and Sohn's numerical result (2004). Fig. 3.1 shows that an application of Goncharov's model to the spike (inappropriately) would result in the opposite behavior at large initial amplitude.³⁰

In ICF applications, the RT instability might be seeded by the RMI (Goncharov, 2002). Liu et al. (2013) evaluated the temporal evolution of the bubble tip velocity in the RTI with different initial perturbation velocities and a discontinuous profile at arbitrary Atwood number. Based on a potential model, the temporal evolutions of the bubble tip velocity in classical

³⁰ Recently, Zhang and co-workers have carried out work on Layzer approximation further to the entire time and to all Atwood numbers. This model produced the result for growth rate of spikes consistent with that of Sohn (Zhang, private communication).

RT fluids for 2D and the 3D geometries were studied analytically and compared with their numerical simulations using a hydrodynamic code previously documented (Ye et al., 2002; Wang et al., 2009a,b, 2010a,b,c).

3.1.3. The Sohn model

Sohn (2003) also generalized the Layzer's model to arbitrary Atwood numbers. In this model, the y -axis is chosen in the direction of the density gradient. The interface amplitude, a , and the jump conditions are expanded near the tip of the bubble, $\{x, y\} = \{0, a(0, t)\}$,

$$a = a_0(t) + a_2(t)x^2. \quad (3.5)$$

The velocity potentials take the forms,

$$\phi^h = \tilde{a}(t) \cos(kx)e^{-ky} \quad (3.6)$$

$$\phi^L = -\tilde{a}(t) \cos(kx)e^{-ky}. \quad (3.7)$$

The prediction for the bubble growth rates of RT and RM instabilities can be obtained by solving only ordinary differential equations of $a_0(t)$, $a_2(t)$, $\tilde{a}(t)$. Through comparisons with numerical results, this three-equation model provided a theory for the evolution of RT and RM bubbles over all time ranges from the small amplitude linear stage to the late nonlinear stage, including the asymptotic growth rates for RT bubbles for finite density ratios in two and three dimensions (Sohn, 2003),

$$v_b = \begin{cases} \sqrt{Ag/(2+A)}k, & \text{for 2D} \\ \sqrt{Ag/k}, & \text{for 3D} \end{cases} \quad (3.8a)$$

and the asymptotic growth rates for RMI bubbles,

$$v_b = \begin{cases} 2/[(2+A)kt], & \text{for 2D} \\ 1/kt, & \text{for 3D.} \end{cases} \quad (3.8b)$$

It should be noted that this early model does suffer from some drawbacks because the potentials grow exponentially away from the interface, i.e. $\sim \exp(-y)$ for $y > 0$ as well as $y < 0$. In more recent work, Sohn (2009) used Goncharov's model instead of above discussed 2003 model for the velocity potentials in order to incorporate the viscosity and surface tension.

3.1.4. The Abarzhi, Nishihara and Glimm model

Jacobs and Krivets (2005) noted that the single-mode approximation for the velocity field by Goncharov and Sohn must be modified in the lighter fluid to satisfy the continuity of the normal velocity component at the interface, resulting in unphysical behavior at infinity. This is really a very minor criticism, however, as Goncharov meant his potentials to be used near the interface only. In any case, Abarzhi et al. (2003) adopted a multiple harmonic approach that retains more of the Fourier modes and thus potentially possesses greater accuracy. The non-local character of the interface dynamics can be taken into account with this approach. The asymptotic growth rate for the RMI bubbles, for example, reads as

$$v_b = \begin{cases} \frac{3}{A} \frac{1}{kt} & \text{for 2D,} \\ \frac{6}{A} \frac{1}{kt} & \text{for 3D.} \end{cases} \quad (3.9)$$

This method also eliminates the problem of unrealistic velocities at infinity. These authors also reported a non-trivial dependence of the bubble curvature and velocity on the density ratio, and reveal an important difference between the dynamics of RTI and RMI bubbles.

3.1.5. The Zhang and Guo potential flow model

Zhang and Guo (2016) studied the asymptotic large-time behavior of RTI and RMI by considering the governing equations for incompressible, inviscid and irrotational fluids with arbitrary density ratio in two dimensions (Layzer, 1955). As both the velocity and the curvature of the finger tip are insensitive to time in the quasi-steady stage (Glimm et al., 2002; Sohn, 2004), an equation for the velocity of the finger for RT instability in the quasi-steady stage can be obtained:

$$\frac{dv}{dt} = -\hat{a}k(v^2 - v_{qs}^2) \quad (3.10a)$$

where

$$\hat{a} = \frac{3}{4} \frac{(1+A)(3+A)}{\left[3+A+\sqrt{2}(1+A)^{1/2}\right]} \frac{\left[4(3+A)+\sqrt{2}(9+A)(1+A)^{1/2}\right]}{\left[(3+A)^2+2\sqrt{2}(3-A)(1+A)^{1/2}\right]} \quad (3.10b)$$

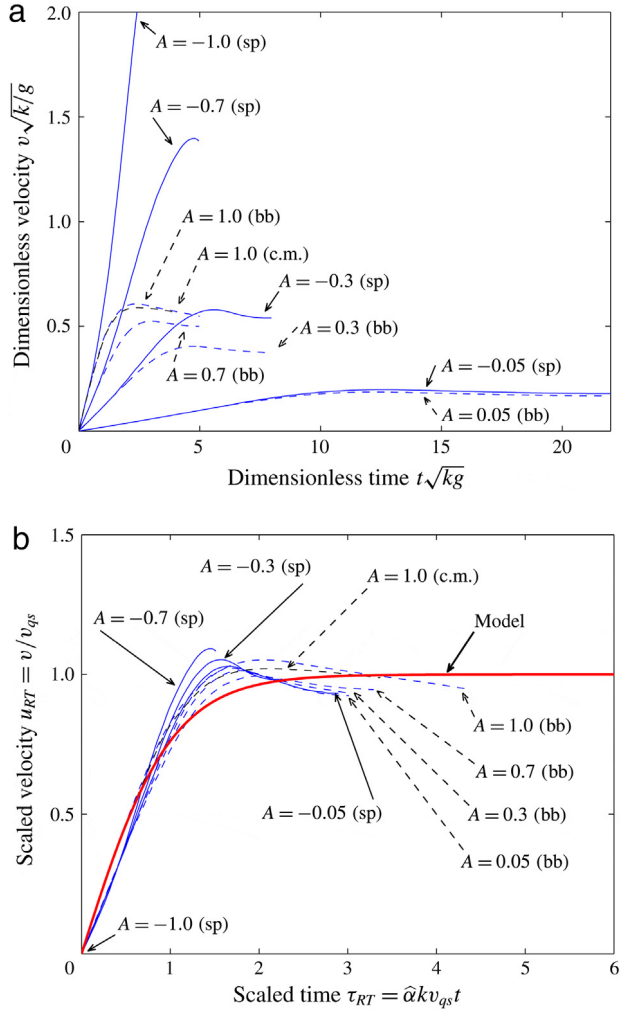


Fig. 3.2. (a) Spike (solid curves) and bubble (dashed curves) velocities at different Atwood numbers A from numerical simulations for RT instability. Blue curves: vortex model results from Sohn (2004), with $a_0k = 0.5$, $v_0 = 0$ and $A = \pm 0.05, \pm 0.3, \pm 0.7, \pm 1$. Black curve (labeled as c.m.): conformal mapping result from Menikoff and Zemach (1983), with the same initial conditions and $A = 1$. (b) Comparison between model curve and scaled data for RT instability at different Atwood numbers. The solid curves are the scaled spike velocities, and the dashed curves are the scaled bubble velocities. Red curve: model prediction. Blue curves: vortex model results from Sohn (2004), with $a_0k = 0.5$, $v_0 = 0$ and $A = \pm 0.05, \pm 0.3, \pm 0.7, \pm 1$. Black curve (labeled as c.m.): conformal mapping result from Menikoff and Zemach (1983), with the same initial conditions and $A = 1$.

Source: Fig. 5 and Fig. 9 of Zhang and Guo, *J. Fluid Mech.* with permission.

and

$$v_{qs}(A) = \left(\frac{Ag}{3k} \frac{8}{(1+A)(3+A)} \frac{\left[3 + A + \sqrt{2}(1+A)^{1/2} \right]^2}{\left[4(3+A) + \sqrt{2}(9+A)(1+A)^{1/2} \right]} \right)^{1/2}. \quad (3.10c)$$

A matched solution for v can be obtained by integrating above equation from 0 to a given time t :

$$u_{RT} = \frac{1 - re^{-2\tau_{RT}}}{1 + re^{-2\tau_{RT}}}, \quad (3.11)$$

where $u_{RT} = \frac{v}{v_{qs}}$, $\tau_{RT} = \hat{\alpha}kv_{qs}t$, and $r = [1 - u_{RT}(0)]/[1 + u_{RT}(0)]$. Eq. (3.11) shows that the relationship between the scaled variables u_{RT} and τ_{RT} is independent of A . Therefore; such a relationship is universal for all Atwood numbers.

Fig. 3.2 (from Fig. 9 of Zhang and Guo, 2016) shows the similarity and the universality between the growth rate of spikes and that of bubbles at different Atwood numbers for RTI. According to the authors, the agreement between the model prediction and the scaled numerical data has been somewhat degraded for several reasons. As the fingers in RTI are driven by gravity, it is much harder to carry out the simulations to the asymptotic regime. Furthermore, the simulations

of Sohn (2004) contained some transient effects and utilized a numerical desingularization parameter to avoid singularities in computation, but also reduce the growth rates. Nevertheless, it appears that the scaled velocity fields for all fingers are gradually approaching the same universality curve.

For RMI, Eq. (3.10) can be simplified by taking the limit $g \rightarrow 0$,

$$\frac{dv}{dt} = -\hat{a}kv^2 \quad (3.12)$$

which resulted in the matched solution

$$v = \frac{v_0}{1 + \hat{a}kv_0 t} \quad (3.13a)$$

where v_0 is the initial velocity and the expression recovers the results shown by Mikaelian (1998) and Buttler et al. (2012) in the $A = 1$ case. Eq. (3.13a) is for dimensional quantities, and therefore it should be rewritten to reveal the desired universality,

$$u_{RM} = \frac{1}{1 + \tau_{RM}} \quad (3.13b)$$

where the scaled velocity $u_{RM} = v/v_0$ and scaled time $\tau_{RM} = \hat{a}kv_0 t$.

Fig. 3.3 illustrates that the model curves agree well with the RMI numerical results from Dimonte and Ramaprabhu (2010) (FLASH), with $a_0 k = 0.125$ and $A = \pm 0.25, \pm 0.5, \pm 0.75, \pm 0.88, \pm 0.94, \pm 0.98$. The comparison between the model and numerical results from Alon et al. (1995) (LEEOR2D) and Sohn (2004) (vortex method) are also satisfactory (not shown). These results indicated that, especially for RTI, longer simulations are needed for spikes with large Atwood numbers to reach the quasi-steady stage.

As noted already in Section 3.1.2, the Goncharov's model only describes a continuous bubble evolution from the earlier exponential growth to the nonlinear regime when the RTI bubble velocity saturates. Indeed, Goncharov's approach is essentially an extension of the Layzer approximation for bubbles in the infinite density ratio system, where one of the phases is vacuum. In such a system, the spike and the bubble are uncoupled. Since the bubble curvature is not sensitive to the Atwood number, the model gives a good approximation for bubbles.

The Zhang–Guo approach provided some clues on why Goncharov's model worked for bubbles but not for spikes. For finite density ratio systems, the spike and the bubble are coupled. As one interchanges the density of the bubble and that of the spike, the result for bubbles should become that for spikes, and vice versa. This symmetry should be preserved not only in the final solution, but also in the entire derivation and approximation. This symmetry would have been broken should one insisted on applying Goncharov's model to the spike side. Recall that he introduced a linear term $\dot{b}_2(t)$ in one of the phases, but not in the other. Such an introduction would incorrectly decouple the spike from the bubble and lead to the conclusion that the absolute values of the asymptotic curvature of all bubbles and spikes are the same. Unfortunately, the asymptotic curvatures for spikes vary from around 0.177 to infinity.

3.1.6. The asymptotic case of high density contrast

3.1.6.1. Experimental evidence at $A = 1$. The asymptotic case of high-density contrast is of interest in a number of circumstances (Buttler et al., 2012; Cherne et al., 2015; Dimonte et al., 2011, 2013; Mikaelian, 2005, 2013; López Ortega et al., 2014; Piriz et al., 2006, 2008, 2009; Plohr and Plohr, 2005; Samulyak and Prykarpatsky, 2004; Williams, 2016). The free surfaces of liquids and solids have densities of 1000 or more times that of their gaseous environment at room temperature and pressure, and density ratios can be far higher at elevated temperatures or reduced pressures. In astrophysical plasmas, density ratios of a factor of 100 or 1000 are common, as the plasma tends to fall into one of several regimes where the temperature is controlled by cooling by molecular, atomic or X-ray emission (e.g. Field et al., 1969).

Buttler and collaborators, including recently Buttler et al. (2012), have performed a series of experiments on shock loaded metal samples (see for example, Buttler et al., 2007a,b, 2014, 2017; Monfared et al., 2015; Prime et al., 2014, 2017; Wood et al., 2017). They have examined in detail the effect of shock strength and perturbation amplitude on the production of ejecta from material surfaces.³¹ Many of these experiments have been studied using proton radiography, a very powerful diagnostic which allows a series of images to be obtained from experiments at very rapid intervals, with high fidelity. This has allowed detailed quantitative comparisons to be made between these experiments, computational modeling and theory.

Shock-driven jetting from isolated features has also been studied using laser experiments (e.g. Foster et al., 2005). Most often laser-driven RM and RT experiments are designed to maintain linear amplitudes, with the buoyant forces used as a well-determined driving force in studies of high strain-rate material strength.

Lund and Dalziel (2014) studied the flows resulting when a balloon filled with water bursts on impact with a surface. Capillary waves on the balloon surface before it ruptures lead to the formation of a strong single-mode perturbation. When the balloon ruptures, the removal of the elastic force from the membrane leads to an impulsively-driven expansion, with many similarities to $A = 1$ RMI, with jets of material growing from the capillary waves, break up into a fine mist of droplets.

³¹ See related work by Bell et al. (2017), Chen et al. (2017b), Georgievskaya and Raevsky (2017), Jensen et al. (2015), Karkhanis et al. (2017), Schauer et al. (2017), Schill et al. (2017) and Sorenson et al. (2017). Recently, an entire volume of the *Journal of Dynamic Behavior of Materials*, guest edited by Buttler, Williams and Najjar, was devoted to the current state of the art in ejecta physics, describing experimental, theoretical and computational work by research groups around the world (Ejecta physics, 2017).

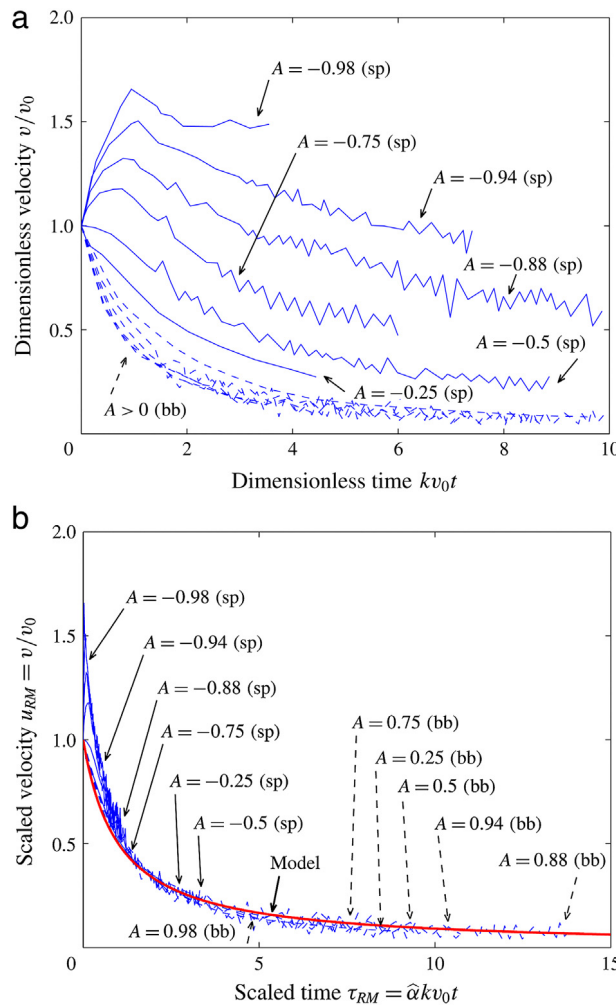


Fig. 3.3. (a) Spike (solid curves) and bubble (dashed curves) velocities at different Atwood numbers A from numerical simulations for RM instability [Dimonte and Ramaprabhu \(2010\)](#). The initial condition is $a_0k = 0.125$, with $A = \pm 0.25, \pm 0.5, \pm 0.75, \pm 0.88, \pm 0.94, \pm 0.98$. (b) Comparison between model curve and scaled data for RM instability at different Atwood numbers. The solid curves are the scaled spike velocities, and the dashed curves are the scaled bubble velocities. Red curve: universality model prediction. Blue curves: numerical results (FLASH) from [Dimonte and Ramaprabhu \(2010\)](#).

Source: Fig. 3 and Fig. 7 from [Zhang and Guo \(2016\)](#), *J. Fluid Mech.* with permission.

3.1.6.2. Numerical modeling at high Atwood number. To study the case of RMI at high Atwood number in real materials, the continuum mechanics can be modeled by most techniques which are robust to the high material strains which can occur as the spikes grow. A number of studies have been performed using either molecular dynamics ([Durand and Soulard, 2012, 2013, 2015, 2017; Durand et al., 2016; Li et al., 2014; Ren et al., 2014; Shao et al., 2013, 2014; Cherne et al., 2015](#)) or continuum modeling (e.g. [Dimonte and Ramaprabhu, 2010; Liu and Grieves, 2014; Cherne et al., 2015; Williams and Grapes, 2017; Yin et al., 2017](#)). Molecular dynamics calculations ([Alder and Wainwright, 1957](#)) are limited in space- and time-scale by the number of atoms which can be treated in the calculation, but simulate directly the material properties, limited only by the accuracy of the interatomic potentials used in the calculations. Several articles have studied the role of ejecta production and the size and velocity distribution of the ejected material. Continuum modeling, by contrast, can be run at a scale appropriate to the experiment being studied, but requires detailed models to be implemented for all the relevant material properties: equations of state, material strength and failure, as well as potentially viscosity and surface tension. Cherne et al. obtained good agreement between the results of these two techniques for a case in the fluid dynamic limit, for a variety of initial surface profiles. [Durand and Soulard \(2015\)](#) discuss in detail the processes by which the initial jets in their calculations break up into discrete particles; however, the large magnitude of surface forces at the scales at which these calculations must be run suggests that these results can only be indicative of the nature of the break up process at more typical perturbation wavelengths.

3.1.6.3. Asymptotic convergence for $A = 1$. [Williams \(2016\)](#) developed a late-time asymptotic theory for single-mode RM for $A = 1$. This limit captures the behavior of general RM mixing layers before the spikes have been subject to significant drag, with the consequent effects on the supply of lower-density material to the bubbles. This transient state of development of

RM mixing layer is seen in the results presented by [Zhang and Guo \(2016\)](#) for values of A approaching unity (see [Fig. 3.3](#)). This is a separate asymptotic behavior to that which they discuss, dependent on the order in which the limits $A \rightarrow 1$ and $t \rightarrow \infty$ are taken.

Based on the theory of [Mikaelian \(1998, 2010\)](#), [Buttler et al. \(2012\)](#), and their MD and continuum calculations, [Cherne et al. \(2015\)](#) suggest a self-similar³² collapse of the mass in the RM spike to

$$M \propto \ln(1 + t/\tau). \quad (3.14a)$$

Assuming that in the spike the material moves ballistically, to good approximation, and that mass is conserved, this suggests that for $A = 1$ the single-mode RM flow must converge to a fixed spatial form at late time, with the velocity of the material in the self-similar frame reducing asymptotically to zero. Assuming the material in the spike moves with roughly constant velocity allows the asymptotic formula for the spike mass derived by Cherne et al. to be generalized to a cumulative mass as a function of both velocity and time³³ ([Williams, 2016](#))

$$M(v, t) \propto \ln \left[\min \left(\frac{v_0}{v}, 1 + \frac{t}{\tau} \right) \right]. \quad (3.14b)$$

At late time, the cumulative mass tends to a form $M(v) \propto \text{constant} - \ln v$: at earlier times, only the parts of this distribution above a velocity $v_0/(1 + t/\tau)$ are present.

Transforming the incompressible flow equations into the decelerating frame of the bubble tip allows potential flow solutions to be developed which capture the full structure of the flow, from the exponentially-damped perturbations on the bubble side through to the $v \propto y$ kinematical behavior of material in the far spike. The material velocity in the dense fluid will be incompressible and irrotational. [Williams \(2016\)](#) suggests that a velocity distribution along the spike axis

$$v = \tilde{a} + \tilde{b} \ln(1 + \exp x) \quad (3.15)$$

satisfies the velocity boundary conditions at both extremes of x . Analytic continuation then allows the velocity distribution throughout the fluid to be derived. While the resulting pressure distribution does not exactly satisfy the surface boundary condition, suggesting that higher order corrections may be required, the analytic form of the velocity distribution and the shape of the surface still agree well with the results of a fluid dynamical simulation.

3.2. Heuristic/interpolation models

3.2.1. The Mikaelian model

[Mikaelian \(2003\)](#) found that a heuristic approach, which was previously attributed to Enrico Fermi by [Layzer \(1955\)](#), is helpful for matching his previous early-time linear solution ([Mikaelian, 1998](#)) with Goncharov's late-time expression. In this model, he assumed that one knows the asymptotic bubble velocity (\dot{a}_∞). The exponentially growing of the linear phase amplitude can be used until a transition time (denoted as t^*) is reached. At this point, \dot{a} equals the asymptotic bubble velocity and is replaced by the constant \dot{a}_∞

$$\dot{a} = \frac{\dot{a}_0}{1 + \dot{a}_0/\dot{a}_\infty}. \quad (3.16)$$

This model essentially joins the linear to the nonlinear regime by making an abrupt change in the growth rate. The remaining issue was to determine the distinctive 2D and 3D transition time for RTI and RMI flows, and this was a subject of a detailed discussion by [Mikaelian \(2003\)](#).

For example, the expression for the RMI perturbation amplitude, takes the form

$$\dot{a}(t) = \begin{cases} a_0 + \frac{3+A}{3(1+A)k} \ln \{1 + 3\dot{a}_0 kt (1+A)/(3+A)\} & \text{for 2D RM} \\ a_0 + \frac{2\mathcal{R}}{(1+A)\beta_1} \ln \{1 + \dot{a}_0 \beta_1 t (1+A)/2\mathcal{R}\} & \text{for 3D RM} \end{cases}$$

where \mathcal{R} is the tube radius for 3D flows. For the asymptotic bubble velocities, they give

$$\dot{a}(t) = \begin{cases} \frac{3+A}{3(1+A)kt} & \text{for 2D RM} \\ \frac{2\mathcal{R}}{(1+A)\beta_1 t} & \text{for 3D RM} \end{cases}$$

in agreement with the results of [Goncharov \(2002\)](#) and [Oron et al. \(2001\)](#).

³² A time-developing phenomenon is called self-similar if the spatial distributions of its properties at various different moments of time can be obtained from one another by a similarity transformation ([Barenblatt, 1996](#)). Statistically, many are "self-similar", meaning that each portion can be considered a reduced-scale image of the whole ([Mandelbrot, 1967](#)).

³³ A misprint in [Williams \(2016\)](#) has been fixed in Eq. (3.14b) – the 'max' in Eq. (8) of the paper should be replaced by 'min'.

Recently, Mikaelian (2014a) proposed an analytic model for the RTI bubble and spike amplitudes and mixing widths in the linear, nonlinear, and turbulent regimes. This approach is appropriate for accelerations that are constant or changing relatively slowly with time and for arbitrary density ratios.

3.2.2. The Sadot et al. model

Sadot et al. (1998) developed an empirical rational function approximation that agrees with late-time models, but also fits the weakly nonlinear solution to second order at early time as well ($v = da/dt$)

$$\frac{v_{b/s}}{v_0} = \frac{1 + v_0 kt}{1 + D_{b/s} v_0 kt + E_{b/s} (v_0 kt)^2}. \quad (3.17)$$

Specifically, this model exploits the fact that as $t \rightarrow 0$, $v_{b/s}/v_0 \rightarrow 1 + (1 - D_{b/s})kv_0 t + \dots$ and the D term dominates. Conversely, as $t \rightarrow \infty$, $v_{b/s}/v_0 \rightarrow 1/E_{b/s}kv_0 t$, and the E term dominates (Long et al., 2009). At large time, the bubble and spike velocities possess the desirable $1/t$ dependence.

Sadot et al. chose a value for D that would match the 2D weakly nonlinear series solution of Zhang and Sohn (1996, 1997a, b) at early time, and an E value that approximates 2D late time behavior observed in the computation of Alon et al. (1995)

$$D_{b/s} = 1 \pm A$$

$$E_{b/s} = \frac{1 \pm A}{1 + A} \frac{1}{2\pi \tilde{C}}.$$

In these expressions, the plus sign is used for the bubble velocity and the minus sign is used for the spike velocity. The constant \tilde{C} is a function of the asymptotic velocity of the bubbles and spikes, $\tilde{C} = 1/3\pi$ for $A > 0.5$ and $\tilde{C} \rightarrow 1/2\pi$ when $A \rightarrow 0$ (Collins and Jacobs, 2002; Niederhaus and Jacobs, 2003).

This model has received much attention and compares favorably with several experiments (see later subsections).

3.3. Padé approximation approaches and compressibility effects

The perturbation expansion method gives solutions in terms of polynomials of time, t , which are divergent series. The higher the order of the polynomial, the faster it diverges. To overcome this problem, Zhang and Sohn (1996, 1997a, b, 1999), and more recently Zhang et al. (2016), took approaches based on Padé approximation (Bender and Orszag, 1978; Pozzi, 1994).

3.3.1. The Zhang–Sohn model (single-point Padé approximant)

Zhang and Sohn (1996, 1997a, b, 1999), constructed a Padé approximant, which is a ratio of two polynomials of t , for the growth rate of RM fingers. The unknown coefficients in the Padé approximant are determined by expanding the approximant in terms of small t and matching the results with the small-time perturbation solution up to $O(a_0^4)$.

For RMI in 2D, the results are:

$$v = \frac{v_0}{1 + v_0 a_0 k^2 t + \max \{0, a_0^2 k^2 - A^2 + \frac{1}{2}\} v_0^2 k^2 t^2} \quad (3.18a)$$

for the overall growth rate, and

$$v_{b/s} = v \mp \frac{A k v_0^2 t}{1 + 2k^2 a_0 v_0 t + 4k^2 v_0^2 [a_0^2 k^2 + \frac{1}{3}(1 - A^2)] t^2} \quad (3.18b)$$

for the bubble/spike growth rate.

For RMI in 3D with $k_x = k_y = k/\sqrt{2}$, the results are:

$$v = \frac{v_0}{1 + a_0 k^2 v_0 \lambda_1 t + \max \{0, a_0^2 k^2 \lambda_1^2 - \lambda_2 k^2 v_0^2 t^2\}} \quad (3.19a)$$

for the overall growth rate, and

$$v_{b/s} = v \mp \frac{v_0^2 k \lambda_3 t}{1 + v_0 a_0 k^2 \lambda_4 \lambda_3^{-1} t + (a_0^2 k^2 \lambda_4^2 \lambda_3^{-2} + \lambda_5 \lambda_3^{-1}) v_0^2 k^2 t^2} \quad (3.19b)$$

for the bubble/spike growth rate, with

$$\begin{aligned} \lambda_1 &= 0.088866A^2 + 0.455671, \\ \lambda_2 &= 0.391357A^2 - 0.227835, \\ \lambda_3 &= 0.01221A^3 + 0.69844A, \\ \lambda_4 &= 0.07035A^3 + 0.56513A, \\ \lambda_5 &= -0.30253A^3 + 0.38270A. \end{aligned} \quad (3.19c)$$

The Zhang and Sohn model (1996, 1997a,b, 1999) has been compared extensively against several RMI experimental numerical data. It has been shown that the model gives good predictions for compressible RMI in the linear and intermediate nonlinear stages. Since this model is based on the single-point Padé approximant, namely, only using the small-time solution information, naturally, it will not be valid at asymptotically large times.

If one insists applying the model to asymptotically large times, it will give a growth rate which decays too fast, namely, it decays at the rate of $1/t^2$ instead of $1/t$, as pointed out by Mikaelian (1998). The shortcoming of $1/t^2$ decay of the Zhang–Sohn single-point Padé approximant model has recently been resolved by a two-point Padé approximant, which is based on both small- and large-time information (see the next subsection).

With a high-resolution numerical method with robust handling of interface reconstruction, Li and Zhang (1997) presented a study of the RMI in two and three dimensions from the linear regime to the intermediate nonlinear regime. The numerical solution was compared with the predictions of Zhang and Sohn (1996, 1997a, b, 1999) based on the Padé approximation and asymptotic matching. Good agreement was found between numerical solutions and predictions of the nonlinear theory in both two and three dimensions and for both the reflected shock and the reflected rarefaction wave cases.

The single-point Padé approximation has been carried out to high orders by Velikovich and Dimonte (1996) for the case of $A = 1$ and by Velikovich et al. (2014) for arbitrary Atwood number. These works showed that the sequence of Padé approximants P_6^6 , P_8^8 , and P_{10}^{10} give a much better prediction than the result from the Taylor series from perturbation theory. Here P_n^m denotes the Padé approximant as a ratio of a polynomial of degree m to a polynomial of degree n . Since $m = n$ in these Padé approximants, these approximants will give constant growth rates at asymptotically large times. However, the growth rates of fingers should decay at the rate of $1/t$ except for the spike at $A = 1$ (Zhang, 1998). This is also caused by the same factor that the model is based on the single-point Padé approximation.

To develop a model valid for asymptotically large times, one should determine the asymptotically large-time behavior of fingers analytically. Such information cannot be extrapolated from the small-time information. This is the approach to be discussed in the next section.

3.3.2. The Zhang–Deng–Guo model (two-point Padé approximant)

In order to develop a theoretical prediction valid from early to late times, one needs the information about the asymptotic growth rate of RMI at all Atwood numbers and for both spikes and bubbles. This information only becomes available recently (Zhang and Guo, 2016). The knowledge at asymptotic large times presented in Zhang (1998) and Zhang and Guo (2016) plays a key role in constructing the two-point Padé approximant valid for all times.

Recently, at the 15th International Workshop on the Physics of Compressible Turbulent Mixing, Zhang, Deng and Guo (2016) presented a theory for the growth rate and the amplitude of fingers at a RM unstable interface. This theory is for compressible fluids with arbitrary Atwood numbers A . Based on a two-point Padé approximant and an asymptotic matching technique, they constructed the following expression for the growth rate of fingers:

$$v(t) = v_{lin}(t) \cdot \frac{1 + a_1(kv_{lin}^\infty t) + a_2(kv_{lin}^\infty t)^2}{1 + b_1(kv_{lin}^\infty t) + b_2(kv_{lin}^\infty t)^2 + b_3(kv_{lin}^\infty t)^3}, \quad (3.20)$$

where $v_{lin}(t)$ is the finger growth rate given by the compressible linear theory (Richtmyer, 1960; Fraley, 1986; Yang et al., 1994), $v_{lin}^\infty = \lim_{t \rightarrow \infty} v_{lin}(t)$ is the asymptotic value of $v_{lin}(t)$. The constants a_1, a_2, b_1, b_2 and b_3 are functions of A and a_0 (initial amplitude). These constants are determined by expanding Eq. (3.20) in terms of small t and in terms of large t to match the small-time perturbation solution and the large-time asymptotic solution. Consequently, the two-point Padé approximant given by Eq. (3.20) has the following properties:

(a) For $t \ll 1$, the growth rate agrees with the compressible linear theory (Richtmyer, 1960; Fraley, 1986; Yang et al., 1994).

(b) At the early nonlinear stage, the growth rate agrees with the solution from the perturbation expansion for small t (Zhang and Sohn, 1997a,b):

$$v = v_{lin}(t) \left[1 - (A + ka_0)kv_{lin}^\infty t + \left(A^2 - \frac{1}{2} + 2Aka_0 \right) (kv_{lin}^\infty t)^2 + \frac{4}{3} (A - A^3) (kv_{lin}^\infty t)^3 \right] + O(t^4). \quad (3.21)$$

(c) At asymptotic large times, i.e., $t \gg 1$, the growth rate agrees with asymptotic expansion of Eq. (3.13a):

$$v_{asym} \sim \frac{1}{\hat{a}(A)kt} \quad (3.22)$$

where \hat{a} is given in Section 3.1.5.

(d) For a system with an infinite density ratio, the expansion agrees with the known result that the spike growth rate asymptotically approaches a constant $v_{lin}^\infty \left(\frac{3+3ka_0}{1+3ka_0} \right)^{1/2}$ (Zhang, 1998).

It is known that singularities may occur in Padé approximation since the denominator of Padé approximant may vanish. It was shown that Eq. (3.20) has no singularities when $a_0k < 1/4$.

The Zhang–Deng–Guo theory shows good agreement with the results from numerical simulations for the case of the reflected rarefaction wave, even when the Mach number of the incident shock is as high as 15.3. The authors have also compared their theory with the numerical and experimental data for the case of reflected shock and agreement were also excellent (Zhang et al., 2017).

3.3.3. Compressibility effects

In addition to nonlinearity, compressibility is also important. The Zhang–Sohn model in Section 3.3.1 and the Zhang–Deng–Guo model in Section 3.3.2 are for compressible RMI. These models are based on the following physical picture. At early times, the dynamics of the system are mainly governed by the linearized Euler equations for compressible fluids, since the initial disturbance at the interface is small. At later times the dynamics are mainly governed by the nonlinear equations for incompressible fluids, as the magnitude of the disturbance at the material interface increases significantly and the transmitted shock and reflected wave move away from the interface. This physical picture received strong support, for example, from the numerical simulations of [Kotelnikov et al. \(2000\)](#). This work concluded that the effect of compressibility on the RM instability is limited to the early times of the interface evolution and that its subsequent development follows approximately incompressible equations.

Although the dynamics of the system at late times is nearly incompressible, the solution in that regime still has strong dependence on compressibility. This is because the functional form for the solutions of nonlinear and incompressible dynamics contains effective initial conditions. These effective initial conditions are determined by the asymptotic matching with the linear compressible theory in the transition regime. Such matching leads to a strong compressibility dependence of the solution, even though the dynamics of the system is nearly incompressible. This is the reason why the theoretical predictions of Zhang–Deng–Guo model ([Zhang et al., 2016, 2017](#)) are in excellent agreement with numerical data of both weak and strong shocks.

3.4. Vortex and vortex Sheet models

3.4.1. Vortex models

Vortex models have proven effective at modeling the late-time RM growth in the limit as $A \rightarrow 0$. In an idealized sense, the vortex model developed by [Jacobs and Sheeley \(1996\)](#) represents an exact solution to the governing equations in the limit of vanishingly small density difference, i.e., $A \rightarrow 0$ (see also, [Jacobs et al., 1995](#)). The authors considered the motion of a sinusoidal material interface induced by an alternating array of vortices placed at the points midway between the crests and troughs. The presence of these vortices generates a velocity field given by the stream function, which in turn will distort the interface. Assuming an Atwood number of zero, the expression for the overall amplitude becomes

$$ka = \sinh^{-1} \left[\frac{2}{\pi} k \dot{a}_0 (t - t_p) + \sinh(k a_p) \right], \quad (3.23)$$

where a_p and t_p are amplitude and time, respectively, when the vorticity is assumed to concentrate. As described in detail by Jacobs and Sheeley, near the vortex centers the induced velocity will effectively wrap the interface around the vortices. In the regions between the vortices, however, the induced motion will tend only to push the interface in the direction perpendicular to the row of vortices.

The vortex methods, like [Jacobs and Sheeley \(1996\)](#), are not appropriate for the simulations of RM instability of finite density contrast. To extend the applicability of the model to finite Atwood number, the vortex row utilized is perturbed such that the vortex spacing is smaller across the spikes and larger across the bubbles, a fact readily observed in experimental images ([Likhachev and Jacobs, 2005](#)). The resulting dimensionless equation, however, must be solved in the implicit form.

[Sohn \(2004\)](#) carried out numerical simulations for RT and RM instabilities from a full vortex model and investigated various aspects of dynamics for unstable interfaces. The point vortex method in his computation used the formulation of the vortex model in [Baker et al. \(1980\)](#) (see also [Tryggvason, 1988; Kerr, 1988; Aref and Tryggvason, 1989](#)) and adopted Krasny's method ([1986](#)) to overcome the numerical instability due to singularities by regularizing point vortices as vortices with finite cores or "blobs" of vorticity. This work found that the bubble velocity in the RT instability converges to a constant limit, and in the RM instability, the bubbles and spikes have decaying growth rates, except for the spike of infinite density ratio. For both RT and RM instabilities, bubbles attain constant asymptotic curvatures. In a related development, [Sohn \(2016\)](#) presented self-similar solution of the double-spiral for an infinite vortex sheet and asymptotic behavior of the solution.

3.4.2. The vortex sheet model of Matsuoka–Nishihara–Fukuda

[Matsuoka et al. \(2003\)](#) studied the problem in Lagrangian picture by developing a model that describes the nonlinear evolution of a non-uniform vortex sheet with a density jump across it. The fundamental assumption of the model was validated by comparing its nonlinear dynamics with that of a shocked interface with the use of two-dimensional hydrodynamic simulations. With the proper kinematic boundary conditions, the authors found that the Lagrangian description of the vortex sheet enables the model to follow its nonlinear dynamics, such as its local shrinking and stretching in the tangential direction. This nonlinear analysis, of course, is limited to the short time behavior of the interface evolution.

In order to describe the entire interface dynamics from the linear regime to a fully nonlinear stage, [Matsuoka and Nishihara \(2006\)](#) considered an interface motion in the RM instability using the Birkhoff–Rott equation³⁴ ([Birkhoff, 1962; Rott, 1956; Saffman, 1992; Baker et al., 1993; Tanveer, 1993](#)) coupled with an evolution equation of the vortex strength at the sheet ([Baker et al., 1982](#)). The coupled equations describe all inviscid and incompressible instabilities of a fluid interface such as the RTI, RMI, and KHI. The authors compared and contrasted the RTI and RMI regarding the singularity formation.

³⁴ [Granero-Belinchón and Shkoller \(2017\)](#) derived so-called h -model using asymptotic expansions in the Birkhoff–Rott integral-kernel formulation for the evolution of an interface separating two incompressible and irrotational fluids. Numerical simulations of the h -model showed good agreement for the growth of the mixing layer with experimental data in the "rocket rig" experiment of [Read \(1984\)](#) and [Youngs \(1984, 1989\)](#).

4. Multi-scale nonlinear models and assessment of models

4.1. Perturbation models

4.1.1. Haan's second order analysis and saturation model

An expansion of the flow equations provided the expression for the early nonlinear evolution (Ingraham, 1954; Jacobs and Catton, 1988a,b and references therein). A second order analysis by Haan (1991) was constructed for an interface between two materials in an imploding ICF capsule. For a slightly perturbed interface, an expansion was carried out in spherical harmonics to derive a second order mode-coupling equation. The importance of mode coupling in the generation of large structure that dominates the late stage evolution, and the relative importance of long-wavelength components in the initial perturbation spectra on the late-stage evolution have also been illustrated, for example, in Shvarts et al. (1995). The mode amplitudes, Z_k , is obtained by expanding the flow equations to second order (Haan, 1991)

$$\ddot{Z}_k = \gamma^2(k) Z_k + Ak \sum_{\mathbf{k}_2} \left[\ddot{Z}_{k_2} Z_{k'_2} \left(1 - \hat{\mathbf{k}}_2 \cdot \hat{\mathbf{k}} \right) + \dot{Z}_{k_2} \dot{Z}_{k'_2} \left(\frac{1}{2} - \hat{\mathbf{k}}_2 \cdot \hat{\mathbf{k}} - \frac{1}{2} \hat{\mathbf{k}}_2 \cdot \hat{\mathbf{k}}' \right) \right], \quad (4.1)$$

where γ is the growth rate, $\hat{\mathbf{k}}$ is the unit vector, and $\mathbf{k}'_2 = \mathbf{k} - \mathbf{k}_2$.

The second-order analysis has proven to be valuable for providing a way of estimating when the nonlinear effects become important and what their character is in the weakly nonlinear regime (Haan, 1991). A technique is applied that couples 2-D linear regime hydrodynamic code results with the analytic model to allow modeling of 3-D RT growth through the linear regime and into the weakly nonlinear regime (Dunning and Haan, 1995). The individual modes may become nonlinear even when their amplitudes are below the single-mode threshold owing to their interaction with nearby modes (Ramaprabhu et al., 2005). Such a picture found applications in relating the nonlinear saturation of the beam-plasma instability for a single mode to the multi-mode case (DeNeef, 1975; Dimonte, 1982).

Haan (1989) also constructed a model built on assuming that the spectral amplitudes of 3D, broadband modulations grow linearly until they reach a saturation level, $S_k = 2/Lk^2$ (L is the size of the analysis box), after which their amplitude is given by a logarithmic construction that depends on how far into the nonlinear regime they have grown. For classical RT, this amounted to assuming that each mode grows exponentially with its own RT growth rate, until reaching the saturation amplitude, after which it grows linearly in time with the velocity $V_s(k)$ with which the mode was growing when it became nonlinear (Birkhoff, 1955; Smalyuk, 2012).

Short-wavelength modes grow initially most rapidly and quickly saturate at levels S_k , while very long-wavelength modes grow more slowly. As a result, the mid-wavelength modes have the largest growth factors, producing a peak in the spectrum. As the evolution continues, this peak moves to longer wavelengths (Smalyuk et al., 2006). The measured nonlinear saturation and the post-saturation growth of the RT instability on the Omega laser system are found to be in excellent agreement with those predicted by the model.³⁵ These spectra and growth velocities are insensitive to initial conditions (Smalyuk et al., 1998, 2005). Since the initial conditions are mostly forgotten in the nonlinear phase, small uncertainties in the initial seeds will not have a large impact on the resulting perturbation growth (Welser-Sherrill et al., 2007). Subsequently, Ofer et al. (1996) proposed a model that includes a description of nonlinear low-order mode coupling, mode growth saturation, and post-saturation mode coupling. This model was shown to significantly extend the range of applicability of a previous model proposed by Haan.

Recently, Rollin and Andrews (2013) have used Haan's model as part of a consistent initialization scheme for the engineering models. While the model only applies in the weakly nonlinear regime for broadband modulation amplitudes around the saturation levels (Smalyuk et al., 1998), it is fully general regarding the acceleration imposed so that it remains valid for both RTI and RMI.

Haan noted that his model is explicitly multi-mode so it is hard to compare to the single-mode models documented in the previous section. It would be interesting to see how the long-time single mode solutions might lead to a somewhat different multi-mode model, and how much they differ.³⁶

4.1.2. Third order nonlinearity

A self-modulation of a primary mode produced by the third-order nonlinearity is a mechanism for deviation from the linear growth (Nishihara and Ikegawa, 1999). Motivated by the experimental data collected from the Nova laser system, Wood-Vasey et al. (2000) explored the amplitude saturation model of Haan (1989) and a 3rd order perturbation theory expansion of Jacobs and Catton (1988a).

Based on the superposition of modes, Ikegawa and Nishihara (2003) developed third-order nonlinear theories that describe continuous transition from the linear to the weakly nonlinear growths of the classical RTI and the ablative RTI (ARTI, see for instance, Bodner, 1974; Verdon et al., 1982; Baker et al., 1987; Kull, 1989; Kilkenny et al., 1994; Betti et al., 1995, 1998; Goncharov et al., 1996; Ikegawa and Nishihara, 2002).³⁷ This theory improved the results of Jacobs and Catton

³⁵ Remington et al. (1995) also compared their multimode RT experiments on the NOVA laser with the Haan's model.

³⁶ S.W. Haan (private communication, 2017).

³⁷ Additional remarks on ablative RTI can be found in Section 15 of the review.

(1988a), where they considered only a single mode and neglected the light fluid (Atwood number $A = 1$). Garnier and Masse (2005) showed that it is necessary to compute the third-order weakly nonlinear corrections in the multimode case to capture the first statistical corrections. Their analytical formulas illustrated the influence of ablation on RT instability in the linear and weakly nonlinear regimes (see also Berning and Rubenchik, 1998).

In another related development, Liu et al. (2012) investigated analytically nonlinear saturation amplitudes of the first two harmonics in RTI for irrotational, incompressible, and inviscid fluids, with a discontinuous profile at arbitrary Atwood numbers by considering nonlinear corrections up to the tenth-order.

4.1.3. The Vandenboomgaerde–Gauthier–Mügler model

Vandenboomgaerde et al. (2002) advanced a simplified perturbation theory for nonlinear regime of a multimode RMI. The authors proposed a way to simplify and accelerate the computation for the perturbation theory in the weakly nonlinear RMI. In the standard approach, expansions appear to be series in time. The authors build accurate approximations by retaining the most secular terms, which are these with the largest unbounded part (Nayfeh, 1973; Bender and Orszag, 1978). The advantage of this approach is that computations for multimode interfaces become tractable.

Later, these authors extended this approach to 9th and 11th order in their Taylor series (Vandenboomgaerde, 2003; Vandenboomgaerde et al., 2003). Furthermore, replacing the Dirac function acceleration by a constant in the momentum equation at the interface (Bernoulli's equation), the RTI can be treated by this perturbation model. For single- and two-mode configurations, Vandenboomgaerde et al. (2003) checked the accuracy of the approximate perturbation method by comparing with simulations performed by Menikoff and Zemach (1983), and with some results of Baker et al. (1980) concerning the influence of the Atwood number on the growth of spikes and bubbles.

Vandenboomgaerde et al. (2002, 2003) and Vandenboomgaerde (2003) stated that their work was a simplification of the “full perturbation method” by Zhang and Sohn (1997a). Indeed, Zhang and Sohn (1997a) carried out nonlinear perturbation solutions for incompressible fluids, which is like the previous work by Holyer (1979) concerning water waves. Yet, it appears that the main features of the Zhang and Sohn theory are the utilization of the Padé approximation (Bender and Orszag, 1978; Pozzi, 1994) for computing the growth rate of the amplitude of a single-mode interface and strong dependence on compressibility, even for late times when the dynamics of the system is approximately incompressible. These matters were discussed in the previous section.

4.2. Competition models

Sharp and Wheeler (1961) proposed a 3D model for bubble rise and merger (see also Sharp, 1984). This model is defined by a simplified set of equations, which when solved, provides a bubble envelope (Glimm and Li, 1988; Gardner et al., 1988). Essentially, competition models postulate that dominant bubbles grow self-similarly by overtaking or assimilating their smaller neighbors; a process usually described statistically (Dimonte et al., 2005).

The term “merger model” was adopted in Glimm and Li (1988), Rikanati et al. (2000) and Cheng et al. (2002). The process discussed here, however, is perhaps better described as “bubble competition” rather than “bubble merger”. It was first observed in the experiments of Lewis (1950) and explained by Layzer (1955, p.11). “Competition between bubbles” was also observed in the experiments of Emmons et al. (1960, p. 189) – this is probably the origin of the term. Several authors, e.g. Zufiria (1988a), prefer the term bubble competition.

In 2D model of Alon et al. (1993, 1994, 1995), the bubble front is treated as an ensemble of bubbles arranged along a line, characterized by their wavelength λ_i . As the bubble rise and merger, the surviving bubbles expand to fill the space vacated by the bubbles swept away from the front. Two adjacent bubbles of wavelengths λ_i and λ_{i+1} merge, at a rate provided by either a potential flow model or a vortex model, to generate a new bubble of wavelength $\lambda_i + \lambda_{i+1}$. Neglecting near-neighbor correlations, the bubble size distribution is obtained by solving a differential–integral equation. Using such mean-field approach, Alon et al. (1995) showed that the bubble size distribution reaches a scale-invariant regime. Shvarts et al. (1995) compared and validated the performance of the merger models with the model of Haan (1989).

Rikanati et al. (1998) constructed a vortex model to account both the single-bubble evolution and two-bubble interaction. The model was an extension of the single-mode vortex models of Jacobs and Sheeley (1996) and Zabusky et al. (1995), and did not rely on the potential flow models where the $A = 1$ limit must be assumed. Instead, a statistical model was used to describe the development of random perturbations based on the mechanism of bubble merger. In addition, the results for the single-mode and two-bubble interaction can be linked to a statistical mechanics merger model (Rikanati et al., 2000) to yield scaling laws for the multimode mixing zone evolution.

Glimm and Sharp (1990) and Zhang (1990) applied a modified Sharp–Wheeler model in two-dimensions, with an additional assumption of superposition (Glimm et al., 1990) between the single bubble and the local front velocities. One of the goals was to provide a theoretical explanation of the constant acceleration and approximate universality of experimentally observed (Read, 1984) and numerically computed (Youngs, 1984; Glimm et al., 1990) mixing rate.

Dimonte et al. (2005) carefully inspected the adjustable parameters employed by the competition models. For instance, the authors noted the different choice made by the models on the Froude number (Fr),

$$v_b = Fr \sqrt{Ag\lambda/(1+A)}, \quad (4.2)$$

which determines the terminal velocity. To agree with the linear electric motor (LEM, see Dimonte et al., 1996a) data, Fr must be set to ~ 1.3 in the model by Glimm and collaborators, but it was set to 0.56 for a periodic potential flow model, along with an increased merger rate in the work by Shvarts and co-workers.

Shvarts et al. (2000), Oron et al. (2001), Cheng et al. (2002) and Kartoon et al. (2003) argued that the discrepancies between the 2D bubble competition model predictions and 3D LEM experimental results (Dimonte, 2000; Dimonte and Schneider, 1996, 1997, 2000; Schneider et al., 1998) are due to dimensionality effects. Cheng, Glimm, and Sharp further argued that effects of bubble radius fluctuations should be incorporated in a 3D bubble merger model. In their model, the reduced description of the bubble front is a statistical ensemble of bubbles of varying heights, with four parameters characterizing the dynamics of this ensemble: (1) the asymptotic velocity of a single bubble; (2) the correlation in height between different bubbles; (3) the mean rate of bubble merger; (4) the variance in the distribution of bubble radii. Cheng, Glimm, and Sharp concluded that their model could predict three experimental measurements with only one phenomenological parameter, the variance of the bubble radii.

Oron et al. (2001) used the mean-field approximation in calculating the average velocity of the bubble ensemble. Their 3D model included three main effects of the dimensionality on the bubble merger model dynamics: (1) the asymptotic single bubble velocity increases in three dimensions by a factor 1.5–2 due to the reduced drag per unit volume in three dimensions; (2) in three dimensions the conserved quantity when two bubbles merge is area rather than length; (3) the average number of neighbors in competition with a single bubble is ≈ 6 in three dimensions, rather than 2 in two dimensions. It is interesting to note that the asymptotic bubble velocities of Oron et al. (2001) and Goncharov (2002) are the same (Chapman and Jacobs, 2006; Mikaelian, 2003). The results of the simulations and the statistical model (Kartoon et al., 2003), together with a simple buoyancy–drag model,³⁸ also agree well with the LEM experimental results.

4.3. Evaluation of nonlinear models with RTI experiments and simulations

The potential flow theory predicted that the perturbation undergoes a nonlinear saturation toward a terminal bubble velocity, Eq. (4.2), for $ka_0 > 1$. For instance, Goncharov (2002) assumes constant late-time velocity with $Fr \approx 0.56$. Using a third-order accurate, finite volume Eulerian 3D solver (Andrews, 1995), Ramaprabhu and Dimonte (2005) found that the scaled velocities of bubbles depend on the density ratio of RT flows, while the Froude numbers defined show no such dependence, in agreement with a model based on potential flow theory (Goncharov, 2002) and buoyancy–drag models (Alon et al., 1995; Oron et al., 2001).

The potential flow models, which assume a single-valued interface, work well up to the point where Kelvin–Helmholtz roll-up occurs. The bubble then reaccelerates and gives $Fr \sim 1$ which is the value estimated for multi-mode RT simulations and experiments. Indeed, for multi-mode RTI, Dimonte et al. (2004) documented that when the actual bubble densities are used, the “ α -group” numerical simulations give $Fr \sim 0.94 \pm 0.06$ which agrees with the previous experiments: Lewis (1950) obtained $Fr \sim 1.1$, Glimm and Li (1988) found $Fr \sim 1.1$ for the rocket rig experiments (Read, 1984) and the LEM experiments (Dimonte et al., 1996a; Dimonte and Schneider, 2000) reported $Fr \sim 0.89 \pm 0.08$, all assuming no entrainment. Scorer (1957) deduced $Fr \sim 1.2$, but with a significant amount of entrainment in rising plumes. In a follow-up numerical work, Ramaprabhu and Dimonte (2005) reported Fr as a function of initial conditions and determined an effective Froude number of 1.07 ± 0.12 .

Fig. 4.1a, adopted from Ramaprabhu et al. (2006), shows the three-dimensional ILES³⁹ Fr numbers obtained for 3D single mode, $\cos(kx) + \cos(ky)$ perturbation. Specifically, Ramaprabhu et al. (2006) plotted late time interfacial velocity measurements (formulated as dimensionless Froude numbers) against the appropriate values of h_b/D_b where h_b is the bubble perturbation amplitude. Per simulations and experiments, the dominant bubbles grow self-similarly with their diameter $D_b \sim \lambda \propto h_b$ (Dimonte, 2004). As demonstrated by these authors, the behavior of the bubble Froude number depends on the values of h_b/D_b . For $h_b/D_b \leq 1$, the numerical simulations indeed obtain a terminal velocity with $Fr \sim 0.56$ for all A . For $h_b/D_b > 1$ and $A \sim 1$, Fr remains near 0.56 for all amplitudes. Both observations are consistent with the potential flow theory. For $h_b/D_b > 1$ and $A < 1$, however, Fr approaching near unity and bubbles accelerate away from a terminal velocity. As noted in Section 2.3, the 2D single-mode results of Wei and Livescu (2012) for the Fr number behavior (Fig. 4.1b, Fig. 11 of Wei and Livescu (2012)) are similar to those obtained from 3D numerical simulations.

In their RTI experiments, Wilkinson and Jacobs (2007) illustrated that the Fr number increases until it reaches an approximately plateau value before increasing again at the latest times (Fig. 4.2). Again, this behavior differs from the result of the Goncharov model, which assume constant late-time velocity with $Fr \approx 0.56$. The models of Sohn (2003) and Abarzhi et al. (2003) appear to have worse agreement with the data. The 3D single-mode simulations of Ramaprabhu et al. (2012), using RTI-3D (Andrews, 1995) and PPM (Woodward et al., 2010) codes and the initial $\cos(kx) + \cos(ky)$ perturbation,

³⁸ See Part II for a detailed discussion for buoyancy–drag models.

³⁹ Ramaprabhu et al. (2006) described the ILES codes used: RTI-3D (Andrews, 1995) is a multiphase, incompressible, Eulerian solver and uses Van Leer flux limiters to prevent nonphysical oscillations. FLASH (Fryxell et al., 2000; Calder et al., 2002) and PROMETHEUS (Fryxell et al., 1989) solve the compressible Euler equations using the piecewise parabolic method on a 3D Cartesian grid. FLASH is a parallel code and has the added feature of adaptive mesh refinement, handled by the PARAMESH (MacNeice et al., 2000) library of routines. NAV/STK is a finite-volume solver for the full Navier–Stokes equations with a physical viscosity, in addition to the capability to handle surface tension effects.

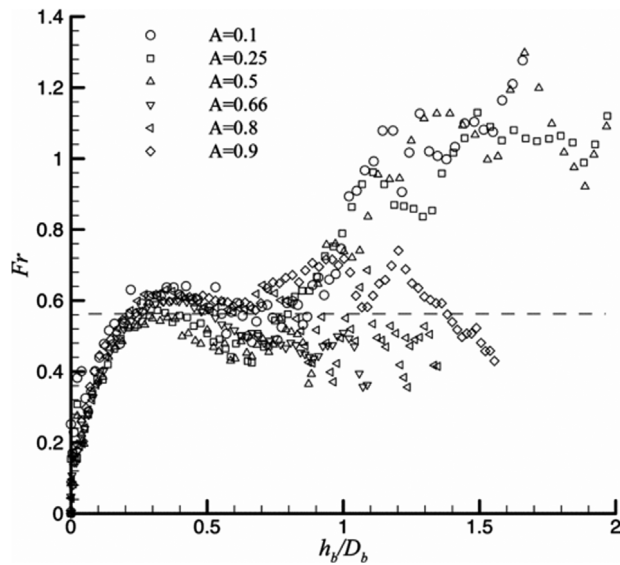


Fig. 4.1a. Froude number vs h_b/D_b from 3D single mode numerical simulations using the FLASH code at different Atwood numbers. Per experiments and simulations, the dominant bubbles grow self-similarly with their diameter $D_b \sim \lambda \sim h_b$. The dashed line represents the 3D prediction of the potential flow model of Goncharov (2002).

Source: Adopted from Fig. 6, (Ramaprabhu et al., 2006), *Physical Review E*, with permission.

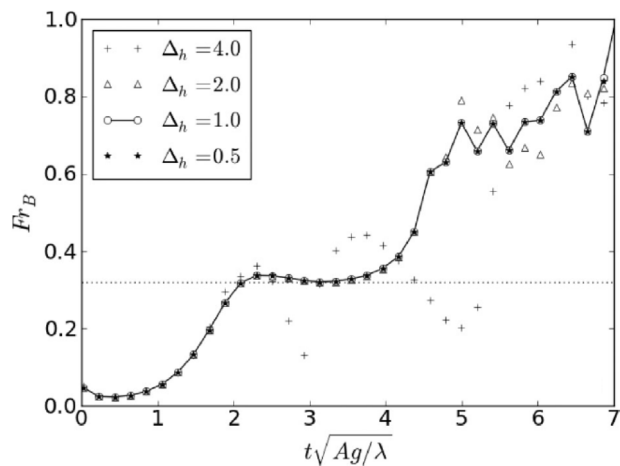


Fig. 4.1b. Froude number vs normalized time from 2D single mode direct numerical simulations. The dashed line represents the 2D prediction of the potential flow model of Goncharov (2002).

Source: Fig. 11 of Wei and Livescu, *Phys. Rev. E* (2012), with permission.

showed excellent agreement with experimental data during the linear, nonlinear, and reacceleration phases.⁴⁰ We note that both Ramaprabhu et al. (2012) and Wei and Livescu (2012) stated that there is no such thing as a terminal velocity, even for the single-mode RTI.

Of course, the other issue is the spike Froude number, and here more research efforts would be desirable. White et al. (2010) observed the free fall at $A = 1$ in their experiments using magnetorheological fluids. The study of Ramaprabhu et al. (2012) showed that, at late times, spikes in RTI may experience reacceleration, and that spikes evolve toward chaotic shapes which contain many small structures. It is not practical to approximate such a complicated interface by a prominent mode. The study also showed that these small structures are suppressed in coarse-grid simulations and in simulations with sufficient amount of viscosity. Before reaching the possible reacceleration stage, Zhang and Guo (2016) showed that the spike evolves toward a constant growth rate for systems with $A < 1$ (see also, Section 3.1). It seems that the theory presented in

⁴⁰ Betti and Sanz (2006) had a model to account for the effect of the secondary vorticity on the Fr number. In their case, the vorticity came from ablation, but Ramaprabhu et al. (2012) adopted their model to describe the vorticity in the case from KH instability. It worked reasonably well.

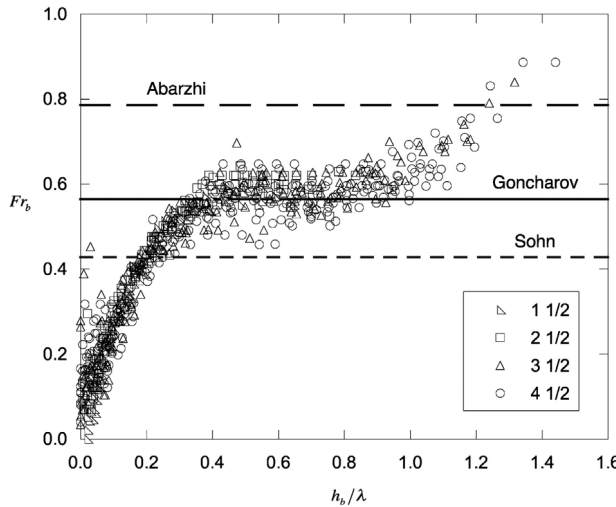


Fig. 4.2. Plot of measured bubble Froude number vs dimensionless bubble amplitude.
Source: From Fig. 15, Wilkinson and Jacobs, *Phys. Fluids*, with the permission of AIP Publishing.

Zhang and Guo gives a good approximation for the behavior of spikes and bubbles before the possible reacceleration stage. However, when the reacceleration occurs, due to the complexity of the interface shape and the effect of vorticity, further mathematical treatment or modeling is needed to handle the complicated interface in this late stage.

4.4. Evaluation of nonlinear models with RMI experiments and simulations

4.4.1. The drop tower

Fig. 4.3, adopted from the 2D RM experiments of Niederhaus and Jacobs (2003), compares the late-time amplitude measurements with a curve generated from vortex model of Jacobs and Sheeley (1996) assuming the vorticity concentrates immediately after impact and at a later time based on experimental observation. Since the vorticity in the experiments does not concentrate until much later, this curve underestimates the amplitude, thus, should be considered a lower bound on the amplitude. Nevertheless, the curves appear to have the same general shape as the experimental data, and differs from the measurements by less than 10% and 5% at late times. Niederhaus and Jacobs (2003) attributed the difference to the fact that the vortex model is strictly valid only for Atwood number of 0. Fig. 4.3 also illustrates that the Sadot et al. model agrees with experimental data reasonably well.

As shown in Fig. 4.4 (reproduced from Chapman and Jacobs, 2006, Fig. 14), the 2D measurements appear to follow the 2D model expressions reasonably well as the data appear to asymptotically approach a line with slope of one at late time. It is also readily apparent that the measured 3D velocities do not show the $1/t$ dependence indicated by the models. Note that Sohn's model gives an identical result for both the bubble and the spike.

Fig. 4.5 shows the asymptotic behavior of the individual bubble and spike velocities. The model of Abarzhi, Nishihara, and Glimm shows considerably worse agreement owing to its singular behavior as $A \rightarrow 0$, and the model of Sohn (2003) shows poorer agreement primarily for the reason given above. The results of Goncharov show the best agreement.

4.4.2. Shock tube experiments with membrane

The single mode RM experiments by Jourdan and Houas (2005) provided helpful information regarding the Atwood number dependence as well as the correction required for the perturbation models for the flows already in the nonlinear regime. Two light/heavy interfaces have been experimentally studied for a low incident shock wave Mach number ($Mach = 1.15$). The Atwood numbers for the air/SF₆ and air/CO₂ are 0.6 and 0.19, respectively. Also, a relatively high initial amplitude (21 mm) was employed to rapidly reach the nonlinear regime.

For the light/heavy gas combinations (air/SF₆ and air/CO₂), Jourdan and Houas (2005) highlighted the reduction of the initial growth rate compared to that predicted by the small-amplitude theory. Coupled with the corresponding Rikanati et al. (2003) reduction factor, the non-linear model of Sadot et al. (1998) shows excellent agreement with the early and late time growth rate measurements (Fig. 4.6).

Jourdan and Houas (2005) also compared the experiments and existing models for the heavy/light gas combinations. The heavy/light air/He experimental data, with a strong negative Atwood number of -0.77 , can be well represented by the Vandenboomgaerde and Lafitte model (2004), initialized with a reduction factor smaller than that used in the light/heavy configurations. The Air/N₂ interface experiment has a relatively short duration and with the Atwood number is close to zero (-0.05). The reversal phase can be described by the classical linear theory of Richtmyer (1960).

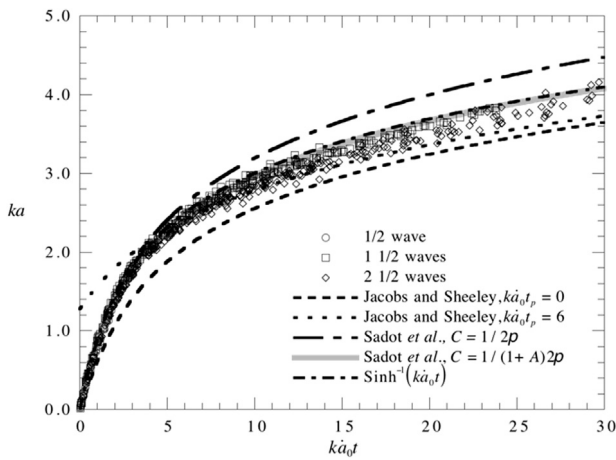


Fig. 4.3. A plot of late-time non-dimensional amplitude versus time along with curves from several nonlinear models.
Source: Fig. 12 of Niederhaus and Jacobs, *J. Fluid Mech.*, 2003 with permission.

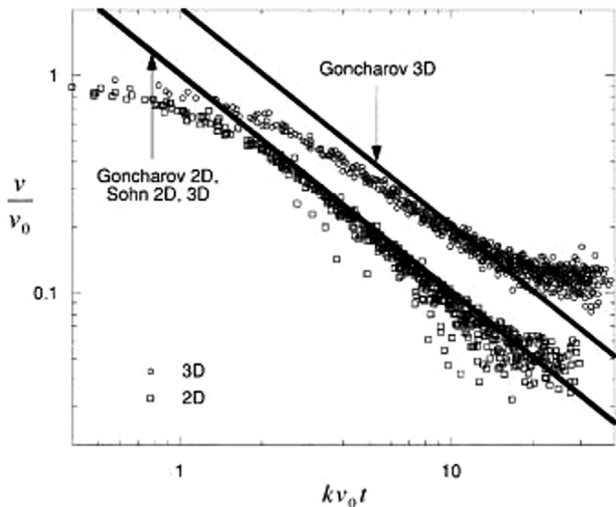


Fig. 4.4. A log-log plot of overall velocity versus time for both 2D and 3D experiments along with lines corresponding to the models of Goncharov (2002) and Sohn (2003).
Source: Fig. 14, (Chapman and Jacobs, 2006), *Phys. Fluids*, with the permission of AIP Publishing.

4.4.3. Shock tube experiments with stereolithographed interfaces

In Section 2.3.4, the shock tube experiments with stereolithographed interfaces performed by Mariani et al. (2008) has been described. As shown in Fig. 4.7, comparisons with the nonlinear theory of Zhang and Sohn (1997a) and with the models of Sadot et al. (1998) and Vandenboomgaerde and Lafitte (2004) showed that the experimental results were always lower than the theoretical predictions. The authors attributed this reduction, in the light-heavy configuration, to membrane effects on the interface dynamics.⁴¹

Vandenboomgaerde et al. (2014) compared the results of their experiments with stereolithographed interfaces with the results from analytical models for two cases (Figs. 4.8 and 4.9). Briefly, both cases have the same Mach number for the incident shock wave (1.45) and Atwood number (0.679), but a different initial amplitude ($ka_0 = 0.17$ and 0.52, respectively).

For a high initial amplitude (case 2), the Sadot et al. (1998) model strongly over-estimates the experimental results. Vandenboomgaerde et al. (2014) noted that this discrepancy is due to an initial growth rate that is too high followed by a saturation that is too low. The Dimonte and Ramaprabhu (2010) and Mikaelian (1998) models are in a relative agreement

⁴¹ Mikaelian (2016) recently urged experimentalists to reassess the utility of using thin membranes to separate the heavy and light fluids. He stressed that a highly complex procedure is required to generate a membraneless interface, it is usually not sharp but diffuse, and of course one can impose only limited shapes on membraneless interfaces.

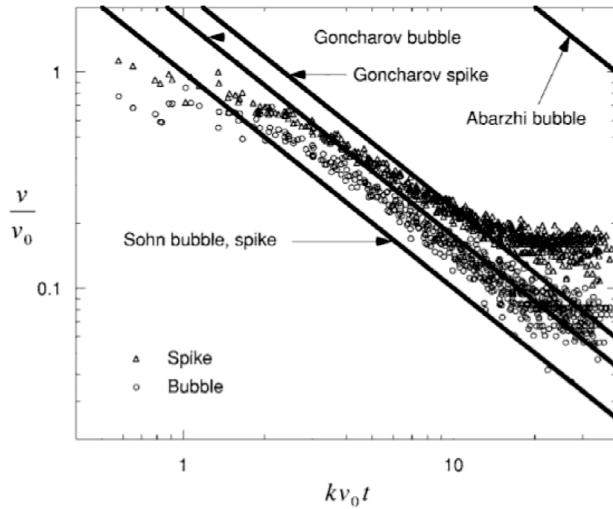


Fig. 4.5. A log–log plot of bubble and spike velocity versus time for the 3D experiments along with lines corresponding to the models of Goncharov (2002), Sohn (2003), and Abarzhi et al. (2003).

Source: Fig. 15, Chapman and Jacobs, *Phys. Fluids*, 2006, with the permission of AIP Publishing.

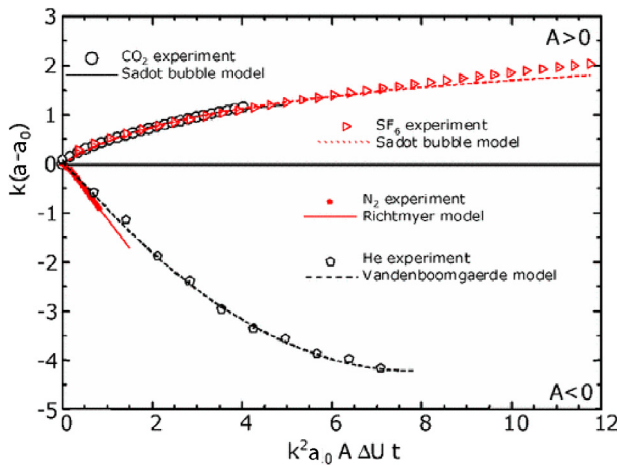


Fig. 4.6. Dimensionless bubble amplitude as a function of dimensionless time considering the positive (air/SF₆, air/CO₂) and negative (air/N₂, air/He) Atwood number cases. While the experiments have a reflected shock from the shock tube end wall, the measurements are shown before the reshock.

Source: Fig. 3 of Jourdan and Houas (2005) with permission from *Phys. Rev. Lett.*

with the experimental data. They border the experimental data, with the Dimonte and Ramaprabhu model as an upper limit and the Mikaelian model as a lower one (Fig. 4.8). These models correctly predict the experimental results at the beginning of the growth because they take into account the effect of the high initial amplitude. This study underlines the necessity for the models to consider the effect of a high initial amplitude.

Fig. 4.9 shows the results of Vandenboomgaerde et al. (2014) experiments of case 1 ($ka_0 = 0.17$) and the predictions from several analytical models.⁴² While the Mikaelian model (1998) slightly underestimates the experimental growth, the Sadot et al. (1998) and Zhang–Sohn (single-point Padé) models slightly over-estimates the experimental results. The Dimonte and Ramaprabhu (2010) and Zhang–Deng–Guo models are in a good agreement with the experimental data.

⁴² To generate Fig. 4.9, we use the same initial conditions as those in Table I from Vandenboomgaerde et al. (2014). Namely, the shock Mach number 1.45, the wavelength $\lambda = 8$ cm, $a_0^- = 0.306$ cm, $ka_0^+ = 0.17$, the asymptotic value of the linear growth rate $\frac{da}{dt}|_\infty = 17.17$ m s⁻¹, and the pre-shock Atwood number $A^- = 0.679$. We also use the adiabatic exponents of air and SF₆ ($\gamma_{\text{air}} = 1.4$, $\gamma_{\text{SF}_6} = 1.0935$). The post-shock Atwood number ($A^+ = 0.734$) is obtained by solving one-dimensional Riemann problem. The Zhang and Sohn model (1997a) and the Zhang et al. model (2016) use the results of the compressible linear theory (Yang et al., 1994), instead of those of the impulsive model, to provide the predictions shown in Fig. 4.9 (as well as Figs. 4.11 and 4.12).

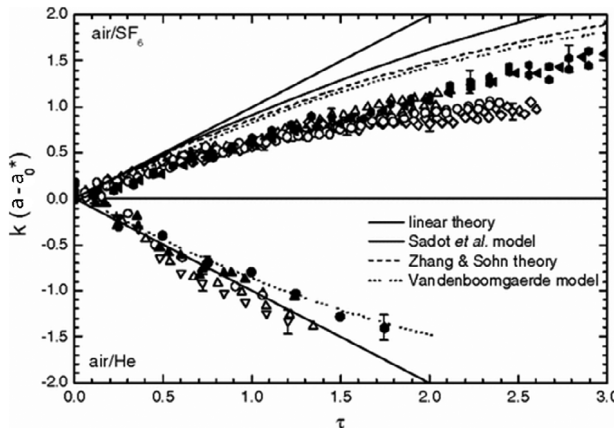


Fig. 4.7. Nondimensionalized time evolutions of the amplitude for light-heavy (up) and heavy-light (down) sinusoidal interfaces. Black and white symbols stand for experimental results at high and low Mach numbers, respectively.

Source: Fig. 2 of Mariani et al. (2008), *Physical Review Letters*, with permission.

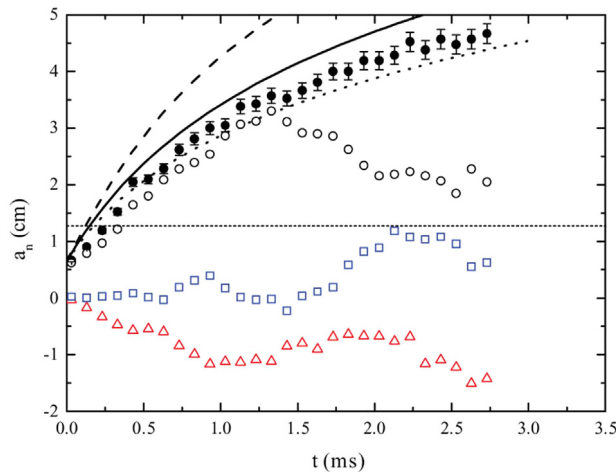


Fig. 4.8. Experimental temporal evolution of the half peak-to-valley amplitude, $a(t)$, and the first three Fourier coefficients, a_i : (○) a_1 , (△) a_2 , (□) a_3 . Case 2 with a high initial amplitude ($ka_0 = 0.52$) The dashed, solid, and dotted curves represent the growths obtained with the Sadot et al. (1998), Dimonte and Ramaprabhu (2010) and Mikaelian (1998) models respectively. The dotted horizontal line represents $ak = 1$.

Source: Fig. 6b of Vandenboomgaerde et al., *Phys. Fluids*, 2014, with the permission of AIP Publishing.

4.4.4. Shock Tube without membrane

Collins and Jacobs (2002) obtained PLIF images of the developing instability from the initial sinusoidal perturbation stage, through the nonlinear growth regime, and into turbulence. Early-time measurements of the growth rate are in good agreement with Richtmyer's (1960) when combined with Brouillette and Sturtevant's (1994) diffuse-interface correction. Late-time amplitude measurements are also in very good agreement with the nonlinear models of Zhang and Sohn (1997a) and Sadot et al. (1998). Latini et al. (2007a) compared the predictions of many analytical, semianalytical, and phenomenological linear and nonlinear, impulsive, perturbation, and potential flow models with fifth- and ninth-order WENO simulations of the Collins and Jacobs experiment, and with the experimental data. The simulation amplitudes were shown to be in very good agreement with the experimental data and with the predictions of linear growth models for small times, and with those of nonlinear models at later times up to the time at which the driver-based expansion in the experiment expands the layer before reshock. Using a local and global quantitative metric, the Zhang and Sohn (1997a) nonlinear Padé model was found to be in best overall agreement with the simulation amplitudes before reshock.

Fig. 4.10 illustrates the dimensionless bubble and spike amplitude measurements of Jacobs and Krivets (2005) 2D RM shock tube experiments. The Mikaelian (2003) model focused on explicit analytic expressions for the evolution of the bubble amplitudes in RT and RM instabilities. The agreement between the model and data for the bubble amplitude is reasonable. It is not surprising that the agreement for the spike amplitude is less satisfactory. The model by Sadot et al. (1998) appears to follow the data well for both bubble and spike amplitudes.

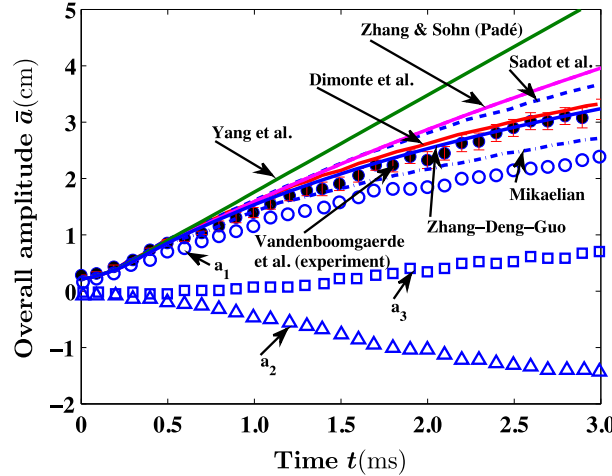


Fig. 4.9. Experimental temporal evolution of the halfpeak-to-valley amplitude, $a(t)$, and the first three Fourier coefficients, a_i : (○) a_1 , (△) a_2 , (□) a_3 . Theoretical predictions of the [Sadot et al. \(1998\)](#), [Dimonte and Ramaprabhu \(2010\)](#), [Mikaelian \(1998\)](#), [Yang et al. \(1994\)](#), [Zhang and Sohn \(1997a\)](#), and [Zhang et al. \(2016\)](#) models are labeled respectively.

Source: The values of the experimental data of Case 2, $kq_0^+ = 0.17$, are obtained from Fig. 6a of Vandenboomgaerde et al., *Phys. Fluids*, 2014, with the permission of AIP Publishing.

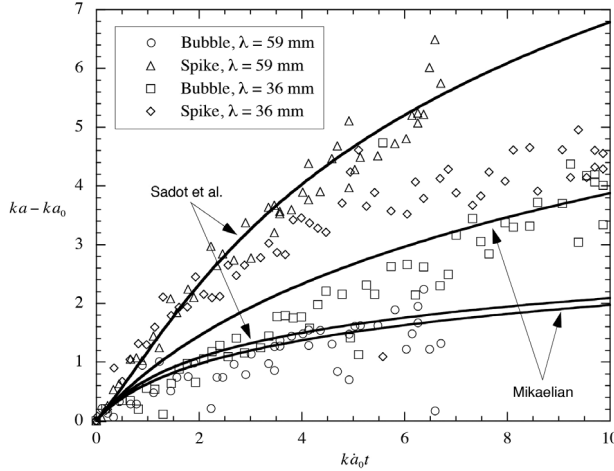


Fig. 4.10. Comparison of the models of [Sadot et al.](#) and [Mikaelian](#) with dimensionless bubble and spike amplitude measurements.
Source: Fig. 8 of Jacobs and Krivets, *Phys. Fluids*, 2005, with the permission of AIP Publishing.

Fig. 4.11a and b provide a quite comprehensive evaluation of the theoretical models in the literature against the 2D single-mode measurements of [Jacobs and Krivets \(2005\)](#). The original figure (Fig. 7 of Jacobs and Krivets) is produced by the averages of parameters from two sets of experiments with different post-shock Atwood numbers and wavelengths. All the theoretical models have also taken the average values as parameters in that figure. However, all these models are not linear functions of these parameters. To get a more precise comparison between theoretical models and experimental data, it is better to compare the models with each set of the data.⁴³

⁴³ To generate **Fig. 4.11a, b**, we use the same pre-shock initial conditions as those in Table I from [Jacobs and Krivets \(2005\)](#). Namely, for **Fig. 4.11a** with $\lambda = 36$ mm, we use $a_0^- = 1.47$ mm, $A^- = 0.656$, the shock Mach number = 1.274, the mean interface velocity $\Delta V = 90.1$ m/s; for **Fig. 4.11b** with $\lambda = 59$ mm, we use $a_0^- = 2.90$ mm, $A^- = 0.605$, Mach number = 1.292, $\Delta V = 92.6$ m/s. We also use the adiabatic exponents of air and SF₆ (in **Fig. 4.11a**, $\gamma_{\text{air}} = 1.38$, $\gamma_{\text{SF}_6} = 1.1$; in **Fig. 4.11b**, $\gamma_{\text{air}} = 1.276$, $\gamma_{\text{SF}_6} = 1.09$). The post-shock conditions are computed by solving one-dimensional Riemann problem. (For **Fig. 4.11a** with $\lambda = 36$ mm, we obtain $a_0^+ = 1.15$ mm, $A^+ = 0.692$; for **Fig. 4.11b** with $\lambda = 59$ mm, we obtain $a_0^+ = 2.19$ mm, $A^+ = 0.635$.) In both **Fig. 4.11a,b**, the curves from theoretical models are all scaled by the dimensionless time $v_0 kt$, where $v_0 = A^+ k a_0^- \Delta V$ is the initial growth rate obtained from the impulsive model (note that the experimental data in Fig. 7 of Jacobs and Krivets are scaled in terms of $k a_0 t$, where a_0 is the measured initial growth rate from the experiments).

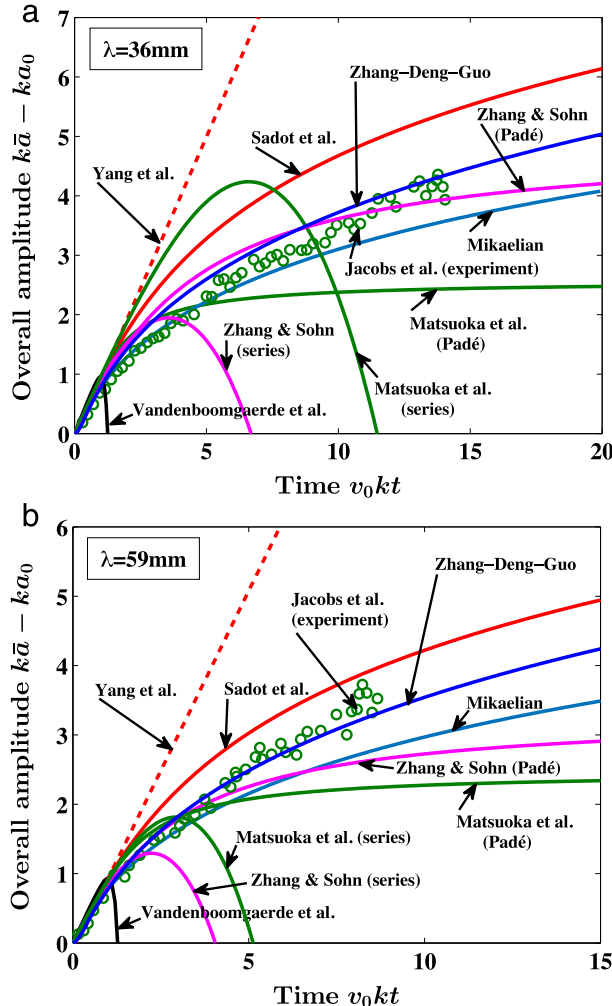


Fig. 4.11. Comparison of the dimensionless amplitude measurements with several nonlinear solutions and models. The experimental data from Jacobs and Krivets (2005) are represented by o. (Fig. 7, Jacobs and Krivets, *Phys. Fluids*, 2005, with the permission of AIP Publishing.) The curve labeled as Yang et al. is the prediction from the linear compressible theory (Yang et al., 1994). The curve labeled as Zhang–Deng–Guo is the prediction from the Zhang et al. model (2016). (a) The pre-shock initial conditions are $\lambda = 36$ mm, $a_0^- = 1.47$ mm, $A^- = 0.656$, Mach number = 1.274, and $\Delta V = 90.1$ m/s. (b) The pre-shock initial conditions are $\lambda = 59$ mm, $a_0^- = 2.90$ mm, $A^- = 0.606$, Mach number = 1.292, and $\Delta V = 92.6$ m/s.

As expected, Figs. 4.11a and b show that the weakly nonlinear perturbation series solution of Zhang and Sohn (1997a), Vandenboomgaerde et al. (2002) and Matsuoka et al. (2003) quickly diverge from the data early in the nonlinear evolution. Of course, the amplitude of unstable finger is a monotonic increasing function of time. When a theory gives a prediction that amplitude decreases with time after some time t^* , the theory is already invalid that at that t^* . (It does not mean that the theory is valid for $t < t^*$).⁴⁴ The expansion cannot be used to determine the behavior for large t . Therefore, expansion more terms is of limited utility.

For sufficient smaller time, the series should converge when t is smaller than its radius of convergence. Therefore, adding more terms will improve the accuracy of the model. Indeed, the mean value theorem guarantees that for the small t , more terms gives more accurate value. However, since the radius of convergence is small, the contribution from these high order terms will not be significant. Indeed, Fig. 4.11a, b show that all models give almost the same predictions for small t . In other words, in mathematical terms, more terms are better for small time; in reality, the improvement is negligible even for small t and the high order terms cause very big errors when t is outside its radius of convergence.

The Padé approximation of Zhang and Sohn (1997a) and Matsuoka et al. (2003) resulted in improved agreement with data at late times. However, single-point Padé approximation will not be able to predict the asymptotic behavior correctly since it contains no information about the asymptotic large time. These approximations give a late-time dependence of $da/dt \propto$

⁴⁴ The value of t^* can be determined very precisely for these expansions.

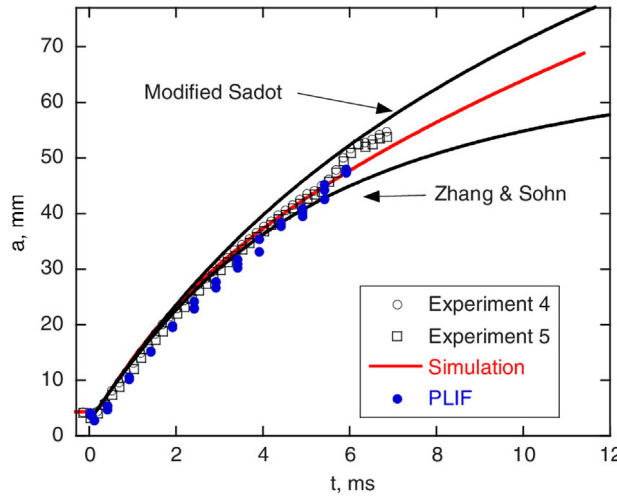


Fig. 4.12. Experimental and numerical amplitude measurements compared with the 3D Sadot model and the Zhang–Sohn model.
Source: Fig. 10 of Long et al., *Phys. Fluids*, 2009 with the permission of AIP Publishing.

$1/t^2$, instead of the correct asymptotic behavior $da/dt \propto 1/t$. The empirical models of Mikaelian (2003) and Sadot et al. (1998) offer reasonable performance, as they were constructed to provide good agreement with data at both early and late-time.

Long et al. (2009) carried out shock tube experiments of the single-mode, 3D RM instability. A three-dimensional numerical simulation of this experiment was also performed using a multidimensional Eulerian adaptive mesh refinement code (Fig. 4.12). As anticipated, the Zhang and Sohn (1997a, 1999) model agreed with the data up to intermediate times $t \approx 5$ ms. A modified Sadot et al. model, which was extended to 3D by Chapman and Jacobs (2006), provided reasonably good late-time behavior.

If one wants to develop a theoretical model valid from small to asymptotically large times without empirical fitting, it is critical to determine theoretically the asymptotically large-time solutions for fingers. That is why it makes sense to determine the large time solution for all A first (Zhang and Guo, 2016), then apply two-point Padé approximation (Zhang et al., 2016, 2017). The Zhang–Deng–Guo model developed in such fashion agrees with the data extremely well. Figs. 4.9 and 4.11a, b show that the Zhang–Deng–Guo model gives the best predictions for the finger growth of RM instability over all time period. The model also has desirable features: it is not based on empirical construction; it contains no fitting parameters; it is for all Atwood numbers and for compressible fluids.

Recently, Luo et al. (2016a) investigated experimentally the RMI of a 3D single-mode interface with a minimum-surface feature. The SF₆–air interface produced by the soap film technique was subjected to a $Mach = 1.28$ planar shock. As shown in Fig. 4.13, the instability at the symmetry plane grows much slower than the prediction of 2D linear models, but matches the extended 3D linear and nonlinear models (Mikaelian, 2003; Luo et al., 2013).

5. Stabilizing mechanisms

In this section, we will discuss how the addition of the viscosity, surface tension, and diffuse interface would change the stability characteristics. The effect of material strength and ablation front stabilization will be discussed in the high-energy-density-physics section of Part II of this review.

5.1. Viscosity

Harrison (1908) was the first to consider the linear RTI of viscous fluids. As shown by Chandrasekhar (1955, 1961), to find the exponential growth rate in incompressible fluids, a fourth order differential equation must be solved with viscosity incorporated. Nonetheless, it is possible to determine a lower and an upper bound to the growth rate (Menikoff et al., 1977). Celani et al. (2009) numerically investigated the goodness of those upper and lower bounds by means of the phase-field model (e.g., Tian and Russell, 2014).

The exact result for the influence of the viscosity is complex. Bellman and Pennington (1954) developed a linear theory and found that viscosity (μ_i) decreases the rate of growth at low wavenumber and causes damping of oscillatory solutions at high wavenumbers. A useful approximation is the upper bound given by the authors,

$$\gamma = \sqrt{kgA + \tilde{\nu}^2 k^4} - \tilde{\nu} k^2 \text{ with } \tilde{\nu} = \frac{\mu_1 + \mu_2}{\rho_1 + \rho_2}. \quad (5.1a)$$

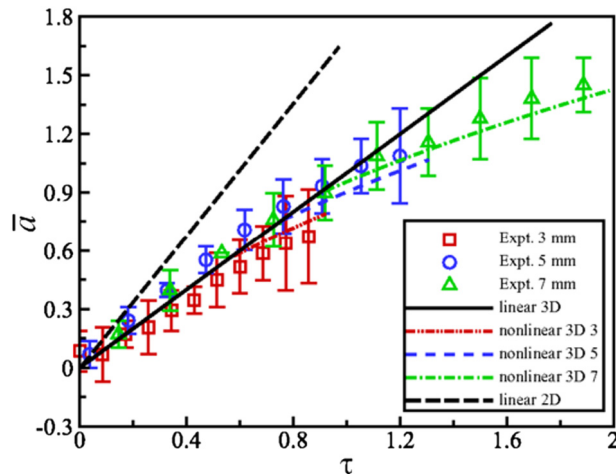


Fig. 4.13. Comparison of the dimensionless growth of the overall amplitude in the symmetry plane extracted from the experiment (symbols) with the theoretical linear and nonlinear models (lines).

Source: Fig. 9 of Luo et al., *Physical Review E*, 2016a, with permission from APS.

Plessset and Whipple (1974) have argued that this gives a reasonably good approximation. The formula implies that γ has a maximum value when the wavelength is λ_{max} where

$$\lambda_{max} = 4\pi \left(\frac{\tilde{v}^2}{Ag} \right)^{1/3}. \quad (5.1b)$$

Plessset and Whipple (1974) also noted that the effect of viscosity is to give some damping to the oscillations, and the damping may easily be estimated for some particular cases. Hunt (1961) computed the exponential rate of growth of perturbations for various density ratios in the limit as the viscosity of one fluid tends to zero, and compared his result with the solution of Chandrasekhar for equal kinematic viscosities. Menikoff et al. (1978) obtained solutions to the linearized equations of motion, which satisfy general initial conditions and without restriction on the density or viscosity of either fluid. Bhatia (1974) applied the variational approach of Vandervoort (1961) and concluded that the viscosity has a stabilizing influence.

Mikaelian (1993) considered the effect of viscosity on RTI and RMI by deriving a moment equation for fluids with arbitrary density. This model is consistent with the pure viscosity limit of Qiu et al. (2008) who present a linear analysis of the RM instability under the effects of magnetic field and viscosity with a single-mode sinusoidal perturbation in amplitude. The functional form of the Mikaelian (1993) formulation is given by

$$\dot{a} = ka_0 A \Delta V e^{-2k^2 v_{avg} t} \quad (5.2)$$

where the kinematic viscosity, v_{avg} , is obtained by a density-weighted average.

Carlès and Popinet (2001, 2002) performed an asymptotic analysis of the Navier-Stokes equations using singular perturbation techniques and obtained a quantitative prediction of the effect of viscosity on the weakly nonlinear impulsive RMI between two fluids of arbitrary density. Using the results of direct numerical simulations as a benchmark, they further argued that their model is superior to that of the Mikaelian model (see Fig. 5.1). To the leading order, the Carlès and Popinet (2001, 2002) model is given by

$$\dot{a} = ka_0 A \Delta V \left[1 - \frac{4}{3\sqrt{\pi}} k \sqrt{v_{CP} t} \right] \quad (5.3a)$$

where the density weighted kinematic viscosity is given by

$$v_{CP} = \frac{16 (\rho_1 \mu_1) (\rho_2 \mu_2)}{[(\rho_1 + \rho_2) (\sqrt{\rho_1 \mu_1} + \sqrt{\rho_2 \mu_2})]^2}. \quad (5.3b)$$

Robey (2004) noted a distinctive feature of these two models regarding the RMI growth rate; The Mikaelian model asymptotes to a zero growth rate as the wavenumber approaches infinity, whereas the Carlès and Popinet method shows a finite wavenumber cutoff due to viscosity. Nevertheless, he concluded that both methods give similar magnitudes for the growth rate reduction. Walchli and Thornber (2017) revisited this issue and found that the discrepancies between these two theories are by no means insignificant, but they do not differ by several orders of magnitude, as claimed by Carlès and Popinet (2001).

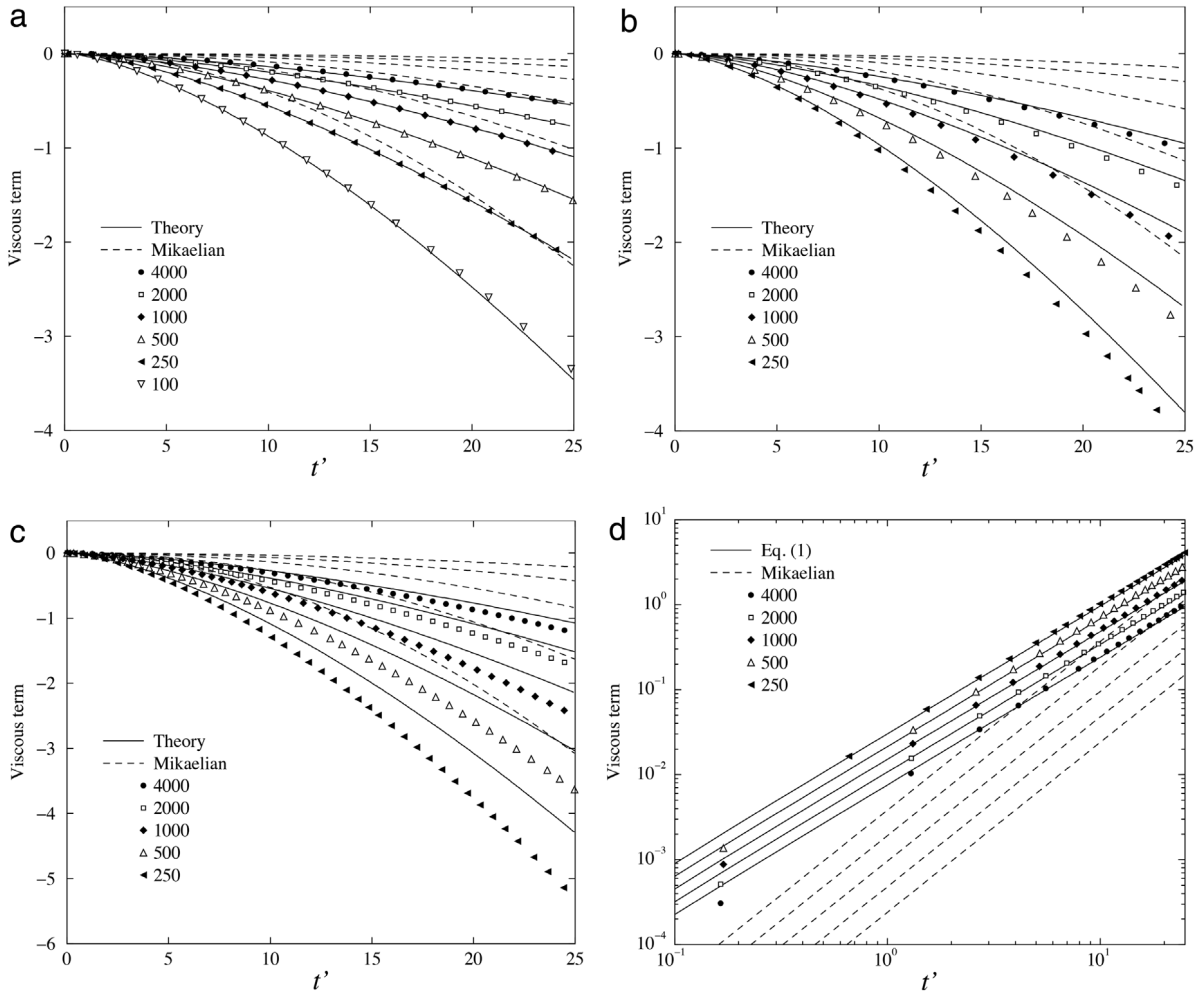


Fig. 5.1. Viscous correction to the linear growth based on the authors' and Mikaelian's models, and numerical simulations for several Reynolds numbers (from 100 to 4000, calculated for the heavier fluid) and several density ratios [(a) $\rho_1/\rho_2 = 2$, (b) $\rho_1/\rho_2 = 4$, (c) $\rho_1/\rho_2 = 8$]. (d) Same conditions as in (b) in log-log plot.

Source: Fig. 3 of Carlès and Popinet (2002), European J. of Mechanics B/Fluids with permission.

Ho (1980) considered the linear RTI stability of viscous fluids with mass and heat transfer and found that the effects of the viscosity and the gravity will depend upon the relative positions of the superposed fluids and the direction of the temperature gradient at the interface.

Extending the inviscid vortex models of Jacobs and Sheeley (1996) and Rikanati et al. (1998), Zhang (2013) derived a viscous single-mode bubble evolution model of RTI. The viscous effect was shown to reduce the growth in the initial small amplitude phase of development. This model was evaluated against the simulation of the miscible fluid Navier-Stokes equations based on a high-order spectral element method. The numerical results give much faster growth of bubble height at early time, and at late stages of development the results appear to be more consistent in terms of the bubble development trends. Using statistical analysis and numerical simulations, Xie et al. (2017a) reported that the growth of the viscous RT mixing zone can be retarded by superimposing an optimized suppression mode on its random initial perturbations.

With a method based on explicit tracking of the interface between the fluids, Tryggvason and Unverdi (1990) and Unverdi and Tryggvason (1992) performed 3D numerical simulations including viscosity. Doludenko and Fortova (2015) analyzed the Rayleigh-Taylor instability in viscous and inviscid compressible media by applying the numerical simulation of the Euler and Navier-Stokes equations. It was found that the viscosity has a weak effect in the energy and inertial ranges and these measurements can be computed on the basis of the Euler equations. Using 2D RTI simulations with a multiple-relaxation-time discrete Boltzmann model, Chen et al. (2016) found that the viscosity showed a significant inhibitory effect on the RT instability, which is mainly achieved by inhibiting the development of the KHI during the reacceleration stage.

The importance of viscosity manifested itself in a 3D numerical simulation reported in Statsenko et al. (2013). Movahed and Johnsen (2013) utilized a solution-adaptive method for efficient compressible multifluid simulations and showed the

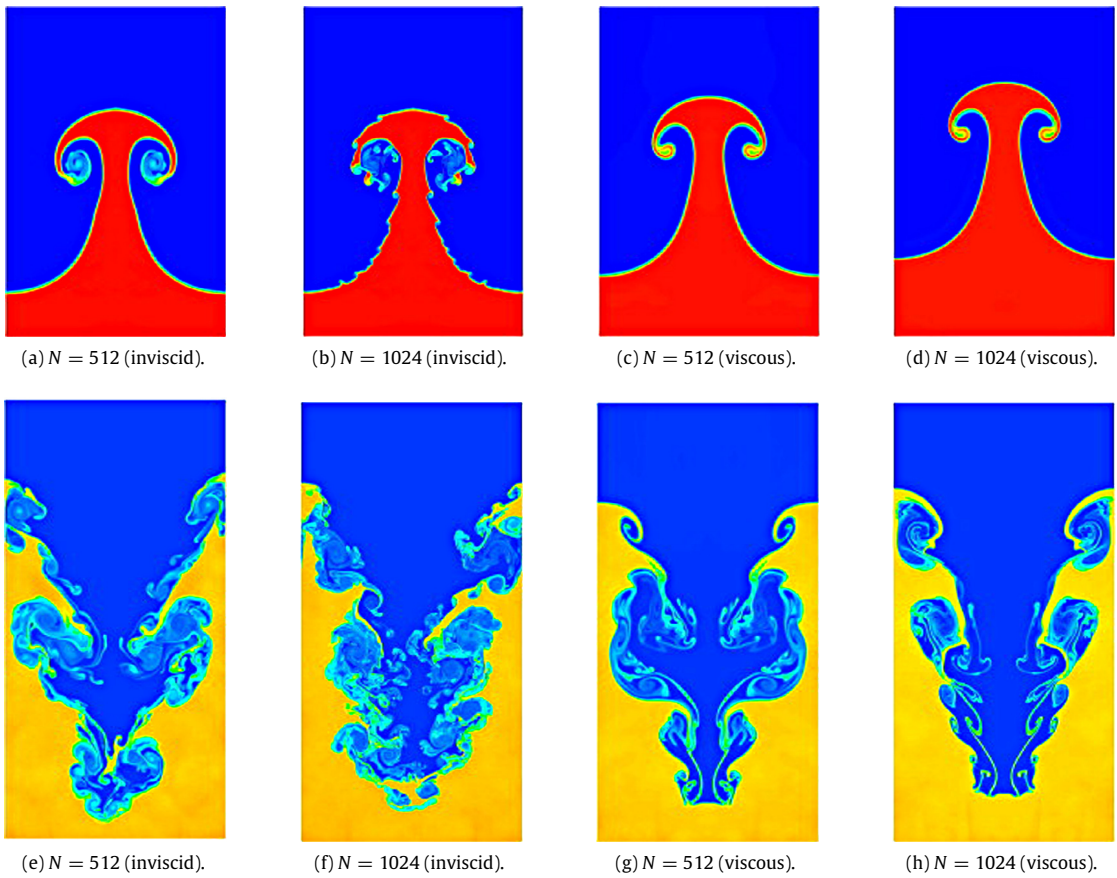


Fig. 5.2. Density contours before reshock at $t = 0.0066$ s (top) and after reshock at $t = 0.0085$ s (bottom) for different resolutions (N : number of cells per wavelength) for the inviscid and viscous Richtmyer–Meshkov simulations.
Source: Fig. 13 of Movahed and Johnsen, *J. Computational Phys.*, 2013.

density fields before reshock and after reshock for a reshocked RMI flow (similar to the experiment of [Collins and Jacobs, 2002](#)). While the shock speed is not affected by viscosity, the contact speed is lower, due to shear as the bubbles and spikes penetrate the other fluid and diffusion of the baroclinic vorticity. Although the spike morphology is almost identical before reshock, the smallest scale structures of the viscous case are much larger than those observed in the inviscid case ([Fig. 5.2](#)).

5.2. Surface tension

At linear and early nonlinear stages, [Bellman and Pennington \(1954\)](#) established that the effect of the surface tension on RT instability; surface tension, σ , produces a cut-off wave number.⁴⁵ Later, [Emmons et al. \(1960\)](#) arrived the same conclusion after carrying out a weakly nonlinear asymptotic analysis of the two dimensional instability. It should be noted that [Nayfeh \(1969\)](#) corrected an error in the analysis of Emmons et al., where they failed to account for the singular nature of the perturbation problem. With numerical calculations, [Daly \(1969\)](#) found that the variation of the linear growth rate with the surface tension coefficient and (for a fixed coefficient) with the wave number of the perturbation is in good agreement with [Chandrasekhar's \(1961\)](#) analytic prediction.

Using the nonlinear analysis elaborated by [Callebaut \(1972\)](#), [El-Ansary et al. \(2002\)](#) studied the effects of surface tension with uniform rotation about a vertical axis for 3-fluid systems having variable densities. [Garnier et al. \(2003\)](#) derived a weakly nonlinear model for studying the RTI in the presence of surface tension. This model addresses the case of an initial multimode perturbation and uses statistical analysis. To capture the nonlinear saturation of the growth of the interface modulation, it is necessary and sufficient to compute the third-order nonlinearity. [Guo et al. \(2017\)](#) considered the weakly nonlinear RMI in incompressible fluids with surface tension and inspected the temporal evolution of a perturbed interface analytically via

⁴⁵ The influence of surface tension on RT corresponds to the effect of surface tension on waves at a stable interface with g reversed.

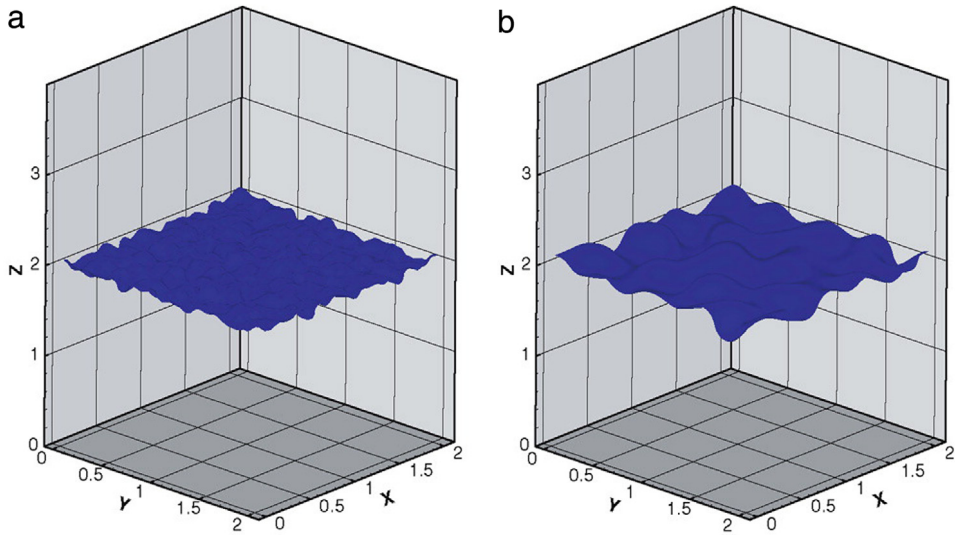


Fig. 5.3. Fluid interface at the onset of nonlinear evolution $t = t_{nl}$ for $A = 0.3$ and (a) $\sigma = 2 \times 10^{-6}$, (b) $\sigma = 1 \times 10^{-3}$.
Source: Fig. 6 of Young and Ham, *J. of Turbulence*, 2006, with permission.

the third-order solution. The authors found that the surface tension has a stabilizing effect that depends on the Atwood number A .

For a single-mode RT instability, Young and Ham (2006) modified the local potential flow analysis in Goncharov (2002) to consider the surface tension effect on the linear stability and the nonlinear terminal bubble velocity. The terminal bubble velocity was reduced by surface tension, and these results from the model were in good agreement with numerical simulations of a viscous, single-mode RT instability. Banerjee and Kanjilal (2015) also found that the magnitude of the suppression of the growth rate of the tip of the bubble highly depends on the surface tension provided surface tension is less than a critical parameter, which depends on the strength of the vorticity and Atwood number. Xia et al. (2013) studied the effect of the surface tension on the RTI with Zufiria and Layzer models and found that both models led to the same asymptotic bubble velocity.

With different values of surface tension and density contrast, Young and Ham (2006) numerically investigated the surface tension effect with random perturbation on the anisotropy. In the RTI mixing flow, the surface tension reduces the flow anisotropy, and redistributes some of the kinetic energy from the longitudinal component to the transverse components. Hence, surface tension tends to reduce the effective mixing rate and homogenizes the Rayleigh–Taylor mixing flow and could influence the energy spectrum or scaling behavior in RT or RM turbulence (Matsuoka, 2009).

Fixing the Atwood number $A = 0.3$, Young and Ham (2006) varied the surface tension to investigate the effect of surface tension on RT mixing. When the surface tension is small, one would expect the flow to be close to the miscible RT mixing with finite density contrast. For $\sigma = 2 \times 10^{-6}$ the linear growth starts after an initial transient, and the nonlinearity becomes “important” at $t_{nl} \sim 2.7$ when the bubble height $h_{nl} \sim 0.10$. As surface tension increases, the random perturbations decay first and undergo a long transient before they start to grow exponentially at a reduced growth rate. For large surface tension, nonlinearity becomes important later in time when the bubble amplitude is large (for $\sigma = 1 \times 10^{-3}$, $t_{nl} \sim 5.0$, $h_{nl} \sim 0.15$) (Fig. 5.3). Fig. 5.4 shows the evolution of the bubble amplitude h_b as a function of time for four different values of σ . The solid lines are from simulation data and the dashed lines are fits to the linear growth.

Young and Ham (2006) also carried out simulations for three Atwood numbers with the surface tension limited to a small value ($\sigma = 4 \times 10^{-6}$). A transition to nonlinear evolution occurs at $h_{nl} \sim 0.04$ for $A = 0.1$, while $h_{nl} \sim 0.1$ for both $A = 0.3$ and $A = 0.6$. The fluid interface at t_{\max} (when the maximum mixing rate is reached) is illustrated in Fig. 5.5 for all three cases.

By using the boundary integral method, Matsuoka (2009) investigated the motion of a planar interface in incompressible RMI and RTI with surface tension. The surface tension term is expressed by the derivative of the curvature of an interface. Therefore, this term contains the highest spatial derivative in the governing equations, and together with the convective term, it governs the interfacial motion at large wave numbers, which in turn causes vortex motion. When the surface tension term is sufficiently large, the surface tension effect may suppress vortex motions such as the rollup of the interface (Matsuoka et al., 2003; Matsuoka and Nishihara, 2006).

For larger surface tension coefficients, Matsuoka (2009) showed that finite amplitude standing wave solutions appear for the RM instability. Such standing wave solutions can also be possible for the RT instability if the condition $Ag < \sigma/2$ is met. However, the motion for the RT instability is more complicated than that for the RM instability, in which there exist both a stable periodic motion and a solution that breaks down for a short time even though σ is large.

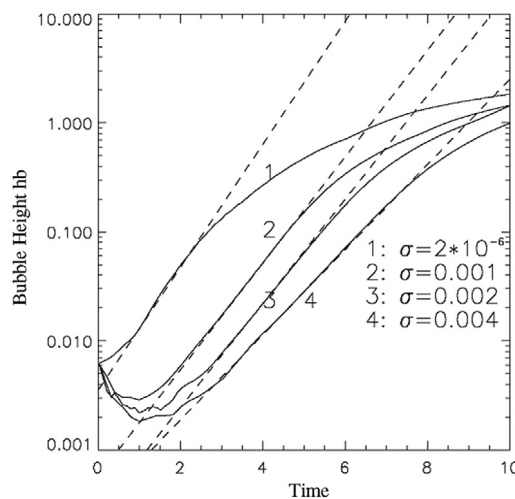


Fig. 5.4. Bubble height versus time for four values of σ on a log-linear plot. $A = 0.3$.
Source: Fig. 5 of Young and Ham, *J. of Turbulence*, 2006, with permission.

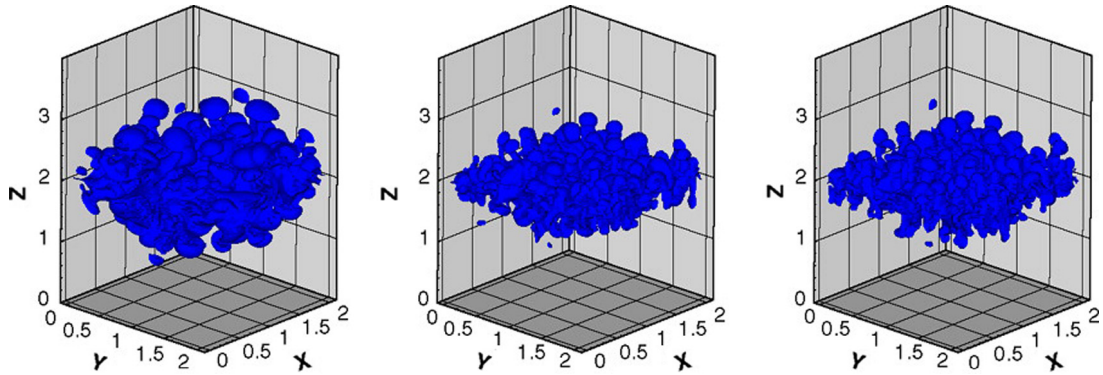


Fig. 5.5. Fluid interface at t_{\max} , when the mixing rate reaches a maximum. $\sigma = 4 \times 10^{-6}$. From left to right, $A = 0.1, 0.3$ and 0.6 .
Source: Fig. 14 of Young and Ham, *J. of Turbulence*, 2006, with permission.

In a phenomenological treatment of 3D RTI flows, Chertkov et al. (2005) found that the surface-tension effects lead to the formation of an emulsion like state, with the typical drop size L decreasing in time. The character of the density fluctuations on the scales larger than L was found insensitive to the immiscible nature of the problem. The energy transfer toward the small scales was carried out by both inertial and wave cascades simultaneously. Turbulence in capillary waves propagating along the drops' surfaces is realized in parallel with the Kolmogorov turbulence inside.

George et al. (2006) reported on a set of 3D RT chaotic mixing simulations based on an improved tracking algorithm in the front tracking code FronTier. It was clear that accurate numerical tracking to control numerical mass diffusion and accurate modeling of physical scale-breaking phenomena surface tension were the critical steps for the simulations to agree with the experiments of Read (1984) and Smeeton and Youngs (1987). More recently, Sohn and Baek (2017) determined that the bubble merger of Rayleigh–Taylor instability follows the same scaling law of the growth of mixing zone even when surface tension exists, but the growth coefficient increases with surface tension.

5.3. Surface tension and viscosity

In a classical work, Reid (1961) incorporated both the effect of surface tension and viscosity into the stability analysis of two superposed fluids. Integrating the general eigenvalue equation (Chandrasekhar, 1961), Mikaelian (1990, 1993, 1996a) also found the growth rate reduction due to viscosity and surface tension. Chhajlani and Vaghela (1989) reached a similar conclusion while investigating the RTI growth rate of superposed incompressible viscous magnetized fluids in a partially ionized medium. Roy et al. (2014) further inspected the combined effect of viscosity, surface tension and compressibility on RT bubble growth between two fluids. For the compressible case, it is seen that the RT bubble growth rate increases due to

compression of the fluids, but introduction of viscosity and surface tension reduces the growth rate. For a moderate value of viscosity and surface tension, the RT bubble growth rate is less than that of the incompressible case. For different density ratios, [Yakovenko \(2014\)](#) performed a numerical study of several real RTI cases corresponding to available experimental data. The surface tension and the viscosity resulted in the suppression of the RTI disturbances and secondary small-scale irregularities of the interface.

The potential flow models could serve as a starting point to investigate the effects of the viscosity and surface tension on the growth of bubbles in RTI and RMI. [Sohn \(2009\)](#) obtained descriptions of the motion of unstable interfaces based on the velocity potentials in [Goncharov \(2002\)](#) and derived the nonlinear asymptotic solution for the bubble velocity. For RMI, the decay rate of the bubble velocity depends on the relative strength of viscosity and surface tension. For RTI, however, both surface tension and viscosity decrease the asymptotic bubble velocity. For non-ideal magnetic RTI fluid, [Li and Luo \(2014\)](#) also reported that the bubble velocity is reduced by viscosity and surface tension, which indicates that viscosity and surface tension suppress the RTI.

In a previous work, [Sohn \(2007, 2008\)](#) showed that the growth rates of the bubble based on Zufiria's model agrees better with experiments than that based on Layzer's model. Motivated by this result, [Cao et al. \(2011\)](#) inspected RTI induced flows, but now with [Zufiria's \(1998a\)](#) potential flow model instead. While an improved agreement with the time evolution of the bubble velocity was found when compared to the measured data of [White et al. \(2010\)](#), both potential flow based models were within the experimental uncertainty. Based on Layzer's approach, [Gupta et al. \(2012\)](#) also analyzed the combined effect of viscosity and surface tension on the two-fluid nonlinear interfacial finger-like structures due to RTI and RMI. Recently, [Li et al. \(2016\)](#) considered the effects of viscosity and surface tension on the bubble growth rate of RTI with special attentions paid to the differences between the Zufiria and Layzer models.

Focused on the RMI flows, [Carlès and Popinet \(2002\)](#) again applied their singular perturbation techniques to the incompressible Navier–Stokes equations written for two superposed immiscible fluids. The weakly non-linear law of interface deformation for the RM instability was written as the following,

$$\begin{aligned} \frac{a_{CP}}{a_0} = & (1 + A\Delta Vkt) \cos(kx) \\ & - \frac{16}{3\sqrt{\pi}} \frac{\sqrt{\rho_1\mu_1}\sqrt{\rho_2\mu_2}}{(\rho_1 + \rho_2)(\sqrt{\rho_1\mu_1} + \sqrt{\rho_2\mu_2})} A\Delta V k^2 t^{3/2} \cos(kx) \\ & - \frac{\sigma}{2(\rho_1 + \rho_2)} k^3 t^2 \left(1 + \frac{1}{3} A\Delta V kt\right) \cos(kx) \\ & - \frac{1}{2} a_0 A^3 (\Delta V)^2 k^3 t^2 \cos(2kx). \end{aligned} \quad (5.4)$$

In above equation, each effect (viscosity, surface tension and non-linearity) appears under the form of a specific term corresponding to an attenuation of the linear growth rate (the first term). Recall that the influence of the viscosity term has been inspected individually in a previous subsection and compared against the model of Mikaelian.

Before closing our discussion on the surface tension and viscosity effects, we note that [Mikaelian \(2014c\)](#) commented on the [Carlès and Popinet \(2002\)](#) work. He stated that this paper on the RMI with surface tension or viscosity has limited application and could yield bad results outside its range of validity at early time. In addition, since the fluid viscosities appear as a product in this model, it predicts that there are no viscous effects if one of the two fluids has zero viscosity. But, as pointed out by [Mikaelian \(2014c\)](#), this is not correct because the viscosity of the other fluid is sufficient to influence the flow, and the viscosities should appear as sum rather than as a product.

5.4. Diffuse interface

[Lord Rayleigh \(1883\)](#) in his pioneering work considered the stabilizing effect of a continuous density gradient. The exact equation, sometimes called the “Rayleigh equation”, can be cast in the form of Schroedinger's equation and eigenvalues from one equation can be related to the eigenvalues of the other ([Mikaelian, 1996b](#)). The RTI growth rate γ_{RT} can be written as $\gamma_{RT} = \sqrt{g}\Gamma$, and the stabilization factor is $\Gamma/\Gamma_{\text{classical}}$ where Γ is the exact (or approximate) solution to Rayleigh's eigenvalue equation with the density gradient, and $\Gamma_{\text{classical}}$ is for a sharp density profile (i.e. no density-gradients) which gives $\Gamma_{\text{classical}} = (kA)^{1/2}$.

Since only a limited number of density profiles (or, equivalently, quantum mechanical potentials) admit exact analytic solutions, approximation techniques are often used. The first such technique was introduced by [Lelevier et al. \(1955\)](#) who considered the effect of a density gradient on RTI when the transition between the low and high density fluids is very smooth. In this report, the authors extended Taylor's derivation of an accelerated surface of density discontinuity to the case in which the density has a smooth transition. The exponential (i.e. diffusive) density distribution used in this study can also be found in [Hide \(1955\)](#) as well as in a subsequent paper by [Case \(1960\)](#), with Hide using approximation techniques and Case finding exact solutions.

[Lelevier et al. \(1955\)](#) derived a modification to the classical RTI growth rate,

$$\gamma = \sqrt{\frac{kgA}{1 + \frac{1}{2}kL_0}} \quad (5.5)$$

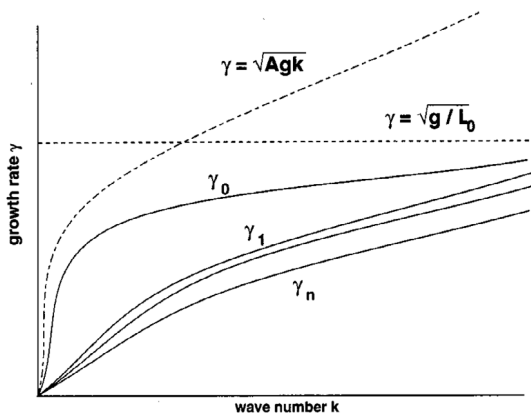


Fig. 5.6. Qualitative representation of γ_n versus wave number k for a fixed Atwood number A and a diffuse layer thickness.
Source: Fig. 2 of Cherfils and Lafitte (2000), with permission from *Phys. Rev. E*.

where $L_0 = (\rho_1 - \rho_2) / (\partial \rho / \partial y)_0$ is the width of the diffuse layer. The diffuse interface prevents $\gamma \rightarrow \infty$ at high wavenumber (the paper credits Edward Teller with suggesting this behavior⁴⁶).

Considering the perturbation on the shell of a laser fusion target and using variational calculus, Munro (1988) attempted to minimize the RTI growth rate for a given wavenumber. The experimental studies by Zaitsev et al. (1991, 1994) and modeling work of Ruev et al. (2004, 2005, 2006) demonstrated that an allowance for the initial finite width of the mixing layer decreases the growth rate of the normalized width of the layer.

Cherfils and Lafitte (2000) obtained the exact analytical expressions for the growth rate with a linear density profile. For a given wavenumber k , the determination of the admissible growth rate becomes an eigenvalue problem (Lord Rayleigh, 1883). Cherfils and Lafitte reported that the growth rate corresponding to the n th eigenvalue is given by

$$\gamma_n^2 = \frac{gk}{kL_0 + \tilde{\omega}_{n+1}(kL_0)^{1/3}} \quad (5.6)$$

where $\tilde{\omega}_{n+1}$ is the $(n + 1)$ th zero of the Airy function (Abramovitz and Stegun, 1968).

Fig. 5.6 shows the growth rate γ_n versus wave number k for a fixed Atwood number A and a diffuse layer thickness. The authors noted the discrepancy between the first order (γ_0) formula and the widely used estimate

$$\sqrt{Akg/(1 + AkL_0)}, \quad (5.7)$$

in the ICF context with $A = 1$ (Lindl, 1995). Nevertheless, it is reassuring that the formula reproduces the correct short- and the long-wavelength limits

$$\lim_{k \rightarrow 0} \gamma(k) = \sqrt{Agk},$$

$$\lim_{k \rightarrow +\infty} \gamma(k) = \sqrt{g/L_0}. \quad (5.8)$$

It should be noted that for most of the papers the interface diffuseness does not change with time. Papers which do consider the case of time-evolving diffuseness (e.g. Duff et al., 1962) must be highlighted. Recently, Morgan et al. (2016) inspected the inviscid, dynamic diffusion model of Duff et al. and numerically solved the RTI linear stability formulation of Chandrasekhar (1955) with an error function diffusion profile. The goal was to have a model for investigating the combined effects of the density gradient and viscosity. They have also performed experiments in which an interface between two gases of differing density is made unstable by acceleration produced by a rarefaction wave.⁴⁷ This rarefaction wave generates a large, but non-constant, acceleration of the order of 1000g, where g is the acceleration due to gravity. When RTI is initiated with a diffuse interface, Morgan et al. found that the growth rates of the instability are reduced and agree well with theoretical values and with the Duff et al. model when diffusion thickness is accounted for.

Recently, Xie et al. (2017b) studied viscous RTI flows with and without diffusion effect by inspecting the classical Bellman and Pennington (1954) and Duff et al. (1962) models. They found that the Duff et al. model inherited the maximum error (~12%) from the approximate solution of Bellman and Pennington (Hide, 1955; Reid, 1961; Menikoff et al., 1977; Mikaelian,

⁴⁶ For Teller's scientific legacy, see Libby and Van Bibber (2010).

⁴⁷ The idea of performing rarefaction experiments can also be found in Mikaelian (2009a).

1993). The authors suggested an explicit solution of the implicit dispersion relation, which improved the accuracy of the models but of course at the expense of added complexity.

Mikaelian (1991) turned his attention to the effect of the density gradient on the Richtmyer–Meshkov instability. Using the profiles considered by Saffman and Meiron (1989) (a hyperbolic-tangent) and Duff et al. (1962) (an error-function), he treated the shock as an instantaneous acceleration of incompressible fluids. In this work, Mikaelian (1991) pointed out that the density-gradient-stabilization in RMI is essentially the square of the density-gradient-stabilization in RTI. As a result, when the RTI stabilization factor $\Gamma/\Gamma_{\text{classical}}$ is squared, the RMI stabilization factor $(\Gamma/\Gamma_{\text{classical}})^2$ can be easily obtained. This can be applied to any density profile such as the one considered by Lelevier et al. (1955) and Cherfils and Lafitte (2000), etc.

Numerically, Tian et al. (2011a) studied the effects of the density gradient by solving the compressible Euler equations with a high resolution, arbitrary Lagrangian–Eulerian (ALE) code (Tian et al., 2011b). The authors confirmed that the density gradient reduced the growth rate of perturbation amplitude significantly and noted that the width of the premixed layer had very limited influence. Also, Gopalakrishnan et al. (2017) showed by combined numerical simulations and experiments on the miscible RT instability that in porous media diffusion can be locally as important as convection.

Over the years, several density gradient profiles have been utilized. As one would expect, if the density profiles are the same or similar the corresponding growth rates are also the same or similar. This point can be illustrated by comparing Fig. 1 of Mikaelian (1986) (an exponential density profile) with Fig. 1 of Mikaelian (1991) (the hyperbolic tangent profile). With the proper choice of the parameters, Mikaelian (1991) determined that the error-function and hyperbolic tangent profiles (Eq. (16) of his article, not shown) coincide within 3.5%. Furthermore, Fig. 5 of Mikaelian (2015) showed a similar profile when an error-function is employed. Clearly, similar growth rates will result regardless one describes the profile by exponentials, hyperbolic tangents, or error-functions.

It should be stressed that the stabilization due to a diffusion is important for ablation front stabilization (see the high-energy-density-physics section of Part II, Zhou, 2017).

6. Similarity, scaling, minimum state of the transition to turbulence

6.1. Late-time RTI similarities

It is widely believed that many “simple” turbulent flows, such as the RTI, RMI, and KHI mixing layers evolve toward self-similarity. In an early work, Sharp and Wheeler (1961) (see also Sharp, 1984) constructed a bubble amalgamation model for the RTI that predicted an average velocity of bubble rise,

$$v_{av} \propto gt \quad (6.1)$$

where g is the acceleration. Youngs (1984) exploited a self-similar modal growth of the RTI interface to arrive at the formula for mixing layer growth

$$h_i(t) = \alpha_i A g t^2. \quad (6.2)$$

Here, $i = b, s$ denotes the bubble and spike and the total mixed width, $h = h_b + h_s$. Two-dimensional simulations of Youngs (1984) showed that α_b should vary little with Atwood number. Asymmetry should increase with Atwood number.

In fact, the t^2 scaling for the RTI mixing layer width was previous reported in Fermi (1951) and Birkhoff (1955). Enrico Fermi, together with John von Neumann, were probably the first to consider a model for the nonlinear stage (Fermi and von Neumann, 1955). Actually written in 1951 and 1953, this work appears to be a single mode analysis: bubble $\sim t^{1/2}$, spike $\sim t^2$.

The significance of the Birkhoff (1955) reference from that era is generally underestimated. His analysis applied the single mode theory (exponential growth to terminal velocity) for bubbles to multimode random perturbations with amplitude \sim wavelength. He derived $\alpha_b = 0.06$ at $A = 1$.

In the earliest Russian publication, Belen'kii and Fradkin (1965) determined that the dimensional argument suggests the length scale should be proportional to gt^2 if the mixing is self-similar. According to V.B. Rozanov,⁴⁸ this paper was based on research carried out much earlier, circa 1950, as Belen'kii died in 1956. Based on a one-equation turbulence model, Belen'kii and Fradkin modeled turbulent mixing caused by RTI by use of an analogy to shear flow mixing. In the instability process, potential energy is converted to turbulence kinetic energy. Mixing then arises from a diffusion process with a turbulent diffusion coefficient (Youngs, 2013). The Andronov et al. (1976) paper considered deceleration by multiple-shocks rather than by RT, but the Schlieren image was the first image of a “turbulent mixing zone” in this area. Also, Neuvazhaev and Yakovlev (1976a, b) treated RTI with g as a function of time.

Using the Euler–Lagrange equations for the variation of the potential and kinetic energy, a simplified Fermi model resulted in the following RTI mixing layer width (also recalled in Boffetta et al., 2011),

$$h_i(t) = \alpha_i A g (t + t_{i,0})^2, \quad (6.3a)$$

⁴⁸ Private communication between V.B. Rozanov and D.L. Youngs (2010).

where $t_{i,0}$ is the time origin of spikes and bubbles (Clark and Zhou, 2003). As remarked by Cabot and Cook (2006), the time origin of the self-similarity scaling of RTI depends on how long it takes for the flow to become self-similar, which in turn depends on the spectrum of initial perturbations.⁴⁹

Eq. (6.3a) can be rewritten as

$$h_i(t) = h_{i,0} + (4\alpha_i Agh_{i,0})^{1/2}t + \alpha_i Agt^2, \quad (6.3b)$$

where $h_{i,0} = \alpha_i Agt_{i,0}^2$ is the virtual starting thickness.

This quadratic scaling relation in time for the mixing layer has found support from a large body of experimental and computational work (see for example, Andrews and Spalding, 1990; Anuchina et al., 1978; Birkhoff, 1955; Cabot and Cook, 2006; Cabot and Zhou, 2013; Cherfils and Mikaelian, 1996; Cook and Dimotakis, 2001; Cook and Zhou, 2002; Cook et al., 2004; Dimonte, 2000; Dimonte and Schneider, 1996, 2000; Glimm and Li, 1988; Glimm et al., 1990, 1998; He et al., 1999a; Inogamov, 1978; Inogamov et al., 1991; Kadau et al., 2004, 2007; Kucherenko et al., 1991; Li and Chu, 2007; Linden et al., 1994; Oparin et al., 2000; Read, 1984; Schneider et al., 1998; Young et al., 2001; Youngs, 1984, 1989, 1994, 2013; Zhou, Cabot, and Thornber, 2016).⁵⁰

With notable exception from Russian literature (e.g. Anuchina et al., 1978), previous experimental work had concentrated on studying the growth of the instability from a single wavelength perturbation rather than turbulent mixing (Lewis, 1950; Allred and Blunt, 1953; Emmons et al., 1960; Duff et al., 1962; Cole and Tankin, 1973; Popil and Curzon, 1979). The major purpose of the Rocket-rig experiments was to study the evolution of the instability from small random perturbations (Read and Youngs, 1983; Read, 1984; Youngs, 1989). The acceleration of the interface was chosen to be high enough for surface tension and viscosity to have a small effect on the over all growth rate of the mixed region (Youngs, 1992). Read and Youngs utilized a novel technique to achieve the desired acceleration. As shown in Fig. 6.1 (from Read, Fig. 1), one or more rocket motors, attached to the top of the tank, were used to drive the tank vertically downwards at the accelerations in the range between 25 and 75 times of the gravity. Two fluids were enclosed in a rectangular tank, the less dense fluid initially resting on top of the denser fluid. Read (1984) and Youngs (1992) found that large and larger structures appear as time proceeds and concluded that the mix width is described well by the scaling law (Eq. (6.2) and Fig. 6.2).

Dimonte et al. (1996a) built the Linear Electric Motor (LEM) facility to investigate turbulent mix with variable acceleration profiles, including a constant acceleration (70 times earth's gravity) for basic studies. The facility is powered by 16 independent capacitor banks to provide arbitrary acceleration profiles up to 1000 times earth's gravity (Fig. 6.3). The Rocket Rig (Read, 1984), LEM (Dimonte and Schneider, 2000), Kucherenko et al. (1991), Andrews and Spalding (1990), Snider and Andrews (1994), Dalziel (1993), Linden et al. (1994), and Dalziel et al. (1999) data provided basic set of experimental values of α_b .

In a comprehensive work, Dimonte et al. (2004) summarized and compared the simulated values of α_b with published experiments. The values ascribed to the simulations were averaged over appropriately and the reported experimental values are shown in histogram form. The sample average and variance are $\alpha_b \sim 0.025 \pm 0.003$ for the simulations and $\alpha_b \sim 0.057 \pm 0.008$ for the experiments. This difference was consistent with the historical record. Fig. 6.2, reproduced from Fig. 13 of Dimonte et al. (2004), compared the values α_b from numerical simulations and experiments (cover publications from 1991 to 2004, see also, Fig. 1 of Ramaprabhu and Dimonte (2005)).

For the numerical results, Dimonte et al. (2004) noted that as grid resolutions have increased, α_b has decreased. Larger values of α_b can be obtained in the presence of additional long wavelength perturbations and this may be more characteristic of experiments. Also, the values of α_b and α_s (the spike growth factor) will become asymmetric as the Atwood number increases. These issues will be addressed later in Part II. It should be stressed here that the simulations were for the “ideal case”—a low level of short-wavelength perturbations and mixing of miscible fluids. It was argued in the Dimonte et al. paper that the ideal case should be a lower bound to what would be expected experimentally.

George et al. (2002) noted that these simulations are from computational codes using numerical schemes with interfacial mass diffusion. They argued that all values of α (experiments and simulations) are consistent if the diffusive calculations of α is renormalized to account for mass diffusion.

⁴⁹ Within the context of homogeneous decaying turbulence, Skrbek and Stalp (2000) discussed the complication caused by the virtual origin when inspecting the growth rate of the integral length scales.

⁵⁰ Kadau et al. (2004, 2007) compared and contrasted the evolution of the mixing process between atomistic simulations, experiments, and continuum simulations (see also Barber et al., 2008). Whereas the continuum calculations exhibit self-similar growth, atomistic simulations showed the change in regime from t^2 behavior to linear- t behavior in the penetration depth. After an interval in which the velocity increases linearly in time, it instead varies around a constant value. As stressed by Kadau et al. (2007), an analysis of previous experimental data (Dimonte et al., 2004) showed that even the best of experiments is not yet able to rule out the possibility of such a regime change. This change in behavior is excluded for any self-similar flow, as in the solution of the Navier-Stokes equations with negligible viscosity, due to the fact that the only relevant length scale is gt^2 (see also, the Lie Group analysis in Section 6.3). The authors noted that the self-similarity could be broken only when the growth of structures horizontally is restricted by the system width, which then introduces an additional length scale into the problem. In fact, the case when the horizontal width is restricted is considered by Lawrie and Dalziel (2011a, b)—actually gives $t^{2/5}$ for the very late time. This is referred to at the later part of this subsection but there is a connection here. In a related development, Barber et al. (2006), Sagert et al. (2015) and Gallis et al. (2016) also investigated the growth of the RTI using the direct simulation Monte Carlo algorithm (Bird, 1976, 1998). Gallis et al. (2016) found that the instability enters the self-similar regime in some of the simulations at late times.

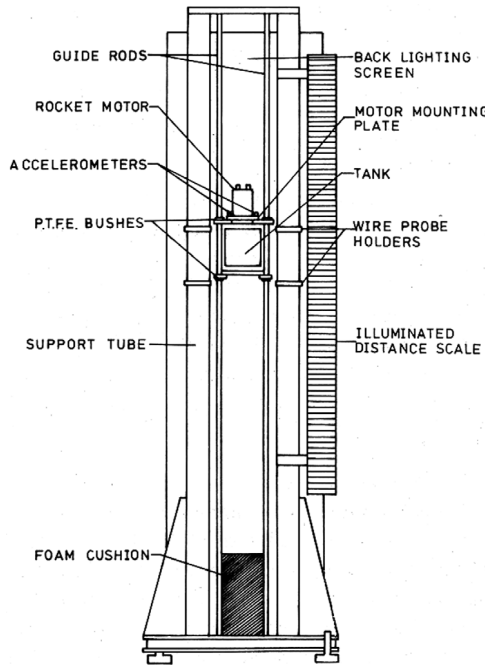


Fig. 6.1. Sketch of the Rocket-rig facility. Rocket-Rig experiments are also described in [Youngs \(1989\)](#). Source: Fig. 1 from [Read \(1984\)](#), *Physica D*.

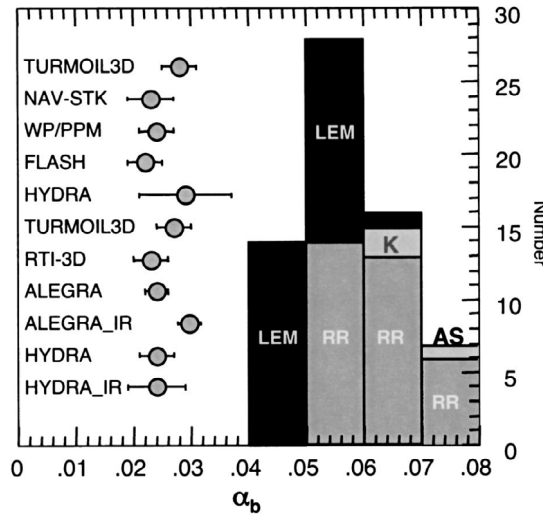


Fig. 6.2. Comparison of α_b from numerical simulations and experiments in histogram form (cover publications from 1991 to 2004). LEM is from Linear Electric Motor ([Dimonte and Schneider, 2000](#)), RR from “rocket rig” ([Read, 1984](#)), K from [Kucherenko et al. \(1991\)](#), AS is from [Andrews and Spalding \(1990\)](#). Source: From Fig. 13 of [Dimonte et al. \(2004\)](#), *Phys. Fluids*, with the permission of AIP Publishing.

[Cabot and Cook \(2006\)](#) attempted to shed some light on the somewhat ironic state of affairs, in that agreement between simulations and experiments is worse today than it was several decades ago because of the availability of ever more powerful computers. Using DNS, they obtained a high Reynolds number RTI induced flow with a resolution $3072^2 \times N_z$. At the beginning of the simulation, N_z was 256; by the end, N_z reached a value of 3072, thus forming a cubic domain (see [Fig. 6.4](#), reproduced from Fig. 1 of [Cabot and Zhou, 2013](#)). [Fig. 6.5](#) showed the evolution of the Reynolds number, Re , which is defined as the inertial influences scaled to dissipative momentum diffusive influences ([Hinze, 1975](#))

$$Re = \tilde{u}\delta/\nu. \quad (6.4)$$

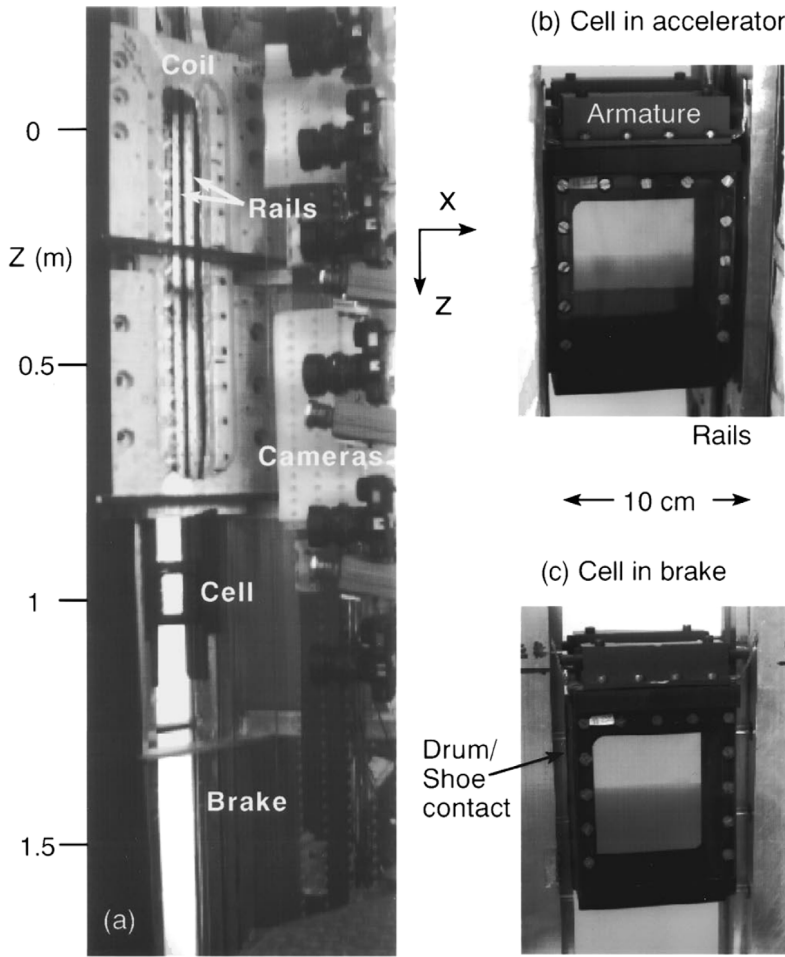


Fig. 6.3. Configuration of a linear electric motor (LEM) Photograph with long pulse coil, brake, and diagnostic cameras. Close-up photographs of the cell in acceleration region with armatures engaged and cell in the brake with armatures disengaged.

Source: Fig. 1 of Dimonte et al. (1996a), Rev. Scientific Instruments, with the permission of AIP Publishing.

Here δ is the characteristic flow structure outer length scale, \tilde{u} is the characteristic velocity, and ν is the kinematic viscosity. For the RTI flow shown in Fig. 6.5, $\delta = h$, $\tilde{u} = \dot{h}$. As will be shown in later part of this section, the Reynolds number plays a critical role for the time-dependent transition of the hydrodynamic instability induced flows.

As shown in Fig. 6.5, the RTI growth parameter can be computed with several methods. First, Eq. (6.2) can be rewritten as

$$\alpha_i = h_i(t)/Agt^2. \quad (6.5)$$

Of course, above equation can also be obtained from Eq. (6.3b),

$$\alpha_i = [h_i(t) - (4\alpha_i Agh_{i,0})^{1/2}t - h_{i,0}](Agt^2)^{-1},$$

but with last two terms neglected. The blue curve in Fig. 6.5, obtained from Eq. (6.5), $h/(Agt^2)$, illustrates why standard curve-fitting techniques have yielded lower α values as simulations have reached higher effective Reynolds numbers.

The second formula,

$$\dot{h}_i^2 = 4\alpha_i Agh_i, \quad (6.6)$$

has been rederived more recently through different derivations (Glimm et al., 2001; Cook et al., 2004, Ristorcelli and Clark, 2004, Jacobs and Dalziel, 2005). For instance, Ristorcelli and Clark (2004) and Jacobs and Dalziel (2005) used a similarity assumption, whereas Cook et al. (2004) used a mass flux and energy balance argument.

From Eq. (6.6), α_i can also be given by the following expression,

$$\alpha_i = \dot{h}_i^2 / 4Agh_i. \quad (6.7)$$

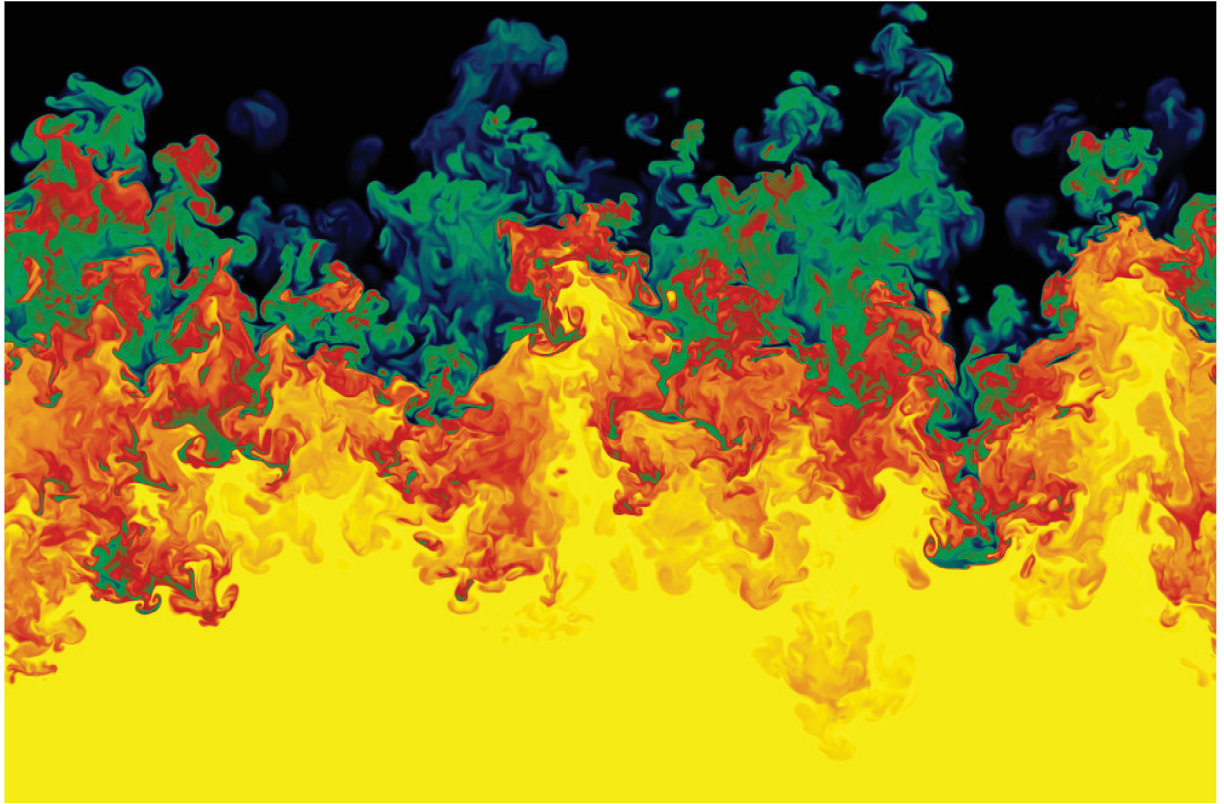


Fig. 6.4. Cabot and Zhou (2013) Visualization of a vertical slice of the density field in the RTI mixing layer at late time for the $A = 0.5$ case. Heavy fluid is dark, light fluid is light. Gravity is directed downwards.

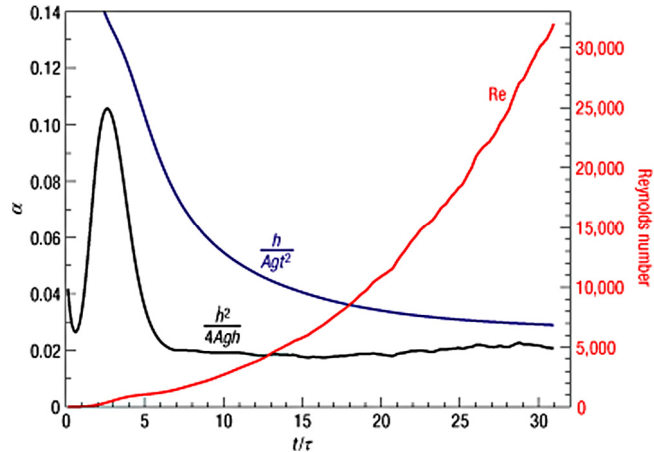


Fig. 6.5. Comparison of measurement techniques for RTI growth parameter, α , including Reynolds number (Re) dependence. The mixing layer thickness (h) and its growth rate (\dot{h}) are normalized by the Atwood number (A), gravity (g) and time (t).
Source: Fig. 4, (Cabot and Cook, 2006), *Nature Physics* with permission.

The similarity method, Eq. (6.7), is relatively robust (black curve in Fig. 6.5). The fact that \dot{h} is finite at $t = 0$ is due to the quick growth of the mixed width immediately following the commencement of the simulation, not because of a utilization of an initial velocity. Nevertheless, the value of α_b from both cases agrees well with other numerical simulations.

Eq. (6.3a) can also be written as

$$h_i(t)^{1/2} = h_{i,0}^{1/2} + (\alpha_i Ag)^{1/2} t. \quad (6.8)$$

Table 6.1

The updated RTI growth factor since the publication of the Alpha group collaboration (Dimonte et al., 2004). Ramaprabhu et al. (2005) and Youngs (2013) considered the impact of the initial wavelength on the values of α_b with their ILES. Lower values were reported for the initial short wavelength while higher values were obtained for initial long wavelength. With DNS, Livescu et al. (2010) found that for $A = 0.04$ and $A = 0.5$, the values of α_b are very similar. The remaining results only consider the RTI growth factor from total mixed width. Boffetta et al. (2010) performed their DNS with equations appropriate under Boussinesq (1877) approximation. With DNS, Cabot and Cook computed the values α using Eqs. (6.5) and (6.7). Cabot and Zhou (2013) found very limited dependence on the Atwood number dependence with three DNS datasets, $A = 0.2, 0.5$, and $A = 0.8$. The ILES of Soulard et al. (2015) provided very low value of α . The experimentally measured α values of Olson and Jacobs (2009) do not show a dependence on the initial perturbation amplitude for the RTI flows with $A = 0.163$ and $A = 0.2$. Using Eq. (6.8), this proposed method for the determination of α yields a value in better agreement with computational studies.

	Alpha	Note
Alpha (from Bubble)		
Ramaprabhu et al. (2005)	0.025–0.087	Mode-coupling or long wavelength
Livescu et al. (2010)	0.022–0.025	$A = 0.5$ and $A = 0.04$
Youngs (2013)	(0.022–0.029) up to 0.12	Initial short wavelength; initial long wavelength
Alpha (from total mixed width)		
Boffetta et al. (2010)	0.036	Small Atwood number; Boussinesq approximation
Cabot and Cook (2006)	0.020 0.028	Computed with Eq. (6.5) or Eq. (6.4) methods
Cabot and Zhou (2013)	0.020–0.024	$A = 0.2$ –0.8
Soulard et al. (2015)	0.02	$A = 0.1$
Olson and Jacobs (2009)	0.031–0.041	$A \approx 0.2$

It is easy to show that Eqs. (6.7) and (6.8) are exactly the same. The value of α_i can be most easily obtained by simply plotting $h^{1/2}$ versus $(Ag)^{1/2}t$ and fitting a line to the late time portion of the curve where the slope is $\alpha^{1/2}$ (see Olson and Jacobs, 2009).

Livescu et al. (2010) stated that the time derivative of $h(t)$ might lead to excessive noise in the value of α , especially if the data are sparse. They used a formula that essentially rewrites Eq. (6.8) within the self-similar range as

$$\alpha_i = [\Delta(h_i(t)^{1/2}) / (Ag)^{1/2}(\Delta t)]^2. \quad (6.9)$$

It should be noted that Eq. (6.5), which is a poor way of calculating α , was rarely used. The Dimonte et al. (2004) paper actually used the late-time slope

$$\alpha_b = \frac{\Delta h_b}{\Delta(Agt^2)}. \quad (6.10)$$

Eq. (6.10) implicitly assumed the domination of the t^2 term in Eq. (6.3) at late times. Most published works made a choice between this and Eq. (6.7). In the asymptotic limit in time where the t^2 term is much larger than the other terms, all of these definitions should converge to the same value.

Dimonte et al. (2004) is an extensive reference article on the simulated and experimental measured values of α_i written for the Alpha group collaboration. To avoid unnecessary duplication, Table 6.1 of the present review, therefore, focuses on research done since that time.

Although many papers have focused on the “ideal case” as described above, some researchers have endeavored to obtain better agreement with experimental data by using initial conditions approximated or parameterized from experiments (see Dalziel et al., 1999; Mueschke and Schilling, 2009a,b; Glimm et al., 2013, see more detailed discussion in Part II). It is also appropriate to note that Inogamov (1978) proposed that random perturbations with amplitude \propto wavelength for wavelengths up to the domain size give self-similar growth at an enhanced rate. This corresponds to a k^{-3} power spectrum for the initial perturbations which has been used in several papers, including Youngs (2003, 2013) and Ramaprabhu et al. (2005) as referred to in Table 6.1.

To conclude our discussion on extracting the value of the RTI growth parameter from data, α_i , one should note several related matters. In high-aspect-ratio domains, RTI has been studied experimentally. Dalziel et al. (2008) and Lawrie and Dalziel (2011a, b) examine RTI in a laterally confined domain (see also Debacq et al., 2003), and in this configuration, the turbulent length-scales present in the RTI are bounded by the domain width, rendering the $h \sim t^2$ scaling inappropriate once h exceeds the dimension of the lateral constraint (which actually gives $t^{2/5}$ for the very late time).

The self-similar RT mixing can occur for the case $g \propto t^p$ where positive and some negative values of p are permissible for a well-developed RT mixing zone (Llor, 2003). More broadly speaking, the implosion phase of the ICF implosion has shown a time-dependent acceleration (Betti et al., 2007) and transients in acceleration histories were also found in the experiments of Read (1984), Dimonte and Schneider (1996, 2000), Jacobs and Sheeley (1996), Zaytsev et al. (2003) and Wang et al. (2001). Motivated by these applications, Mikaelian (2009b, 2010, 2014a), Zhang et al. (2015), Ramaprabhu et al. (2016) and Pandian et al. (2017) have carried out extensive analytical and numerical studies on nonlinear hydrodynamic instabilities driven by various time-dependent accelerations (see also Youngs, 1997). Table 6.2 summarizes several acceleration profiles investigated by Ramaprabhu et al. (2016).

Livescu, Wei, and Petersen (2011) noted that “gravity reversal” occurs in practical situations (e.g. pulsating stars or ICF). After the layer width had developed substantially, the authors carried out additional branched simulations under the

Table 6.2

(Table 1 of Ramaprabhu et al. (2016), Phys. Rev. E with permission) Selected acceleration profiles. Several minor typos in the original table have been corrected.

Acceleration history	Scaled acceleration distance	Velocity profile	Displacement
g	$s \equiv \left[\int \sqrt{g(t)} dt \right]^2$	$u \equiv \int g(t) dt$	$Z \equiv \int_0^t \int_0^{t''} g(t') dt' dt''$
$g_0 t^n$	$\frac{4g_0}{(n+2)^2} t^{n+2}$	$\frac{g_0}{n+1} t^{n+1}$	$\frac{g_0}{(n+1)(n+2)} t^{n+2}$
$g_0 (1 + \check{\alpha} t^2)$	$g_0 \left\{ \frac{1}{2} t \sqrt{1 + \check{\alpha} t^2} + \frac{\sinh^{-1}(\sqrt{\check{\alpha}} t)}{2\sqrt{\check{\alpha}}} \right\}^2$	$g_0 t + \frac{1}{3} g_0 \check{\alpha} t^3$	$\frac{1}{2} g_0 t^2 + \frac{1}{12} g_0 \check{\alpha} t^4$
$\begin{cases} \frac{g_0}{t_0} t, t \leq t_0 \\ g_0 \left\{ 1 - \frac{t - t_0}{t_L - t_0} \right\}, t > t_0 \end{cases}$	$\frac{4}{9} g_0 \left\{ t_L - \frac{(t_L - t)^{\frac{3}{2}}}{\sqrt{t_L - t_0}} \right\}^2, \quad t > t_0$	$\frac{g_0}{2(t_L - t_0)} \left\{ -t^2 + 2t_L t - t_L t_0 \right\}, \quad t > t_0$	$\frac{\frac{g_0 t_0^2}{6} + \frac{g_0}{2(t_L - t_0)}}{\left\{ -\frac{1}{3} t^3 + t_L t^2 - t_L t_0 t + \frac{1}{3} t_0^3 \right\}}, \quad t > t_0$
$\begin{cases} 0, t < t_0 \\ g_0 \left(\frac{t}{t_0} \right)^{\check{b}}, t \geq t_0, \check{b} < -1 \end{cases}$	$\frac{4}{(\check{b} + 2)^2} \frac{g_0}{t_0^{\check{b}}} \left(t^{\left(\check{b} + 2 \right)/2} - t_0^{\left(\check{b} + 2 \right)/2} \right)^2, \quad t > t_0$	$\frac{g_0 \left(t^{\check{b} + 1} - t_0^{\check{b} + 1} \right)}{(\check{b} + 1) t_0^{\check{b}}}, \quad t > t_0$	$\frac{g_0}{(\check{b} + 1) t_0^{\check{b}}} \left\{ \frac{t^{\check{b} + 2} - t_0^{\check{b} + 2}}{(\check{b} + 2)} - t_0^{\check{b} + 1} (t - t_0) \right\}, \quad t > t_0$
$\frac{g_0}{\left(1 - \frac{t}{\check{T}} \right)^2}$	$\check{T}^2 g_0 \left\{ \ln \left(1 - \frac{t}{\check{T}} \right) \right\}^2$	$\frac{g_0 \check{T}}{\left(1 - \frac{t}{\check{T}} \right)} - g_0 \check{T}$	$- \check{T}^2 g_0 \ln \left(1 - \frac{t}{\check{T}} \right) - g_0 \check{T} t$
$\frac{g_0}{\left(1 - \frac{t}{\check{T}} \right)^3}$	$4 \check{T}^2 g_0 \left\{ \frac{1}{\sqrt{1-t/\check{T}}} - 1 \right\}^2$	$\frac{g_0 \check{T}}{2 \left(1 - \frac{t}{\check{T}} \right)^2} - \frac{g_0 \check{T}}{2}$	$\frac{g_0 \check{T}^2}{2 \left(1 - \frac{t}{\check{T}} \right)} - \frac{g_0 \check{T}}{2} t - \frac{g_0 \check{T}^2}{2}$

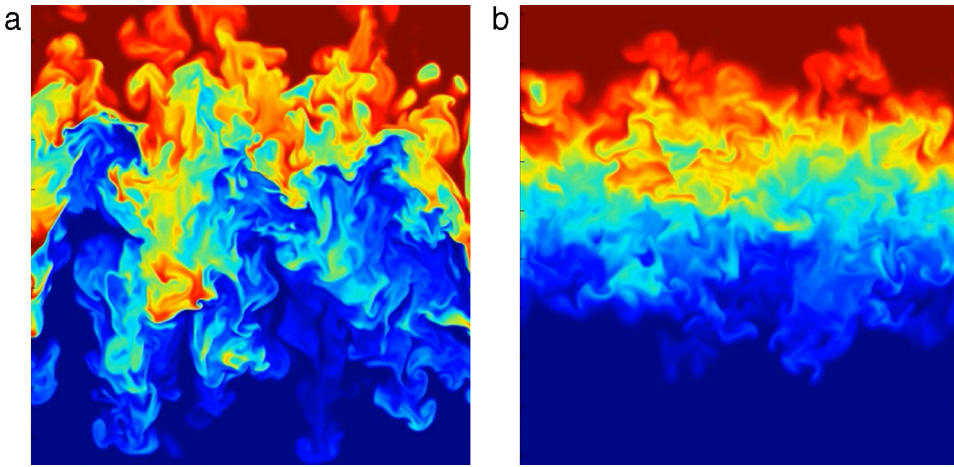


Fig. 6.6. Snapshots of the density field from an $A = 0.5$ simulation. (a) Gravity, (b) reversed gravity. The images are taken at the same time. Source: Fig. 3 of Livescu, Wei, and Petersen (2011), with permission.

reversed condition (Fig. 6.6).⁵¹ They found that the gravity reversal leads to significant small-scale turbulence production. Since the existent turbulence models, in general, do not capture well this process, the gravity reversal simulations could be utilized as an important test case for mix model development.

Using an ILES solver (Lawrie, 2009; Lawrie and Dalziel, 2011a,b), Aslangil et al. (2016) studied the influence of initial conditions on miscible incompressible RTI undergoing nonuniform acceleration. The acceleration profile used for this so-called Accel-Decel-Accel (ADA) problem (Dimonte et al., 2007; Ramaprabhu et al., 2013) is approximated by the Heaviside (step) function as

$$g_z = g[1 - H(t - 2)(2) + H(t - 4)(2)].$$

This should be compared with the LEM acceleration profile of the LEM experiments (Dimonte et al., 2007) used in the ILES simulation of Ramaprabhu et al. (2013) (g_z : 2, 4, and 8 cm/s^2). Aslangil et al. (2016) focused their attention on the effects of ICs (Table 6.3) and used the constant acceleration case $g_z = 4 \text{ cm/s}^2$ for benchmarking their simulations.

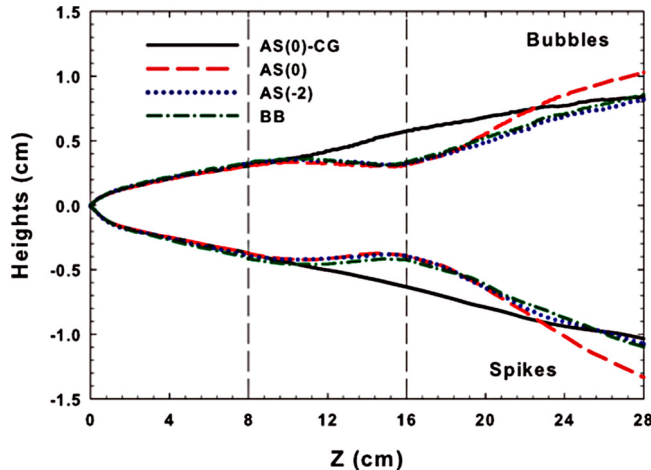
The time evolution of bubble and spike amplitudes, measured as the Z-locations of the 1% and 99% iso-surfaces of the x-y planar-averaged light fluid volume fraction, is given in Fig. 6.7 (Fig. 5 of Aslangil et al., 2016). Here, the length-scale interface

⁵¹ Livescu et al. (2011) also considered the zero-gravity case.

Table 6.3

List of simulations reported in Aslangil et al. (2016).

Shorthand reference	Wave-number range	Spectral index	Acceleration history
AS(0)-CG	32–64	0	Constant gravity
AS(0)	32–64	0	A–D–A
AS(-2)	32–64	-2	A–D–A
BB	4–64	0	A–D–A

**Fig. 6.7.** Evolution of the bubble (hb) and spike (hs) heights vs interface displacement (Z). Linear growth through the origin would represent quadratic growth from zero amplitude.Source: Fig. 5 of Aslangil et al. (2016) with permission from *Phys. Rev. E*.displacement $Z(t)$

$$Z(t) = \int_0^t \int_0^{t''} g(t') dt' dt'',$$

so that $h_{b,s} = 2\alpha_{b,s}AZ(t)$ for constant acceleration history.

At the end of the first acceleration period ($t = 2$ s, $Z = 8$ cm), the system switches from an RT-unstable mixing problem extracting potential energy from a statically unstable density stratification to a wavelike regime where kinetic energy does work against a mean stable stratification. After reacceleration ($t = 4$ s, $Z = 16$ cm), the flow is RT unstable again and the mixing layer continues its expansion. The structure of the flow at the time it enters the deceleration phase has a substantial influence on the later evolution despite apparent convergence of averaged statistics during the reacceleration.

Figs. 6.8 and 6.9 show the density contours of the RT mixing layer x - z and x - y planar slices taken along the center of the domain. During the deceleration period, the large coherent structures typical of an accelerating flow rapidly disintegrate during deceleration, leaving only smaller scales in the flow and a smaller range of densities. After reacceleration, the familiar and bubble and spike structures reemerging and interacting to form ever-larger structures (Aslangil et al., 2016).

Burlot et al. (2015) and Gréa et al. (2016a, b) modeled the RTI induced flows as unsteady stratified homogeneous turbulence (Thoroddsen et al., 1998; Livescu and Ristorcelli, 2007; Griffond et al., 2014; Soulard et al., 2014) using the eddy-damped-quasi-normal Markovian (EDQNM) approximation (Orszag, 1970, 1977; Lesieur, 1990).⁵² This correspondence is appropriate when the ratio between the integral length scale of turbulence and the characteristic scale of the mixing region is small (Vladimirova and Chertkov, 2009). As with any EDQNM closure, the choice of the eddy-damping timescale is critical and must incorporate sufficient physics, as discussed by Zhou et al. (2004). In any case, the usage of the EDQNM closure allowed the computation of the long-term evolution of unstably stratified turbulence at high Reynolds number. The model further predicts a strong anisotropy at large scales, but isotropy of scales in the inertial range as well as in the dissipative one.

Gréa (2013) did not directly tackle the issue of the self-similar state of RTI, i.e., the nonlinear interaction between turbulent quantities and the mixing zone length. Instead, the rapid distortion theory (RDT) (Batchelor and Proudman, 1954; Batchelor, 1953; Townsend, 1976) was used to investigate the response of a fully developed turbulent mixing zone to a rapid acceleration.⁵³ As pointed out by the author, this simple approach was proposed to model the short-time

⁵² Mons et al. (2016) applied an anisotropic EDQNM procedure for homogeneous shear driven turbulence.⁵³ Here, rapidly means that the characteristic frequencies of the turbulent quantities are much smaller than the frequency built with the acceleration and the mixing zone's size (equivalent of the Brunt–Väisälä frequency for the stable case).

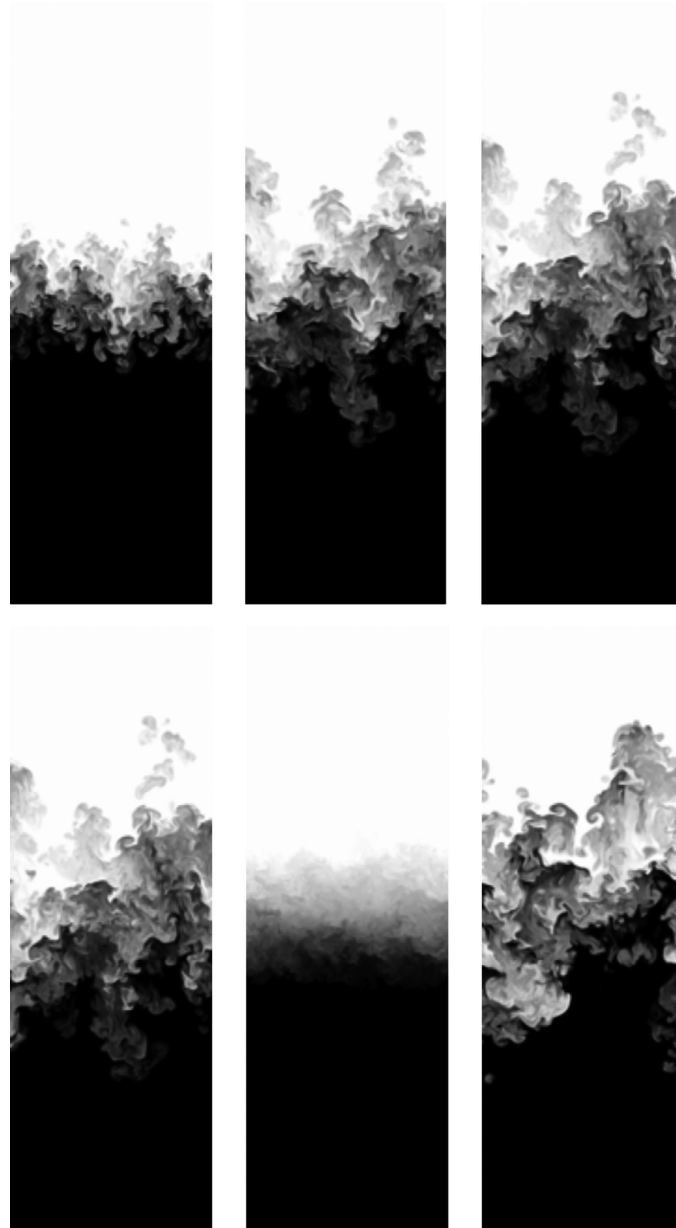


Fig. 6.8. Density contours of the RT mixing layer (a) x - z planar slices taken along the center of the domain; cases are defined in Table 6.3. Top panel: constant gravity AS(0)-CG case and bottom panel AS(0) Accel-Decel-Accel cases.

Source: Fig. 4 of Aslangil et al. (2016), *Phys. Rev. E*, with permission from APS; additional photos courtesy of Mr. D. Aslangil and Dr. A. Banerjee, Lehigh University.

dynamics (as opposed to the long-time self-similar one) of a strongly accelerated turbulent mixing zone. The approach is in the continuation of weakly nonlinear rapid distortion methods described in Hunt and Carruthers (1990). This state is a nonequilibrium one, contrary to the classical self-similar RT case. The RDT analysis not only provides information on the short-time dynamics of a rapidly accelerated mixing zone, but also allows the study of the nonlinear mechanism coupling the turbulent quantities and the mean concentration field. To investigate a particularly simple problem using RDT as a proof-of-principle for its application to more realistic astrophysical flows, Johnson (2014) studied the evolution of vorticity due to a planar rarefaction in an ideal gas. Gréa et al. (2014) also demonstrated that the coupling between a mean strain and stratification is able to generate strong anisotropic structures. The authors remarked that the nonlinear phenomenology in stratified turbulence is more complex than in purely hydrodynamic turbulence, partly because distant and local interactions expressed by the sweeping and straining effects (for a review, see Zhou, 2010; Zhou et al., 2004) are modified.

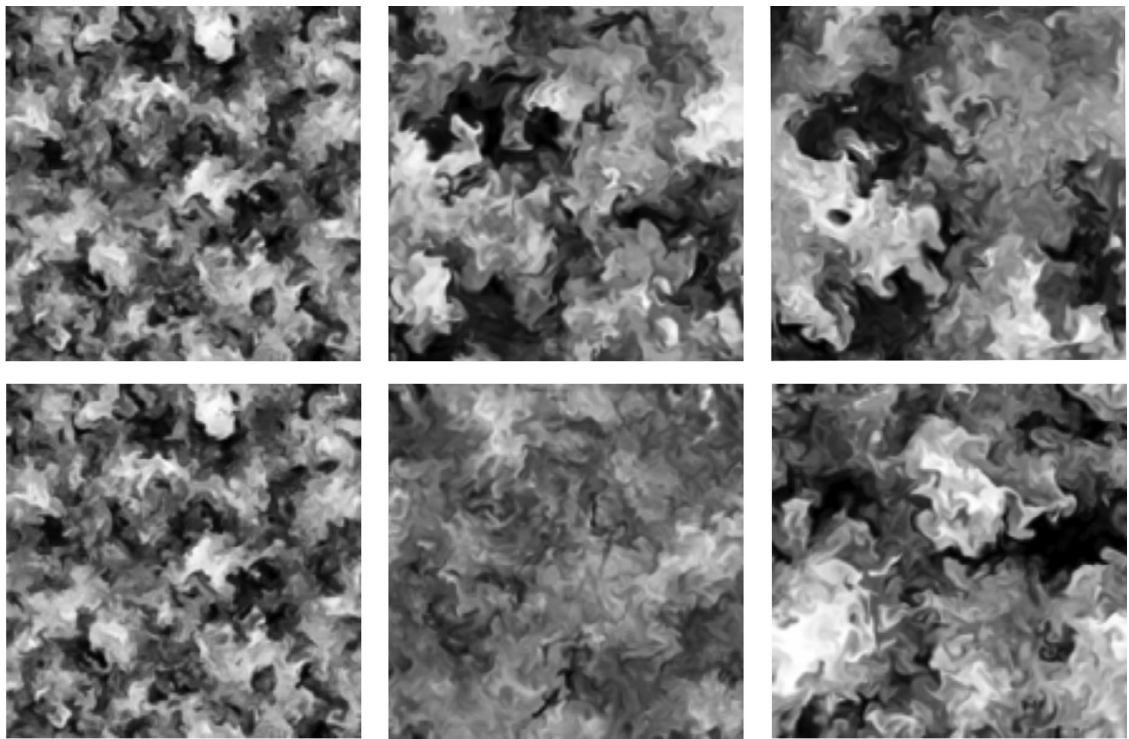


Fig. 6.9. Corresponding x-y planar slices are taken along $z = 0$.
Source: See Fig. 6.8 for other detail; *Phys. Rev. E*, with permission from APS.

6.2. Late-time RMI similarities

The corresponding late-time scaling for RMI driven flows is less well-established. A number of researchers have suggested, however, that a power-law appears to describe the growth of the mixing zone for the case of multi-mode initial perturbations

$$h_i(t) \propto \tau_i^{\theta_i}, \quad (6.11)$$

where τ is a linear function of time, t , and depends on the model.⁵⁴ Determination of the values of θ_i has been a subject of active research (see Table 6.4).

Most of the analyses are carried out for moderate Atwood numbers. Youngs (1994) employed the model equations:

$$\frac{d(LK)}{dt} = -C_1(\Delta V)^3, \quad \frac{dh}{dt} = \Delta V, \quad \text{where } L = C_2h + C_3\lambda_m \quad (6.12a)$$

where h is the width of the mixing layer, K is the kinetic energy, L is the reference length-scale, ΔV is the velocity jump, and C_i ($i = 1, 2, 3$) are model constants, λ_m is the minimum perturbation length scale. From Eq. (6.12a), one obtains

$$\frac{h}{\lambda_m} = \frac{C_3}{C_2} \left[\left(1 + \frac{C_2 \Delta V t}{C_3 \theta \lambda_m} \right)^\theta - 1 \right], \quad (6.12b)$$

where $\theta = 2/(3 + C_1 C_2)$, recovering $\theta = 2/3$ for the case of zero dissipation ($C_1 = 0$).

Zhou (2001) has presented an analysis that draws a connection between the exponents and the growth of the length-scale in a decaying, weakly anisotropic turbulence. The physical picture is one of an initially quiescent flow field subject to an impulsive injection of energy perhaps at all scales and then subsequently allowed to freely decay. Although there are undoubtedly significant corrections due to strong anisotropy and lack of an equilibration of the statistical quantities at early time (see for example, Cohen et al., 2002), the analogy between the RM induced flow and decaying isotropic turbulence becomes better and better as the shock-induced anisotropy decays toward isotropy after the shock passes. Indeed, the LES calculations of Lombardini et al. (2012) have shown that for all Mach numbers considered the late time flow resembles

⁵⁴ The issue of the virtual time origin for the RM self-similar form has been discussed in Clark and Zhou (2006).

Table 6.4

The values of RM scaling exponents.

Models		Experiments		Simulations	
Barenblatt (1983)	2/3	Dimonte et al. (1995)	0.6 ± 0.1	Pham and Meiron (1993)	0.170–0.483
Gauthier and Bonnet (1990)	1/3	Prasad et al. (2000)	0.26–0.33	Youngs (1994) Youngs (2004)	0.30 (flat spectrum) 0.243 (narrow band)
Alon et al. (1993, 1994, 1995) Oron et al. (2001)*	0.4 (2D) 0.25 (3D)	Dimonte and Schneider (1997, 2000), Dimonte (2000)	0.25 ± 0.05 (bubble); 0.25–0.43 (spike); Atwood number dependent	Thornber et al. (2010), Thornber (2016)	0.275 or 0.3 (low/high Atwood number, narrow band); 0.62(broad band)
Youngs (1994)	<2/3	Weber et al. (2012, 2014b)	0.58 0.43 ± 0.01	Thornber et al. (2011b)	0.62 (before reshock) 0.36 (after reshock)
Ramshaw (1998)	2/3	Jacobs et al. (2013)	0.3–0.4	Tritschler et al. (2014a)	7/12 (before reshock) 2/7 (after reshock)
Inogamov (2002)	2/5 (2D) 1/3 (3D)	Krivets et al. (2017)	0.19–0.55 (bubble) 0.18–0.57 (spike)	Oggian et al. (2015)	0.244 (compressible); 0.225 or 0.213 (Hybrid)
Zhou (2001), Zhou et al. (2003a)	7/12 (Batchelor-Proudman) 5/8 (Saffman)			Liu and Xiao (2016)	0.25–0.67 (short to long wavelength initial conditions)
Llor (2006)	1/3–2/7			Lombardini et al. (2012)	0.20–0.33 (depending on the Mach numbers)
Clark and Zhou (2006)	2/7–1/2				
Poujade and Peybernes (2010)	1/4–2/7				
Weber et al. (2013)	0.24				

homogeneous decaying turbulence of Batchelor type (Batchelor and Proudman, 1956) with a kinetic decay energy exponent ≈ 1.4 and a large scale energy spectrum $\approx k^4$. Without other energy deposition, the energy balance equation is reduced to a decaying one.

Thornber (2016) demonstrated that the data fitting of the RMI mixing layer scaling might be rather sensitive to how long a period a simulation or experiment has been run. He basically carried out the same ILES (low Atwood number, narrow band) simulation as Thornber et al. (2010) but to a much later time. Here it appears that $\theta \sim 0.275$ taking a data fit of the last half of the data, however by starting the fit earlier θ is increasing marginally, implying that may decrease further. This is a higher value than the 2010 paper, which may be due to the impact of the spikes on the overall integral width, which could be causing a higher measured ‘slow down’ than expected from the previous case which was $\theta \sim 0.26$.

The RT and RM self-similar parameters compiled in Tables 6.1 and 6.4, α_b and θ , are influenced by the initial conditions. Much of the variation seen in the two tables can be thus explained. In Table 6.4, the pre- and post-reshock values of the RM parameter θ are given for Thornber et al. (2011b) and Tritschler et al. (2014a). The issue of the initial conditions and reshock are considered further in Part II.

6.3. Lie group analysis

The intention of this subsection is to provide a more general self-similar description of self-similar mixing layers that is not dependent upon a particular mathematical model of the flow.

The more general approach is to exploit the underlying scaling groups that define the self-similarity. This latter method owes much to the work on Lie groups (Ibragimov, 1999; Olver, 1993), although the present use of this approach is greatly limited for utilitarian purposes (Clark and Zemach, 1995, 1998). It requires no detailed physical model, or governing equation, relying instead on the consequences of self-similarity of the functional forms. The underlying viewpoint is that the physical system acts dynamically upon an initial state, and under this dynamical action the system relaxes to an invariant state. By invariant state, we mean a state that is invariant under appropriate classes of subgroups of the full group of space-time symmetries.

The appropriate scaling group consisted of a simple time-scaling with time-translation

$$t' = \tau(t + t_0) - t_0 \quad (6.13)$$

and a simple scaling of length

$$L' = \xi L. \quad (6.14)$$

The existence of a virtual time origin, t_0 , is a statement of time-translation invariance – the behavior of the system should be independent of the absolute time of the “clock” used to measure the system. Self-similarity assumes

$$\xi h(t) = h(\tau(t + t_0) - t_0). \quad (6.15)$$

One anticipates that the solutions will be in terms of power laws (this may be deduced from a classical similarity analysis, and is also the generally accepted notion of the behavior of the RT and KH mixing layers). For this two-parameter group was restricted to a simple power-law subgroup,

$$\xi = \tau^\varsigma, \quad (6.16)$$

so

$$\tau^\varsigma h(t) = h(\tau(t + t_0) - t_0). \quad (6.17)$$

Differentiating with respect to τ yields

$$\varsigma \tau^{(\varsigma-1)} h(t) = \frac{dh(t)}{dt} (\tau(t + t_0)). \quad (6.18)$$

Now set $\tau = 1$ to give the determining equation

$$\varsigma h(t) = \frac{dh(t)}{dt} (t + t_0). \quad (6.19)$$

The solution of this ordinary differential equation is

$$h(t) = h_0 \left[\frac{t + t_0}{t_0} \right]^\varsigma. \quad (6.20)$$

For the RT mixing layer, [Clark and Zhou \(2003\)](#) required the acceleration, g (dimensions [length/time²]) be made invariant.

$$g' = g \frac{\xi}{\tau^2} = g \tau^{\varsigma-2}. \quad (6.21)$$

From this we see that $\varsigma - 2 = 0$ or $\varsigma = 2$ makes g invariant and gives a length-scale (for example the mixing layer width) that grows as t^2 .

The analysis also yielded the self-similar form of the length-scale which was found to be

$$h(t) = h_0 \left(\frac{t + t_0}{|t_0|} \right)^\theta \quad (6.22)$$

for RMI mixing layers ([Clark and Zhou, 2006](#)). Self-similarity of a physical law implies not only that the scaled functions of the unscaled arguments are equal to the unscaled functions of the scaled arguments, but also that physical parameters (e.g., viscosity, acceleration, etc.) scale onto themselves, that is, that the relevant dimensional parameters remain invariant. Thus the parameter θ may be determined by requiring the physical parameters of the problem be invariant.

For “permanent large eddies” assumption, the low wave number energy spectrum

$$\lim_{k \rightarrow 0} E(k, t) = e_0 k^m \quad (6.23)$$

where the value of e_0 is time independent constant during the decay process for any scaling exponent $2 \leq m \leq 4$ and has dimensions of length^{3+m}/time². Permanence of large-eddies (or equivalently, invariance of the infra-red spectrum of the energy) establishes a connection between θ and the low-wave-number power-law behavior of the spectrum ([Batchelor and Proudman, 1956; Saffman, 1967; Zhou, 2001; Clark and Zhou, 2006](#)). Specifically, the invariance of e_0 requires that

$$\tau^{\theta(3+m)-2} e_0 = e_0,$$

which has a solution for θ of

$$\theta = 2/(m+3). \quad (6.24)$$

[Eq. \(6.24\)](#) relates the value of θ to the energy spectrum in the large-scale eddies. It is interesting to discuss how this is related to similar scaling laws derived by other authors. [Youngs \(2004\)](#) and [Thornber et al. \(2010\)](#) give $\theta = 2/(\tilde{m} + 5)$ for an initial perturbation amplitude power spectrum $P(k) \propto k^{\tilde{m}}$.

Table 6.5

Linear growth rate for several instabilities having the form $n(k) \sim C_n k^{\tilde{r}}$. Here, $\Delta U = U_1 - U_2$, where U_i is the fluid velocity parallel to the interface. ΔV is the jump velocity normal to the interface induced by a shock.

Source: (Based on Table 1 of Mikaelian, 1989).

Instability type	C_n	\tilde{r}
Rayleigh–Taylor	\sqrt{gA}	1/2
Richtmyer–Meshkov	$A\Delta V$	1
Kelvin–Helmholtz	$\frac{\sqrt{\rho_1\rho_2}}{\rho_1+\rho_2} \Delta U $	1

An equivalent argument was given earlier by Inogamov (1999), p. 316

$$\theta = 1/(\tilde{\delta} + 1) \quad \text{where} \quad \frac{\text{amplitude}}{\text{wavelength}} = \frac{a}{\lambda} = k^{\tilde{\delta}}.$$

Inogamov did not reason in terms of spectra, so amplitude, a , needed to be related to the power spectrum. Dimonte (2004) uses

$$a^2 = \int_{k-\Delta k}^{k+\Delta k} P(k') dk' \quad (6.25)$$

and assumes $\Delta k \propto k$. This then implies $\tilde{\delta} = (\tilde{m} + 3)/2$ and gives the same results as Youngs (2004) and Thornber et al. (2010) above. Now for a single mode, the perturbed velocity is $u \sim kaA\Delta V$ and this implies $E(k) \sim k^{\tilde{m}+2}$ for an amplitude power spectrum $P(k) \propto k^{\tilde{m}}$. Therefore, the models of Inogamov (1999), Youngs (2004) and Thornber et al. (2010) are equivalent to Eq. (6.24) above. Note also that Thornber et al. (2010) calculated the $\tilde{m} = -2$ case and obtained θ close to 2/3 suggested by the model. This is the result quoted in Table 6.4.

6.4. Phenomenological theory and inertial range spectra

The scaling property of the width of the mixing region is appropriate for the nonlinear, late-time phase of the development of the RTI or RMI driven flows where bubble growth and merging leads to distinct blobs and bubbles. However, a more appropriate descriptor is required for the fully turbulent phase of the instability associated with the development of a broad spectrum of length scales. For a turbulent flow, two-point measurements are needed for a more complete statistical description of the flow. The energy spectrum provides the required two-point information and is the lowest order descriptor for a turbulent flow.

Mikaelian (1989) apply a model previous proposed by Canuto and Goldman (1985) to turbulence generated by the class of instabilities which have a power-law growth rate,

$$n(k) \sim C_n k^{\tilde{r}}. \quad (6.26)$$

A number of instabilities have growth rate of this form, examples of which are given in Table 6.5.

The basic result of the Canuto and Goldman model is

$$F \propto \frac{1}{k^2} \frac{d}{dk} \left\{ k \sqrt{n(k)} \int_{k_0}^k k \sqrt{n(k)} \frac{d}{dk} \left(\frac{n(k)}{k^2} \right) dk \right\}, \quad (6.27)$$

where k_0 is wavenumber corresponding to the largest eddy and $dE = F dk$ is the turbulent energy per unit mass in the interval between k and $k + dk$.

When the growth rate is given by Eq. (6.26), one finds

$$F \propto k^{2\tilde{r}-3} \left(\frac{2-\tilde{r}}{2-3\tilde{r}} \right) \left\{ \left(1 + \frac{\tilde{r}}{2} \right) \left(\frac{k_0}{k} \right)^{(3\tilde{r}/2)-1} - 2\tilde{r} \right\}. \quad (6.28)$$

Zhou (2001) argued that the extended Kolmogorov–Kraichnan phenomenology developed for turbulent flows with an external agent (Kolmogorov, 1941; Kraichnan, 1965) should also be applicable to these instabilities driven turbulent flows. In this framework, excitation in the energy-containing range does not affect energy transfer within the inertial range. Therefore, the average rate of energy dissipation is identified with the rate of spectral energy transfer and the rate of energy production (denoted here as ε). In order to infer the form of the inertial-range spectrum, it is necessary to estimate the magnitude of the transfer function correlations. The time scale for decay of transfer function correlations, τ_T , which is responsible for inducing turbulent spectral transfer, may depend on any relevant turbulence parameters. Turbulence theories indicate that the energy flux \tilde{P} is explicitly proportional to τ_T and depends on the wave number and on the power of the omnidirectional energy spectrum. In the inertial range, because energy is conserved by the nonlinear interaction and a local cascade has been assumed, the energy flux \tilde{P} becomes independent of the wave number k . A simple dimensional analysis leads to

$$\varepsilon = C_\tau^2 \tau_T(k) k^4 E^2(k) \quad (6.29)$$

where C_τ is a constant (Zhou and Matthaeus, 1990).

The well-known Kolmogorov spectrum can be recovered within this framework for homogeneous, isotropic, statistically steady turbulence. In this case, the energy-containing range excitation due to external agents is absent. Therefore, the local dynamical time scale is the only available time scale of homogeneous, isotropic, statistically steady turbulence. Hence, $\tau_T(k)$ equals to $\tau_{nl}(k) = [k^3 E(k)]^{-1/2}$. A direct substitution of $\tau_T(k) = \tau_{nl}(k)$ into (6.29) reproduces the Kolmogorov spectrum,

$$E(k) = C_K \varepsilon^{2/3} k^{-5/3}, \quad (6.30)$$

where C_K is the Kolmogorov constant (Kolmogorov, 1941; Saddoughi and Veeravalli, 1994; Yeung and Zhou, 1997).

The viewpoint of the extended phenomenology is that the lifetime of transfer function correlations τ_T is more accurately treated by considering the influences of both the external agent and turbulent nonlinear interactions. Here, the external time scale, τ_{EX} , represents any time scale other than the nonlinear cascade time scale. Matthaeus and Zhou (1989), Zhou (1995) and Zhou and Matthaeus (1990) have developed a framework in which both time scales, τ_{nl} and τ_{EX} , coexist, in a fashion analogous to the composition of triple decay times in the EDQNM closures (Pouquet et al., 1976)

$$\frac{1}{\tau_T} = \frac{1}{\tau_{nl}} + \frac{1}{\tau_{EX}} \quad (6.31)$$

where

$$\frac{1}{\tau_{EX}} = \frac{1}{\tau_{RT}} + \frac{1}{\tau_{RM}}. \quad (6.32)$$

For RTI driven flow, the time scale can be constructed from the external agent, g ,

$$\tau_{RT} = (kgA)^{-1/2}. \quad (6.33)$$

The external time scale associated with the RMI is

$$\tau_{RM} = (kA\Delta u)^{-1}. \quad (6.34)$$

Combining Eqs. (6.29) and (6.31), the extended energy spectrum is obtained. When τ_{EX} is much shorter than τ_{nl} , we should reproduce the external agent modified spectra “−7/4” (RTI driven turbulent flow) or “−3/2” spectrum (RMI driven turbulent flow). The inertial range of the RTI or RMI spectrum will exhibit a split spectrum that varies between the classical Kolmogorov spectrum ($m = -5/3$) at higher wave numbers and one with a modified slope at lower wave numbers.

$$E(k) = \begin{cases} k^m, & \text{for } k < k_Z \quad m = -\frac{7}{4} \text{ (RTI) or } -\frac{3}{2} \text{ (RMI)} \\ k^{-5/3}, & \text{for } k \geq k_Z \quad (\text{Kolmogorov}) \end{cases} \quad (6.35)$$

A controlling parameter, k_Z , indicates the extended range of influences exerted by the external agents in wave number space. It changes, in a reasonable quasi-steady state, from the state where turbulence is induced primarily by the instability to the state of fully developed turbulence with a broad spectrum of length scales (Zhou, 2001).

The inertial range must be sufficiently long to exhibit this split RTI energy spectra. Fig. 6.10 reproduced the density and velocity spectra of Cabot and Cook (2006) at the end of their simulation.⁵⁵ A fiducial line corresponding to Kolmogorov scaling is drawn for reference. The compensated 2D horizontal spectra are also shown in Fig. 6.11 (Cabot and Zhou, 2013) using the Kolmogorov scaling and the RTI scaling appropriate for the $m = -7/4$ range (DNS of 3072^3). In one case we use only the vertical components in the energy $E_{33}(k)$ normalized with vertical dissipation term ε_{33} ; and in the other case we sum over all velocity components, $E_{ii}(k)$, and normalize with the total dissipation rate ε . The slope of the vertical component alone is seen to be consistent with either a $k^{-5/3}$ Kolmogorov spectrum or the $k^{-7/4}$ spectrum proposed by Zhou for RTI flow. However, the narrowness of the inertial range and the level of noise in the numerical simulation data unfortunately make it difficult to distinguish clearly the small difference in slopes between these two scaling or to observe the predicted change in slopes.

More recently, Rao et al. (2017) study the variation of norms of even powers in the vorticity and density gradient, based on the DNS data provided by Livescu to the Johns Hopkins turbulence database, for a homogeneous buoyancy-driven flow calculation similar to that discussed by Livescu and Ristorcelli (2007). The statistically homogeneous form of these calculations allows the dynamics of buoyancy-driven turbulence, similar to that in the core of a RT mixing layer, to be studied independently of the spatial structure of such a region. Rao et al. (2017) show that the density gradients within the flows can reach extremely large values at intermediate times, the effect of which being that turbulence is driven by barotropic effects at small scales in such flows, exactly where it can most efficiently contribute to material mixing.

For RMI flow, Thorner et al. (2010) illustrated the fluctuating kinetic energy spectra with a narrow band initial perturbation at several time instants (Fig. 6.12). At early times the spectrum is peaked around the highest perturbation

⁵⁵ See a related work by Hazak et al. (2006).

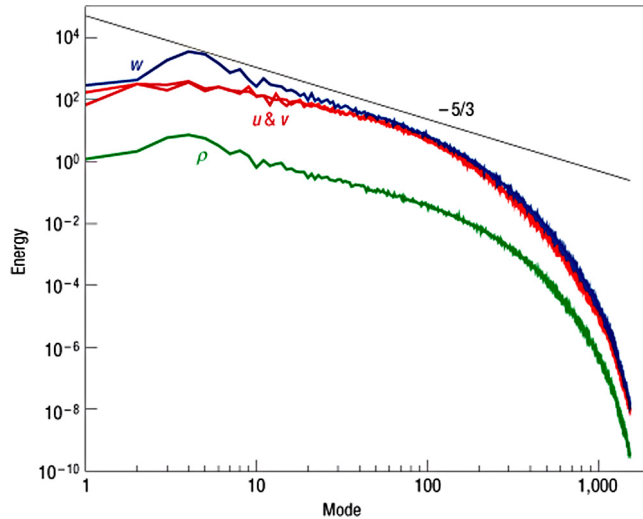


Fig. 6.10. Data are from the $z = 0$ plane. The RTI turbulent spectra are computed by taking two-dimensional Fourier transforms of density (ρ) and velocity components (u, v, w), multiplying by the complex conjugate and summing over each wavenumber annulus.
Source: From Fig. 2 of Cabot and Cook (2006), *Nature Physics*, with permission.

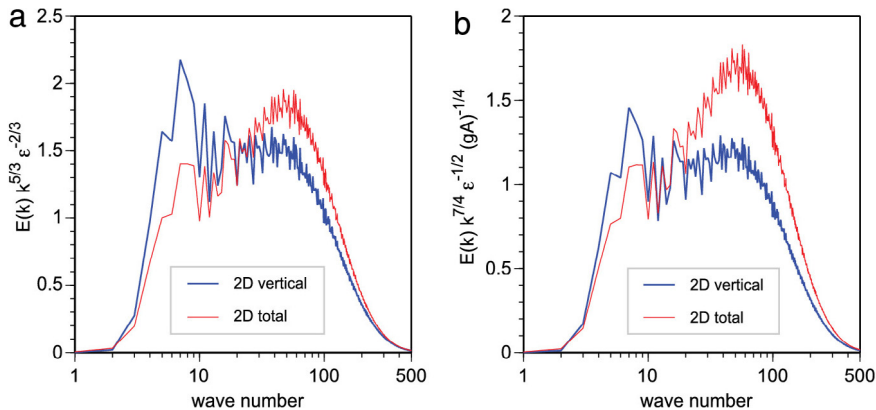


Fig. 6.11. Compensated 2D horizontal spectra for the vertical velocity component $E_{33}(k)$ (thick lines) and for the sum of all velocity components $E_{ii}(k)$ (thin lines) calculated near the midplane at $t = 25$ for the $A = 0.5$ case. In (a) the $k^{-5/3}$ Kolmogorov scaling is used, and in (b) the $k^{-7/4}RT$ scaling proposed by Zhou is used.

Source: Fig. 8 of Cabot and Zhou (2013), *Phys. Fluids*.

frequency k_{max} . By $\tau = 50$, a $k^{-5/3}$ inertial range appears (possibly only a transient toward a steady state spectrum); however, at later times a clear $k^{-3/2}$ inertial range of Zhou (2001) can be seen from $\tau = 100$ to $\tau = 500$. Tritschler et al. (2014a) used two independently developed and essentially different numerical methods to study the prediction uncertainties of RMI simulations. As shown in Fig. 6.13, a RMI modified $k^{-3/2}$ scaling of Zhou (2001) has also been observed.

Chertkov (2003) focused his phenomenological approach on the low Atwood number limit. At such case, the Boussinesq approximation might be appropriate.⁵⁶ The dynamics of the velocity field is coupled to the temperature field, T ,

$$\partial_t \mathbf{u} + \mathbf{u} \cdot \nabla \mathbf{u} = -\frac{1}{\rho_0} \nabla p + \nu \nabla^2 \mathbf{u} - \beta \mathbf{g} T \quad (6.36)$$

$$\partial_t T + \mathbf{u} \cdot \nabla T = \kappa \nabla^2 T \quad (6.37)$$

along with the incompressibility condition $\nabla \cdot \mathbf{u} = 0$. Here, β is the thermal expansion coefficient and ν and κ are the kinematic viscosity and molecular diffusivity, respectively.

⁵⁶ Mikaelian (2014b) showed that the Boussinesq approximation might be applied to high- A systems in certain regimes.

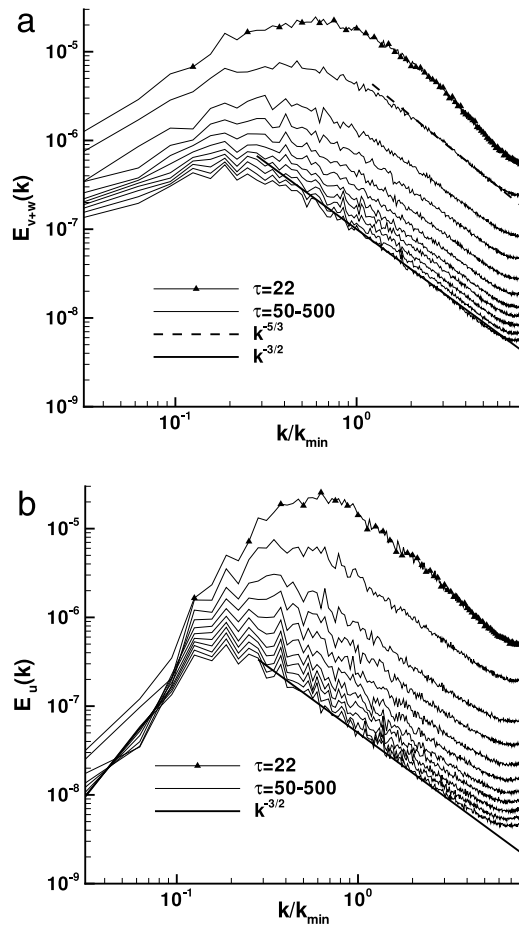


Fig. 6.12. Fluctuating radial energy spectra for the narrowband simulations for (a) the homogeneous components and (b) the inhomogeneous component.
Source: Adopted from Fig. 9, Thornber et al., *J. Fluid Mech.*, 2010 with permission.

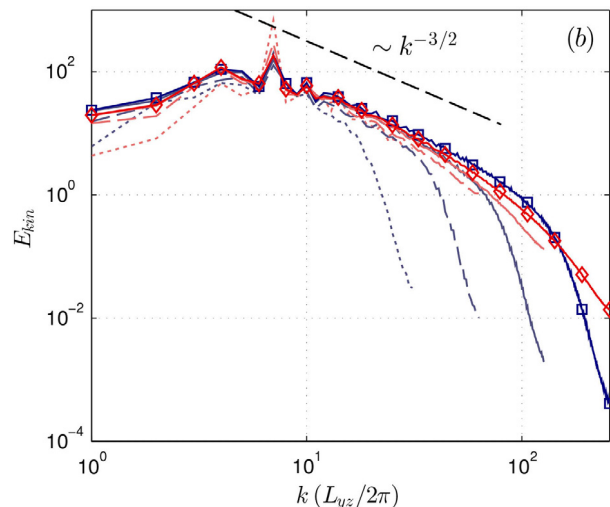


Fig. 6.13. Power spectra of density from Miranda code (Cook and Cabot, 2004) (dark gray; blue) and INCA code (Tritschler et al., 2013a, b) (light gray; red online) before reshock at $t = 2$ ms. The different resolutions are represented as dotted line (64), dashed line (128), solid line (256) and solid line with open squares for Miranda and open diamonds for INCA (512).
Source: Fig. 14b of Tritschler et al. (2014a, b), *J. Fluid Mech.* with permission.

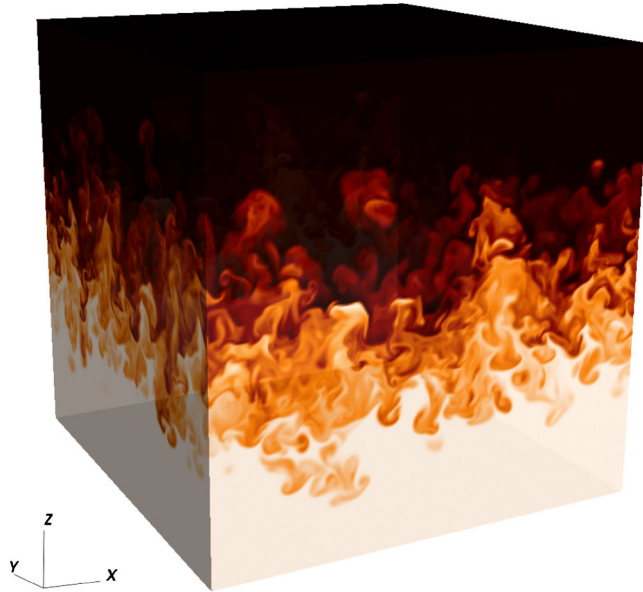


Fig. 6.14. Snapshot of temperature field for the RT simulation at $t = 2\tau$. White (black) regions correspond to hot (cold) fluid. Source: Fig. 1 of [Boffetta et al. \(2010\)](#), *Phys. Fluids*, with the permission of AIP Publishing.

[Chertkov \(2003\)](#) found a large-scale relation on the temporal behavior of L from the energy balance between the buoyancy term on the right-hand side of Eq. (6.36) and the temporal derivative term on the left-hand side.

$$\frac{u_L}{t} \sim \frac{L(t)}{t^2} \sim \beta g \Delta T, \quad (6.38)$$

where u_L is the typical velocity on the scale L and ΔT is the temperature jump. For the 3D case, one assumes that buoyancy force balances the inertia term at the integral scale at L . Hence, according to the Kolmogorov scaling

$$\delta u_r(t) \sim \delta u_L(t) \left(\frac{r}{L(t)} \right)^{1/3} \sim (\beta g \Delta T)^{2/3} r^{1/3} t^{1/3}. \quad (6.39)$$

As summarized neatly by [Boffetta et al. \(2010\)](#), the phenomenological theory proposed by Chertkov is based on the notion of adiabaticity where small scales are slaved to large ones. The latter is forced by conversion of potential energy into kinetic energy and the former undergoes a turbulence cascade flowing to smaller scales until molecular viscosity becomes important. In this picture, temperature actively forces hydrodynamic degrees of freedom at large scales, while it behaves like a passive scalar field at small scales where a constant kinetic-energy flux develops.

[Matsumoto \(2009\)](#) numerically studied three-dimensional RT incompressible turbulence with the Boussinesq approximation. At time $t = 0$ the system is at rest with cooler, heavier fluid placed above the hotter, lighter one. The Atwood number is set to 0.15 and the grid points is $256^2 \times 2048$. The focus of this work is on scaling properties of the moments of the density and the velocity differences. [Boffetta et al. \(2010\)](#) extend this mean-field analysis for velocity and temperature fluctuations to take into account intermittency, both in time and space domains (the grid points is $512^2 \times 2048$). A visualization of the temperature field is presented in Fig. 6.14.

It is interesting to compare and contrast the work of [Chertkov \(2003\)](#) and [Zhou \(2001\)](#) as they were constructed based on different approaches. First, both treatments resulted in the standard Kolmogorov $-5/3$ inertial scaling for high wavenumbers, but [Zhou \(2001\)](#) argued that one must expect the coexistence of a RTI or RMI modified inertial scaling. Second, while Zhou's treatment is applicable to both RTI- or RMI-driven flows, the phenomenological approach of [Chertkov \(2003\)](#) is restricted to RTI flows. For 3D RTI flows, [Chertkov \(2003\)](#) essentially assumes that the action of buoyancy forces would only provide the forcing to the classical Kolmogorov inertial range.

The effect of buoyancy forces in the production scales is a particularly important issue for RTI induced flows. With the Boussinesq approximation, [Boffetta et al. \(2009\)](#) reported that, at small scales, the contribution of buoyancy forces to the energy flux becomes much smaller than the contribution of the inertial non-linear forces. Motivated by this result, [Soulard and Griffond \(2012\)](#) applied the spectral equilibrium theory of [Ishihara et al. \(2002\)](#) to RT turbulence. Adapting the Monin-Yaglom relation ([Yaglom, 1949](#); [Monin and Yaglom, 1975](#)), [Soulard \(2012\)](#) concluded that the standard Kolmogorov theory should apply to Rayleigh-Taylor turbulence in the limit of a large Reynolds number, large times, and small scales.

[Poujade \(2006\)](#) argued, however, that self-similarity hypothesis together with equilibrium of spectral energy transfer with buoyancy at low wave numbers constrained velocity spectrum in a way incompatible with Kolmogorov mechanism.

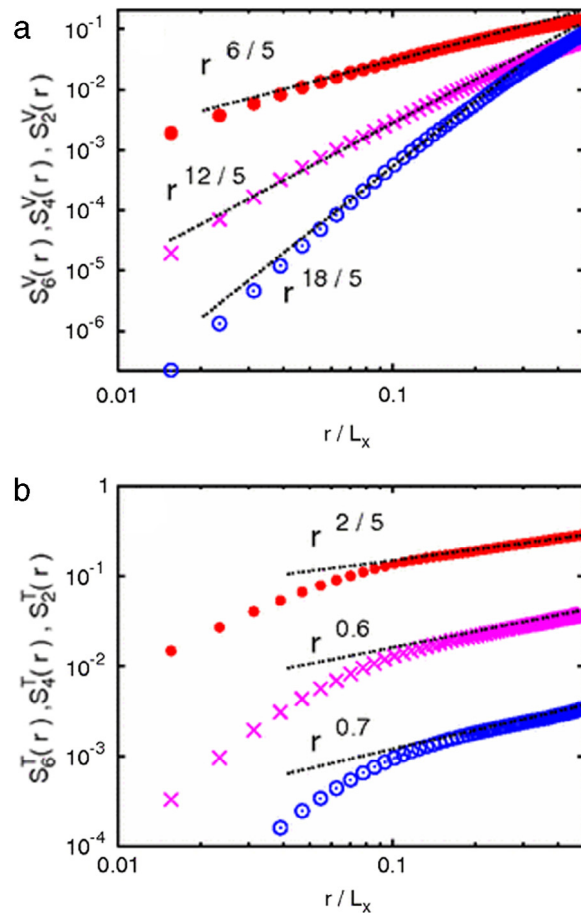


Fig. 6.15. The moment of longitudinal (a) velocity differences $S_n^V(r)$ and (b) temperature differences $S_n^T(r)$. The dashed lines are the Bolgiano dimensional predictions.

Source: Fig. 3 of Celani et al. (2006), Phys. Rev. Lett. with permission.

Instead, a -2 slope of the energy spectrum was proposed. Also, Abarzhi (2010a) suggested that based on dimensional grounds, the invariance of the rate of momentum loss (Abarzhi, 2010b; Abarzhi and Rosner, 2010) leads to -2 spectrum index for specific kinetic energy.

In 2D flows, the inverse cascade of energy requires a different scaling (Batchelor, 1969; Kraichnan, 1967; Leith, 1968; Kraichnan and Montgomery, 1980). Chertkov (2003) postulated that the buoyancy term injects energy at all scales, an assumption that received support from a high-resolution numerical study (Zhou, 2013; Qiu et al., 2014; Zhou, Huang, Lu, et al., 2016; Zhou and Jiang, 2016). Hence, the Bolgiano scaling (1959) resulted

$$\delta u_r(t) \sim \delta u_L(t) \left(\frac{r}{L(t)} \right)^{3/5} \sim (\beta g \Delta T)^{2/5} r^{3/5} t^{-1/5}. \quad (6.40)$$

Celani et al. (2006) numerically showed the scaling of the structure functions follow the Bolgiano scaling (Fig. 6.15). The resolution of their DNS is 128×4096 collocation points. The Bolgiano scaling is also observed using a thermal lattice Boltzmann scheme (Biferale et al., 2010) as well as by a DNS of Zhou (2013) with the number of grid points sets to $4096 \times 10\,000$ and 2048×8193 , respectively. Adjusting the aspect ratio of the simulations (Ngan et al., 2005; Celani et al., 2010; Boffetta et al. (2012) found that the system undergoes a dimensional transition from 3D to 2D, where the Bolgiano scale of the system was obtained.

6.5. Hydrodynamic scaling

High energy density physics (HEDP) platforms are effective facilities to study space and astrophysical systems of significant interest (Remington et al., 2000, 2006; Drake, 1999, 2006; Drake et al., 1998; Takabe, 2001; Takabe et al., 2008; Foster et al., 2005; Kuramitsu et al., 2009, 2011a,b, 2015; Zhong et al., 2010; Falize et al., 2012; Zhang et al., 2015; Cross et

al., 2016; Casey et al., 2017; Keiter et al., 2017; Young et al., 2017). Supernova evolutions and young supernova remnants (Müller et al., 1991) are often presented as the case studies (Drake et al., 2000, 2002; Kuranz et al., 2011; Robey et al., 2001; Malamud et al., 2013; Flraig et al., 2014). The hydrodynamics associated with these flows are extremely complex, with a great variety of physical processes occurring on very disparate spatial and temporal scales. In particular, the turbulent flow and mixing in observed astrophysical events such as supernovae are associated with very high outer scale Reynolds numbers ($Re \sim 10^{10}$, Ryutov et al., 1999).

In the laboratory setting, the spatial and temporal scales are, roughly speaking, in the range of tens of micrometers and tens of nanoseconds. These scales are 10 to 20 orders of magnitude less than those of real astrophysical events (Ryutov et al., 1999). The HEDP procedure frequently makes use of scaled astrophysical hydrodynamics from experiments performed on the HEDP platforms (Ryutov et al., 1999; Ryutov and Remington, 2002, 2003; Bouquet et al., 2010; Falize et al., 2009, 2011a,b,c; Cross et al., 2014). Such similarity scaling is a familiar tool widely used to study physics issues generally (Zeldovich and Raizer, 1966; Sedov, 1997) and receive special emphasis in plasma physics (see, for example, Connor and Taylor, 1977; Murakami and Iida, 2002).

The compressible Navier–Stokes equation anchors the appropriate governing system (Landau and Lifshitz, 1987)

$$\partial \rho \mathbf{u} / \partial t + \nabla \bullet (\rho \mathbf{u} \mathbf{u}) + \nabla p = \mu \nabla^2 \mathbf{u} \quad (6.41)$$

where \mathbf{u} is the fluid velocity, ρ is the density, p is the pressure, and $\mu \equiv \rho \nu$ is the viscosity (ν denotes the kinematic viscosity).

The density is given by the continuity equation,

$$\partial \rho / \partial t + \nabla \bullet (\rho \mathbf{u}) = 0 \quad (6.42)$$

and the pressure is determined by an entropy conservation equation for polytropic gas

$$\partial p / \partial t - \zeta \partial \rho / \partial t + \mathbf{u} \bullet \nabla p - \zeta p / \rho \mathbf{u} \bullet \nabla \rho = 0. \quad (6.43)$$

Note that ζ is an adiabatic index. Applying the Euler transformation described Ryutov et al.

$$\mathbf{r} = \hat{a} \mathbf{r}_1; \rho = \hat{b} \rho_1; p = \hat{c} p_1; t = \hat{a}(\hat{b}/\hat{c})^{1/2} t_1; \mathbf{u} = (\hat{c}/\hat{b})^{1/2} \mathbf{u}_1 \quad (6.44)$$

where $\hat{a}, \hat{b}, \hat{c}$ are positive numbers, it is easy to demonstrate that this Euler invariant breaks down for the Navier–Stokes equations, except when the following condition is satisfied for the viscous term

$$\nu = \hat{a}(\hat{b}\hat{c})^{1/2} \nu_1. \quad (6.45)$$

From the values collected from Ryutov et al. (1999), the scaling factor of Eq. (6.45) is found to be approximately 5.48×10^{12} . This should be compared to the viscosity scaling factor of 2.0×10^{11} , which one can derive using the parameters of SNe He plasma at 2000 s and corresponding Cu plasma in the experiment at 20 ns.

Instead of the Navier–Stokes equation, Ryutov et al. (1999) and Ryutov and Remington (2002) utilized the Euler equation

$$\rho(\partial \mathbf{u} / \partial t + \mathbf{u} \bullet \nabla \mathbf{u}) + \nabla p = 0 \quad (6.46)$$

and obtained the Euler similarity scaling (Eq. (6.44)). This assumes that the small-scale dynamics involved with the viscous (momentum diffusive) interactions can be neglected when the Reynolds number of the flows is high. Ryutov and Remington (2003) were aware of this important issue and have suggested several novel experiments to isolate the effect of the Reynolds number.

The Euler similarity has been now used as a standard procedure to make the HEDP experiments relevant (Robey et al., 2001; Drake et al., 2002; Kuranz et al., 2005, 2009a,b; Rosen et al., 2005; Hartigan et al., 2009; Casner et al., 2015b). As an example, the simulated interface velocity histories of the SN He–H interface computed using the astrophysical code PROMETHEUS9 are shown (Fig. 6.16) to compare well with that of a scaled laboratory experiment computed using the one-dimensional radiation-hydrodynamics code HYADES.3 (Kane et al., 1999; Remington et al., 2006).

The limitation to Euler scaling is that significant physical viscous features such as growth and dissipation of vorticity only develop when the full Navier–Stokes equation is applied. In particular, Euler scaling does not provide information on the specific size range of statistical dynamic flow structures that can be scaled accurately, an issue that will be considered in next subsection.

6.6. Minimum state and transition to turbulence

This subsection addresses the following questions for RTI and RMI induced flows. First, at what flow conditions can investigators be sure that their numerical simulations or physical experiments have reproduced all of the most influential physics of the flows and scalar fields? A second, perhaps more specific question is can one define a metric to indicate whether the necessary physics of the flows of interest have been captured and suitably resolved using the tools available to the researcher?

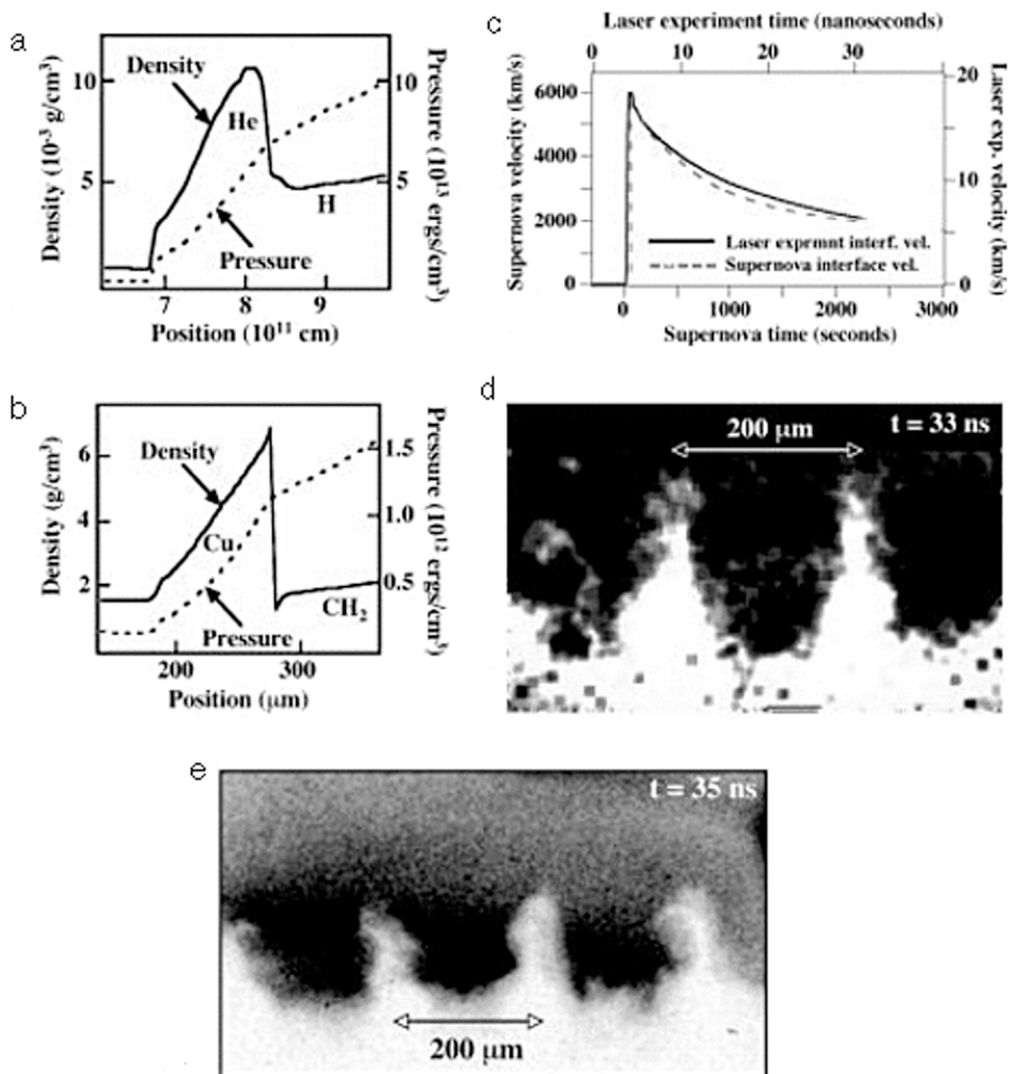


Fig. 6.16. Hydrodynamic simulations for the supernova and laboratory experiment (Remington et al., Rev. Mod. Phys., 2006, Fig. 9 with permission). (a) Spatial profiles of the pressure and the density for the SN at 2000 s, and (b) the laboratory experiment at 20 ns. (c) The velocity of the He-H interface in the supernova and in the scaled laser experiment. The curves are essentially identical, up to the scale transformation. See also, Ryutov et al. (1999) and Kane et al. (1999). (d) A radiograph obtained at $t = 33 \text{ ns}$ of the nonlinear RT induced mixing in the first scaled SNe experiment. Adapted from Remington et al. (1997). (e) A sum over multiple images from the same experiment as shown in (d), corresponding to an average time of $t_{\text{ave}} = 35 \text{ ns}$. Source: Adapted from Remington et al. (1999).

6.6.1. Spatial criterion

The mixing transition concept for stationary fluid flows refers to the transition to a turbulent state in which the flow drives rapid mixing at the molecular scale (Dimotakis, 2000). This turbulent state leads to rapid dissipation of momentum and of concentration fluctuations (mixing). The extent of the effective inertial range could be narrowed to

$$\lambda_K < \lambda_v \ll \lambda \ll \lambda_{LT} < \delta. \quad (6.47)$$

Here the lower-limit of the inertial range is the inner viscous scale $\lambda_v = 50\lambda_K$, where the Kolmogorov microscale can be rewritten as $\lambda_K = \delta Re^{-3/4}$. The upper-limit of the inertial range is the Liepmann-Taylor scale $\lambda_{LT} = 5\lambda_T$, where $\lambda_T = \delta Re^{-1/2}$ is the well known Taylor correlation microscale (Tennekes and Lumley, 1972).

To ensure the integrity of the physics of the large-scale dynamics of the flows of practical interest, the corresponding large-scale modes computed or measured in a simulation or a laboratory setting should not be contaminated because of their interaction with the dissipation range, which is not universal (Martinez et al., 1997). This requirement can be satisfied by maintaining a sufficiently broad inertial range. The required length of the inertial range needed can be deduced, for example, from our understanding of the interacting scales discussed in Zhou (1993a, b).

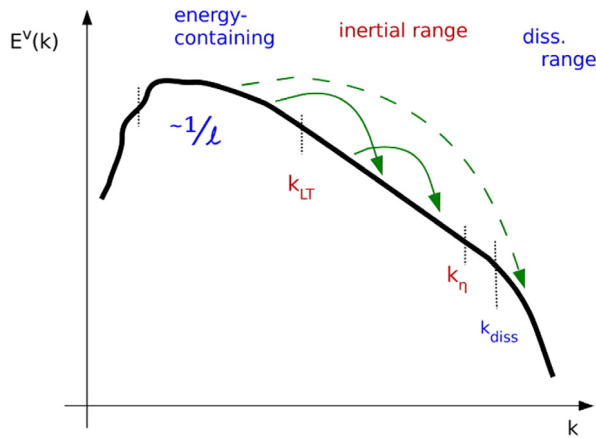


Fig. 6.17. Sketch of a kinetic energy spectrum indicating the energy-containing, inertial, and dissipation ranges and their wavenumber boundaries. Note that the inner-viscous wavenumber, k_ν , is denoted here as k_η . The idea behind the minimum state is that the inertial range should be long enough so that direct interactions between modes in the energy-containing and dissipation ranges are energetically weak, indicated by the dashed (green) arrow. Some “strong” interactions are indicated via the solid (green) arrows.

Source: (Zhou and Oughton, Fig. 1)

The *minimum state* is defined as the turbulent flow which has the *lowest* Reynolds number that captures the energy containing scales of the astrophysics problems in a laboratory or simulation setting (Zhou et al., 2003a,b; Zhou, 2007; Zhou et al., 2009). The *minimum state* is therefore the lowest Reynolds number turbulent flow where all the modes in the energy containing scales will only interact with modes in the same spectral range or those within the inertial range. Obviously, this requirement is introduced to take full advantage of the universality of the inertial range.

The *minimum state*, according to the interacting scale analysis, is the turbulent flow that takes the value of $k^*_Z \equiv 2k^*_{LT}$ equal to the inner-viscous wavenumber, k_ν (the end of the inertial range, see Fig. 6.17). Using the definition of k_{LT} and k_ν , one finds that the *critical* Reynolds number of the *minimum state* is (Zhou, 2007)

$$Re^* = 1.6 \times 10^5. \quad (6.48)$$

The outer-scale Reynolds number is approximately related to the Taylor microscale Reynolds number by $R_\lambda = (20/3)^{1/2} Re^{1/2}$ in isotropic flow (Tennekes and Lumley, 1972) and $R_\lambda \approx 1.4 Re^{1/2}$ for turbulence in the far field of jet (Dowling and Dimotakis, 1990; Miller and Dimotakis, 1991). As a result, the corresponding *critical* Taylor-microscale Reynolds number of the *minimum state* is $R_\lambda^* \approx 1.4 \times Re^{1/2}$ ($R_\lambda^* \approx 560$).

Fig. 6.18 provides another way to illustrate this argument using the variation of the physical length scales with Reynolds number. The Reynolds numbers where an inertial range first occurs (mixing transition of Dimotakis, 2000 and the “minimum state” of Zhou, 2007, Zhou et al. 2003a,b, 2009) can be located for a simulated RTI flow. Any high Reynolds number flow may be scaled down to a very high, but computationally achievable Reynolds number flow.

6.6.2. Temporal criterion

Many experiments have been conducted in classical fluid dynamics facilities, shock tubes, and laser facilities (such as the Omega laser and National Ignition Facility) to understand the complex flows induced by various instabilities. Yet, it is only after a finite period of time, that perturbations initiated by instability mechanisms can give rise to a turbulent spectrum (Zhou, 2007). In strongly accelerated flows, this time scale for the onset of turbulence can be comparable to the duration of the flow itself (Robey et al., 2003; Zhou et al., 2003a,b).

Due to diagnostic limitations, typical measurements consist solely of the growth of the mixing zone width. While these widths (of the bubble and spike fronts, individually or combined) are usually measured, it is difficult to know whether an experiment has reached the state of fully developed turbulence. The so-called Zhou-Robey hypothesis (Zhou et al., 2003a,b, 2009; Robey et al., 2003; Zhou, 2007) has been advanced as a temporal criterion for the onset of turbulence (Drake et al., 2008). Here, the Liepmann-Taylor scale essentially describes the internal laminar vorticity growth layer generated by viscous shear along the boundaries of a large-scale feature of size δ . The temporal development of such a laminar viscous layer is well known to go as $(vt)^{1/2}$ (Stokes, 1851; Lamb, 1932).

$$\lambda_D = C_D(vt)^{1/2}. \quad (6.49)$$

Hence, the upper bound of the developing inertial range is the smaller of the Liepmann-Taylor scale, λ_{LT} and λ_D . The coefficient of the diffusion layer, C_D , was suggested as $\sqrt{15}$ both for isotropic, homogeneous turbulence (Tennekes and Lumley, 1972) and for steady parallel flows, and as 5 for laminar boundary layer flows (Dimotakis, 2000). The length scales discussed in this section have been summarized in Table 6.6.

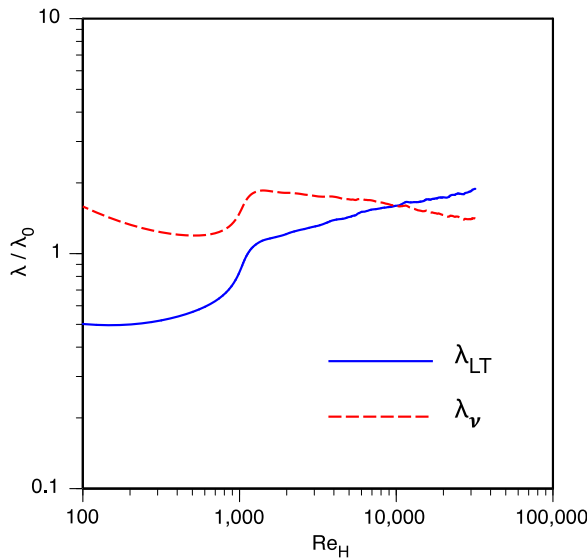


Fig. 6.18. Length scale vs outer scale Reynolds number from a RTI simulation. It should be noted that in a RTI induced flow, the length scale grows with time or Re . This is an illustration of the mixing transition of Dimotakis (2000) and the minimum state of Zhou et al. (2003a, b) and Zhou (2007). Data from DNS discussed in Cabot and Zhou (2013).

Table 6.6

Nomenclature of all relevant length scales.

Source: Table II of (Zhou, 2007).

Length scale	δ	λ_K	λ_{LT}	λ_v	λ_z	λ_c	λ_d
Wave number ($2\pi/\text{length}$)	k_δ	k_K	k_{LT}	k_v	k_z	k_c	k_d
Note and remarks	The outer scale	The Kolmogorov length scale	The Liepmann–Taylor length scale	The inner-viscous length scale	The smallest physical scale beyond which the energy-containing scale will not interact directly. It is defined as $\lambda_{LT}/2$	The length scale that separates the resolvable and subgrid scales	The diffusion layer scale
(The remarks on this row will be based on the physical length scales)	This is the largest scale of the flow	The viscous actions dominate at the smallest length scales	This is the upper boundary of the inertial range. This length scale separates the energy-containing and inertial ranges	This is the lower boundary of the inertial range. This length scale separates the inertial and dissipation ranges	The minimum state theory demands it resides within the inertial range	This is the smallest physical length scale that the diagnostic instruments or numerical schemes can be resolved	The temporal development of a laminar viscous layer is known to go as \sqrt{vt}
			Note that the minimum state requires that the energy-containing scale, $[\lambda_{LT}, \Delta]$, is resolved	Note that $2\lambda_v$ is the finest length scale needed for diagnostics			

The inertial range is presumed to be established when the evolution of the large-scale, $\min \{\lambda_{LT}, \lambda_d\}$, is decoupled from the inner viscous scale, λ_v . For time-dependent flows, the mixing transition is achieved when a range of scales exists such

that the temporally evolving upper bound [$\min\{\lambda_{LT}(t), \lambda_D(t)\}$] is significantly larger than the temporally evolving lower bound, $\lambda_v(t)$. Thus, the *minimum state* is achieved if the inequality

$$\min\{\lambda_{LT}(t), \lambda_D(t)\} > \lambda_v(t) \equiv 50\lambda_K(t) \quad (6.50)$$

is satisfied (Zhou, 2007).

Achieving the *minimum state* is a highly desirable goal for high energy density physics (HEDP) experimentalists when designing and developing their investigations (for example, Di Stefano et al., 2012; Drake et al., 2008; Doss et al., 2013; Haines, 2015; Haines et al., 2013a,b; Hurricane et al., 2009, 2012; Rosen et al., 2005; Welser-Sherrill et al., 2013; Merritt et al., 2015). The Reynolds number of the minimum state appears achievable already for some of the most advanced experimental platforms by optimizing the maximum potential of existing experimental facilities.

6.7. Numerical turbulence

As a brief aside, we note a couple of issues regarding numerical simulations of these hydrodynamic instability induced flows. Results from these simulations will be discussed later. As noted by Moin and Mahesh (1998), the wide range of scales in turbulent flows requires that care must be taken in their numerical solution. Over the past three decades, direct numerical simulations (DNS) has emerged as an accepted surrogate for experiment when detailed information is not readily measured in the laboratory. The benefit of a DNS is that the calculation can faithfully resolve all the scales that can be handled by the computational resource allocated to the researcher (Rogallo and Moin, 1984; Moin and Mahesh, 1998). DNS has proven capable of following the three phases of turbulent mixing identified by Eckart (1948), i.e., entrainment, stirring, and molecular mixing. DNS also provides a complete, three-dimensional, time-dependent description of the flow field. As an example, Youngs (2017) noted that the early stages of the mixing process are influenced by viscosity and diffusivity and DNS is essential for understanding the influence of Reynolds number and Schmidt number on the mixing process. For quantities such as enstrophy, which are determined by the small scales present in the flow, DNS is required to get meaningful results (probably with higher resolution or with higher order numerics being required to obtain accurate results). Also, Mueschke and Schilling (2009b) obtained from the DNS several quantities not measured in the experiment, such as the integral- and Taylor-scale Reynolds numbers, Reynolds stress and dissipation anisotropy, two-dimensional density and velocity variance spectra, hypothetical chemical product formation measures, other local and global mixing parameters, and the composition of mixed fluid.⁵⁷

It should be stressed, however, that the Reynolds numbers of the flows for the problems of interest are extremely high and still beyond the current capabilities of the supercomputers. Fortunately, the problem of the turbulent flow mixing at very high Reynolds number has been tackled successfully using large-eddy simulation methods (LES). The work by Cook et al. (2004) showed that the essential results for large-scale properties are very consistent between a DNS and an LES for RTI-induced turbulent flow. In LES, the large scales of the flow field are resolved, while the unresolvable scales are represented by the subgrid models (see for example, Sagaut, 2006) or by numerical methods in an implicit fashion (implicit LES or ILES, see for example, Boris et al., 1992; Grinstein et al., 2007). A crucial practical aspect of LES computations is the need to distinctly separate the effects of spatial filtering and subgrid-scale reconstruction models from their unavoidable implicit counterparts due to discretization. Indeed, it has been noted (Hirt, 1969; Ghosal, 1996) that in typical LES strategies truncation terms due to discretization and filtering (Zhou et al., 1989a; Domaradzki and Adams, 2002) have contributions directly comparable with those of the explicit models. Seeking to address the seemingly insurmountable issues posed to LES by under-resolution, the possibility of using the subgrid-scale (SGS) modeling and filtering provided implicitly by the numerics has been considered as an option generally denoted as *numerical LES* by Pope (2004). Arbitrary numerics will not work for LES: *good or bad* SGS physics can be built into the simulation model depending on the choice of numerics and its particular implementation (Boris et al., 1992; Drikakis and Tsangaris, 1993; Grinstein et al., 2007; Margolin and Rider, 2002, 2005; Hickel et al., 2006).

Recently, ILES have emerged as an effective approach for calculating high Reynolds number flows frequently encountered in scientific and engineering applications (Drikakis, 2003; Drikakis et al., 2005; Grinstein et al., 2012; Fureby and Grinstein, 2002; Grinstein, 2016). The numerical methods used for ILES were specifically devised for the accurate simulation of flows with contact discontinuities and shocks – key aspects of the RT and RM mixing processes. Youngs (1991) was the first application of ILES to RTI induced flows (TURMOIL code) and one of the first ILES papers. Recently, he showed comparisons of DNS and ILES using the same computational framework for four test cases: (i) single-mode RTI, (ii) self-similar RT mixing, (iii) three-layer mixing and (iv) a tilted-rig RT experiment. It has been demonstrated that, provided the mesh resolution is sufficient to resolve fine-scale structure within the mixing zone, ILES and DNS give very similar results. This applies to quantities such as distributions mean volume fractions, molecular mixing parameter or turbulence kinetic energy (Youngs, 2017).

⁵⁷ DNS could also offer helpful information for developing mix models (Part II). For example, the budgets of the mean vertical momentum, heavy-fluid mass fraction, turbulent kinetic energy, turbulent kinetic energy dissipation rate, heavy-fluid mass fraction variance, and heavy-fluid mass fraction variance dissipation rate equations were constructed using Reynolds averaging applied to the DNS data (Schilling and Mueschke, 2010). The relative importance of mean and turbulent production, turbulent dissipation and destruction, and turbulent transport were investigated as a function of Reynolds number and across the mixing layer to provide insight into the flow dynamics not presently available from experiments.

It is a challenge, however, to estimate the Reynolds number (Re) of the flows because the subgrid scale modeling is only provided implicitly by the numerics. A method for estimating numerical dissipation in LES was proposed based on using the energy flux from large, resolved scales as the numerical dissipation estimate (Zhou et al., 2014) and related the inertial range scaling (Zhou and Thornber, 2016). A number of models have also been suggested for estimating the effective viscosity (Domaradzki et al., 2003; Fureby and Grinstein, 1999; Margolin et al., 2002; Domaradzki and Radhakrishnan, 2005; Aspden et al., 2008b; Olson and Greenough, 2014; Castiglioni and Domaradzki, 2015; Schranner et al., 2015) and the reader is referred to their publications for details.

Clearly, the ILES has been very useful in understanding aspects of the RTI and RMI induced flows. Yet, many physical subgrid models have been developed for large-eddy simulations for applied and engineering flows (for a summary, see Sagaut, 2006). For the RTI flows, Amala and Rodrigue (1994a, b) and Amala (1995) performed large-eddy simulations including a combined subgrid model: a modified Smagorinsky (1963) eddy viscosity and a stochastic backscatter (Leith, 1990; Zhou, 1991). Burton (2011) computed RTI flows using his nonlinear large-eddy simulation (nLES) method (Burton, 2008, see also, Rasthofer et al., 2014a,b). He demonstrated the utility of a convective subgrid model with a deterministic backscatter limiter, which applies neither an eddy-viscosity or other artificial dissipation, in calculating ultrahigh Atwood numbers RTI flows. His results indicated that method may remain accurate for Atwood numbers beyond $A = 0.96$, the highest test in that study. Wang and Li (2005) and Wang et al. (2002) also performed 3D LES of RTI induced flows. Here, representation of the subgrid scale flux is given by a simple eddy viscosity coefficient and a dynamical equation for the subgrid scale turbulence intensity (Deardorff, 1980). Darlington et al. (2002) applied a single equation LES to Arbitrary Lagrangian–Eulerian (ALE) (Hirt et al., 1974) simulations of RTI (Darlington et al., 2001) and investigates its effects.⁵⁸

Also, LES simulations have provided detailed analysis of the three-dimensional planar RMI flows with reshock (Hill et al., 2006; Lombardini et al., 2011) and turbulent mixing driven by spherical implosions (Lombardini et al., 2014a,b). These LES utilized the stretched-vortex subgrid-scale model developed by Misra and Pullin (1997). On the other hand, Bai et al. (2010, 2012a, b) and Wang et al. (2016) have carried LES of RMI induced flows with reshock, but with the subgrid model proposed by Vreman (2004). Recently, Wang et al. (2015) have compared and contrasted the performance of the dynamic Smagorinsky model (Germano et al., 1991), the stretched-vortex model (Misra and Pullin, 1997; Pullin, 2000), as well as the approach advanced by Vreman (2004).

The hyperviscosity has been shown as a very effective method for a LES to avoid wasting numerical resolution by reducing the range of scales over which dissipation is effective (Schumann, 1975; McWilliams, 1984; Holloway, 1992; Borue and Orszag, 1995a, b; Haugen and Brandenburg, 2004). Essentially, the normal Laplacian dissipation is replaced by a higher power one (Frisch et al., 2008) so that the fluid transport coefficient is altered to provide the sharpest possible cutoff near the Nyquist wavenumber. For a RTI induced flow, Cook et al. (2004) confirmed that the LES converges to DNS at low Schmidt and Reynolds numbers. In this case, a DNS was first carried out for a case very similar to that described in Cook and Zhou (2002), i.e. $A = 0.5$ with isotropic perturbations peaked at mode 16. An accompanying LES was subsequently performed with a set-up identical to the DNS, but with the filter and hyperviscosity SGS models active. Based on visual inspection, the flows appear identical; illustrating that convergence is achieved (Fig. 3 of Cook et al. 2004, not shown).

This hyperviscosity scheme has been successfully adopted as a computational approach for modeling shock and turbulence interactions (Cook and Cabot, 2004, 2005; Fiorina and Lele, 2007). Moreover, Cook (2007) has extended this work to include hyperconductivity for contact discontinuities and hyperdiffusivity for material interfaces. His models are based on the idea that artificial viscosity/diffusivity should impart a high-wavenumber bias to the dissipation and therefore approximate the cusp in the closure theories based spectral viscosity. In so-called artificial-fluid large-eddy simulation (AFLES) technique, the grid-dependent components are added to the transport coefficients of the equations governing the compressible flows comprised of several miscible fluids. More recently, Williams (2017) derived an artificial viscous stress terms for finite difference hydrodynamics codes based on the LES technique for the modeling of turbulent flows.

It is helpful to recall that the statistical closure theories are the first to demonstrate that the eddy spectral viscosity should exhibit the following wave number (k) characteristics: (i) as $k \rightarrow 0$, it should asymptotically approach a constant, while (ii) as $k \rightarrow k_c$, where k_c is the cutoff wavenumber, it should exhibit a strong cusp (Kraichnan, 1976; Chollet and Lesieur, 1981; Zhou et al., 1988, 1989b, 2002; Schilling and Zhou, 2002; Frederiksen et al., 1996). The cusp like behavior is also confirmed with data from the simulated numerical datasets (Domaradzki et al., 1987; Zhou and Vahala, 1993).

Cook (2009) pointed out that, regardless of methodology ILES, DNS, LES, or RANS, the enthalpy diffusion plays a critical role in multicomponent flow simulations whenever differences in molecular weights are large. The enthalpy diffusion flux in the multicomponent energy equation accounts for energy changes associated with compositional changes resulting from species diffusion. The enthalpy diffusion also enhances the acoustic field of mixing layers. As an example, he showed that large gradients are observed in the RTI simulation neglecting the enthalpy diffusion term (Fig. 7 of Cook, 2009, not shown). He also demonstrated that in the simulation with enthalpy diffusion, the temperature varies by less than $5.2 \cdot 10^{-3}$ eV; whereas, in the simulation without enthalpy diffusion, the temperature ranges from 0.5 to 2 eV (see Fig. 6.19). Therefore, the term prevents local violations of the entropy condition in flows where significant mixing occurs between species of dissimilar molecular weight. The term is furthermore responsible for smoothing density gradients in diffusion regions by indirectly causing local dilatations of the velocity field.

⁵⁸ Andronov et al. (1995) is an excellent reference in English that discussed the Lagrangian–Eulerian methods implanted within the EGAK code (Yanilkin et al., 1993; Darova et al., 1994).

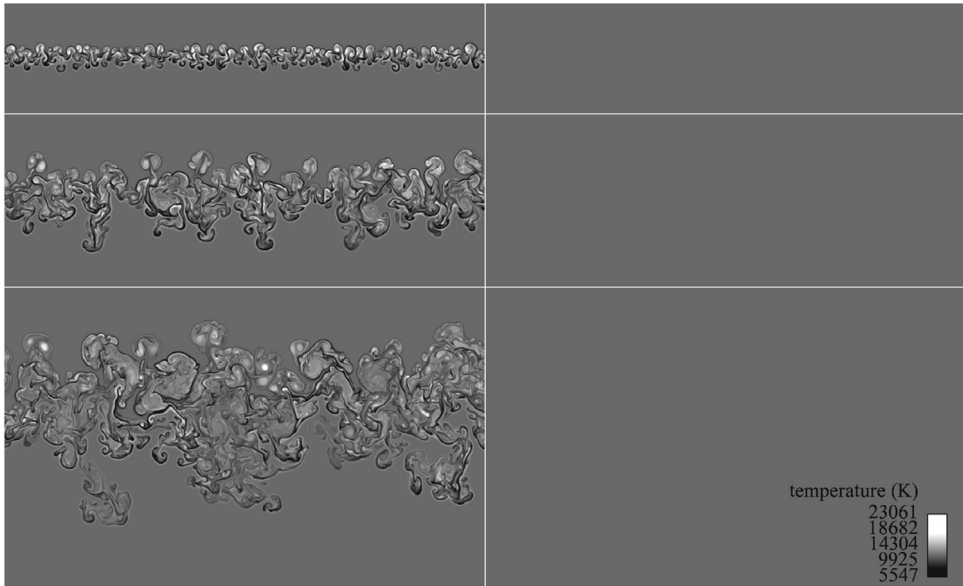


Fig. 6.19. Temperature at 20 (top), 40 (middle), and 60 (bottom) ms from Rayleigh–Taylor simulations neglecting (left) and including (right) enthalpy diffusion.

Source: Fig. 8 of Cook (2009), *Phys. Fluids*, with the permission of AIP Publishing.

7. Energy injection and transfer process

Almost all turbulence theories and models rely on assumptions about the energy transfer process. In order to improve the performance of the models, one needs to understand how the energy is produced, transferred, and dissipated in an instability-induced flow.

7.1. The nature of the energy injection in RTI

There is negligible kinetic energy (KE) associated with velocity fluctuations at the initial state of the flow. The potential energy (PE) is converted into kinetic energy in the RTI induced flow. From their experimental measurements, Ramaprabhu and Andrews (2004) determined the ratio of KE/PE is 0.51, which is almost identical with that of three-dimensional ILES, 0.52 (Youngs, 1991, 1994). Youngs (2013) showed KE/PE increasing up to ~ 0.75 if long wavelength initial perturbations are added to give self-similar growth at an enhanced rate. In the LES of Cook et al. (2004) and DNS of Cabot and Cook (2006), the KE/PE ratio has reached a value of 0.50 with a fairly shallow rise, but has not quite come into balance at the end of the runs.

This is a good point to clarify the issue of conservation of energy in numerical simulations. The governing equation for the kinetic energy budget (Cabot and Cook, 2006) reads,

$$\frac{dK}{dt} = - \int_V \rho g u_3 dV - \int_V \tau_{ij} \frac{\partial u_i}{\partial x_j} dV. \quad (7.1)$$

The energy input is provided by the release of the potential energy, through the acceleration (g) in the first term on the right-hand side of above equation. The dissipation is given in the second term on the right-hand side,

$$\tau_{ij} \frac{\partial u_i}{\partial x_j} = 2\rho\nu S_{ij}S_{ij} = \rho\varepsilon. \quad (7.2)$$

Here, μ is the dynamical viscosity, ε is the dissipation rate, S_{ij} is the symmetric strain-rate tensor and τ_{ij} denotes the viscous stress tensor,

$$\tau_{ij} = 2\mu \left(S_{ij} - \frac{1}{3}\delta_{ij} \frac{\partial u_k}{\partial x_k} \right),$$

$$S_{ij} = \frac{1}{2} \left(\frac{\partial u_i}{\partial x_j} + \frac{\partial u_j}{\partial x_i} \right).$$

Nevertheless, for incompressible Navier–Stokes solvers, the heat generated by the dissipation term is not tracked, as these codes do not have an internal energy equation. Note also that the DNS has a real dissipation term with a physical viscosity, ν .

This should be compared to the KE/PE obtained from ILES computations, such as that of [Youngs \(1991\)](#), where the dissipation is provided by the numerics.

[Fig. 7.1](#) shows the snapshots of density field evolution from DNS of RTI ([Cabot and Cook, 2006](#); [Cabot and Zhou, 2013](#)). The flows were initialized with a stationary interface between the high and low-density fluids whose vertical position was perturbed with random variations having a characteristic horizontal wavelength λ_0 , which act to seed the instability. The simulations proceeded until the mixing layer filled 60%–70% of the domain in the vertical direction. The $A = 0.5(\rho_2/\rho_1 = 3)$ simulation used 3072^3 grid points.⁵⁹

To fully address the anisotropy of RTI induced flows (see Part II), detailed spectral information on the energy injection can be extremely helpful. [Cabot and Zhou \(2013\)](#) investigated several key statistical measurements of turbulence induced by RTI using data from well resolved numerical simulations at moderate Reynolds number with the goal of determining the degree of departure of this inhomogeneous flow from that of homogeneous, isotropic turbulence ([Ishihara et al., 2008](#); [Kaneda et al., 2003](#); [Yeung and Zhou, 1997](#)). The vertical and horizontal kinetic energy equations can be used to illustrate (horizontal) scale distribution ([Cabot and Zhou, 2013](#)),

$$\begin{aligned} \left(\frac{1}{2} \rho u_3^2 \right)_{,t} + \left(\frac{1}{2} \rho u_3^2 u_j - u_3 \tau_{3j} \right)_j &= \rho u_3 g - u_3 p_{,3} - u_{3,j} \tau_{3j}, \\ \left(\frac{1}{2} \rho u_i^2 \right)_{,t} + \left(\frac{1}{2} \rho u_i^2 u_j - u_i \tau_{ij} \right)_j &= -u_i p_{,i} - u_{i,j} \tau_{ij} \end{aligned} \quad (7.3)$$

whose global averages, denoted by angle brackets, are given by

$$\begin{aligned} \left\langle \frac{1}{2} \rho u_3^2 \right\rangle_{,t} &= +\langle \rho u_3 \rangle g - \langle -p u_{3,3} \rangle - \langle u_{3,j} \tau_{3j} \rangle \equiv +\mathcal{P}_b - \Pi_z - \varepsilon_3 \\ \left\langle \frac{1}{2} \rho u_i^2 \right\rangle_{,t} &= +\langle \rho u_{i,i} \rangle - \langle u_{i,j} \tau_{ij} \rangle \equiv +\Pi_h - \varepsilon_h \end{aligned} \quad (7.4)$$

where g is the buoyancy production term, and the index i is summed over only x and y in (7.3) and (7.4). (Note that ε_3 and ε_h here are volume-specific dissipation rates.) We have also used $(\cdot)_{,i} \equiv \partial(\cdot)/\partial x_i$ and $(\cdot)_{,t} \equiv \partial(\cdot)/\partial t$. Buoyancy production, pressure-strain, and dissipation terms appear on the right-hand sides of (7.3) and (7.4) with + and – signs to indicate if they are sources or sinks.

[Fig. 7.2](#) shows the two-dimensional horizontal spectra calculated near the midplane using their constituent terms. Because the flow is nearly incompressible at late times, the pressure-strain terms nearly balance, i.e., $\Pi_h \approx \Pi_z$. The vertical component is forced at the largest scales by buoyancy production (\mathcal{P}_b). The horizontal scales, on the other hand, have energy injected at intermediate scales via the pressure-strain (Π_h) at the expense of the vertical kinetic energy ($-\Pi_z$).

7.2. The vorticity and energy deposited for RMI

The RMI induced mixing will begin when the vorticity is initially deposited and then spread throughout the layer ([Zabusky, 1999](#); [Brouillette, 2002](#)). The pressure perturbations across the interface can also be directly related to the vorticity initially deposited by the shock interaction (e.g., [Fraley, 1986](#)). The RMI evolution can be characterized by the inviscid compressible vorticity equation

$$\frac{D\boldsymbol{\omega}}{Dt} = \underbrace{\frac{\nabla \rho \times \nabla p}{\rho^2}}_{\text{baroclinic production}} + \underbrace{\boldsymbol{\omega} \cdot \underbrace{\nabla \mathbf{u}}_{\text{vortex stretching}}}_{\text{vortex}} - \underbrace{\boldsymbol{\omega} (\nabla \cdot \mathbf{u})}_{\text{dilatation}}, \quad (7.5)$$

where the physical mechanism of the terms are identified. The baroclinic torque vorticity production term is a driver of RMI resulted from a misalignment of the pressure and density gradients. Vortex stretching term only exists in 3D, but absent in 2D flows since the velocity vector is everywhere normal to vorticity vector.

The initial vorticity deposition of RMI could also be inspected experimentally, using an early post-shock image and a model (Eq. (15) of [Weber et al., 2012](#)).⁶⁰ A new type of broadband initial condition for RMI induced flows has been generated at Wisconsin vertical shock tube (see [Fig. 7.3](#)) described by [Anderson et al. \(2000\)](#). After setting up a gravitationally stable stagnation plane between the gases, the same two gases would then be injected horizontally at the interface to create a shear layer ([Weber et al., 2012](#)). The perturbations along the shear layer create a statistically repeatable broadband initial

⁵⁹ [Kamath et al. \(2009\)](#) described how one could use image-processing techniques to identify and count coherent structures for such terabyte-sized data sets.

⁶⁰ [Picone et al. \(1985, 1986\)](#) proposed a nonlinear model on vorticity created by shock-interface interactions. The vorticity generation is not equal to zero in this model when there is an initial perturbation ([Houas et al., 1988](#)). [Samtaney and Zabusky \(1998\)](#) obtained analytical results for the baroclinic circulation generation on simple 2D (sinusoidal and oblique-planar) interfaces.

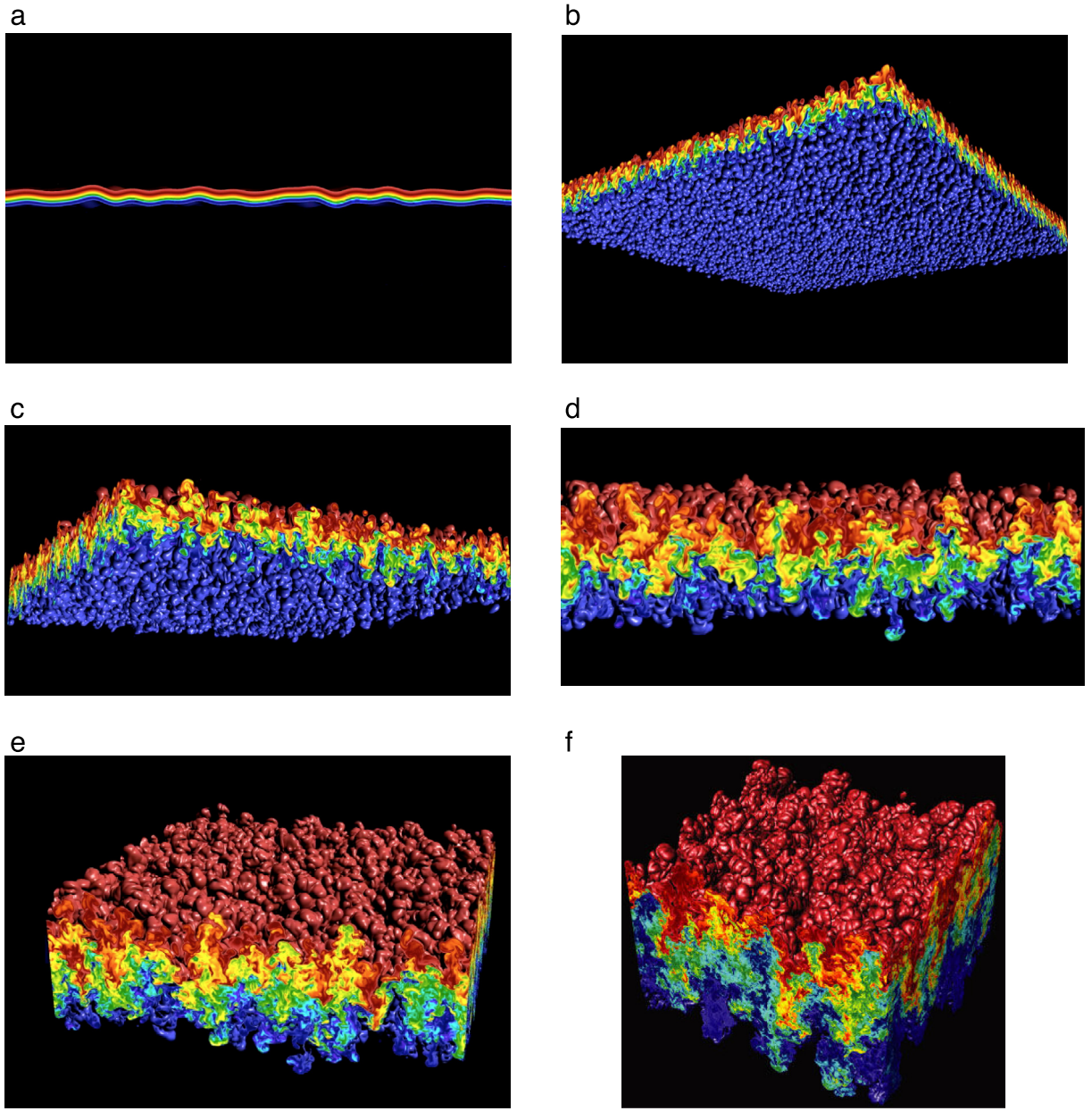


Fig. 7.1. (a–f) Snapshots of density field from DNS of RTI. Images, proceeding from upper to lower, were taken from a movie at $t = 1, 6, 10, 12, 16, 31$ (courtesy Dr. A.W. Cook, Lawrence Livermore National Laboratory). The heavy fluid is red ($\rho = 3$), the light fluid is blue ($\rho = 1$), and the mixed fluid is green ($\rho = 2$). The other colors represent mixed fluid of various compositions. Note that Fig. 7.1(f) shows Rayleigh–Taylor instability in the fully turbulent regime and appeared in Cabot and Cook (2006). (With permission from *Nature Physics*.)

condition. The initial interface between a helium–acetone mixture and argon ($A = 0.7$) has undergone shear driven mixing prior to shock acceleration and is characterized by a fairly thick region. The top of Fig. 7.4a shows the post-shock image taken immediately after shock compression where it is expected that little interface growth has occurred.

While the vorticity is spread throughout the interface, it is concentrated near the bottom where the mole fraction, X , is smallest (the bottom of Fig. 7.4a). As nearly all of the enstrophy is concentrated below $X = 0.5$, the interface growth and mixing will originate near where the vorticity is concentrated (Fig. 7.4b). Experiments (Layes et al., 2005) as well as two- and three-dimensional simulations (Zabusky and Zeng, 1998; Ranjan et al., 2005; Niederhaus et al., 2008a,b) have also been performed to illuminate the physics of the vorticity evolution after the shock–bubble interaction.

As described succinctly by Morgan et al. (2012), the deposited vorticity causes the interface to roll up into mushroom-like spikes of heavy fluid penetrating into the light fluid, separated by bubbles of light fluid moving into the heavy fluid. The

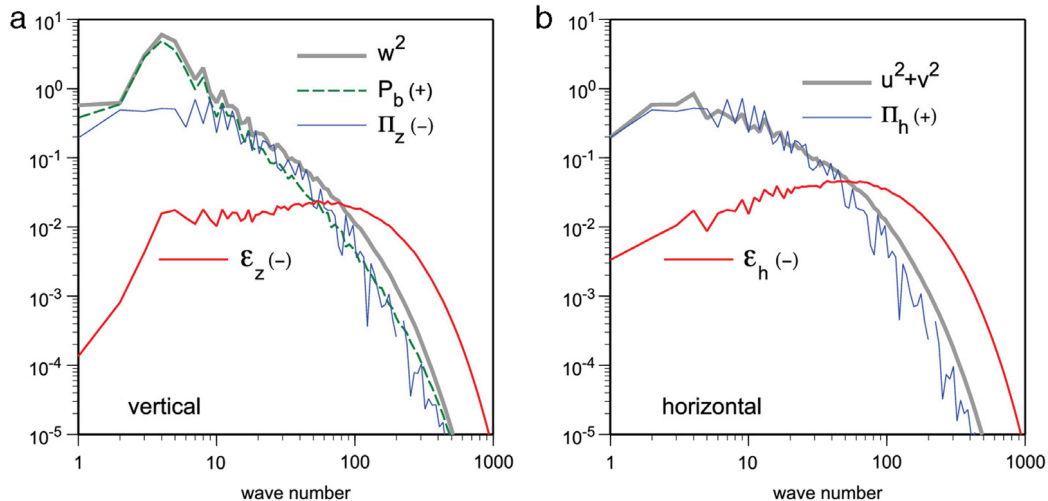


Fig. 7.2. Horizontal midplane spectra for (a) vertical and (b) horizontal kinetic energy rate terms: buoyancy production (dashed line), pressure-strain (thin solid line), and dissipation (medium solid line). The pressure-strain term is a sink (−) for the vertical kinetic energy and a source (+) for the horizontal kinetic energy. The thick curves show the corresponding vertical and horizontal velocity spectra. Here, the velocity components are denoted as u , v , w , instead of u_i , $i = 1, 2, 3$.

Source: Fig. 9 of Cabot and Zhou (2013).

total amount of vorticity deposited by the shock wave determines the growth rate of the instability. The misalignment of the interfacial density gradient and the centripetal acceleration of the vortex cores causes the generation of secondary baroclinic vorticity (Peng et al., 2003; Reinaud et al., 2000). The rolling up of the vorticity will also generate shear on the thin arms of the mushroom structure, leading to the growth of a secondary instability. Over time, this secondary instability eventually becomes turbulent, and the mushroom structures begin to disintegrate as the stems thin and the arms mix due to turbulent diffusion.

The vorticity production from the shock wave and subsequent mode coupling will depend on the particular Atwood number, Mach number, light-heavy or heavy-light configuration considered (Gowardhan et al., 2011). Depending on initial root of the mean-square (rms) of the slope of the interface, the evolution of the multimode planar RMI evolves into either linear or nonlinear regimes, with distinctly different flow features. In the linear regime, the growth rate increases as the initial rms slope increases. Less mode coupling is seen and the primary production of enstrophy is baroclinic (Richtmyer, 1960). In the nonlinear regime, there is significant mode coupling, which suggests that stretching becomes an important enstrophy production mechanism.

The growth of the Richtmyer–Meshkov instability and the consequent mixing is illustrated by the visualizations in Fig. 7.5. The particular experiment Cohen et al. (2002) have chosen to simulate is one where the shock passes from the low- to high-density fluids, and the membrane is initially on the same side of the mesh as the shock. Of the various combinations studied by Vetter and Sturtevant (1995), this is the one that led to rupturing of the membrane and thus leads to subsequent mixing layer growth unencumbered by properties of the membrane. Also, because the membrane is pushed into the mesh, there is a distinct imprint of the mesh spacing on the initial contact discontinuity shape. The variable plotted is the entropy chosen because it vividly displays the contact discontinuity while, for the parameters of the simulation, it has a relatively small change across the shock. The color mapping is chosen to be transparent red on the high-density (low entropy, low-temperature) side and transparent blue on the low-density side of the contact discontinuity (Cohen et al., 2002). The regular egg–carton interface plus the superimposed random small-scale structures resemble those measured from a recent ablative RMI experiment. Fig. 7.6 displayed the atomic force microscope micrographs showing the RMI structures in the central region of the spot generated by the laser pulse of Gaussian-like power profile (Lugomer, 2016a,b).

The RMI induced flows present significant complexity, such as the development of strong anisotropy and non-equilibrium, upon the passage of the shock wave. Nevertheless, the RMI induced turbulence can be viewed (Zhou, 2001) as a freely decaying, incompressible one (Thormann and Meneveau, 2014; Zhou and Speziale, 1998) after the passage of the planar shock wave (Zhou, 2001; Clark and Zhou, 2006).

The LES calculations of Lombardini et al. (2012) have shown that for all 5 Mach numbers considered the late time flow resembles a quasi-homogeneous decaying turbulence of Batchelor type (Batchelor, 1953; Batchelor and Proudman, 1956) with a kinetic decay energy exponent ≈ 1.4 and a large-scale energy spectrum $\approx k^4$.

Tritschler et al. (2014b) also concluded at turbulence evolving from the Richtmyer–Meshkov instability is not fundamentally different from decaying isotropic turbulence despite being only isotropic and homogeneous in two spatial directions. Also, the probability density functions of the velocity and its longitudinal and transverse derivatives are also in agreement with those for decaying isotropic turbulence.



Fig. 7.3. The Wisconsin vertical shock tube.
Source: Anderson et al. (2000), Shock Waves, with permission.

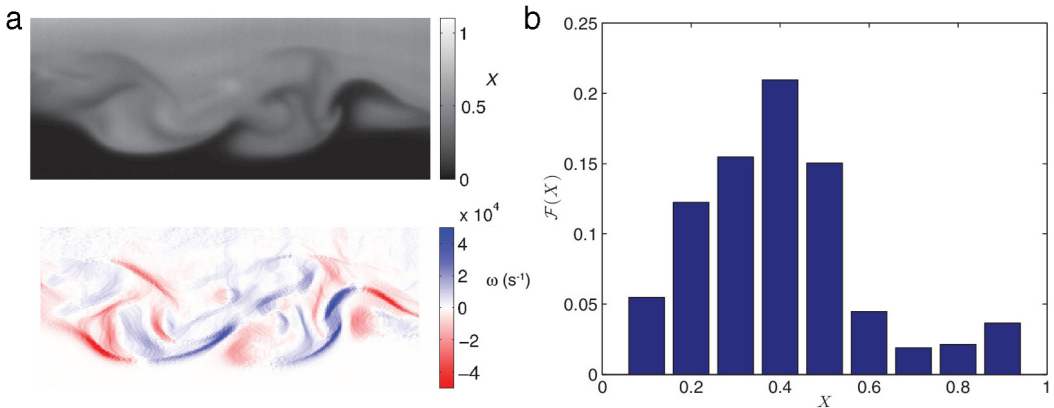


Fig. 7.4. (a) Estimate of the initial vorticity deposition using an early post-shock image and a model (Eq. (15) of Weber et al. 2012). (b) Fraction of the total enstrophy, ω^2 , within a select mole fraction range.
Source: Fig. 7 of Weber et al. (2012), Phys. Fluids, with the permission of AIP Publishing.

In their direct numerical simulation, Liu and Xiao (2016) injected the turbulent kinetic energy at the perturbation scales of a Mach 1.6 RMI flow and found that at early times the energy is transferred both backward to the larger scales and forward to the small scales. At late times, however, no inverse energy cascade is observed and large-scale motions continuously lose turbulent kinetic energy, similar to the case in decaying homogeneous isotropic turbulence. A visualization of the simulated flow field is shown in Fig. 7.7.

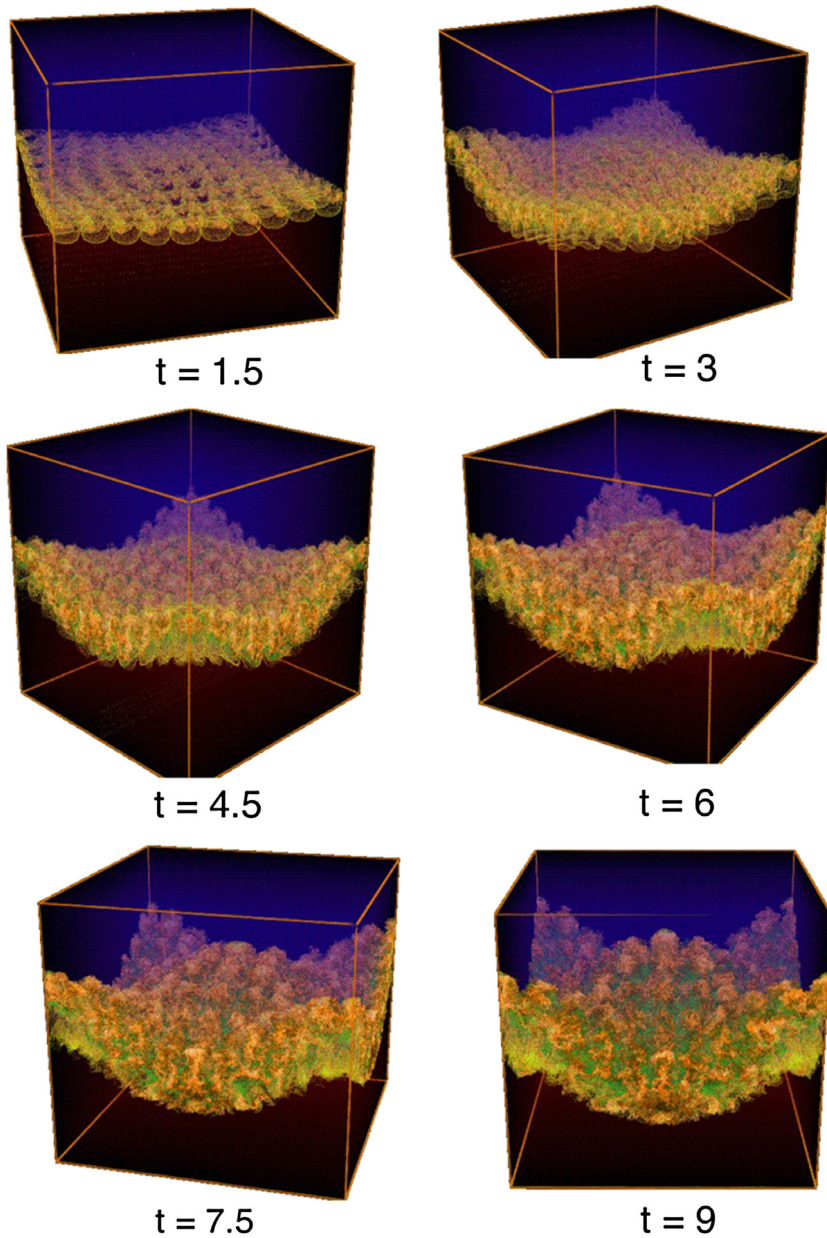


Fig. 7.5. Volume renderings of the RMI simulation at successive times.
Source: Cohen et al. (2002), *Physics of Fluids*.

At the Vertical Shock Tube facility (see Fig. 7.8a) newly developed at LANL, several flow quantities, including the vorticity, enstrophy, and strain, have been acquired experimentally (Wilson et al., 2016). Two types of dynamic measurements (PIV and PLIF diagnostics), time-series ($N = 5$ realizations at 10 locations) and statistics ($N = 100$ realizations at a single location) of the density and velocity fields (Fig. 7.8b) are used for a study where a perturbed stable light-to-heavy (air–SF₆, $A = 0.64$) interface is impulsively accelerated with a shock wave at Mach 1.45 and 1.3. Data from such direct measurements would allow one to inspect the physics of both large- and small-scales. The preliminary results already suggest that the large-scale mixing, such as the mix width, is strongly dependent on Mach number, whereas small scales are strongly influenced by initial conditions instead.

7.3. Basic governing and energy budget equations

The dynamic equation for the energy transfer process, constructed from the Navier–Stokes equations, requires the input of three-dimensional velocity flows. Obtaining such time-dependent fields is a major challenge for the laboratory experiments

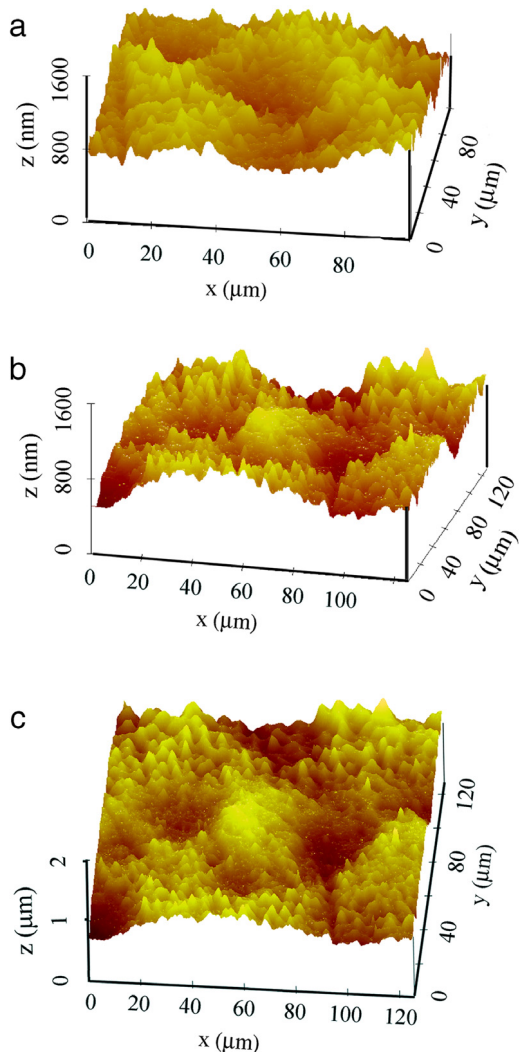


Fig. 7.6. Atomic force microscope micrographs measured RMI structures in the central region of the spot.
Source: Fig. 3 of [Lugomer \(2016a\)](#), permission from *Laser and Particle Beams*

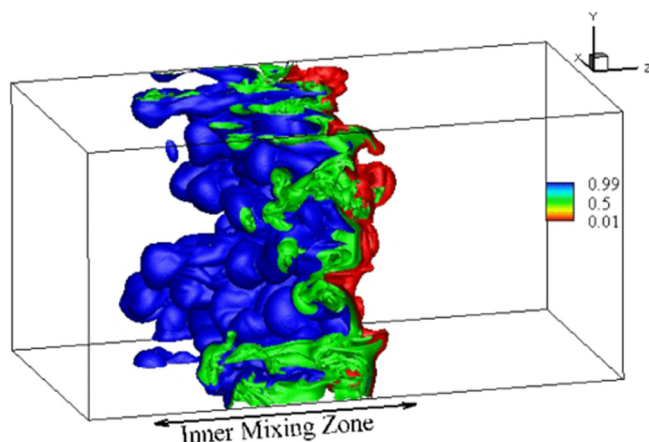


Fig. 7.7. The inner mixing zone visualized by an instantaneous contour of Y_{air} from a simulation at $t = 40t_5$. The fine-grid region resolution is $512^2 \times 1024$. The inner mixing zone is indicated by the z locations of $Y_{air} = 0.01, 0.99$.
Source: Fig. 3 of Liu and Xiao, *Phys. Rev. E* with permission.

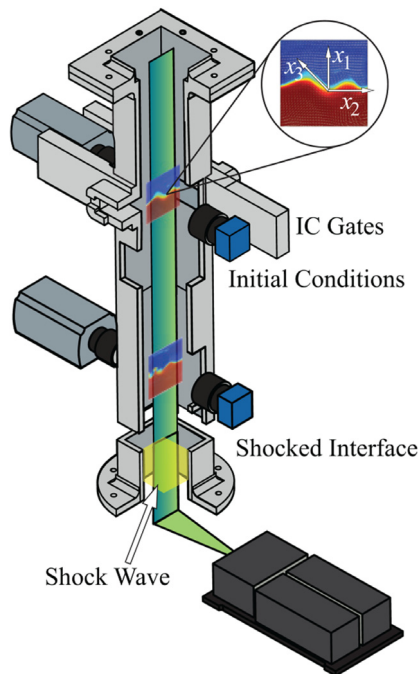


Fig. 7.8a. The test section in the LANL Vertical Shock Tube showing the gates that close off before the shock interacts with the initial conditions, the PLIF–PIV measurement locations, and the orientation of the diagnostic laser sheets.

Source: Wilson et al., (2016), ASME J. Fluids Eng. with permission.

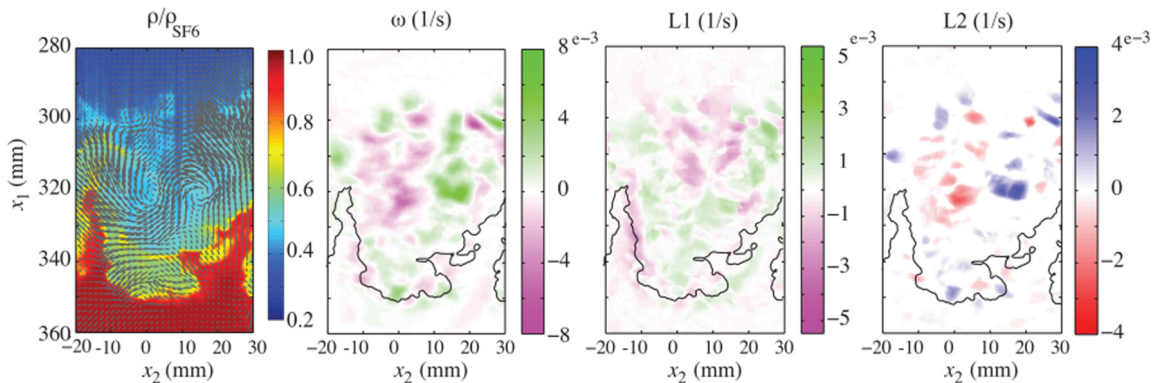


Fig. 7.8b. Example of the instantaneous density, velocity, and vorticity field. The symmetric (strain, $L1$) and asymmetric (rotation, $L2$) tensors of the velocity gradients are also shown. (Air– SF_6 , $A = 0.64$.)

Source: Fig. 12 of Wilson et al., (2016), ASME J. Fluids Eng. with permission.

as well as for the closure theories (Leslie, 1973; Orszag, 1970, 1977; Lesieur, 1990; Zhou et al., 2004; Sagaut and Cambon, 2008; Zhou, 2010). Indeed, while the laboratory experiments can be carried out in any setting, the data collection is often limited by the diagnostic methodologies. On the other hand, the closure theories can be used to inspect high Reynolds number flows for incompressible (Kraichnan, 1959, 1971) and weakly-compressible (Bataille and Zhou, 1999) flows. Despite some early attempts (Kraichnan, 1963, 1964), the closure theories are unfortunately limited to the homogeneous and isotropic turbulence.

There is a well-established procedure for studying the energy transfer process. Indeed, in last quarter century, numerical simulations have demonstrated their capabilities in providing high quality data for studying the energy transfer process. The previous works on homogeneous, isotropic turbulence have confirmed Kolmogorov's assumptions on the locality of the energy transfer (Domaradzki and Rogallo, 1990) and interacting scales (Zhou, 1993a,b). A variable-density formulation is proposed for energy transfer analyses previously performed for isotropic (Domaradzki and Rogallo, 1990; Yeung and Brasseur, 1991; Ohkitani and Kida, 1992; Zhou, 1993a,b), anisotropic (Zhou et al., 1996), and wall-bounded (Domaradzki

et al., 1994; Marati et al., 2004; Serra et al., 2012a,b; Cimarelli et al., 2013; Bolotnov et al., 2010; Cimarelli and Angelis, 2014; Aulery et al., 2015, 2017) flows.

Two remarks are in order here. First, in ILES, the explicit dynamic viscosity, μ , should be set to zero in Eqs. (7.1) and (7.2). Instead, the ILES subgrid scale modeling is provided implicitly by the numerics (Boris et al., 1992; Grinstein et al., 2007). As noted already, several schemes have been advanced to estimate the effective viscosity for ILES. Second, the acceleration g_i equals zero as the RMI flow is impulsive driven. On the other hand, $g_i = (0, 0, -g)$ for the RTI induced flow in the gravitation field. Indeed, the mixing problem induced by RTI and RMI for many applications is a transitional problem.

In this section, the energy transfer process for RTI and RMI induced flows will be reviewed in the same framework. This investigation will utilize the databases from the direct numerical simulation (DNS) for a RTI flow and implicit large-eddy simulations (ILES) for a RMI flow, respectively.

The conservation laws governing the flow of two incompressible fluids are

$$\frac{\partial \rho Y_l}{\partial t} + \frac{\partial \rho u_j Y_l}{\partial x_j} = \frac{\partial}{\partial x_j} \left(\rho D \frac{\partial Y_l}{\partial x_j} \right) \quad (l = 1, 2), \quad (7.6)$$

$$\frac{\partial \rho u_i}{\partial t} + \frac{\partial \rho u_i u_j}{\partial x_j} = -\frac{\partial p}{\partial x_i} + \frac{\partial \tau_{ij}}{\partial x_j} + \rho g_i \quad (7.7)$$

where g_i denotes the acceleration for RTI and equals to 0 for RMI. Again, the viscous action is taken by the numerics in ILES calculations.

Here ρ is the mixture density, Y_l is the mass fraction of species l , u_i is the mass-averaged mixture velocity, p is the pressure, D is the Fickian diffusivity, μ is the dynamic viscosity.

The mass fractions satisfy

$$Y_1(\mathbf{x}, t) + Y_2(\mathbf{x}, t) = 1. \quad (7.8)$$

It is important to add the zero-divergence condition here. The mass-weighted velocity of the mixture is not divergence-free when diffusion is present. The zero divergence, Livescu (2013) for example, is now

$$\nabla \cdot \mathbf{u} = -\nabla \cdot \left(\frac{D}{\rho} \nabla \rho \right). \quad (7.9)$$

In order to extend the methodology of constant-density energetics to the variable-density case, a new variable is introduced, i.e.,

$$v_i \equiv \rho^{1/2} u_i, \quad (7.10)$$

such that, the kinetic energy may be written as $K = v_i v_i / 2$. This variable has been used for similar purposes by various authors (Yih, 1960; Rodriguez Azara and Emanuel, 1988; Kida and Orszag, 1990). The Navier–Stokes equation can then be written as

$$\frac{\partial v_i}{\partial t} = \rho^{1/2} g_i - \frac{\partial v_i u_j}{\partial x_j} - \rho^{-1/2} \frac{\partial p}{\partial x_i} + \frac{1}{2} v_i \frac{\partial u_k}{\partial x_k} + 2\rho^{-1/2} \frac{\partial}{\partial x_j} \left[\mu \left(S_{ij} - \frac{1}{3} \delta_{ij} \frac{\partial u_k}{\partial x_k} \right) \right]. \quad (7.11)$$

For simplicity, Eq. (7.12) can be rewritten as

$$\frac{\partial v_i}{\partial t} = \mathcal{F}_i + \mathcal{N}_i + \mathcal{D}_i, \quad (7.12)$$

There are three contributions to the nonlinear term,

$$\begin{aligned} \mathcal{N}_q &= - \sum_i \frac{\partial v_i u_j}{\partial x_j}, \\ \mathcal{N}_p &= - \sum_i \rho^{-\frac{1}{2}} \frac{\partial p}{\partial x_i}, \\ \mathcal{N}_d &= \sum_i \frac{1}{2} v_i \frac{\partial u_k}{\partial x_k} \end{aligned} \quad (7.13)$$

where $m = q, p, d$ stands for quadratic, pressure, and dilatational components of the non-linear transfer.

The first contribution is from the quadratic term, which is responsible for passive-vector advection, while the second and third contributions are from pressure and dilatation effects.

The equation for the energy budget studies reviewed in this section is given in shorthand as

$$\frac{\partial}{\partial t} E(k, z, t) = P(k, z, t) + T(k, z, t) + \mathcal{E}(k, z, t), \quad (7.14)$$

where E is the variable-density kinetic energy spectrum,

$$E = \frac{1}{2} \oint (\hat{v}_i^* \hat{v}_i) d\Omega, \quad (7.15)$$

the nonlinear transfer term is

$$T = \frac{1}{2} \oint (\hat{v}_i^* \hat{N}_i + \hat{v}_i \hat{N}_i^*) d\Omega, \quad (7.16)$$

and the viscous dissipation is

$$\varepsilon = \frac{1}{2} \oint (\hat{v}_i^* \hat{\mathcal{D}}_i + \hat{v}_i \hat{\mathcal{D}}_i^*) d\Omega, \quad (7.17)$$

with $d\Omega$ being a differential element of a wave space annulus, $(\hat{\cdot})$ indicates a Fourier transform, $(\cdot)^*$ indicates the complex conjugate.

For a RTI induced flow, P is the production term due to gravitational force. The RM instability is driven via an impulse in the initial time and then decays freely ($P = 0$). Thus, the only terms of physical importance at the large scales simulated are the rate of change of the variable-density energy spectrum E and the nonlinear transfer term T as ε is furnished implicitly by numerics in an ILES calculation.

In order to ascertain the relative importance of each process, the total nonlinear transfer is subdivided into each individual component, i.e.,

$$T(k, z, t) = T_q(k, z, t) + T_p(k, z, t) + T_d(k, z, t) \quad (7.18)$$

where

$$T_m = \frac{1}{2} \oint (\hat{v}_i^* \hat{N}_{m,i} + \hat{v}_i \hat{N}_{m,i}^*) d\Omega \quad (m = q, p, d). \quad (7.19)$$

7.4. RTI energy transfer

A detailed investigation on the energy transfer process will provide a complete picture on how the energy is produced, transferred in both the homogeneous and inhomogeneous directions, and finally, dissipated. The role of the pressure will also be inspected. The time evolution of the energy, production, transfer, and dissipation spectra can be found in [Cook and Zhou \(2002\)](#) and [Cabot et al. \(2004\)](#).

The production P , transfer T , and dissipation ε spectra are plotted in [Fig. 7.9](#) on the same z versus $\log_{10}(k)$ domain for the highest turbulent state of the simulation. By the end of the simulation ($t = 6$), there is some k separation between the two, i.e., as structures merge within the mixing layer, energy is deposited at larger scales. The increasing separation of peaks between the production and dissipation spectra is a direct result of the increasing Reynolds number for this transitional flow.

The transfer spectrum, T , however, behaves in a very complicated manner. At higher wave numbers T is mostly positive, indicating a net cascade of energy to smaller scales. Inside the mixing zone, backscatter appears approximately equal to forward scatter. It further appears that some z locations may be undergoing forward energy cascade, while neighboring regions are simultaneously experiencing inverse cascade. The transfer spectrum is also positive at the top and bottom of the mixing zone, suggesting production of energy at the bubble and spike fronts.

In order to unravel the irregular patchwork that constitutes T , each individual component (T_q and T_p) is plotted separately in [Fig. 7.10](#). The dilatation, T_d is roughly two orders of magnitude smaller, therefore, its influence on the energetics is likely negligible.

As shown in [Fig. 7.10](#), the quadratic term is mostly negative at lower wave numbers inside the mixing zone and mostly positive at higher wave numbers and near the edges of the mixing envelope. Regarding the pressure term, nearly the opposite is true, except at higher wave numbers where positive and negative regions appear to be roughly equally distributed. Hence, their net contribution to T is the result of extensive cancellation between these two contributions. The net positive transfer of energy to the higher wave numbers (usual cascade picture) and to the bubble/spike fronts is thus a result of quadratic interactions, (T_q), with pressure counterbalancing advection, for the most part.

The actual measurement of the raw interaction statistics, the triad nonlinear transfer function, is the building block of the energy transfer process ([Domaradzki and Rogallo, 1990](#); [Yeung and Brasseur, 1991](#); [Ohkitani and Kida, 1992](#); [Zhou, 1993a,b](#); [Zhou et al., 1996](#)). Without resort to any modeling, subgrid-scale eddy viscosity is computed from the results of high-resolution direct numerical simulations of 3D RTI induced turbulence. Using a sharp Fourier cutoff filter, [Cabot et al. \(2004\)](#) decomposed the kinetic energy transfer into (1) the resolved part; (2) a part corresponding to the interaction between resolved and unresolved scales; and (3) a part corresponding to the interaction between unresolved scales. The decomposition into resolved and unresolved scales is used to define an effective eddy viscosity and backscatter viscosity. This scheme follows the previous applications to the isotropic turbulence ([Domaradzki et al., 1987](#); [Zhou and Vahala, 1993](#)) as well as channel flow and Rayleigh-Bénard convection ([Domaradzki et al., 1994](#); [Domaradzki and Liu, 1995](#)). The principal conclusions of the Cabot et al. analysis are the transfer spectra and eddy viscosities exhibit a strong dependence on the wave number cutoff. Furthermore, the contributions from the interaction between resolved and unresolved scales dominate

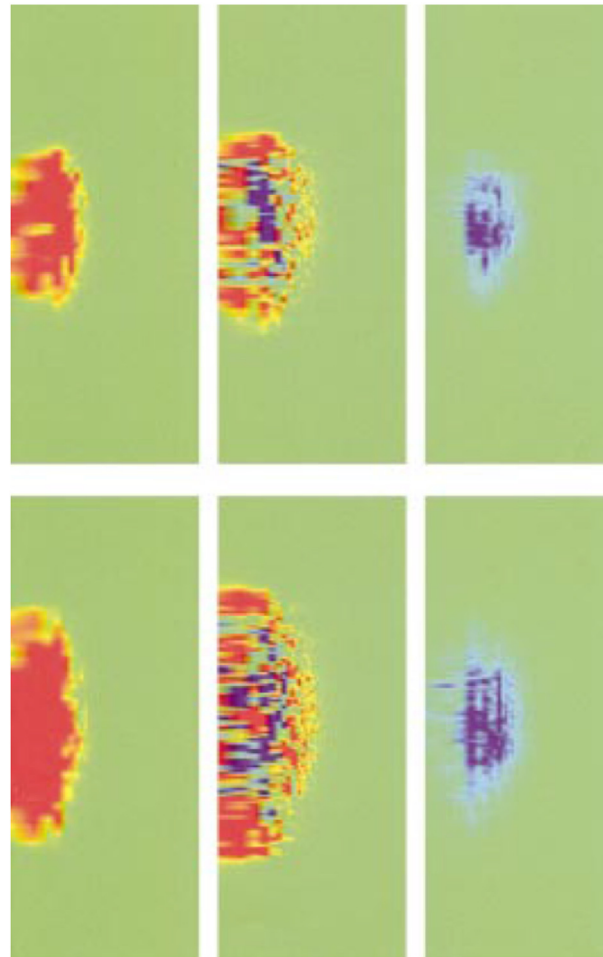


Fig. 7.9. Production (P : left), transfer (T : middle), and dissipation (ε : right) spectra versus z (vertical) and $\log_{10}(k)$ (horizontal) at $t = 5$ (top) and 6 (bottom). Blue = -2×10^{-4} , green = 0, and red = 2×10^{-4} .
Source: From Cook and Zhou (2002), Fig. 14.

the contribution to the total subgrid eddy viscosities and are responsible for the cusp near the cutoff wavenumber (see Section 6.7).

7.5. RMI energy transfer

The RMI simulations were conducted using a high-order accurate ILES algorithm (Thornber et al., 2008a,b, 2011a; Thornber and Drikakis, 2007) at a grid resolution of 512^3 , where the initial conditions employed represent the passage of a shock wave through an initial interface with a narrow-band multimode perturbation (Thornber and Zhou, 2012). The multimode perturbation has an initial power spectrum which is constant for wavelengths $16\Delta x \leq \lambda \leq 32\Delta x$, where λ is the wavelength, and Δx is the grid spacing and is equal in all directions. The power is zero for all other wavelengths and is adjusted such that the initial modes are linear and well resolved on the computational grid. These RMI simulations have been demonstrated to be grid converged in terms of spatial means, spectral data, and mixing parameters (Thornber et al., 2010).

The RM instability is driven via an impulse in the initial time instant and then decays freely. Thus, the only terms of physical importance at the large scales simulated are the rate of change of the variable-density energy spectrum E and the nonlinear transfer term T in Eq. (7.14) (Thornber and Zhou, 2012). The shock travels in the positive x direction from the heavy fluid to the light. In this case study, the location of the initial interface perturbation in Fourier space lies between $1.2 \lesssim \log(k) \lesssim 1.5$. This is where the kinetic energy is initially injected into the flow through RMI. The center of the mixing layer, defined as the point where the cross-section-averaged mass fractions are 0.5, is at $x = 3.05$ for all time instants (only results from $\tau = 37$ will be reviewed here).

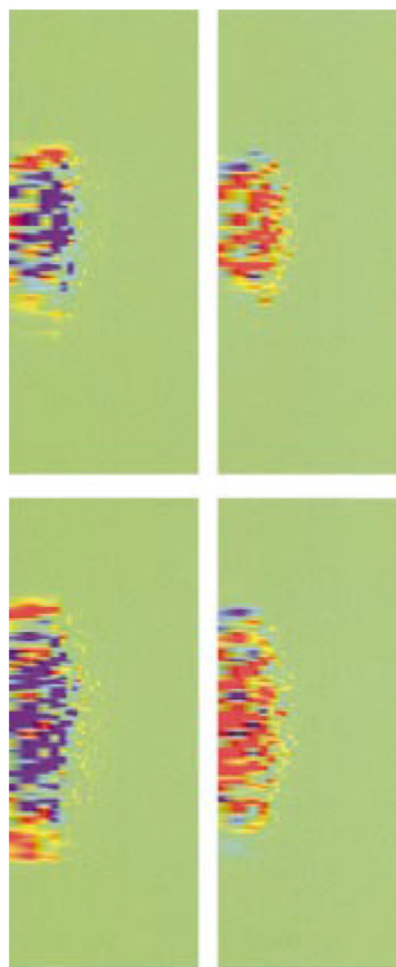


Fig. 7.10. Quadratic (T_q : left) and pressure (T_p : right) contributions to transfer function versus z (vertical) and $\log_{10}(k)$ (horizontal) at $t = 5$ (top) and 6 (bottom). Blue = -5×10^{-4} , green = 0, and red = 5×10^{-4} .

Source: From Cook and Zhou (2002), Fig. 16.

There are clear parallels in the development of the mixing layer with a previous analysis of the RTI. There is a large region of negative energy transfer in the center of the mixing layer at $0.8 \lesssim \log(k) \lesssim 1.5$, where the kinetic energy deposited by the shock is being redistributed to higher and lower wave numbers. This is principally due to the quadratic component of nonlinear transfer and is counteracted in some regions by positive transfer from the pressure component (Fig. 7.11).

The transfer spectra are clearly asymmetric: most of the activity is occurring on the spike side where the flow density is higher. The quadratic and pressure components nearly cancel each other out at high x on the spike side, where alternating regions of high positive levels of quadratic transfer and high negative levels of pressure components arise. The pressure transfer is both positive and negative, like that reported for the RT instability. This is most likely due to the continuing isentropic exchange of internal and kinetic energy as vortices collide and break up. Fig. 7.12 is a close-up of an escaping vortex ring, which highlights the intense vorticity transported from the mixing layer and the wake trailing it. The velocity vectors illustrate that the velocities induced within this vortex ring are larger than those found in the mixing layer itself, and the peaks in nonlinear transfer are associated with these spikes. The vortex ring is preceded by a region of positive quadratic transfer and negative pressure transfer, which, when summed, make a weaker positive transfer. This is reversed in the core of the vortex. This process is repeated in the weaker vortex rings, which have been shed downstream of the head of the spike. The strongly alternating regions of high positive and negative quadratic and pressure observed at high x advect away from the mixing layer and out of the computational domain in synchrony with the spike motion. This effect can also be seen in the RTI results of Cook and Zhou.

Using direct numerical simulation, Liu and Xiao (2016) studied the scale-to-scale energy transfer in a RMI flow induced by a Mach 1.6 planar shock wave. Three multi-mode initial perturbations are considered for the material interface formed by

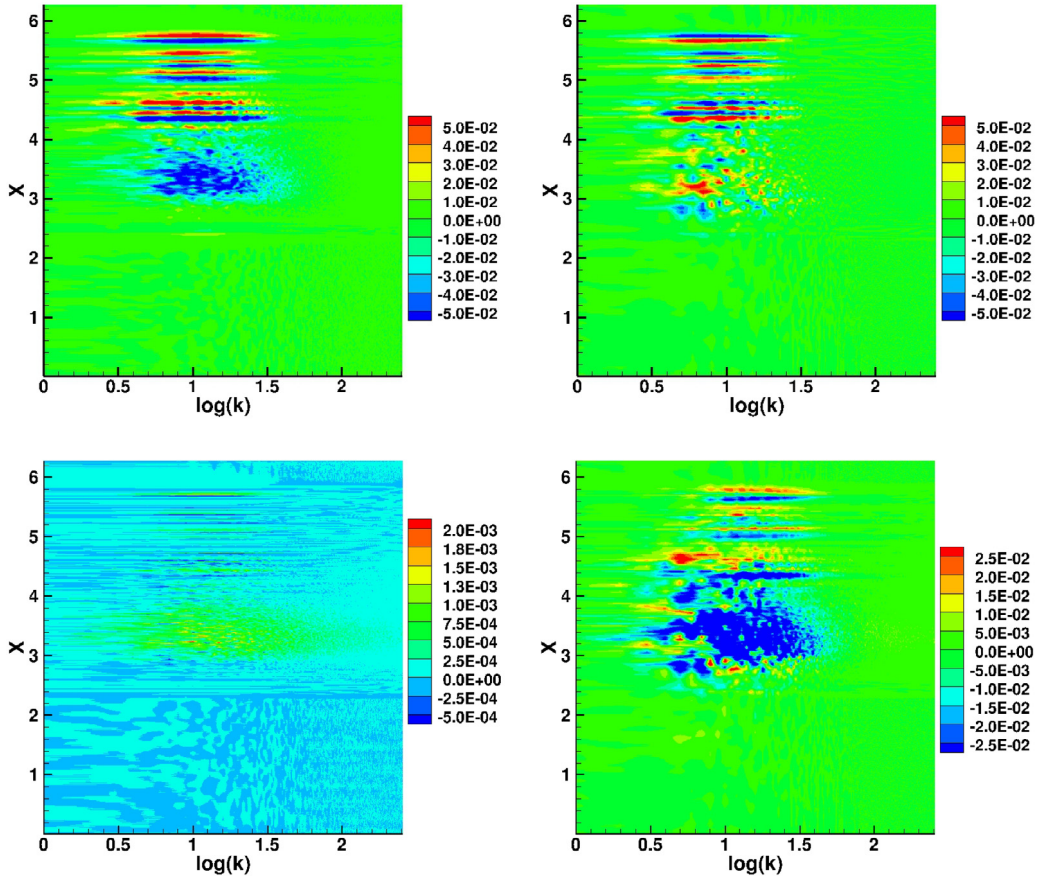


Fig. 7.11. Transfer due to quadratic (upper left), pressure (upper right), dissipation (lower left), and the total transfer function at $\tau = 37$.
Source: From [Thornber and Zhou \(2012\)](#), Fig. 6.

Air and SF₆. The authors found that the predominant events take place in the spike side of the inner mixing zone, consistent with the property of energy transfer spectra reported by Thornber and Zhou.

8. Summary, reflections, and outlook

The objective of Part I of this review is to provide the basic properties of the flow, turbulence, and mixing induced by Rayleigh–Taylor, Richtmyer–Meshkov, and Kelvin–Helmholtz instabilities. Part II ([Zhou, 2017](#)) is designed to provide a much broader and in-depth understanding of this critical area of research.

The flows induced by RT and RM instabilities are time dependent and undergo both the linear and nonlinear phases of growth. After a quick tour of elementary stability analysis and early experimental work, images from modern single-mode RTI and RMI experiments in the laboratory are presented to illustrate the temporal development of RT and RM instabilities, as well as the critical role of the KH instability. Linear and nonlinear models are documented and compared with available laboratory experiments and numerical simulations. Vortex models are also presented, which could overcome some of the restrictions of traditional nonlinear models even after the vortex roll-up begins. The roles of viscosity, surface tension, and diffuse interfaces in enhancing stability are examined.

In some cases, these flows with single-mode or multi-mode initial conditions can transition to turbulence. In Part I, both the spatial and temporal criteria to achieve the transition to turbulence have been examined. Forcing from gravity or time-varying acceleration in RTI flows, vorticity and energy deposition from the shock in RMI flows, and the resulting energy transfer process for inhomogeneous cases of both flows are discussed.

A key element of Part I is the discussion of the late-time self-similar scaling specified by the RT and RM growth factors, α and θ . These parameters are influenced by the initial conditions and much of the variation seen in the tables can be explained by this.

In Part II ([Zhou, 2017](#)), special attention is paid not only to the influence of the initial conditions but also to the dependence of multi-mode flows on Atwood number (for both RTI and RMI) and Mach number (for RMI). Moreover, RMI flows undergoing

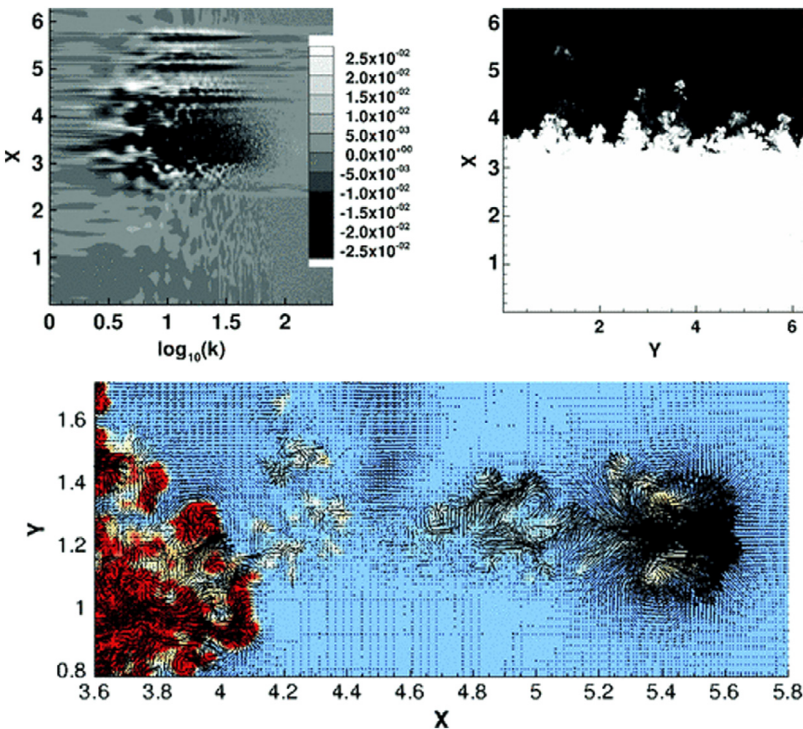


Fig. 7.12. Total nonlinear transfer T at $\tau = 37$ (left) with the corresponding mass fraction field (right) and a close-up of the mass fraction contours around a spike with velocity vectors superimposed (bottom). Note that the contour flood is from $0 < Y_1 < 0.05$ to highlight the spikes. The left-hand part of the bottom image shows the spike side of the mixing layer.

Source: Fig. 11 of [Thornber and Zhou \(2012\)](#).

reshock or multiple shocks will introduce distinctive new physics. For all these cases, the flow properties are further evaluated based on the mixed width, mixedness parameters, normalized mixed mass, and anisotropy of the mixing layers.

Additional physics and external factors, such as the compressibility, rotation, stratification, and magnetic field, usually enhance stability with very few possible exceptions. Further complicating issues are that multiple instabilities might interact with each other, and the significant impact of convergent geometry in the growth of RTI and RMI.

Of course, mix models are required for practical scientific and engineering applications. A comprehensive overview will be offered, with increasingly more sophisticated models – with many more equations – that attempt to incorporate additional physics. Part II concludes by discussing issues which arise in the modeling of astrophysical and high-energy-density physics applications.

Acknowledgments

The author is deeply indebted to Prof. D.L. Youngs (Atomic Weapons Establishment, United Kingdom, now with University of Strathclyde), Dr. K.O. Mikaelian, Dr. M.G. Mustafa, and Dr. O. Schilling (Lawrence Livermore National Laboratory), Dr. T.T. Clark (Los Alamos National Laboratory, now with University of New Mexico), Dr. R.J.R. Williams (Atomic Weapons Establishment, United Kingdom), and Dr. R. Rubinstein (NASA Langley Research Center) for their careful review and insightful suggestions. He is extremely grateful to Drs. W.H. Cabot, D.S. Clark, S.G. Glendinning, M. Ulitsky, and Q. Zhang for their fruitful discussions and detailed feedback. He acknowledges many stimulating discussions over the years with Drs. M.J. Andrews, A. Banerjee, R. Bonazza, A.C. Buckingham, A.W. Cook, S.B. Dalziel, G. Dimonte, P.E. Dimotakis, R.P. Drake, D. Drikakis, S. Gauthier, F.F. Grinstein, S.W. Haan, O.A. Hurricane, J.W. Jacobs, C.E. Leith, D. Livescu, D.I. Meiron, E.E. Meshkov, K.P. Prestridge, P. Ramaprabhu, B.A. Remington, H.F. Robey, D.D. Ryutov, C.-W. Shu, B. Thornber, L. Welser-Sherrill, and G.B. Zimmerman. The author also thanks the valuable comments and assistances by Drs. P. Anninos, C. Batha, G.C. Burton, P. Carlès, G. Carnevale, R. Cohen, M. Davies Wykes, T.R. Dittrich, F.W. Doss, D. Eliason, K.A. Flippo, R.A. Gore, J. Griffond, C.M. Huntington, B.I. Jun, V.V. Krivets, A.L. Kuhl, A. Lawrie, E. Leinov, M. Lombardini, S. Lugomer, S.A. McLaren, W.D. Mostert, S.D. Murray, S.R. Nagel, B.J. Olson, C. Pantano, L. J. Perkins, K.S. Raman, D. Ranjan, S. Reckinger, M.M. Scase, J.D. Schwarzkopf, M.A.R. Skinner, K.L. Stalsberg-Zarling, C. Tomkins, P. Wang, and C. Weber. Finally, the author is appreciative of Prof. D. Jewitt for providing his original photograph. This work was performed under the auspices of the Lawrence Livermore National Security, LLC under Contract No. DE-AC52-07NA27344.

References

- Abakumov, A.I., et al., 1996. Studies of film effects on the turbulent mixing zone evolution in shock tube experiments. In: Young, R., Glimm, J., Boston, B. (Eds.), Proc. 5th Int. Workshop on Compressible Turbulent Mixing. Singapore, World Scientific, p. 118.
- Abarzhi, S.I., 1998. Stable steady flows in Rayleigh–Taylor instability. *Phys. Rev. Lett.* 81, 337.
- Abarzhi, S.I., 2000. Regular and singular late-time asymptotes of potential motion of fluid with a free-boundary. *Phys. Fluids* 12, 3112.
- Abarzhi, S.I., 2010a. On fundamentals of Rayleigh–Taylor turbulent mixing. *Europhys. Lett.* 91, 35001.
- Abarzhi, S.I., 2010b. Review of theoretical modeling approaches of Rayleigh–Taylor instabilities and turbulent mixing. *Phil. Trans. R. Soc. A* 368, 1809.
- Abarzhi, S.I., Rosner, R., 2010. A comparative study of approaches for modeling Rayleigh–Taylor turbulent mixing. *Phys. Scr. T* 142, 014012.
- Abarzhi, S.I., Nishihara, K., Glimm, J., 2003. Rayleigh–Taylor and Richtmyer–Meshkov instabilities for fluids with finite density ratio. *Phys. Lett. A* 317, 470.
- Abd-El-Fattah, A.M., Henderson, L.F., 1978a. Shock waves at a fast slow interface. *J. Fluid Mech.* 86, 15.
- Abd-El-Fattah, A.M., Henderson, L.F., 1978b. Shock waves at a slow fast gas interface. *J. Fluid Mech.* 89, 79.
- Abd-El-Fattah, A.M., Henderson, L.F., Lozzi, A., 1976. Precursor shock waves at a slow–fast gas interface. *J. Fluid Mech.* 76, 157.
- Abramovitz, M., Stegun, I. (Eds.), 1968. HandBook of Mathematical Functions. Dover, New York.
- Abzaev, F.M., Bel'kov, S.A., Bessarab, A.V., 1998. Investigations on the indirect (X ray) irradiation of high-aspect shell micro-targets at the Iskra-5 facility. *Zh. Eksp. Teor. Fiz.* 114, 1993.
- Adams, C.S., Moser, A.L., Hsu, S.C., 2015. Observation of Rayleigh–Taylor-instability evolution in a plasma with magnetic and viscous effects. *Phys. Rev. E* 92, 051101.
- Adkins, J.F., McIntyre, K., Schrag, D.P., 2002. The salinity temperature and $\delta^{18}\text{O}$ of the glacial deep ocean. *Science* 298, 1769.
- Adkins, R., Shelton, E.M., Renoult, M.-C., Carles, P., Rosenblatt, C., 2017. Interface coupling and growth rate measurements in multilayer Rayleigh–Taylor instabilities. *Phys. Rev. Fluids* 2, 062001.
- Aglitskiy, Y., Velikovich, A.L., Karasik, M., Serlin, V., Pawley, C.J., Schmitt, A.J., Obenschain, S.P., Mostovych, A.N., Gardner, J.H., Metzler, N., 2001. Direct observation of mass oscillations due to ablative Richtmyer–Meshkov instability in plastic targets. *Phys. Rev. Lett.* 87, 265001.
- Aglitskiy, Y., Velikovich, A.L., Karasik, M., Serlin, V., Pawley, C.J., Schmitt, A.J., Obenschain, S.P., Mostovych, A.N., Gardner, J.H., Metzler, N., 2002. Direct observation of mass oscillations due to ablative Richtmyer–Meshkov instability and feedout in planar plastic targets. *Phys. Plasmas* 9, 2264.
- Aglitskiy, Y., Velikovich, A.L., Karasik, M., Metzler, N., Zalesak, S.T., Schmitt, A.J., Phillips, L., Gardner, J.H., Serlin, V., Weaver, J.L., Obenschain, S.P., 2010. Basic hydrodynamics of Richtmyer–Meshkov-type growth and oscillations in the inertial confinement fusion-relevant conditions. *Phil. Trans. R. Soc. A* 368, 1739.
- Aglitskiy, Y., Karasik, M., Velikovich, A.L., Serlin, V., Weaver, J.L., Kessler, T.J., Nikitin, S.P., Schmitt, A.J., Obenschain, S.P., Metzler, N., Oh, J., 2012. Observed transition from Richtmyer–Meshkov jet formation through feedout oscillations to Rayleigh–Taylor instability in a laser target. *Phys. Plasmas* 19, 102707.
- Al'bikov, Z.A., Velikhov, E.P., Veretennikov, A.I., Glukhikh, V.A., Grabovskii, E.V., Grjaznov, G.M., Gusev, O.A., et al., 1990. Experimental complex ‘Angara-5-1’. *Soviet Atom Energ.* 68, 34.
- Alder, B.J., Wainwright, T.E., 1957. Phase transition for a hard sphere system. *J. Chem. Phys.* 27, 1208.
- Aleksandrov, V.V., Volkov, G.S., Grabovski, E.V., Gribov, A.N., Gritsuk, A.N., Laukhin, Ya.N., Mitrofanov, K.N., Oleinik, G.M., Sasorov, P.V., Frolov, I.N., 2012. Study of the implosion characteristics of quasi-spherical wire arrays on the Angara-5-1 facility at currents of up to 4 MA. *Plasma Phys. Rep.* 38, 315.
- Aleksandrov, V.V., Bolkhovitinov, E.A., Volkov, G.S., Grabovski, E.V., Gritsuk, A.N., Medovshchikov, S.F., Oleinik, G.M., Rupasov, A.A., Frolov, I.N., 2016. Implosion dynamics of a megampere wire-array Z-pinch with an inner low-density foam shell at the Angara-5-1 facility. *Plasma Phys. Rep.* 42, 1091.
- Aleshin, A.N., Gamalii, E.G., Zaitsev, S.G., Lazareva, E.V., Lebo, I.G., Rozanov, V.B., 1988. Nonlinear and transitional states in the onset of the Richtmyer–Meshkov instability. *Sov. Tech. Phys. Lett.* 14, 466.
- Aleshin, A.N., Lazareva, E.V., Zaitsev, S.G., Rozanov, V.B., Gamali, E.G., Lebo, I.G., 1990. Linear, nonlinear and transient stages in development of Richtmyer–Meshkov instability. *Sov. Phys. Dokl.* 35, 159.
- Aleshin, A.N., Lazareva, E.V., Chebotareva, E.I., Sergeev, S.V., Zaytsev, S.G., 1997. Investigation of Richtmyer–Meshkov instability induced by the incident and the reflected shock waves. In: Jourdan, G., Houas, L. (Eds.), Proceedings of The Sixth international Workshop on Compressible Turbulent Mixing, Marseille, 1997. IUSTI Universite de Provence, France, p. 1.
- Allred, J.C., Blount, G.H., 1953. Experimental Studies of Taylor Instability, Los Alamos Scientific Laboratory Report LA-1600.
- Almarcha, C., Trevelyan, P.M.J., Grosfils, P., De Wit, A., 2010. Chemically driven hydrodynamic instabilities. *Phys. Rev. Lett.* 104, 044501.
- Almgren, A.S., Bell, J.B., Rendleman, C.A., Zingale, M., 2006. Low Mach number modelling of type Ia supernovae. Part I. Hydrodynamics. *Astrophys. J.* 637, 922.
- Alon, U., Shvarts, D., Mukamel, D., 1993. Scale invariant regime in Rayleigh–Taylor bubble-front dynamics. *Phys. Rev. E* 48, 1008.
- Alon, U., Hecht, J., Mukamel, D., Shvarts, D., 1994. Scale invariant mixing rates of hydrodynamically unstable interfaces. *Phys. Rev. Lett.* 72, 2867.
- Alon, U., Hecht, J., Ofer, D., Shvarts, D., 1995. Power laws and similarity of Rayleigh–Taylor and Richtmyer–Meshkov mixing fronts at all density ratios. *Phys. Rev. Lett.* 74, 534.
- Amala, P.A.K., 1995. Large-Eddy Simulation of the Rayleigh–Taylor Instability on a Massively Parallel Computer. Lawrence Livermore National Laboratory Report UCRL-LR-119748.
- Amala, P.A.K., Rodrigue, G.H., 1994a. Programming models for three-dimensional hydrodynamics on the CM-5 (Part I). *Comput. Phys.* 8, 181.
- Amala, P.A.K., Rodrigue, G.H., 1994b. Programming models for three-dimensional hydrodynamics on the CM-5 (part II). *Comput. Phys.* 8, 300.
- Amendt, P., Colvin, J.D., Tipton, R.E., Hinkel, D.E., Edwards, M.J., Landen, O.L., Ramshaw, J.D., Suter, L.J., Varnum, W.S., Watt, R.G., 2002. Indirect-drive noncryogenic double-shell ignition targets for the National Ignition Facility: Design and analysis. *Phys. Plasmas* 9, 2221.
- Amendt, P., Robey, H.F., Park, H.-S., Tipton, R.E., Turner, R.E., Milovich, J.L., Bono, M., Hibbard, R., Louis, H., Wallace, R., Glebov, V.Yu., 2005. Hohlraum-driven ignitionlike double-shell implosions on the Omega laser facility. *Phys. Rev. Lett.* 94, 065004.
- Amendt, P., Cerjan, C., Hamza, A., Hinkel, D.E., Milovich, J.L., Robey, H.F., 2007. Assessing the prospects for achieving double-shell ignition on the National Ignition Facility using vacuum hohlraums. *Phys. Plasmas* 14, 056312.
- Amendt, P., Milovich, J., Perkins, L.J., Robey, H., 2010. An indirect-drive non-cryogenic double-shell path to 1ω Nd-laser hybrid inertial fusion–fission energy. *Nucl. Fusion* 50, 105006.
- Anderson, M.H., Puranik, B.P., Oakley, J.G., Brooks, P.W., Bonazza, 2000. Shock tube investigation of hydrodynamic issues related to inertial confinement fusion. *Shock Waves* 10, 377.
- Andre, M.L., 1999. The French Megaloule Laser project (LMJ). *Fusion Eng. Des.* 44, 43.
- Andrews, M.J., 1995. Accurate computation of convective transport in transient two-phase flow. *Int. J. Numer. Methods Fluids* 21, 205.
- Andrews, M.J., Spalding, D.B., 1990. A simple experiment to investigate two-dimensional mixing by Rayleigh–Taylor instability. *Phys. Fluids A* 2, 922.
- Andronov, V.A., Bakhrakh, S.M., Meshkov, E.E., Mokhov, V.N., Nikiforov, V.V., Pevnitskii, A.V., Tolshmyakov, A.I., 1976. Turbulent mixing at contact surface accelerated by shock waves. *Sov. Phys. JETP* 44, 424.
- Andronov, V.A., Zhidov, I.G., Meskov, E.E., Nevezmerzhitskii, N.V., Nikiforov, V.V., Razin, A.N., Rogatchev, V.G., Tolshmyakov, A.I., Yanilkin, Y.V., 1995. Computational and experimental studies of hydrodynamic instabilities and turbulent mixing (Review of NVIIEF efforts) (No. LA-12896). Los Alamos National Lab., NM (United States).

- Annamalai, S., Parmar, M.K., Ling, Y., Balachandar, S., 2014. Nonlinear Rayleigh–Taylor instability of a cylindrical interface in explosion flow. *ASME J. Fluids Eng.* 136, 060910.
- Annenkov, V.I., Bagretsov, V.A., Bezuglov, V.G., Vinogradskii, L.M., Gaĭdash, V.A., Galakhov, I.V., Gashev, A.S., et al., 1991. Iskra-5 pulsed laser with an output power of 120 TW. *Quantum Electron.* 21, 487.
- Annenkov, V.I., Bezuglov, V.G., Bessarab, A.V., Bogunenko, Yu.D., Bondarenko, G.A., Galakhov, I.V., Garanin, S.G., et al., 2006. New possibilities of the Iskra-5 facility. *Quantum Electron.* 36, 508.
- Anuchina, N.N., Kucherenko, Yu.A., Neuvazhaev, V.E., O gibina, V.N., Shabarshov, L.I., Yakovlev, V.G., 1978. Turbulent mixing at an accelerating interface between liquids of different densities. *Izv. Akad. Nauk SSSR Mekh. Zhidk. Gaza* 6, 157.
- Anuchina, N.N., Volkov, V.I., Gordychuk, V.A., Es'kov, N.S., Il'yutina, O.S., Kozyrev, O.M., 2004. Numerical simulations of Rayleigh–Taylor and Richtmyer–Meshkov instability using MAH-3 code. *J. Comput. Appl. Math.* 168, 11.
- Aref, H., Tryggvason, G., 1989. Model of Rayleigh–Taylor instability. *Phys. Rev. Lett.* 62, 749.
- Arnett, D., 1996. Supernova and Nucleosynthesis. Princeton University Press, Princeton.
- Arnett, D., 2000. The role of mixing in astrophysics. *Astrophys. J. Suppl.* 127, 213.
- Arnett, W.D., Bahcall, J.N., Kirshner, R.P., Woosley, S.E., 1989. Supernova 1987A. *Annu. Rev. Astron. Astrophys.* 27, 629.
- Asay, J.R., Mix, L.P., Perry, F.C., 1976. Ejection of material from shocked surfaces. *Appl. Phys. Lett.* 29, 284.
- Aschenbach, B., Egger, R., Tromper, J., 1995. Discovery of explosion fragments outside the Vela supernova remnant shock-wave boundary. *Nature* 373, 587.
- Aslangil, D., Banerjee, A., Lawrie, A.G.W., 2016. Numerical investigation of initial condition effects on Rayleigh–Taylor instability with acceleration reversals. *Phys. Rev. E* 94, 053114.
- Aspden, A.J., Bell, J.B., Day, M.S., Woosley, S.E., Zingale, M., 2008a. Turbulence-flame interactions in type Ia supernovae. *Astrophys. J.* 689, 1173.
- Aspden, A., Nikiforakis, N., Dalziel, S., Bell, J.B., 2008b. Analysis of implicit LES methods. *Commun. Appl. Math. Comput. Sci.* 3, 103.
- Attal, N., Ramaprabhu, P., 2015. Numerical investigation of a single-mode chemically reacting Richtmyer–Meshkov instability. *Shock Waves* 25, 307.
- Attal, N., Ramaprabhu, P., Hossain, J., Karkhanis, V., Uddin, M., Gord, J.R., Roy, S., 2015. Development and validation of a chemical reaction solver coupled to the FLASH code for combustion applications. *Comput. & Fluids* 107, 59.
- Atzeni, S., Meyer-ter-Vehn, J., 2004. The Physics of Inertial Fusion. Oxford University Press, Oxford, UK.
- Aulery, F., Toutant, A., Bataille, F., Zhou, Y., 2015. Energy transfer process of anisothermal wall-bounded flows. *Phys. Lett. A.* 379, 1520.
- Aulery, F., Dupuy, D., Toutant, A., Bataille, F., Zhou, Y., 2017. Spectral analysis of turbulence in anisothermal channel flows. *Comput. & Fluids* 151, 115.
- Aure, R., Jacobs, J.W., 2008. Particle image velocimetry study of the shock-induced single mode Richtmyer–Meshkov instability. *Shock Waves* 18, 161.
- Bai, J.S., Liu, J.H., Wang, T., Zou, L.Y., Li, P., Tan, D.W., 2010. Investigation of the Richtmyer–Meshkov instability with double perturbation interface in nonuniform flows. *Phys. Rev. E* 81, 056302.
- Bai, J.S., Wang, B., Wang, T., Liu, K., 2012a. Numerical simulation of the Richtmyer–Meshkov instability in initially nonuniform flows and mixing with reshock. *Phys. Rev. E* 86 6, 066319.
- Bai, J.S., Wang, T., Liu, K., Li, L., Zhong, M., Jiang, Y., Tang, M., Yu, J.D., Pei, X.Y., Li, P., 2012b. Large-Eddy simulation of the three-dimensional experiment on Richtmyer–Meshkov instability induced turbulence. *Int. J. Astron. Astrophys.* 2, 28.
- Bai, X., Deng, X.L., Jiang, L., 2017. A comparative study of the single-mode Richtmyer–Meshkov instability. *Shock Waves*. <http://dx.doi.org/10.1007/s00193-017-0764-2>.
- Baker, G.R., Meiron, D.I., Orszag, S.A., 1980. Vortex simulations of the Rayleigh–Taylor instability. *Phys. Fluids* 23, 1485.
- Baker, G.R., Meiron, D.I., Orszag, S.A., 1982. Generalized vortex methods for free-surface flow problems. *J. Fluid Mech.* 123, 477.
- Baker, G.R., McCrory, R.L., Verdon, C.P., Orszag, S.A., 1987. Rayleigh–Taylor instability of fluid layers. *J. Fluid Mech.* 178, 161.
- Baker, G.R., Caflisch, R.E., Siegel, M., 1993. Singularity formation during Rayleigh–Taylor instability. *J. Fluid Mech.* 252, 51.
- Baker, W.L., Clark, M.C., Degnan, J.H., Kiuttu, G.F., McClenahan, C.R., Reinovsky, R.E., 1978. Electromagnetic-implosion generation of pulsed high-energy-density plasma. *J. Appl. Phys.* 49, 4694.
- Bakrakhov, S.M., Drennov, O.B., Kovalev, N.P., Lebedev, A.I., Meshkov, E.E., Mikhailov, A.L., Neumerzhitsky, N.V., Nizovtsev, P.N., Rayevsky, V.A., Simonov, G.P., Solov'yev, V.P., Zhidov, I.G., 1997. Lawrence Livermore National Laboratory Report No. UCRL-CR-126710.
- Balakrishnan, K., Menon, S., 2010. On turbulent chemical explosions into dilute aluminum particle clouds. *Combust. Theory Model.* 14, 583.
- Balakrishnan, K., Genin, F., Nance, D.V., Menon, S., 2010. Numerical study of blast characteristics from detonation of homogeneous explosives. *Shock Waves* 20, 147.
- Balick, B., Frank, A., 2002. Shapes and Shaping of Planetary Nebulae. *Ann. Rev. Astron. Astrophys.* 40, 439.
- Balsara, D., Shu, C.-W., 2000. Monotonicity preserving weighted essentially non-oscillatory schemes with increasingly high order of accuracy. *J. Comput. Phys.* 160, 405.
- Banerjee, R., Kanjilal, S., 2015. Effect of surface tension on single mode nonlinear Rayleigh–Taylor instability. *J. Pure Appl. Ind. Phys.* 5, 73.
- Banerjee, R., Mandal, L., Roy, S., Khan, M., Gupta, M.R., 2011. Combined effect of viscosity and vorticity on single mode Rayleigh–Taylor instability bubble growth. *Phys. Plasmas* 18, 022109.
- Banerjee, R., Mandal, L., Khan, M., Gupta, M.R., 2013. Bubble and spike growth rate of Rayleigh Taylor and Richtmeyer Meshkov instability in finite layers. *Indian J. Phys.* 87, 929.
- Barber, J.L., Kadau, K., Germann, T.C., Lomdahl, P.S., Holian, B.L., Alder, B.J., 2006. Atomistic simulation of the Rayleigh–Taylor instability. *J. Phys. Conf. Ser.* 46, 58.
- Barber, J.L., Kadau, K., Germann, T.C., Alder, B.J., 2008. Initial growth of the Rayleigh–Taylor instability via molecular dynamics. *Eur. Phys. J. B* 64, 271.
- Barenblatt, G.I., 1983. Self-similar turbulence propagation from an instantaneous plane source. In: Barenblatt, G.I., Looss, G., Joseph, D.D. (Eds.), *Nonlinear Dynamics and Turbulence*. Pitman Publishing, London.
- Barenblatt, G.I., 1996. Scaling, Self-Similarity, and Intermediate Asymptotics. Cambridge University Press, Cambridge, UK.
- Barnes, C.W., Batha, S.H., Dunne, A.M., Magelssen, G.R., Rothman, S., Day, R.D., Elliott, N.E., Haynes, D.A., Holmes, R.L., Scott, J.M., Tubbs, D.L., Youngs, D.L., Boehly, T.R., Jaanimagi, P., 2002. Observation of mix in a compressible plasma in a convergent cylindrical geometry. *Phys. Plasmas* 9, 4431.
- Barnes, J.F., Blewett, P.J., McQueen, R.G., Meyer, K.A., Venable, D., 1974. Taylor instability in solids. *J. Appl. Phys.* 45, 727.
- Barnes, J.F., Janney, D.H., London, R.K., Meyer, K.A., Sharp, D.H., 1980. Further experimentation on Taylor instability in solid. *J. Applied Phys.* 51, 4678.
- Bataille, F., Zhou, Y., 1999. Nature of the energy transfer process in compressible turbulence. *Phys. Rev. E* 59, 5417.
- Batchelor, G.K., 1953. The Theory of Homogeneous Turbulence. Cambridge University Press, Cambridge, UK.
- Batchelor, G.K., 1969. Computation of the energy spectrum in homogeneous two-dimensional turbulence. *Phys. Fluids* 12, II-233.
- Batchelor, G.K., Proudman, I., 1954. The effect of rapid distortion of a fluid in turbulent motion. *Quart. J. Mech. Appl. Math.* 7, 83.
- Batchelor, G.K., Proudman, I., 1956. The large-scale structure of homogeneous turbulence. *Philos. Trans. R. Soc. Lond. Ser. A Math. Phys. Eng. Sci.* 248, 369.
- Bazarov, Y.B., Levushov, A.E., Logvinov, A.I., Meshkov, E.E., Popov, V.V., 2007. Application of the method of defocused grids for flow visualization in shock experiments. *Trans RFNC-VNIIEF* 11, 294 (in Russian).
- Beale, J.C., Reitz, R.D., 1999. Modeling spray atomization with Kelvin–Helmholtz / Rayleigh–Taylor hybrid model. *Atomization Sprays* 9, 623.
- Belen'kii, S.Z., Fradkin, E.S., 1965. Theory of turbulent mixing. *Tr. Fiz. Inst. Nauk SSSR* 29, 207.

- Bel'kov, S.A., Abzaev, F.M., Bessarab, A.V., Bondarenko, S.V., Veselov, A.V., Gaidach, V.A., Dolgoleva, G.V., Zhdikov, N.V., Izgorodin, V.M., Kirillov, G.A., Kochemasov, G.G., 1999. Compression and heating of indirectly driven spherical fusion targets on the ISKRA-5 facility. *Laser Part. Beams* 17, 591.
- Bell, D.J., Routley, N.R., Millett, J.C.F., Whiteman, G., Collinson, M.A., Keightley, P.T., 2017. Investigation of ejecta production from tin at an elevated temperature and the eutectic alloy lead–bismuth. *J. Dyn. Behav. Mater.* 3, 208.
- Bell, J.B., Colella, P., Trangenstein, J.A., 1989. Higher order Godunov methods for general systems of hyperbolic conservation laws. *J. Comput. Phys.* 92, 362.
- Bell, J.B., Berger, M., Saltzman, J., Welcome, M., 1994. A three-dimensional adaptive mesh refinement for hyperbolic conservation laws. *SIAM J. Sci. Stat. Comput.* 15, 127.
- Bell, J.B., Day, M.S., Rendleman, C.A., Woosley, S.E., Zingale, M., 2004. Direct numerical simulations of type Ia supernovae flames I. The Rayleigh–Taylor instability. *Astrophys. J.* 608, 883.
- Bellman, R., Pennington, R.H., 1954. Effect of surface tension and viscosity on Taylor instability. *Quart. Appl. Math.* 12, 151.
- Bender, C.M., Orszag, S.A., 1978. Advanced Mathematical Methods for Scientists and Engineers. McGraw-Hill, New York.
- Berger, T.E., Slater, G., Hurlburt, N., Shine, R., Tarbell, T., Title, A., Lites, B.W., Okamoto, T.J., Ichimoto, K., Katsukawa, Y., Magara, T., Suematsu, Y., Shimizu, T., 2010. Quiescent prominence dynamics observed with the HINODE solar optical telescope I. Turbulent upflow plumes. *Astrophys. J.* 716, 1288.
- Berning, M., Rubenchik, A.M., 1998. A weekly nonlinear theory for the dynamical Rayleigh–Taylor instability. *Phys. Fluids* 10, 1564.
- Bethe, H.A., 1990. Supernova mechanisms. *Rev. Modern Phys.* 62, 801.
- Betti, R., Hurricane, O.A., 2016. Inertial-confinement fusion with lasers. *Nature Phys.* 12, 435.
- Betti, R., Sanz, J., 2006. Bubble acceleration in the ablative Rayleigh–Taylor instability. *Phys. Rev. Lett.* 97, 205002.
- Betti, R., Goncharov, V.N., McCrory, R.L., Verdon, C.P., 1995. Self-consistent cutoff wave number of the ablative Rayleigh–Taylor instability. *Phys. Plasmas* 2, 3844.
- Betti, R., Goncharov, V.N., McCrory, R.L., Sorotkin, P., Verdon, C.P., 1996. Self-consistent stability analysis of ablation fronts in inertial confinement fusion. *Phys. Plasmas* 3, 2122.
- Betti, R., Goncharov, V.N., McCrory, R.L., Verdon, C.P., 1998. Growth rates of the ablative Rayleigh–Taylor instability in inertial confinement fusion. *Phys. Plasmas* 5, 1446.
- Betti, R., Umansky, M., Lobatchev, V., Goncharov, V.N., McCrory, R.L., 2001. Hot-spot dynamics and deceleration-phase Rayleigh–Taylor instability of imploding inertial confinement fusion capsules. *Phys. Plasmas* 8, 5257.
- Betti, R., Anderson, K., Goncharov, V.N., McCrory, R.L., Meyerhofer, D.D., Skupsky, S., Town, R.P.J., 2002. Deceleration phase of inertial confinement fusion implosions. *Phys. Plasmas* 9, 2277.
- Betti, R., Zhou, C.D., Anderson, K.S., Perkins, L.J., Theobald, W., Solodov, A.A., 2007. Shock ignition of thermonuclear fuel with high areal density. *Phys. Rev. Lett.* 98, 155001.
- Betti, R., Chang, P.Y., Spears, B.K., Anderson, K.S., Edwards, J., Fatenejad, M., Lindl, J.D., McCrory, R.L., Nora, R., Shvarts, D., 2010. Thermonuclear ignition in inertial confinement fusion and comparison with magnetic confinement. *Phys. Plasmas* 17, 058102.
- Bhatia, P.K., 1974. Rayleigh–Taylor instability of a viscous compressible plasma of variable density. *Astrophys. Space Sci.* 26, 319.
- Biferale, L., Mantovani, F., Sbragaglia, M., Scagliarini, A., Toschi, F., Tripiccione, R., 2010. High resolution numerical study of Rayleigh–Taylor turbulence using a thermal lattice Boltzmann scheme. *Phys. Fluids* 22, 115112.
- Billet, G., 2005. Improvement of convective concentration fluxes in a one step reactive flow solver. *J. Comput. Phys.* 204, 319.
- Billet, G., Abgrall, R., 2003. An adaptive shock-capturing algorithm for solving unsteady reactive flows. *Comput. & Fluids* 32, 1473.
- Billet, G., Giovangigli, V., De Gassowski, G., 2008. Impact of volume viscosity on a shock–hydrogen–bubble interaction. *Combust. Theory Model.* 12, 221.
- Bird, G.A., 1976. Molecular Gas Dynamics. Clarendon, Oxford.
- Bird, G.A., 1998. Molecular Gas Dynamics and The Direct Simulation of Gas Flows. Clarendon, Oxford.
- Birk, G.T., 2002. The onset of Rayleigh–Taylor instabilities in magnetized partially ionized dense dusty plasmas. *Phys. Plasmas* 9, 745.
- Birkhoff, G., 1955. Taylor Instability and Laminar Mixing. University of California Report No. LA-1862.
- Birkhoff, G., 1962. Hydrodynamic instability. In: Proc. of The Symp. Appl. Math XIII. American Math. Soc., Providence RI, pp. 55–76.
- Birkhoff, G., Carter, D., 1957. Rising plane bubbles. *J. Math. Mech.* 6, 769.
- Blondin, J.M., Ellison, D.C., 2001. Rayleigh–Taylor instabilities in young supernova remnants undergoing efficient particle acceleration. *Astrophys. J.* 560, 244.
- Bodner, S.E., 1974. Rayleigh–Taylor instability and laser-pellet fusion. *Phys. Rev. Lett.* 33, 761.
- Boehly, T.R., Brown, D.L., Craxton, R.S., Keck, R.L., Knauer, J.P., Kelly, J.H., Kessler, T.J., Kumpan, S.A., bucks, S.J., Letzring, S.A., Marshall, F.J., McCrory, R.L., Morse, S.F.B., Seka, W., Sowes, J.M., Verdon, C.P., 1997. Initial performance results of the OMEGA laser system. *Opt. Commun.* 133, 495.
- Boffetta, G., Mazzino, A., Musacchio, S., Vozella, L., 2009. Kolmogorov scaling and intermittency in Rayleigh–Taylor turbulence. *Phys. Rev. E* 79, 065301.
- Boffetta, G., Mazzino, A., Musacchio, S., Vozella, L., 2010. Statistics of mixing in three-dimensional Rayleigh–Taylor turbulence at low Atwood number and Prandtl number one. *Phys. Fluids* 22, 035109.
- Boffetta, G., Mazzino, A., Musacchio, S., 2011. Effects of polymer additives on Rayleigh–Taylor turbulence. *Phys. Rev. E* 83, 056318.
- Boffetta, G., De Lillo, F., Mazzino, A., Musacchio, S., 2012. Bolgiano scale in confined Rayleigh–Taylor turbulence. *J. Fluid Mech.* 690, 426.
- Bolgiano, R., 1959. Turbulent spectra in a stably stratified atmosphere. *J. Geophys. Res.* 64, 2226.
- Bolotnov, I.A., Lahey Jr., R.T., Drew, D.A., Jansen, K.E., Oberai, A.A., 2010. Spectral analysis of turbulence based on the DNS of a channel flow. *Comput. & Fluids* 39, 640.
- Bonazza, R., Sturtevant, B., 1996. X-ray measurements of growth rates at a gas interface accelerated by shock waves. *Phys. Fluids* 8, 2496.
- Bondarenko, S.V., Dolgoleva, G.V., Novikova, E.A., 2007. Numerical simulation of three-dimensional X-ray and laser field inhomogeneities in experiments with spherical box converters on the Iskra-5 facility. *Quantum Electron.* 37, 372.
- Boris, J.P., 1989. On large eddy simulations using sub-grid turbulence models, Wither turbulence?. In: Lumley, J.L. (Ed.), Turbulence at the Crossroads. In: Lecture Notes in Physics, vol. 257, Springer, Berlin, pp. 344–353.
- Boris, J., Grinstein, F., Oran, E., Kolbe, R., 1992. New insights into large eddy simulation. *Fluid Dyn. Res.* 10, 199.
- Borue, V., Orszag, S.A., 1995a. Forced three-dimensional homogeneous turbulence with hyperviscosity. *Europhys. Lett.* 29, 687.
- Borue, V., Orszag, S.A., 1995b. Self-similar decay of three-dimensional homogeneous turbulence with hyperviscosity. *Phys. Rev. E* 51, R856.
- Bouquet, S., Falize, E., Michaut, C., Gregory, C.D., Loupias, B., Vinci, T., Koenig, M., 2010. From lasers to the universe: scaling laws in laboratory astrophysics. *High Energy Density Phys.* 6, 368.
- Bourgade, J.L., Marmoret, R., Darbon, S., Rosch, R., Troussel, P., Villette, B., Glebov, V., et al., 2008. Diagnostics hardening for harsh environment in Laser Mégajoule. *Rev. Sci. Instrum.* 79, 10F301.
- Boussinesq, V.J., 1877. Essai sur la théorie des eaux courantes, Mémoires présentés par divers savants à l'Académie des Sciences. Paris 23, 1.
- Bouzgarrou, G., Bury, Y., Jamme, S., Joly, L., Haas, J.-F., 2014. Laser Doppler velocimetry measurements in turbulent gaseous mixing induced by the Richtmyer–Meshkov instability: Statistical convergence issues and turbulence quantification. *ASME J. Fluids Eng.* 136, 091209.
- Bradley, P.A., 2014. The effect of mix on capsule yields as a function of shell thickness and gas fill. *Phys. Plasmas* 21, 062703.
- Bradley, P.A., Cobble, J.A., Tregillis, I.L., Schmitt, M.J., Obrey, K.D., Glebov, V., Batha, S.H., Magelssen, G.R., Fincke, J.R., Hsu, S.C., Krasheninnikova, N.S., Murphy, T.J., Wysocki, F.J., 2012. Role of shocks and mix caused by capsule defects. *Phys. Plasmas* 19, 092703.

- Branch, D., Tamman, G.A., 1992. Type Ia supernovae as standard candles. *Annu. Rev. Astron. Astrophys.* 30, 359.
- Bratsun, D.A., De Wit, A., 2011. Buoyancy-driven pattern formation in reactive immiscible two-layer systems. *Chem. Eng. Sci.* 66, 5723.
- Brenner, M.P., Lohse, D., Dupont, T.F., 1995. Bubble shape oscillations and the onset of sonoluminescence. *Phys. Rev. Lett.* 75, 954.
- Britten, R.E., Hanna, S.R., 2003. Flow and dispersion in urban areas. *Annu. Rev. Fluid. Mech.* 35, 469.
- Brode, H.L., 1957. A Calculation of the Blast Wave from a Spherical Charge of TNT. Rand Report RM-196. Rand Corp, Santa Monica CA.
- Brouillette, M., 2002. The Richtmyer–Meshkov Instability. *Annu. Rev. Fluid Mech.* 34, 445.
- Brouillette, M., Sturtevant, B., 1993. Experiments on the Richtmyer–Meshkov instability: Small-scale perturbations on a plane interface. *Phys. Fluids A* 5, 916.
- Brouillette, M., Sturtevant, B., 1994. Experiments on the Richtmyer–Meshkov instability: single-scale perturbations on a continuous interface. *J. Fluid Mech.* 263, 271.
- Brueckner, K.A., Jorna, S., 1974. Laser-driven fusion. *Rev. Modern Phys.* 46, 325.
- Bryson, A.E., Gross, R.W.F., 1961. Diffraction of strong shocks by cones, cylinders and spheres. *J. Fluid Mech.* 10, 1.
- Bucciantini, N., Amato, E., Bandiera, R., Blondin, J.M., Del zanna, L., 2004. Magnetic Rayleigh–Taylor instability for Pulsar Wind Nebulae in expanding Supernova Remnants. *Astron. Astrophys.* 423, 253.
- Budzinski, J.M., Benjamin, R.F., Jacobs, J.W., 1994. Influence of initial conditions on the flow patterns of a shock-accelerated thin fluid layer. *Phys. Fluids* 6, 3510.
- Buffett, B.A., 2000. Earth's core and the geodynamo. *Science* 288, 2007.
- Burlot, A., Gréa, B.-J., Godefert, F.S., Cambon, C., Griffond, J., 2015. Spectral modelling of high Reynolds number unstably stratified homogeneous turbulence. *J. Fluid Mech.* 765, 17.
- Burrows, A., 2000. Supernova explosions in the Universe. *Nature* 403, 727.
- Burrows, A., 2013. Colloquium: Perspectives on core-collapse supernova theory. *Rev. Modern Phys.* 85, 245.
- Burrows, A., Hayes, J., Fryxell, B.A., 1995. On the nature of core-collapse supernova explosions. *Astrophys. J.* 450, 830.
- Burshtein, A.I., 2008. Introduction to Thermodynamics and Kinetic Theory of Matter. Wiley.
- Burton, G.C., 2008. The nonlinear large-eddy simulation method (nLES) applied to $Sc \approx 1$ and $Sc \gg 1$ passive-scalar mixing. *Phys. Fluids* 20, 035103.
- Burton, G.C., 2011. Study of ultrahigh Atwood-number Rayleigh–Taylor mixing dynamics using the nonlinear large-eddy simulation method. *Phys. Fluids* 23, 045106.
- Busschaert, C., Falize, É., Loupias, B., Michaut, C., Ravasio, A., Pelka, A., Yurchak, R., Koenig, M., 2013. POLAR project: a numerical study to optimize the target design. *New J. Phys.* 15, 035020.
- Buttler, W.T., Routley, N., Hixson, R.S., King, N.S.P., Olson, R.T., Rigg, P.A., Rimmer, A., Zellner, M.B., 2007a. Method to separate and determine the amount of ejecta produced in a second material-fragmentation event. *Appl. Phys. Lett.* 90, 151921.
- Buttler, W.T., Zellner, M.B., Olson, R.T., Rigg, P.A., Hixson, R.S., Hammerberg, J.E., Obst, A.W., Payton, J.R., Iverson, A., Young, J., 2007b. Dynamic comparisons of piezoelectric ejecta diagnostics. *J. Appl. Phys.* 101, 063547.
- Buttler, W.T., Oró, D.M., Preston, D.L., Mikaelian, K.O., Cherne, F.J., Hixson, R.S., Mariam, F.G., Morris, C., Stone, J.B., Terrones, G., Tupa, D., 2012. Unstable Richtmyer–Meshkov growth of solid and liquid metal in vacuum. *J. Fluid Mech.* 703, 60.
- Buttler, W.T., Oró, D.M., Olson, R.T., Cherne, F.J., Hammerberg, J.E., Hixson, R.S., Monfared, S.K., et al., 2014. Second shock ejecta measurements with an explosively driven two-shockwave drive. *J. Appl. Phys.* 116, 103519.
- Buttler, W.T., Lamoreaux, S.K., Schulze, R.K., Schwarzkopf, J.D., Cooley, J.C., Grover, M., Hammerberg, J.E., La Lone, B.M., Llobet, A., Manzanares, R., Martinez, J.I., Schmidt, D.W., Sheppard, D.G., Stevens, G.D., Turley, W.D., Veeser, L.R., 2017. Ejecta transport breakup conversion. *J. Dyn. Behav. Mater.* 3, 334.
- Bychkov, V., Golberg, S.M., Liberman, M.A., 1994. Self-consistent model of the Rayleigh–Taylor instability in ablatively accelerated laser plasma. *Phys. Plasmas* 1, 2976.
- Bychkov, V., Marklund, M., Modestov, M., 2008. The Rayleigh–Taylor instability and internal waves in quantum plasmas. *Phys. Lett. A* 372, 3042.
- Cabot, W., Cook, A.W., 2006. Reynolds number effects on the Rayleigh–Taylor instability with possible implications for type-Ia supernovae. *Nature Phys.* 2, 562.
- Cabot, W., Zhou, Y., 2013. Statistical measurements of scaling and anisotropy of turbulent flows induced by Rayleigh–Taylor instability. *Phys. Fluids* 25, 015107.
- Cabot, W., Schilling, O., Zhou, Y., 2004. Influence of subgrid scales on resolvable turbulence and mixing in Rayleigh–Taylor flow. *Phys. Fluids* 16, 495.
- Calder, A.C., Fryxell, B., Plewa, T., Rosner, R., Dursi, L.J., Weirs, V.G., Dupont, T., Robey, H.F., Kane, J.O., Remington, B.A., Drake, R.P., Dimonte, G., Zingale, M., Timmes, F.X., Olson, K., Ricker, P., MacNeice, P., Tufo, H.M., 2002. On validating as astrophysical simulation code. *Astrophys. J. Suppl. Ser.* 143, 201.
- Callebaut, D.K., Lineaire en niet-lineaire Perturbaties in Hydro-, Magneto-en Gravitodynamika. Rijksuniversiteit, Instituut voor Nukleaire Wetenschappen, 1972.
- Cameron, I.G., Pike, H.H.M., 1965. The instability of an interface between two fluid under variable normal acceleration. In: Proceedings Fourth Symposium (international) on Detonation. Office of Naval Research, United States Dept. of the Navy, p. 305.
- Canaud, B., Laffite, S., Temporal, M., 2011. Shock ignition of direct-drive double-shell targets. *Nucl. Fusion* 51, 062001.
- Canuto, V.M., Goldman, I., 1985. Analytical model for large-scale turbulence. *Phys. Rev. Lett.* 54, 430.
- Cao, Y.G., Guo, H.Z., Zhang, Z.F., Sun, Z.H., Chow, W.K., 2011. Effect of viscosity on the growth of Rayleigh–Taylor instability. *J. Phys. A* 44, 275501.
- Caproni, A., Lanfranchi, G.A., Luiz da Silva, A., Falceta-Gonçalves, D., 2015. Three-dimensional hydrodynamical simulations of the supernovae-driven gas loss in the dwarf spheroidal galaxy Ursa Minor. *Astrophys. J.* 805, 109.
- Carlès, P., Popinet, S., 2001. Viscous nonlinear theory of Richtmyer–Meshkov instabilities. *Phys. Fluids* 13, 1833.
- Carlès, P., Popinet, S., 2002. The effect of viscosity surface tension and nonlinearity on Richtmyer–Meshkov instabilities. *Eur. J. Mech. B Fluids* 21, 511.
- Carlès, P., Huang, Z., Carbone, G., Rosenblatt, C., 2006. Rayleigh–Taylor instability for immiscible fluids of arbitrary viscosities: a magnetic levitation investigation and theoretical model. *Phy. Rev. Lett.* 104501.
- Case, K.M., 1960. Taylor instability of an inverted atmosphere. *Phys. Fluids* 3, 366.
- Casey, D.T., Woods, D.T., Smalyuk, V.A., Hurricane, O.A., Glebov, V.Y., Stoeckl, C., Theobald, W., Wallace, R., Nikroo, A., Schoff, M., Shuldberg, C., Wu, K.J., Frenje, J.A., Landen, O.L., Remington, B.A., Glendinning, G., 2015a. Performance and mix measurements of indirect drive Cu-doped Be implosions. *Phys. Rev. Lett.* 114, 205002.
- Casey, D.T., Milovich, J.L., Smalyuk, V.A., Clark, D.S., Robey, H.F., Pak, A., Macphee, A.G., et al., 2015b. Improved performance of high areal density indirect drive implosions at the National Ignition Facility using a four-shock adiabat shaped drive. *Phys. Rev. Lett.* 115, 105001.
- Casey, D.T., Sayre, D.B., Brune, C.R., Smalyuk, V.A., Weber, C.R., Tipton, R.E., Pino, J.E., Grim, G.P., Remington, B.A., Dearborn, D., Benedetti, L.R., et al., 2017. Thermonuclear reactions probed at stellar-core conditions with laser-based inertial-confinement fusion. *Nature Phys.* 13, 1227.
- Casner, A., Caillaud, T., Darbon, S., Duval, A., Thfouin, I., Jadaud, J.P., LeBreton, J.P., Reverdin, C., Rosse, B., Rosch, R., Blanchot, N., Villette, B., Wrobel, R., Miquel, J.L., 2014., 2015a. LMJ/PETAL laser facility: Overview and opportunities for laboratory astrophysics. *High Energy Density Phys.* 17, 2.
- Casner, A., Martinez, D., Smalyuk, V., Masse, L., Kane, J.O., Villette, B., Fariaut, J., et al., 2015b. Long duration X-ray drive hydrodynamics experiments relevant for laboratory astrophysics. *High Energy Density Phys.* 17, 146.

- Castiglioni, G., Domaradzki, J.A., 2015. A numerical dissipation rate and viscosity in flow simulations with realistic geometry using low-order compressible Navier–Stokes solvers. *Comput. & Fluids* 119, 37.
- Catherasoo, C.J., Sturtevant, B., 1983. Shock dynamics in non-uniform media. *J. Fluid Mech.* 127, 539.
- Cavailler, C., Mercier, P., Rodriguez, G., Haas, J.F., 1990. A new vertical shock tube for Rayleigh–Taylor instability measurements. *AIP Conf. Proc.* 208, 564.
- Celani, A., Mazzino, A., Vozella, L., 2006. Rayleigh–Taylor turbulence in two dimensions. *Phys. Rev. Lett.* 96, 134504.
- Celani, A., Mazzino, A., Muratore-Ginanneschi, P., Vozella, L., 2009. Phase-field model for the Rayleigh–Taylor instability of immiscible fluids. *J. Fluid Mech.* 622, 115.
- Celani, A., Musacchio, S., Vincenzi, D., 2010. Turbulence in more than two and less than three dimensions. *Phys. Rev. Lett.* 104, 184506.
- Chandrasekhar, S., 1931. The maximum mass of ideal white dwarfs. *Astrophys. J.* 74, 81.
- Chandrasekhar, S., 1938. Stellar Structure. University of Chicago Press, Chicago.
- Chandrasekhar, S., 1955. The character of equilibrium of an incompressible heavy viscous fluid of variable density. *Proc. Cambridge Philos. Soc.* 51, 162.
- Chandrasekhar, S., 1961. Hydrodynamic and Hydromagnetic Stability. Oxford Univ. Press, Oxford, UK.
- Chapman, P.R., Jacobs, J.W., 2006. Experiments on the three-dimensional incompressible Richtmyer–Meshkov instability. *Phys. Fluids* 18, 074101.
- Chen, F., Xu, A.-G., Zhang, G.-C., 2016. Viscosity, heat conductivity and Prandtl number effects in the Rayleigh–Taylor Instability. *Front. Phys.* 11, 114703.
- Chen, H.B., Hilko, B., Panarella, E., 1994. The Rayleigh–Taylor instability in the spherical pinch. *J. Fusion Res.* 13, 275.
- Chen, Q., Chen, B., Shi, L., Yi, Y., Wang, Y., 2015. Numerical study on Rayleigh–Taylor instabilities in the lightning return stroke. *Phys. Plasmas* 22, 092902.
- Chen, S., Doolen, G.D., 1998. Lattice Boltzmann method for fluid flows. *Annu. Rev. Fluid. Mech.* 30, 329.
- Chen, X., Dong, G., Jiang, H., 2017a. A three-dimensional numerical study on instability of sinusoidal flame induced by multiple shock waves. *Acta Mech. Sin.* 33, 316.
- Chen, Y.-T., Hong, R.-K., Chen, H.-Y., Tang, T.G., Ren, G.W., 2017b. Experimental examination of ejecta production on shock-melted Sn targets under various surface roughnesses. *J. Dyn. Behav. Mater.* 3, 174.
- Cheng, B., Glimm, J., Sharp, D.H., 2002. A three-dimensional renormalization group bubble merger model for Rayleigh–Taylor mixing. *Chaos* 12, 267.
- Cherfils, C., Lafitte, O., 2000. Analytic solutions of the Rayleigh equation for linear density profiles. *Phys. Rev. E* 62, 2967.
- Cherfils, C., Mikaelian, K.O., 1996. Simple model for the turbulent mixing width at an ablating surface. *Phys. Fluids* 8, 522.
- Cherne, F.J., Hammerberg, J.E., Andrews, M.J., Karkhanis, V., Ramaprabhu, P., 2015. On shock driven jetting of liquid from non-sinusoidal surfaces into a vacuum. *J. Appl. Phys.* 118, 185901.
- Chertkov, M., 2003. Phenomenology of Rayleigh–Taylor Turbulence. *Phys. Rev. Lett.* 91, 115001.
- Chertkov, M., Kolokolov, I., Lebedev, V., 2005. Effects of surface tension on immiscible Rayleigh–Taylor turbulence. *Phys. Rev. E* 71, 055301.
- Chertkov, M., Lebedev, V., Vladimirova, N., 2009. Reactive Rayleigh–Taylor turbulence. *J. Fluid Mech.* 633, 1.
- Chevalier, R.A., Blondin, J.M., Emmering, R.T., 1992. Hydrodynamic instabilities in supernova remnants – Self-similar driven waves. *Astrophys. J.* 392, 118.
- Chhajlani, R.K., Vaghela, D.S., 1989. Rayleigh–Taylor instability of ionized viscous fluids with FLR-corrections and surface-tension. *Astrophys. Space Sci.* 155, 257.
- Chollet, J.-P., Lesieur, M., 1981. Parameterization of small scales of three-dimensional isotropic turbulence utilizing spectral closures. *J. Atmos. Sci.* 38, 2747.
- Chou, Y.-J., Shao, Y.-C., 2016. Numerical study of particle-induced Rayleigh–Taylor instability: Effects of particle settling and entrainment. *Phys. Fluids* 28, 043302.
- Cimarelli, A., De Angelis, E., 2014. The physics of energy transfer toward improved subgrid-scale models. *Phys. Fluids* 26, 055103.
- Cimarelli, A., De Angelis, E., Casciola, C.M., 2013. Paths of energy in turbulent channel flows. *J. Fluid Mech.* 715, 436.
- Clark, D.H., Stephenson, F.R., 1977. The Historical Supernovae. Pergamon, Oxford.
- Clark, D.S., Haan, S.W., Cook, A.W., Edwards, M.J., Hammel, B.A., Koning, J.M., Marinak, M.M., 2011. Short-wavelength and three-dimensional instability evolution in National Ignition Facility ignition capsule designs. *Phys. Plasmas* 18, 082701.
- Clark, D.S., Hinkel, D.E., Eder, D.C., Jones, O.S., Haan, S.W., Hammel, B.A., Marinak, M.M., Milovich, J.L., Robey, H.F., Suter, L.J., Town, R.P.J., 2013. Detailed implosion modeling of deuterium-tritium layered experiments on the National Ignition Facility. *Phys. Plasmas* 20, 056318.
- Clark, D.S., Tabak, M., 2005. Acceleration- and deceleration-phase nonlinear Rayleigh–Taylor growth at spherical interfaces. *Phys. Rev. E* 72, 056308.
- Clark, D.S., Tabak, M., 2006. Linear and nonlinear Rayleigh–Taylor growth at strongly convergent spherical interfaces. *Phys. Fluids* 18, 064106.
- Clark, D.S., Weber, C.R., Milovich, J.L., Salmonson, J.D., Kritcher, A.L., Haan, S.W., Hammel, B.A. et al., 2016. Three-dimensional simulations of low foot and high foot implosion experiments on the National Ignition Facility. *Phys. Plasmas* 23, 056302.
- Clark, T.T., Zemach, C., 1995. A spectral model applied to homogeneous turbulence. *Phys. Fluids* 7, 1674.
- Clark, T.T., Zemach, C., 1998. Symmetries and the approach to statistical equilibrium in isotropic turbulence. *Phys. Fluids* 10, 2846.
- Clark, T.T., Zhou, Y., 2003. Self-similarity of two flows induced by instabilities. *Phys. Rev. E* 68, 066305.
- Clark, T.T., Zhou, Y., 2006. Growth rate exponents of Richtmyer–Meshkov mixing layers. *ASME J. Appl. Mech.* 73, 461.
- Clavin, P., Williams, F., 2005. Asymptotic spike evolution in Rayleigh–Taylor instability. *J. Fluid Mech.* 525, 105.
- Clery, D., 2015. Laser fusion with a difference. *Science* 347, 111.
- Cobos Campos, F., Wouchuk, J.G., 2014. Analytical asymptotic velocities in linear Richtmyer–Meshkov-like flows. *Phys. Rev. E* 90, 053007.
- Cobos Campos, F., Wouchuk, J.G., 2016. Analytical scalings of the linear Richtmyer–Meshkov instability when a shock is reflected. *Phys. Rev. E* 93, 053111.
- Cobos Campos, F., Wouchuk, J.G., 2017. Analytical scalings of the linear Richtmyer–Meshkov instability when a rarefaction is reflected. *Phys. Rev. E* 96, 013102.
- Cohen, I.M., Kundu, P.K., 2004. Fluid Mechanics, third ed. Elsevier, Amsterdam.
- Cohen, R.H., Dannevick, W.P., Dimits, A.M., Eliason, D.E., Mirin, A.A., Zhou, Y., Porter, D.H., Woodward, P.R., 2002. Three-dimensional simulation of a Richtmyer–Meshkov instability with a two-scale initial perturbation. *Phys. Fluids* 14, 3692.
- Cole, R.H., 1948. Underwater Explosions. Princeton University Press, Princeton, New Jersey.
- Cole, R.L., Tankin, R.S., 1973. Experimental study of Taylor instability. *Phys. Fluids* 16, 1810.
- Collins, B.D., Jacobs, J.W., 2002. PLIF flow visualization and measurements of the Richtmyer–Meshkov instability of an air/SF₆ interface. *J. Fluid Mech.* 464, 113.
- Connor, J.W., Taylor, J.B., 1977. Scaling laws for plasma confinement. *Nucl. Fusion* 17, 5.
- Contopoulos, I., Kazanas, D., Papadopoulos, D.B., 2016. The magnetic Rayleigh–Taylor instability in astrophysical discs. *Mon. Not. R. Astron. Soc.* 462, 565.
- Cook, A.W., 2007. Artificial fluid properties for large-eddy simulation of compressible turbulent mixing. *Phys. Fluids* 19, 055103.
- Cook, A.W., 2009. Enthalpy diffusion in multicomponent flows. *Phys. Fluids* 21, 055109.
- Cook, A.W., Cabot, W.H., 2004. A high-wavenumber viscosity for high-resolution numerical methods. *J. Comput. Phys.* 195, 594.
- Cook, A.W., Cabot, W.H., 2005. Hyperviscosity for shock-turbulence interactions. *J. Comput. Phys.* 203, 379.
- Cook, A.W., Dimotakis, P.E., 2001. Transition stages of Rayleigh–Taylor instability between miscible fluids. *J. Fluid Mech.* 443, 69.
- Cook, A.W., Zhou, Y., 2002. Energy transfer in Rayleigh–Taylor instability. *Phys. Rev. E* 66, 026312.
- Cook, A.W., Cabot, W., Miller, P.L., 2004. The mixing transition in Rayleigh–Taylor instability. *J. Fluids Mech.* 511, 333.
- Cook, R.C., Kozioziemski, B.J., Nikroo, A., Wilkens, H.L., Bhandarkar, S., Forsman, A.C., Haan, S.W., Hoppe, M.L., Huang, H., Mapoles, E., Moody, J.D., Sater, J.D., Seugling, R.M., Stephens, R.B., Takagi, M., Xu, H.W., 2008. National Ignition Facility target design and fabrication. *Laser Part. Beams* 26, 479.

- Craxton, R.S., Anderson, K.S., Boehly, T.R., Goncharov, V.N., Harding, D.R., Knauer, J.P., McCrory, R.L., et al., 2015. Direct-drive inertial confinement fusion: A review. *Phys. Plasmas* 22, 110501.
- Cross, J.E., Gregori, G., Foster, J.M., Graham, P., Bonnet-Bidaud, J.M., Busschaert, C., Charpentier, N., Danson, C.N., Doyle, H.W., Drake, R.P., Fyrrh, J., 2016. Laboratory analogue of a supersonic accretion column in a binary star system. *Nature Commun.* 7, 11899.
- Cross, J.E., Reville, B., Gregori, G., 2014. Scaling of magneto-quantum-radiative hydrodynamic equations: from laser-produced plasmas to astrophysics. *Astrophys. J.* 795, 59.
- Crowther, P.A., 2007. Physical properties of Wolf-Rayet stars. *Annu. Rev. Astron. Astrophys.* 45, 177.
- Cui, A., Street, R.L., 2004. Large-eddy simulation of coastal upwelling flow. *Environ. Fluid Mech.* 4, 197.
- Curzon, F.L., Folkerski, A., Latham, R., Nation, J.A., 1960. Experiments on the growth rate of surface instabilities in a linear pinched discharge. *Proc. R. Soc. A* 257, 386.
- Dahlburg, J.P., Gardner, J.H., Doolen, G.D., Haan, S.W., 1993. The effect of shape in the three-dimensional ablative Rayleigh–Taylor instability I. Single-mode perturbations. *Phys. Fluids B* 5, 571.
- Dahlburg, J.P., Fyfe, D.E., Gardner, J.H., Haan, S.W., Bodner, S.E., Doolen, G.D., 1995. Three dimensional multimode simulations of the ablative Rayleigh–Taylor instability. *Phys. Plasmas* 2, 2453.
- Daly, B.J., 1967. Numerical study of two fluids Rayleigh–Taylor instability. *Phys. Fluids* 10, 297.
- Daly, B.J., 1969. Numerical study of the effect of surface tension on interface instability. *Phys. Fluids* 12, 1340.
- Dalziel, S.B., 1993. Rayleigh–Taylor instability: experiments with image analysis. *Dyn. Atmos. Oceans* 20, 127.
- Dalziel, S.B., Linden, P.F., Youngs, D.L., 1999. Self-similarity and internal structure of turbulence induced by Rayleigh–Taylor instability. *J. Fluid Mech.* 399, 1.
- Dalziel, S.B., Patterson, M.D., Caulfield, C.P., Coomaraswamy, I.A., 2008. Mixing efficiency in high-aspect-ratio Rayleigh–Taylor experiments. *Phys. Fluids* 20, 065106.
- d'Angelo, N., 1993. The Rayleigh–Taylor instability in dusty plasmas. *Planetary and space science* 41, 469.
- Darlington, R.M., McAbee, T.L., Rodrigue, G., 2001. A study of ALE simulations of Rayleigh–Taylor instability. *Comput. Phys. Comm.* 135, 58.
- Darlington, R.M., McAbee, T.L., Rodrigue, G., 2002. Large eddy simulation and ALE mesh motion in Rayleigh–Taylor instability simulation. *Comput. Phys. Comm.* 144, 261.
- Darova, N.S., Dibirov, O.A., Shanin, A.A., Yanilkin, Yu.V., Zharova, G.V., 1994. EGAK codes. Lagrangian-Eulerian method for 2D gas-dynamic flows in multicomponent medium. *VANT. Ser. Mat. Mod. Fiz. Proc. N2*, 49 (in Russian).
- Davidson, K., Fesen, R.A., 1985. Recent developments concerning the Crab Nebula. *Annu. Rev. Astron. Astrophys.* 23, 119.
- Davies, R.M., Taylor, G.I., 1950. The mechanics of large bubbles rising through extended liquids and through liquids in tubes. *Proc. R. Soc. Lond. Ser. A Math. Phys. Eng. Sci.* 200, 375.
- Deardorff, J.W., 1980. Stratocumulus-capped mixed layers derived from a three-dimensional model. *Bound.-Layer Meteorol.* 18, 495.
- Debacq, M., Hulin, J.-P., Salin, D., Perrin, B., Hinch, E.J., 2003. Buoyant mixing of miscible fluids of varying viscosities in vertical tubes. *Phys. Fluids* 15, 3846.
- Debnath, L., 1994. Nonlinear Water Waves. Academic Press, Boston.
- Degnan, J.H., Lehr, F.M., Beason, J.D., Baca, G.P., Bell, D.E., Chesley, A.L., Coffey, S.K., Dietz, D., Dunlap, D.B., Englert, S.E., Englert, T.J., Gale, D.G., Graham, J.D., Havranek, J.J., Holmberg, C.D., Hussey, T.W., Lewis, R.A., Outten, C.A., Peterkin Jr., R.E., Price, D.W., Roderick, N.F., Ruden, E.L., Shumlak, U., Smith, G.A., Turchi, P.J., 1995. Electromagnetic Implosion of Spherical Liner. *Phys. Rev. Lett.* 74, 98.
- De Groot, J.S., Toor, A., Golberg, S.M., Liberman, M.A., 1997. Growth of the Rayleigh–Taylor instability in an imploding Z-pinch. *Phys. Plasmas* 4, 737.
- de la Calleja, E.M., Zetina, S., Zenit, R., 2014. Rayleigh–Taylor instability creates provocative images in painting. *Phys. Fluids* 26, 091102.
- DeNeef, P., 1975. Two waves on a beam plasma system. *Phys. Fluids* 18, 1209.
- Dickel, J.R., Eilek, J.A., Jones, E.M., Reynolds, S.P., 1989. Radio emission from young supernova remnants - Effects of an inhomogeneous circumstellar medium. *Astrophys. J. Suppl. Ser.* 70, 497.
- Diegelmann, F., Tritschler, V., Hückel, S., Adams, N., 2016a. On the pressure dependence of ignition and mixing in two-dimensional reactive shock-bubble interaction. *Combust. Flame* 163, 414.
- Diegelmann, F.R., Hückel, S., Adams, N.A., 2016b. Shock Mach number influence on re-action wave types and mixing in reactive shock-bubble interaction. *Combust. Flame* 174, 085.
- Diegelmann, F.R., Hückel, S., Adams, N.A., 2017. Three-dimensional reacting shock-bubble interaction. *Combust. Flame* 181, 300.
- Dimonte, G., 1982. Experimental test of modulational theory and stochasticity of nonlinear oscillations. *Phys. Fluids* 25, 604.
- Dimonte, G., 2000. Spanwise homogeneous buoyancy-drag model for Rayleigh–Taylor mixing and experimental verification. *Phys. Plasmas* 7, 2255.
- Dimonte, G., 2004. Dependence of turbulent Rayleigh–Taylor instability on initial perturbations. *Phys. Rev. E* 69, 056305.
- Dimonte, G., Ramaprabhu, P., 2010. Simulations and model of the nonlinear Richtmyer–Meshkov instability. *Phys. Fluids* 22, 014104.
- Dimonte, G., Remington, B., 1993. Richtmyer–Meshkov experiments on the Nova laser at high compression. *Phys. Rev. Lett.* 70, 1806.
- Dimonte, G., Schneider, M., 1996. Turbulent Rayleigh–Taylor instability experiments with variable acceleration. *Phys. Rev. E* 54, 3740.
- Dimonte, G., Schneider, M., 1997. Turbulent Richtmyer–Meshkov instability experiments with strong radiatively driven shocks. *Phys. Plasmas* 4.
- Dimonte, G., Schneider, M., 2000. Density ratio dependence of Rayleigh–Taylor mixing for sustained and impulsive acceleration histories. *Phys. Fluids* 12, 304.
- Dimonte, G., Frerking, C.E., Schneider, M., 1995. Richtmyer–Meshkov instability in the turbulent regime. *Phys. Rev. Lett.* 74, 4855.
- Dimonte, G., Morrison, J., Hulsey, S., Nelson, D., Weaver, S., Susoeff, A., Hawke, R., Schneider, M., Batteaux, J., Lee, D., Ticehurst, J., 1996a. A linear electric motor to study turbulent hydrodynamics. *Rev. Sci. Instrum.* 67, 302.
- Dimonte, G., Frerking, C.E., Schneider, M., Remington, B., 1996b. Richtmyer–Meshkov instability with strong radiatively driven shocks. *Phys. Plasmas* 3, 614.
- Dimonte, G., Youngs, D.L., Dimits, A., Weber, S., Marinak, M., Wunsch, S., Garasi, C., Robinson, A., Andrews, M.J., Ramaprabhu, P., Calder, A.C., Fryxell, B., Biello, J., Dursi, L., MacNeice, P., Olson, K., Ricker, P., Rosner, R., Timmes, F., Tufo, H., Young, Y.-N., Zingale, M., 2004. A comparative study of the turbulent Rayleigh–Taylor instability using high-resolution three-dimensional numerical simulations: The Alpha-Group collaboration. *Phys. Fluids* 16, 1668.
- Dimonte, G., Ramaprabhu, P., Youngs, D.L., Andrews, M.J., Rosner, R., 2005. Recent advances in the turbulent Rayleigh–Taylor instability. *Phys. Plasmas* 12, 056301.
- Dimonte, G., Ramaprabhu, P., Andrews, M.J., 2007. Rayleigh–Taylor instability with complex acceleration history. *Phys. Rev. E* 76, 046313.
- Dimonte, G., Terrones, G., Cherne, F.J., German, T.C., Dupont, V., Kadau, K., Buttler, W.T., Oro, D.M., Morris, C., Preston, D.L., 2011. Use of the Richtmyer–Meshkov instability to infer yield stress at high-energy densities. *Phys. Rev. Lett.* 107, 264502.
- Dimonte, G., Terrones, G., Cherne, F.J., Ramaprabhu, P., 2013. Ejecta source model based on the nonlinear Richtmyer–Meshkov instability. *J. Appl. Phys.* 113, 024905.
- Dimotakis, P.E., 2000. The mixing transition in turbulent flow. *J. Fluid Mech.* 409, 69.
- Dimotakis, P.E., 2005. Turbulent mixing. *Annu. Rev. Fluid Mech.* 37, 329.
- DiPrima, R.C., Swinney, H.L., 1981. Hydrodynamic instabilities and The Transition to Turbulence. Springer, Berlin.
- Di Stefano, C.A., Kuranz, C.C., Keiter, P.A., Klein, S.R., Marion, D.C., Drake, R.P., 2012. Late-time breakup of laser-driven hydrodynamics experiments. *High Energy Density Phys.* 8, 360.

- Di Stefano, C.A., Merritt, E.C., Doss, F.W., Flippo, K.A., Rasmus, A.M., Schmidt, D.W., 2017. Evolution of surface structure in laser-preheated perturbed materials. *Phys. Rev. E* 95, 023202.
- Dittrich, T.R., Hammel, B.A., Keane, C.J., McEachern, R., Turner, R.E., Haan, S.W., Suter, L.J., 1994. Diagnosis of pusher-fuel mix in indirectly driven Nova implosions. *Phys. Rev. Lett.* 73, 2324.
- Dittrich, T.R., Hurricane, O.A., Callahan, D.A., Dewald, E.L., Döppner, T., Hinkel, D.E., Berzak Hopkins, L.F., Le Pape, S., Ma, T., Milovich, J.L., Moreno, J.C., Patel, P.K., Park, H.-S., Remington, B.A., Salmonson, J.D., Kline, J.L., 2014. Design of a high-foot/high-adiabat ICF capsule for the National Ignition Facility. *Phys. Rev. Lett.* 112, 055002.
- Dolence, J.C., Burrows, A., Murphy, J.W., Nordhaus, J., 2013. Dimensional dependence of the hydrodynamics of core-collapse supernovae. *Astrophys. J.* 765, 110.
- Doludenko, A.N., Fortova, S.V., 2015. Numerical simulation of Rayleigh–Taylor instability in inviscid and viscous media. *Comput. Math. Math. Phys.* 55, 874.
- Domaradzki, J.A., Adams, N.A., 2002. Direct modeling of subgrid scales of turbulence in large eddy simulations. *J. Turbul.* 3, 24.
- Domaradzki, J.A., Liu, W., 1995. Approximation of subgrid-scale energy transfer based on the dynamics of resolved scales in turbulence. *Phys. Fluids* 7, 2025.
- Domaradzki, J.A., Radhakrishnan, S., 2005. Effective eddy viscosities in implicit large eddy simulations of decaying high Reynolds number turbulence with and without rotation. *Fluid Dyn. Res.* 36, 385.
- Domaradzki, J.A., Rogallo, R.S., 1990. Local energy transfer and non-local interactions in homogeneous, isotropic turbulence. *Phys. Fluids A* 2, 413.
- Domaradzki, J.A., Metcalfe, R.W., Rogallo, R.S., Riley, J.J., 1987. Analysis of subgrid-scale eddy viscosity with use of results from direct numerical simulations. *Phys. Rev. Lett.* 58, 547.
- Domaradzki, J.A., Liu, W., Hartel, C., Kleiser, L., 1994. Energy transfer in numerically simulated wall-bounded turbulent flows. *Phys. Fluids A* 6, 1583.
- Domaradzki, J.A., Xiao, Z., Smolarkiewicz, P., 2003. Effective eddy viscosities in implicit large eddy simulations of turbulent flows. *Phys. Fluids* 15, 3890.
- Doss, F.W., Loomis, E.N., Welser-Sherrill, L., Fincke, J.R., Flippo, K.A., Keiter, P.A., 2013. Instability, mixing, and transition to turbulence in a laser-driven counterflowing shear experiment. *Phys. Plasmas* 20, 012707.
- Douglas, M.R., Deeney, C., Roderick, N.F., 1997. Effect of sheath curvature on Rayleigh–Taylor mitigation in high-velocity uniform-fill. Z-Pinch implosions. *Phys. Rev. Lett.* 78, 4577.
- Dowling, D.R., Dimotakis, P.E., 1990. Similarity of the concentration field of gas-phase turbulent jets. *J. Fluid Mech.* 218, 109.
- Drake, R.P., 1999. Laboratory experiments to simulate the hydrodynamics of supernova remnants and supernovae. *J. Geophys. Res.* 104, 14505.
- Drake, R.P., 2006. High Energy Density Physics: Fundamentals, Inertial Fusion, and Experimental Astrophysics. Springer, Berlin.
- Drake, R.P., 2009. Perspectives on high-energy-density physics. *Phys. Plasmas* 16, 055501.
- Drake, R.P., Carroll III, J.J., Estabrook, K., Glendinning, S.G., Remington, B.A., Wallace, R., McCray, R., 1998. Development of a laboratory environment to test models of supernova Remnant formation. *Astrophys. J.* 500, L157.
- Drake, R.P., Smith, T.B., Carroll III, J.J., Yan, Y., Glendinning, S.G., Estabrook, Kent, Ryutov, D.D., Remington, B.A., Wallace, R.J., McCray, R., 2000. Progress toward the laboratory simulation of young supernova remnants. *Astrophys. J. Suppl. Ser.* 127, 305.
- Drake, R.P., Robey, H.F., Hurricane, O.A., Zhang, Y., Remington, B.A., Knauer, J., Glimm, J., et.al., 2002. Experiments to produce a hydrodynamically unstable, spherically diverging system of relevance to instabilities in supernovae. *Astrophys. J.* 564, 896.
- Drake, R.P., Harding, E.C., Kuranz, C.C., 2008. Approaches to turbulence in high-energy-density experiments. *Phys. Scr. T* 132, 014022.
- Dray, L.M., Tout, C.A., Karakas, A.I., Lattanzio, J.C., 2003. Chemical enrichment by Wolf–Rayet and asymptotic giant branch stars. *Mon. Not. R. Astron. Soc.* 338, 973.
- Drazin, P.G., Reid, W.H., 1981. Hydrodynamic Stability. Cambridge Univ. Press, Cambridge.
- Drikakis, D., 2003. Advances in turbulent flow computations using high-resolution methods. *Prog. Aerosp. Sci.* 39, 405.
- Drikakis, D., Tsangaris, S., 1993. On the solution of the compressible Navier–Stokes equations using improved flux vector splitting methods. *Appl. Math. Model.* 17, 282.
- Drikakis, D., Grinstein, F., Youngs, D., 2005. On the computation of instabilities and symmetry-breaking in fluid mechanics. *Prog. Aerosp. Sci.* 41, 609.
- Dryden, H.L., Murnaghan, F.D., Bateman, H., 1956. Hydrodynamics. Dover, NY.
- Dudin, V.I., Zubkov, E.V., Meshkov, E.E., Nikulin, A.A., Stadnik, A.L., Statsenko, V.P., Til'kunov, V.A., Vlasov, Y.A., Bashurov, V.V., Bykova, E.A., Tarasov, V.I., Yanilkin, Y.V., Zhrnailo, V.A., 1997. The perturbations and turbulent mixing evolution at the plane gas–gas interface in GEM-driven shock-tube experiments. In: Jourdan, G., Houas, L. (Eds.), Proc. 6th int. Workshop on The Physics of Compressible Turbulent Mixing. Marseille, France, p. 152.
- Duff, R.E., Harlow, F.H., Hirt, C.W., 1962. Effects of diffusion on interface instability between gases. *Phys. Fluids* 5, 417.
- Dumitrescu, D.T., 1943. Strömung an einer Luftblase im senkrechten Rohr. *ZAMM Z. Angew. Math. Mech.* 23, 139.
- Dunning, M.J., Haan, S.W., 1995. Analysis of weakly nonlinear three-dimensional Rayleigh–Taylor instability growth. *Phys. Plasmas* 2, 1669.
- Durand, O., Soulard, L., 2012. Large-scale molecular dynamics study of jet breakup and ejecta production from shock-loaded copper with a hybrid method. *J. Appl. Phys.* 111, 044901.
- Durand, O., Soulard, L., 2013. Power law and exponential ejecta size distributions from the dynamic fragmentation of shock-loaded Cu and Sn metals under melt conditions. *J. Appl. Phys.* 114, 194902.
- Durand, O., Soulard, L., 2015. Mass-velocity and size-velocity distributions of ejecta cloud from shock-loaded tin surface using atomistic simulations. *J. Appl. Phys.* 117, 165903.
- Durand, O., Soulard, L., 2017. Modeling from molecular dynamics simulations of ejecta production induced by shock-loaded metallic surfaces. *J. Dyn. Behav. Mater.* 3, 280.
- Durand, O., Soulard, L., Bourasseau, E., Filippini, G., 2016. Investigation of the static and dynamic fragmentation of metallic liquid sheets induced by random surface fluctuations. *J. Appl. Phys.* 120, 045306.
- Dziewonski, A.M., Anderson, D.L., 1981. Preliminary reference Earth model. *Phys. Earth Planet. Inter.* 25, 297.
- Eckart, C., 1948. An analysis of the stirring and mixing processes in incompressible fluids. *J. Mar. Res.* VII 265.
- Edwards, M.J., Patel, P.K., Lindl, J.D., Atherton, L.J., Glenzer, S.H., Haan, S.W., Kilkenny, J.D., Landen, O.L., Moses, E.I., Nikroo, A., Petrasso, R., Sangster, T.C., Springer, P.T., Batha, S., Benedetti, R., Bernstein, L., Betti, R., Bleuel, D.L., Boehly, T.R., Bradley, D.K., Caggiano, J.A., Callahan, D.A., Celliers, P.M., Cerjan, C.J., Chen, K.C., Clark, D.S., Collins, G.W., Dewald, E.L., Divol, L., Dixit, S., Doeppner, T., Edgell, D.H., Fair, J.E., Farrell, M., Fortner, R.J., Frenje, J., Gatu Johnson, M.G., Giraldez, E., Glebov, V.Yu., Grim, G., Hammel, B.A., Hamza, A.V., Harding, D.R., Hatchett, S.P., Hein, N., Herrmann, H.W., Hicks, D., Hinkel, D.E., Hoppe, M., Hsing, W.W., Izumi, N., Jacoby, B., Jones, O.S., Kalantar, D., Kauffman, R., Kline, J.L., Knauer, J.P., Koch, J.A., Kozioziemski, B.J., Kyrala, G., LaFortune, K.N., Le Pape, S., Leeper, R.J., Lerche, R., Ma, T., MacGowan, B.J., MacKinnon, A.J., Macphee, A., Mapoles, E.R., Marinak, M.M., Mauldin, M., McKenty, P.W., Meezan, M., Michel, P.A., Milovich, J., Moody, J.D., Moran, M., Munro, D.H., Olson, C.L., Opachich, K., Pak, A.E., Parham, T., Park, H.-S., Ralph, J.E., Regan, S.P., Remington, B., Rinderknecht, H., Robey, H.F., Rosen, M., Ross, S., Salmonson, J.D., Sater, J., Schneider, D.H., Séguin, F.H., Sepke, S.M., Shaughnessy, D.A., Smalyuk, V.A., Spears, B.K., Stoeckl, C., Stoeffl, W., Suter, L., Thomas, C.A., Tommasini, R., Town, R.P., Weber, S.V., Wegner, P.J., Widman, K., Wilke, M., Wilson, D.C., Yeamans, C.B., Zylstra, A., 2013. Progress towards ignition on the National Ignition Facility. *Phys. Plasmas* 20, 070501.
- Ejecta physics (2017). A special issue of Journal of Dynamic Behavior of Materials, 3, Buttler, W.T., Williams, R.J.R., Najjar, F.M. (eds.). Available online at: <https://link.springer.com/journal/40870/3/2/page/1>.
- El-Ansary, N.F., Hoshoudy, G.A., Abd-Elrady, A.S., Ayyad, A.H.A., 2002. Effects of surface tension and rotation on the Rayleigh–Taylor instability. *Phys. Chem. Chem. Phys.* 4, 1464.

- Elgawainy, A., Ashgriz, N., 1997. The Rayleigh–Taylor instability of viscous fluid layers. *Phys. Fluids* 9, 1635.
- Emmons, H.W., Chang, C.T., Watson, B.C., 1960. Taylor instability of finite surface waves. *J. Fluid Mech.* 7, 177.
- Erez, L., Sadat, O., Oron, D., Erez, G., Levin, L.A., Shvarts, D., Ben-Dor, G., 2000. Study of the membrane effect on turbulent mixing measurements in shock tubes. *Shock Waves* 10, 241.
- Esteban, C., Peimbert, M., 1995. The chemical enrichment by massive stars in Wolf-Rayet galaxies. *Astron. Astrophys.* 300, 78.
- Falize, É., Bouquet, S., Michaut, C., 2009. Scaling laws for radiating fluids: the pillar of laboratory astrophysics. *Astrophys. Space Sci.* 322, 107.
- Falize, É., Diziére, A., Loupias, B., 2011b. Invariance concepts and scalability of two-temperature astrophysical radiating fluids. *Astrophys. Space Sci.* 336, 201.
- Falize, É., Loupias, B., Ravasio, A., Gregory, C.D., Diziére, A., Koenig, M., Michaut, C., et al., 2011a. The scalability of the accretion column in magnetic cataclysmic variables: the POLAR project. *Astrophys. Space Sci.* 336, 81.
- Falize, É., Michaut, C., Bouquet, S., 2011c. Similarity properties and scaling laws of radiation hydrodynamic flows in laboratory astrophysics. *Astrophys. J.* 730, 96.
- Falize, É., Ravasio, A., Loupias, B., Diziére, A., Gregory, C.D., Michaut, C., Busschaert, C., Cavet, C., Koenig, M., 2012. High-energy density laboratory astrophysics studies of accretion shocks in magnetic cataclysmic variables. *High Energy Density Phys.* 8, 1.
- Farley, D.R., Peyster, T.A., Logory, L.M., Murray, S.D., Burke, E.W., 1999. High Mach number mix instability experiments of an unstable density interface using a single-mode, nonlinear initial perturbation. *Phys. Plasmas* 6, 4304.
- Fermi, E., 1951. Taylor instability at the boundary of two incompressible fluids. In: Amaldi, E. (Ed.), (1965), Reprinted in The Collected Papers of Enrico Fermi, vol 2. University of Chicago Press, Chicago, Ill.
- Fermi, E., von Neumann, J., 1955. Taylor Instability of Incompressible Liquids. US atomic Energy Commission Report AECU-2979.
- Fermigier, M., Limat, L., Wesfreid, J.E., Boudinet, P., Quilliet, C., 1992. Two-dimensional patterns in Rayleigh–Taylor instability of a thin layer. *J. Fluid Mech.* 236, 349.
- Feynman, R., Leighton, R.B., Sands, M., 1964. The Feynman Lectures on Physics. Addison-Wesley, Boston, MA.
- Field, G.B., Goldsmith, D.W., Habing, H.J., 1969. Cosmic-ray heating of the interstellar gas. *Astrophys. J.* 155, L149.
- Finn, J.M., 1993. Nonlinear interaction of Rayleigh–Taylor and shear instabilities. *Phys. Fluids* B 5, 415.
- Fiorina, B., Lele, S.K., 2007. An artificial nonlinear diffusivity method for supersonic reacting flows with shocks. *J. Comput. Phys.* 222, 246.
- Flaig, M., Plewa, T., Keiter, P.A., Drake, R.P., Grosskopf, M., Kuranz, C., Park, H.-S., 2014. Design of a supernova-relevant Rayleigh–Taylor experiment on the National Ignition Facility I. Planar target design and diagnostics. *High Energy Density Phys.* 12, 35.
- Fleurot, N., Cavailler, C., Bourgade, J.L., 2005. The Laser Megajoule (LMJ) Project dedicated to inertial confinement fusion: Development and construction status. *Fusion Eng. Des.* 74, 147.
- Fontaine, G., Mariani, C., Martinez, S., Jourdan, G., Houas, L., Vandenboomgaerde, M., Souffland, D., 2009. An attempt to reduce the membrane effects in Richtmyer–Meshkov instability shock tube experiments. *Shock Waves* 19, 285.
- Fortov, V.E., 2011. Extreme States of Matter: On Earth and in the Cosmos. Springer, Berlin.
- Foster, J.M., Wilde, B.H., Rosen, P.A., Williams, R.J.R., Blue, B.E., Coker, R.F., Drake, R.P., Frank, A., Keiter, P.A., Khokhlov, A.M., Knauer, J.P., Knauer, J.P., 2005. High-energy-density laboratory astrophysics studies of jets and bow shocks. *Astrophys. J. Lett.* 634, L77.
- Fraley, G., 1986. Rayleigh–Taylor stability for a normal shock wave–density discontinuity interaction. *Phys. Fluids* 29, 376.
- Frederiksen, J.S., Dix, M.R., Kepert, S.M., 1996. Systematic energy errors and tendency toward canonical equilibrium in atmospheric circulation models. *J. Atmos. Sci.* 53, 887.
- Frisch, U., Kurien, S., Pandit, R., Pauls, W., Ray, S.S., Wirth, A., Zhu, J.-Z., 2008. Hyperviscosity, Galerkin truncation and bottlenecks in turbulence. *Phys. Rev. Lett.* 101, 144501.
- Fryxell, B.A., Müller, E., Arnett, W.D., 1989. Hydrodynamics and nuclear burning. Preprint MPA-449. MPI für Astrophysik, Garching.
- Fryxell, B., Müller, E., Arnett, D., 1991. Instabilities and clumping in SN 1987A. I. Early evolution in two dimensions. *Astrophys. J.* 367, 619.
- Fryxell, B., Olson, K., Ricker, P., Timmes, F.X., Zingale, M., Lamb, D.Q., MacNeice, P., Rosner, R., Truran, J.W., Tufo, H., 2000. FLASH: An adaptive mesh hydrodynamics code for modeling astrophysical thermonuclear flashes. *astrophys. J. Suppl. Ser.* 131, 273.
- Fukumoto, Y., Lugomer, S., 2003. Instability of vortex filaments in laser–matter interactions. *Phys. Lett. A* 308, 375.
- Fureby, C., Grinstein, F.F., 1999. Monotonically integrated large eddy simulation of free shear flows. *AIAA J.* 37, 544.
- Fureby, C., Grinstein, F.F., 2002. Large eddy simulation of high-Reynolds-number free and wall-bounded flows. *J. Comput. Phys.* 181, 68.
- Gallis, M.A., Koehler, T.P., Torczynski, J.R., Plimpton, S.J., 2015. Direct simulation Monte Carlo investigation of the Richtmyer–Meshkov instability. *Phys. Fluids* 27, 084105.
- Gallis, M.A., Koehler, T.P., Torczynski, J.R., Plimpton, S.J., 2016. Direct simulation Monte Carlo investigation of the Rayleigh–Taylor instability. *Phys. Rev. Fluids* 1, 043403.
- Gamezo, V.N., Khokhlov, A.M., Oran, E.S., Chtchelkanova, A.Y., Rosenberg, R.O., 2003. Thermonuclear supernovae: simulations of the deflagration stage and their implications. *Science* 299, 77.
- Garabedian, P.R., 1957. On steady-state generated by Taylor instability. *Proc. R. Soc. Lond. Ser. A Math. Phys. Eng. Sci.* 241, 423.
- Garanin, S.G., 2011. High-power lasers and their applications in high-energy-density physics studies. *Phys.-Usp.* 54, 415.
- Gardner, C.L., Glimm, J., McBryan, O., Menikoff, R., Sharp, D.H., Zhang, Q., 1988. The dynamics of bubble growth for Rayleigh–Taylor unstable interfaces. *Phys. Fluids* 31, 447.
- Gardner, J.H., Bodner, S.E., Dahlburg, J.P., 1991. Numerical simulation of ablative Rayleigh–Taylor instability. *Phys. Fluids* B 3, 1070.
- Garnier, J., Masse, L., 2005. Statistical approach of weakly nonlinear ablative Rayleigh–Taylor instability. *Phys. Plasmas* 12, 062707.
- Garnier, J., Cherfils-Clérouin, C., Holstein, P.-A., 2003. Statistical analysis of multimode weakly nonlinear Rayleigh–Taylor instability in the presence of surface tension. *Phys. Rev. E* 68, 036401.
- Gauthier, S., Bonnet, M., 1990. A $K - \epsilon$ model for turbulent mixing in shock-tube flows induced by Rayleigh–Taylor instability. *Phys. Fluids A* 2, 1685.
- Gawryszczak, A., Guzman, J., Plewa, T., Kifonidis, K., 2010. Non-spherical core collapse supernovae, III. Evolution towards homology and dependence on the numerical resolution. *Astron. Astrophys.* 521, A38.
- Geers, T.L., Hunter, K.S., 2002. An integrated wave-effects model for an underwater explosion bubble. *J. Acoust. Soc. Amer.* 111, 1584.
- George, E., Glimm, J., Li, X.-L., Marchese, A., Xu, Z.-L., 2002. A comparison of experimental theoretical, and numerical simulation Rayleigh–Taylor mixing rates. *Proc. Natl. Acad. Sci. USA* 99, 2587.
- George, E., Glimm, J., Li, X.-L., Li, Y., Liu, X.-F., 2006. Influence of scale-breaking phenomena on turbulent mixing rates. *Phys. Rev. E* 73, 016304.
- Georgievskaya, A.B., Raevsky, V.A., 2017. A model of a source of shock wave metal ejection based on Richtmyer–Meshkov instability theory. *J. Dynam. Behav. Mater.* 3, 321.
- Germano, M., Piomelli, U., Moin, P., Cabot, W.H., 1991. A dynamic subgrid-scale eddy-viscosity model. *Phys. Fluids A* 3, 1760.
- Ghosal, S., 1996. An analysis of numerical errors in large-eddy simulations of turbulence. *J. Comput. Phys.* 125, 187.
- Glendinning, S.G., Bolstad, J., Braun, D.G., Edwards, M.J., Hsing, W.W., Lasinski, B.F., Louis, H., Miles, A., Moreno, J., Peyster, T.A., Remington, B.A., Robey, H.F., Turano, E.J., Verdon, C.P., Zhou, Y., 2003. Effect of shock proximity on Richtmyer–Meshkov growth. *Phys. Plasmas* 10, 1931.

- Glenzer, S.H., MacGowan, B.J., Michel, P., Meezan, N.B., Suter, L.J., Dixit, S.N., Kline, J.L., Kyrala, G.A., Bradley, D.K., Callahan, D.A., Dewald, E.L., Divol, L., Dzenitidis, E., Edwards, M.J., Hamza, A.V., Haynam, C.A., Hinkel, D.E., Kalantar, D.H., Kilkenny, J.D., Landen, O.L., Lindl, J.D., LePape, S., Moody, J.D., Nikroo, A., Parham, T., Schneider, M.B., Town, R.P.J., Wegner, P., Widmann, K., Whitman, P., Young, B.K.F., Van wonterghem, B., Atherton, L.J., Moses, E.I., 2010. Symmetric inertial confinement fusion implosions at ultra-high laser energies. *Science* 327, 1228.
- Glimm, J., Li, X.L., 1988. Validation of the Sharp-Wheeler bubble merger model from experimental and computational data. *Phys. Fluids* 31, 2077.
- Glimm, J., Sharp, D.H., 1990. Chaotic mixing as a renormalization group fixed point. *Phys. Rev. Lett.* 64, 2137.
- Glimm, J., Li, X.L., Menikoff, R., Sharp, D.H., Zhang, Q., 1990. A numerical study of bubble interactions in Rayleigh–Taylor instability for compressible fluids. *Phys. Fluids A* 2, 2046.
- Glimm, J., Saltz, D., Sharp, D.H., 1998. Statistical evolution of chaotic fluid mixing. *Phys. Rev. Lett.* 80, 712.
- Glimm, J., Grove, J.W., Li, X.L., Oh, W., Sharp, D.H., 2001. A critical analysis of Rayleigh–Taylor growth rates. *J. Comput. Phys.* 169, 652.
- Glimm, J., Li, X.-L., Lin, A.-D., 2002. Nonuniform approach to terminal velocity for single mode Rayleigh–Taylor instability. *Acta Math. Appl. Sin.* 18, 1.
- Glimm, J., Sharp, D.H., Kaman, T., Lim, H., 2013. New directions for Rayleigh–Taylor mixing. *Philos. Trans. R. Soc. Lond. Ser. A Math. Phys. Eng. Sci.* A371, 20120183.
- Gomez, M.R., Slutz, S.A., Sefkow, A.B., Sinars, D.B., Hahn, K.D., Hansen, S.B., Harding, E.C., Knapp, P.F., Schmit, P.F., Jennings, C.A., Awe, T.J., Geissel, M., Rovang, D.C., Chandler, G.A., Cooper, G.W., Cuneo, M.E., Harvey-Thompson, A.J., Herrmann, M.C., Hess, M.H., Johns, O., Lamppa, D.C., Martin, M.R., McBride, R.D., Peterson, K.J., Porter, J.L., Robertson, G.K., Rochau, G.A., Ruiz, C.L., Savage, M.E., Smith, I.C., Stygar, W.A., Vesey, R.A., 2014. Experimental demonstration of fusion-relevant conditions in magnetized liner inertial fusion. *Phys. Rev. Lett.* 113, 155003.
- Goncharov, V.N., 1999. Theory of the ablative Richtmyer–Meshkov instability. *Phys. Rev. Lett.* 82, 2091.
- Goncharov, V.N., 2002. Analytical model of nonlinear-single-mode, classical Rayleigh–Taylor instability at arbitrary Atwood numbers. *Phys. Rev. Lett.* 88, 134502.
- Goncharov, V.N., Li, D., 2005. Effects of temporal density variation and convergent geometry on nonlinear bubble evolution in classical Rayleigh–Taylor instability. *Phys. Rev. E* 71, 046305.
- Goncharov, V.N., Betti, R., McCrory, R.L., Sorotkin, P., Verdon, C.P., 1996. Self-consistent stability analysis of ablation fronts with large Froude numbers. *Phys. Plasmas* 3, 1402.
- Gopalakrishnan, S.S., Carballido-Landeira, J., De Wit, A., Knaepen, B., 2017. Relative role of convective and diffusive mixing in the miscible Rayleigh–Taylor instability in porous media. *Phys. Rev. Fluids* 2, 012501.
- Gowardhan, A.A., Ristorcelli, J.R., Grinstein, F.F., 2011. The bipolar behavior of the Richtmyer–Meshkov instability. *Phys. Fluids* 23, 071701.
- Grabovskii, E.V., Mitrofanov, K.N., Oleinik, G.M., Porofeev, I.Y., 2004. X-ray backlighting of the periphery of an imploding multiwire array in the Angara-5-1 facility. *Plasma Phys. Rep.* 30, 121.
- Granero-Belinchón, R., Shkoller, S., 2017. A Model for Rayleigh–Taylor Mixing and Interface Turnover. *Multiscale Model. Simul.* 15, 274.
- Gréa, B.-J., 2013. The rapid acceleration model and the growth rate of a turbulent mixing zone induced by Rayleigh–Taylor instability. *Phys. Fluids* 25, 015118.
- Gréa, B.-J., Griffond, J., Godeferd, F., 2014. Strain and stratification effects on the rapid acceleration of a turbulent mixing zone. *ASME J. Fluids Eng.* 136, 091203.
- Gréa, B.-J., Burlot, A., Godeferd, F., Griffond, J., Soulard, O., Cambon, C., 2016a. Dynamics and structure of unstably stratified homogeneous turbulence. *J. Turbul.* 1.
- Gréa, B.-J., Burlot, A., Griffond, J., Llor, A., 2016b. Challenging mix models on transients to self-similarity of unstably stratified homogeneous turbulence. *ASME J. Fluids Eng.* 071204.
- Gregori, G., Reville, B., Miniati, F., 2015. The generation and amplification of intergalactic magnetic fields in analogue laboratory experiments with high power lasers. *Phys. Rep.* 601, 1.
- Griffond, J., Gréa, B.-J., Soulard, O., 2014. Unstably stratified homogeneous turbulence as a tool for turbulent mixing modeling. *ASME J. Fluids Eng.* 136, 091201.
- Grinstein, F.F. (Ed.), 2016. Coarse Grained Simulation and Turbulent Mixing. Cambridge University Press.
- Grinstein, F.F., Margolin, L.G., Rider, W.G. (Eds.), 2007. Implicit Large Eddy Simulation: Computing Turbulent Flow Dynamics, 2nd printing. Cambridge University Press, New York.
- Grinstein, F.F., Gowandhan, A.A., Ristorcelli, J.R., Wachtor, A.J., 2012. On coarse-grained simulations of turbulent material mixing. *Phys. Scr.* 86, 058203.
- Guan, B., Zhai, Z., Si, T., Lu, X., Luo, X., 2017. Manipulation of three-dimensional Richtmyer–Meshkov instability by initial interfacial principal curvatures. *Phys. Fluids* 29, 032106.
- Gull, S.F., 1973. A numerical model of the structure and evolution of young supernova remnants. *Mon. Not. R. Astron. Soc.* 161, 47.
- Guo, H.-Y., Wang, L.-F., Ye, W.-H., Wu, J.-F., Zhang, W.-Y., 2017. Weakly nonlinear Rayleigh–Taylor instability in incompressible fluids with surface tension. *Chin. Phys. Lett.* 34, 045201.
- Gupta, M.R., Banerjee, R., Mandal, L.K., Bhar, R., Pant, H.C., Khan, M., Srivastava, M.K., 2012. Effect of viscosity and surface tension on the growth of Rayleigh–Taylor instability and Richtmyer–Meshkov instability induced two fluid interfacial nonlinear structure. *Indian J. Phys.* 86, 471.
- Guzman, J., Plewa, T., 2009. Non-spherical core-collapse supernovae: evolution towards homologous expansion. *Nonlinearity* 22, 2775.
- Haan, S.W., 1989. Onset of nonlinear saturation for Rayleigh–Taylor growth in the presence of a full spectrum of modes. *Phys. Rev. A* 39, 5812.
- Haan, S.W., 1991. Weakly nonlinear hydrodynamic instabilities in inertial fusion. *Phys. Fluids B* 3, 2349.
- Haan, S.W., Pollaine, S.M., Lindl, J.D., Suter, L.J., Berger, R.L., Powers, L.V., Edward alley, W., et al., 1995. Design and modeling of ignition targets for the National Ignition Facility. *Phys. Plasmas* 2, 2480.
- Haan, S.W., Lindl, J.D., Callahan, D.A., Clark, D.S., Salmonson, J.D., Hammel, B.A., Atherton, L.J., Cook, R.C., Edwards, M.J., Glenzer, S., Hamza, A.V., Hatchett, S.P., Herrmann, M.C., Hinkel, D.E., Ho, D.D., Huang, H., Jones, O.S., Kline, J., Kyrala, G., Landen, O.L., MacGowan, B.J., Marinak, M.M., Meyerhofer, D.D., Milovich, J.L., Moreno, K.A., Moses, E.I., Munro, D.H., Nikroo, A., Olson, R.E., Peterson, K., Pollaine, S.M., Ralph, J.E., Robey, H.F., Spears, B.K., Springer, P.T., Suter, L.J., Thomas, C.A., Town, R.P., Vesey, R., Weber, S.V., Wilkens, H.L., Wilson, D.C., 2011. Point design targets specifications and requirements for the 2010 ignition campaign on the National Ignition Facility. *Phys. Plasmas* 18, 051001.
- Haas, J.F., Sturtevant, B., 1987. Interaction of weak shock waves with cylindrical and spherical gas inhomogeneities. *J. Fluid Mech.* 181, 41.
- Hachisu, I., Matsuda, T., Nomoto, K., Shigeyama, T., 1991. Rayleigh–Taylor instabilities and mixing in the helium star models for type Ib/Ic supernovae. *Astrophys. J.* 368, L27.
- Haehn, N., 2012. Experimental Investigation of The Reactive Shock–Bubble Interaction (Ph.D. dissertation), University of Wisconsin-Madison.
- Haehn, N., Ranjan, D., Weber, C., Oakley, J.G., Anderson, M.H., Bonazza, R., 2010. Experimental investigation of a twice-shocked spherical density inhomogeneity. *Phys. Scr. T* 142, 014067.
- Haehn, N., Weber, C., Oakley, J., Anderson, M., Ranjan, D., Bonazza, R., 2011. Experimental investigation of a twice-shocked spherical gas inhomogeneity with particle image velocimetry. *Shock Waves* 21, 225.
- Haehn, N., Ranjan, D., Weber, C., Oakley, J., Rothamer, D., Bonazza, R., 2012. Reacting shock bubble interaction. *Combust. Flame* 159, 1339.
- Hager, J.D., Collins, T.J.B., Smalyuk, V.A., Knauer, J.P., Meyerhofer, D.D., Sangster, T.C., 2013. Study of Rayleigh–Taylor growth in laser irradiated planar SiO₂ targets at ignition-relevant conditions. *Phys. Plasmas* 20, 072707.

- Haines, B.M., 2015. Exponential yield sensitivity to long-wavelength asymmetries in three-dimensional simulations of inertial confinement fusion capsule implosions. *Phys. Plasmas* 22, 082710.
- Haines, B.M., Grinstein, F.F., Schwarzkopf, J.D., 2013a. Reynolds-averaged Navier–Stokes initialization and benchmarking in shock-driven turbulent mixing. *J. Turbul.* 14 (2), 46.
- Haines, B.M., Grinstein, F.F., Welser-Sherrill, L., Fincke, J.R., 2013b. Simulation of material mixing in laser-driven shear experiments. *Phys. Plasmas* 20, 022309.
- Halliday, A.N., 2004. Mixing, volatile loss and compositional change during impact-driven accretion of the Earth. *Nature* 427, 505.
- Hammel, B.A., Haan, S.W., Clark, D.S., Edwards, M.J., Langer, S.H., Marinak, M.M., Patel, M.V., Salmonson, J.D., Scott, H.A., 2010. High-mode Rayleigh–Taylor growth in NIF ignition capsules. *High Energy Density Phys.* 6, 171.
- Hammel, B.A., Scott, H.A., Regan, S.P., Cerjan, C., Clark, D.S., Edwards, M.J., Epstein, R., Glenzer, S.H., Haan, S.W., Izumi, N., Koch, J.A., Kyrala, G.A., Landen, O.L., Langer, S.H., Peterson, K., Smalyuk, V.A., Suter, L.J., Wilson, D.C., 2011. Diagnosing and controlling mix in National Ignition Facility implosion experiments. *Phys. Plasmas* 18, 056310.
- Hammer, N.J., Janka, H.-Th., Müller, E., 2010. Three-dimensional simulations of mixing instability in supernova explosion. *Astrophys. J.* 714, 1371.
- Hao, Y., Prosperetti, A., 1999. The dynamics of vapor bubbles in acoustic pressure fields. *Phys. Fluids* 11, 2008.
- Harkness, R.P., Wheeler, J.C., 1990. Classification of Supernovae. In: Petschek, A. (Ed.), *Supernovae*. Springer, Berlin, p. 1.
- Harris, E.G., 1962. Rayleigh–Taylor instabilities of a collapsing cylindrical shell in a magnetic field. *Phys. Fluids* 5, 1057.
- Harrison, W.J., 1908. The influence of viscosity on the oscillations of superposed fluids. *Proc. Lond. Math. Soc.* 2, 396.
- Hartigan, P., Foster, J.M., Wilde, B.H., Coker, R.F., Rosen, P.A., Hansen, J.F., Blue, B.E., Williams, R.J.R., Carver, R., Frank, A., 2009. Laboratory Experiments numerical simulations and astronomical observations of deflected supersonic jets: Application to HH 110. *Astrophys. J.* 705, 1073.
- Haugen, N.E.L., Brandenburg, A., 2004. Inertial range scaling in numerical turbulence with hyperviscosity. *Phys. Rev. E* 70, 026405.
- Hazak, G., 1996. Lagrangian formalism for the Rayleigh–Taylor instability. *Phys. Rev. Lett.* 76, 4167.
- Hazak, G., Elbaz, Y., Gardner, J.H., Velikovich, A.L., Schmitt, A.J., Zalesak, S.T., 2006. Size distribution and energy spectrum in the mixed state induced by Rayleigh–Taylor instability. *Phys. Rev. E* 73, 047303.
- He, C.-J., Zhou, H.-B., Hang, Y.-H., 2010. A numerical study on Rayleigh–Taylor instability of aluminum plates driven by detonation. *Sci. China phys. Mech. Astron.* 53, 195.
- He, S., Ding, Y., Miao, W., Zhang, X., Tu, S., Yuan, Y., Pu, Y., Yan, J., Wei, M., Yin, C., 2016. Diagnostic for determining the mix in inertial confinement fusion capsule hotspot. *Phys. Plasmas* 23, 072708.
- He, X., Zhang, R., Chen, S., Doolen, G.D., 1999a. On the three-dimensional Rayleigh–Taylor instability. *Phys. Fluids* 11, 1143.
- He, X., Chen, S., Zhang, R., 1999b. A lattice Boltzmann scheme for incompressible multiphase flow and its application in simulation of Rayleigh–Taylor instability. *J. Comput. Phys.* 152, 642.
- He, X.T., Zhang, W.Y., 2007. Inertial fusion research in China. *Eur. Phys. J. D* 44, 227.
- Hecht, J., Alon, U., Shvarts, D., 1994. Potential flow models of Rayleigh–Taylor and Richtmyer–Meshkov bubble fronts. *Phys. Fluids* 6, 4019.
- von Helmholtz, H., 1868. On discontinuous movements of fluid. *Phil. Mag.* 36, 337.
- Henry de frahan, M.T., Belof, J.L., Cavallo, R.M., Raevsky, V.A., Ignatova, O.N., Lebedev, A., Ancheta, D.S., El-dasher, B.S., Florando, J.N., Gallegos, G.F., Johnsen, E., LeBlanc, M.M., 2015. Experimental and numerical investigations of beryllium strength models using the Rayleigh–Taylor instability. *J. Appl. Phys.* 117, 225901.
- Herrmann, M., Moin, P., Abarzhi, S.I., 2008. Nonlinear evolution of the Richtmyer–Meshkov instability. *J. Fluid Mech.* 612, 311.
- Herrmann, M.C., Tabak, M., Lindl, J.D., 2001. Ignition scaling laws and their application to capsule design. *Phys. Plasmas* 8, 2296.
- Hester, J.J., 2008. The Crab Nebula: An astrophysical chimera. *Annu. Rev. Astron. Astrophys.* 46, 127.
- Hester, J.J., Stone, J.M., Scowen, P.A., et al., 1996. WFC2 studies of the Crab Nebula. III. Magnetic Rayleigh–Taylor instabilities and the origin of the filaments. *Astrophys. J.* 456, 225.
- Hickel, S., Adams, N.A., Domaradzki, J.A., 2006. An adaptive local deconvolution method for implicit LES. *J. Comput. Phys.* 213, 413.
- Hicks, E.P., 2015. Rayleigh–Taylor unstable flames—fast or faster?. *Astrophys. J.* 803, 72.
- Hide, R., 1955. Waves in a heavy viscous incompressible electrically conducting fluid of variable density, in the presence of a magnetic field. *Proc. R. Soc. Lond. Ser. A Math. Phys. Eng. Sci.* 233, 376.
- Hill, D.J., Pantano, C., Pullin, D.I., 2006. Large-eddy simulation and multiscale modelling of a Richtmyer–Meshkov instability with reshock. *J. Fluid Mech.* 557, 29.
- Hill, R.D., 1991. Spark channel stability. *Phys. Fluids B* 3, 1787.
- Hill, R.D., Rinker, R.G., Dale Wilson, H., 1980. Atmospheric nitrogen fixation by lightning. *J. Atmos. Sci.* 37, 179.
- Hillebrandt, W., Höflich, P., 1989. The supernova 1987A in the large Magellanic cloud. *Prog. Phys.* 52, 1421.
- Hillebrandt, W., Niemeyer, J.C., 2000. Type IA supernova explosion models. *Annu. Rev. Astron. Astrophys.* 38, 191.
- Hinds, W., Ashley, A., Kennedy, N., Bucknam, P., 2002. Conditions for cloud settling and Rayleigh–Taylor instability. *Aerosol Sci. Technol.* 36, 1128.
- Hinkel, D.E., Schneider, M.B., Young, B.K., Langdon, A.B., Williams, E.A., Rosen, M.D., Suter, L.J., 2006. Creation of hot radiation environment in laser–driven targets. *Phys. Rev. Lett.* 96, 195001.
- Hinze, J., 1975. Turbulence, second ed. McGraw-Hill.
- Hirt, C.W., 1969. Computer studies of time-dependent turbulent flows. *Phys. Fluids* 12, II-219.
- Hirt, C.W., Amsden, A.A., Cook, J.L., 1974. An arbitrary Lagrangian–Eulerian computing method for all flow speeds. *J. Comput. Phys.* 14, 227.
- Ho, S.P., 1980. Linear Rayleigh–Taylor stability of viscous fluids with mass and heat transfer. *J. Fluid Mech.* 101, 111.
- Hogan, W.J., Moses, E.I., Warner, B.E., Sorensen, M.S., Soures, J.M., 2001. The National Ignition Facilities. *Nucl. Fusion* 41, 567.
- Holder, D.A., Smith, A.V., Barton, C.J., Youngs, D.L., 2003. Shock-tube experiments on Richtmyer–Meshkov instability growth using an enlarged double-bump perturbation. *Laser Part. Beams* 21, 411.
- Holloway, G., 1992. Representing topographic stress for large-scale ocean models. *J. Phys. Oceanogr.* 22, 1033.
- Holmes, R.L., Dimonte, G., Fryxell, B., Gittings, M.L., Grove, J.W., Schneider, M., Sharp, D.H., Velikovich, A.L., Weaver, R.P., Zhang, Q., 1999. Richtmyer–Meshkov instability growth: experiment, simulation, and theory. *J. Fluid Mech.* 389, 55.
- Holton, J.R., 1992. An Introduction to Dynamic Meteorology, third ed. Academic Press.
- Hoyer, J.Y., 1979. Large amplitude progressive interfacial waves. *J. Fluid Mech.* 93, 433.
- Hopkins, P.F., Quataert, E., Murray, N., 2011. Self-regulated star formation in galaxies via momentum input from massive stars. *Mon. Not. R. Astron. Soc.* 417, 950.
- Hopps, N., Danson, C., Duffield, S., Egan, D., Elsmere, S., Girling, M., Harvey, E., et al., 2013. Overview of laser systems for the Orion facility at the AWE. *Appl. Opt.* 52, 3597.
- Hopps, N., Oades, K., Andrew, J., Brown, C., Cooper, G., Danson, C., Daykin, S., et al., 2015. Comprehensive description of the Orion laser facility. *Plasma Phys. Control. Fusion* 57, 064002.
- Houas, L., Chemouni, I., 1996. Experimental investigation of Richtmyer–Meshkov instability in shock tube. *Phys. Fluids* 8, 614.
- Houas, L., Farhat, A., Brun, R., 1988. Shock induced Rayleigh–Taylor instability in the presence of a boundary layer. *Phys. Fluids* 31, 807.

- Houas, L., Jourdan, G., Schwaederlé, L., Carrey, R., Diaz, F., 2003. A new large cross-section shock tube for studies of turbulent mixing induced by interfacial hydrodynamic instability. *Shock Waves* 12, 431.
- Houseman, G.A., Molnar, P., 1997. Gravitational (Rayleigh–Taylor) instability of a layer with non-linear viscosity and convective thinning of continental lithosphere. *Geophys. J. Int.* 128, 125.
- Hsu, S.C., Merritt, E.C., Moser, A.L., Awe, T.J., Brockington, S.J.E., Davis, J.S., Adams, C.S., et al., 2012. Experimental characterization of railgun-driven supersonic plasma jets motivated by high energy density physics applications. *Phys. Plasmas* 19, 123514.
- Hsu, S.C., Moser, A.L., Merritt, E.C., Adams, C.S., Dunn, J.P., Brockington, S., Case, A., et al., 2015. Laboratory plasma physics experiments using merging supersonic plasma jets. *J. Plasma Phys.* 81, 345810201.
- Huang, Z., De Luca, A., Atherton, T.J., Bird, M., Rosenblatt, C., Carles, P., 2007. Rayleigh–Taylor instability experiments with precise and arbitrary control of the initial interface shape. *Phys. Rev. Lett.* 99, 204502.
- Hunt, J., Carruthers, D., 1990. Rapid distortion theory and the problems of turbulence. *J. Fluids Mech.* 502, 233.
- Hunt, J., Kevlahan, N., 1993. Rapid distortion theory and the structure of turbulence. In: Dracos, T., et al. (Eds.), *New Approaches and Concepts in Turbulence*. Birkhauser Verlag, Basel.
- Hunt, J.N., 1961. A note on instability at a viscous interface. *Quart. J. Mech. Appl. Math.* 14, 359.
- Hunt, J.T., Speck, D.R., 1989. Present and future performance of the Nova laser system. *Opt. Eng.* 28, 461.
- Hurricane, O.A., Burke, E., Maples, S., Viswanathan, M., 2000. Saturation of Richtmyer's impulsive model. *Phys. Fluids* 12, 2148.
- Hurricane, O.A., Hansen, J.F., Robey, H.F., Remington, B.A., Bono, M.J., Harding, E.C., Drake, R.P., Kuranz, C.C., 2009. A high energy density shock driven Kelvin–Helmholtz shear layer experiment. *Phys. Plasmas* 16, 056305.
- Hurricane, O.A., Herrmann, M.C., 2017. High-energy-density physics at the National Ignition Facility. *Annu. Rev. Nucl. Part. Sci.* 67, 213.
- Hurricane, O.A., Smalyuk, V.A., Raman, K., Schilling, O., Hansen, J.F., Langstaff, G., Martinez, D., Park, H.-S., Remington, B.A., Robey, H.F., Greenough, J.A., Wallace, R., Di Stefano, C.A., Drake, R.P., Marion, D., Krauland, C.M., Kuranz, C.C., 2012. Validation of a turbulent Kelvin–Helmholtz shear layer model using a high-energy-density OMEGA laser experiment. *Phys. Rev. Lett.* 109, 15.
- Hurricane, O.A., Callahan, D.A., Casey, D.T., Celliers, P.M., Cerjan, C., Dewald, E.L., Dittrich, T.R., Doppner, T., Hinkel, D.E., Berzak Hopkins, L.F., Kline, J.L., Le Pape, S., Ma, T., MacPhee, A.G., Milovich, J.L., Pak, A., Park, H.-S., Patel, P.K., Remington, B.A., Salmonson, J.D., Springer, P.T., Tommasini, R., 2014a. Fuel gain exceeding unity in an inertially confined fusion implosion. *Nature* 506, 343.
- Hurricane, O.A., Callahan, D.A., Casey, D.T., Dewald, E.L., Dittrich, T.R., Döppner, T., Barrios Garcia, M.A., et al., 2014b. The high-foot implosion campaign on the National Ignition Facility. *Phys. Plasmas* 21, 056314.
- Ibragimov, N.H., 1999. *Elementary Lie Group Analysis and Ordinary Differential Equations*. Wiley, New York.
- Ikegawa, T., Nishihara, K., 2002. Ablation effects on weakly nonlinear Rayleigh–Taylor instability with a finite bandwidth. *Phys. Rev. Lett.* 89, 115001.
- Ikegawa, T., Nishihara, K., 2003. Saturation and postsaturation phenomena of Rayleigh–Taylor instability with adjacent modes. *Phys. Rev. E* 67, 026404.
- Ingram, R.L., 1954. Taylor instability of the interface between superposed fluids–solution by successive approximations. *Proc. Phys. Soc. London B* 67, 748.
- Inogamov, N.A., 1978. Turbulent stage of the Rayleigh–Taylor instability. *Sov. Tech. Phys. Lett.* 4, 299.
- Inogamov, N.A., 1999. The role of Rayleigh–Taylor and Richtmyer–Meshkov instabilities in astrophysics: an Introduction. *Astrophys. Space Phys.* 10, 1.
- Inogamov, N.A., 2002. Statistics of long-wavelength fluctuations and the expansion rate of Richtmyer–Meshkov turbulence zone. *JETP Lett.* 75 547.
- Inogamov, N.A., Abarzhi, S.I., 1995. Dynamics of fluid surface in multidimension. *Physica D* 87, 339.
- Inogamov, N.A., Oparin, A.M., 1999. Development of Rayleigh–Taylor and Richtmyer–Meshkov instabilities in three-dimensional space: topology of vortex surfaces. *JETP Lett.* 69, 739.
- Inogamov, N.A., Chekhlov, A.V., Dem'yanov, Al.Yu., Anisimov, S.I., Belotserkovskii, O.M., 1991. In: Dautray, R. (Ed.), *Proceedings of the Third International Workshop on Physics Compressible Turbulent Mixing*. Commissariat Energie Atomique, Cesta, France, p. 409.
- Inoue, T., Yamazaki, R., Inutsuka, S., 2009. Turbulence and magnetic field amplification in supernova remnants: interactions between a strong shock wave and multiphase interstellar medium. *Astrophys. J.* 695, 825.
- Isenberg, C., 1992. *The Science of Soap Films and Soap Bubbles*. Dover.
- Ishihara, T., Yoshida, K., Kaneda, Y., 2002. Anisotropic velocity correlation spectrum at small scales in a homogeneous turbulent shear flow. *Phys. Rev. Lett.* 88, 154501.
- Ishihara, T., Gotoh, T., Kaneda, Y., 2008. Study of high-Reynolds number isotropic turbulence by direct numerical simulation. *Annu. Rev. Fluid Mech.* 41, 165.
- Isobe, H., Miyagoshi, T., Shibata, K., Yokoyama, T., 2005. Filamentary structure on the Sun from the magnetic Rayleigh–Taylor instability. *Nature* 434, 478.
- Isobe, H., Miyagoshi, T., Shibata, K., Yokoyama, T., 2006. Three-dimensional simulation of solar emerging flux using the Earth Simulator I. Magnetic Rayleigh–Taylor instability at the top of the emerging flux as the origin of filamentary structure. *Publ. Astron. Soc. Japan* 58, 423.
- Jacobs, J.W., Catton, I., 1988a. Three-dimensional Rayleigh–Taylor instability part 1. Weakly nonlinear theory. *J. Fluid Mech.* 187, 329.
- Jacobs, J.W., Catton, I., 1988b. Three-dimensional Rayleigh–Taylor instability part 2. Experiment. *J. Fluid Mech.* 187, 353.
- Jacobs, J.W., Dalziel, S.B., 2005. Rayleigh–Taylor instability in complex stratifications. *J. Fluid Mech.* 542, 251.
- Jacobs, J.W., Krivets, V.V., 2005. Experiments on the late-time development of single-mode Richtmyer–Meshkov instability. *Phys. Fluids* 17, 034105.
- Jacobs, J.W., Sheeley, J.M., 1996. Experimental study of incompressible Richtmyer–Meshkov instability. *Phys. Fluids* 8, 405.
- Jacobs, J.W., Klein, D.L., Jenkins, D.G., Benjamin, R.F., 1993. Instability growth patterns of a shock-accelerated thin fluid layer. *Phys. Rev. Lett.* 70, 583.
- Jacobs, J.W., Jenkins, D.G., Klein, D.L., Benjamin, R.F., 1995. Nonlinear growth of the shock-accelerated instability of a thin fluid layer. *J. Fluid Mech.* 295, 23.
- Jacobs, J.W., Krivets, V.V., Tsiklashvili, V., Likhachev, O.A., 2013. Experiments on the Richtmyer–Meshkov instability with an imposed random initial perturbation. *Shock Waves* 23, 407.
- Janka, H-Th., Langanke, K., Marek, A., Martínez-Pinedo, G., Müller, B., 2007. Theory of core-collapse supernovae. *Phys. Rep.* 442, 38.
- Jeanloz, R., 1989. Shock wave equation of state and finite strain theory. *J. Geophys. Res.* 94, 5873.
- Jensen, B.J., Cherne, F.J., Prime, M.B., Fezzaa, K., Iverson, A.J., Carlson, C.A., Yeager, J.D., Ramos, K.J., Hooks, D.E., Cooley, J.C., Dimonte, G., 2015. Jet formation in cerium metal to examine material strength. *J. Appl. Phys.* 118, 195903.
- Jevons, W.S., 1857. On the cirrus form of cloud London Edinburgh Dublin. *Phil. Mag. J. Sci IV* 14, 22.
- Jiang, G.-S., Shu, C.-W., 1996. Efficient implementation of weighted ENO schemes. *J. Comput. Phys.* 126, 202.
- Jiang, H., Dong, G., Chen, X., Li, B., 2016. A parameterization of the Richtmyer–Meshkov instability on a premixed flame interface induced by the successive passages of shock waves. *Combust. Flame* 169, 229.
- Johnson, B.M., 2014. On the interaction between turbulence and a planar rarefaction. *Astrophys. J.* 784, 117.
- Johnson, B.M., 2015. Buoyancy instability of homologous implosions. *J. Fluid Mech.* 774, R4.
- Jones, M.A., Jacobs, J.W., 1997. A membraneless experiment for the study of Richtmyer–Meshkov instability of a shock-accelerated gas interface. *Phys. Fluids* 9, 3078.
- Jones, T.W., De Young, D.S., 2005. Magnetohydrodynamic simulations of relic radio bubbles in clusters. *Astrophys. J.* 624, 586.

- Jourdan, G., Houas, L., 1996. Experimental investigation of Richtmyer–Meshkov instability before and after reflected shock compression. *Phys. Fluids* 8, 1353.
- Jourdan, G., Houas, L., 2005. High-amplitude single-mode perturbation evolution at the Richtmyer–Meshkov instability. *Phys. Rev. Lett.* 95, 204502.
- Jourdan, G., Houas, L., Billiotte, M., 1996. Density evolution within a shock accelerated gaseous interface. *Phys. Rev. Lett.* 78, 452.
- Jun, B.I., 1998. Interaction of a pulsar wind with the expanding supernova remnant. *Astrophys. J.* 499, 282.
- Jun, B.I., Norman, M.L., 1996a. Interaction of Rayleigh–Taylor fingers and circumstellar cloudlets in young supernova remnants. *Astrophys. J. Lett.* 468, L59.
- Jun, B.I., Norman, M.L., 1996b. On the origin of strong magnetic fields in young, supernova remnants. *Astrophys. J.* 465, 800.
- Jun, B.I., Norman, M.L., 1996c. On the origin of radial magnetic fields in young supernova remnants, supernova remnants. *Astrophys. J.* 472, 245.
- Kadou, K., German, T.C., Hadjiconstantinou, N.G., Lomdahl, P.S., Dimonte, G., Holian, B.L., Alder, B.J., 2004. Nanohydrodynamics simulations: an atomistic view of the Rayleigh–Taylor instability. *Proc. Natl. Acad. Sci. USA* 101, 5851.
- Kadou, K., Rosenblatt, C., Barber, J.L., German, T.C., Huang, Z., Carlès, P., Alder, B.J., 2007. The importance of fluctuations in fluid mixing. *Proc. Natl. Acad. Sci. USA* 104, 7741.
- Kamath, C., Gezahgne, A., Miller, P., 2009. Identification of coherent structures in three-dimensional simulations of a fluid-mix problem. *Int. J. Image Graph.* 9, 389.
- Kane, J., Arnett, D., Remington, B.A., Glendinning, S.G., Castor, J., Wallace, R., Rubenchik, A., Fryxell, B.A., 1997. Supernova-relevant hydrodynamic instability experiments on the Nova laser. *Astrophys. J. Lett.* 478, L75.
- Kane, J., Arnett, D., Remington, B.A., Glendinning, S.G., Bazan, G., Drake, R.P., Fryxell, B.A., Tessier, R., Moore, K., 1999. Scaling supernova hydrodynamics to the laboratory. *Phys. Plasmas* 6, 2065.
- Kane, J., Arnett, D., Remington, B.A., Glendinning, S.G., Bazan, G., Muller, E., Fryxell, B.A., Teyssier, R., 2000. Two-dimensional versus three-dimensional supernova hydrodynamic instability growth. *Astrophys. J.* 528, 989.
- Kaneda, Y., Ishihara, T., Yokokawa, M., Itakura, K., Uno, A., 2003. Energy dissipation rate and energy spectrum in high resolution direct numerical simulations of turbulence in a periodic box. *Phys. Fluids* 15, L21.
- Karkhanis, V., Ramaprabhu, P., Buttler, W.T., Hammerberg, J.E., Cherne, F.J., Andrews, M.J., 2017. Ejecta production from second shock: Numerical simulations and experiments. *J. Dyn. Behav. Mater.* 3, 265.
- Kartoon, D., Oron, D., Arazi, L., Shvarts, D., 2003. Three-dimensional multimode Rayleigh–Taylor and Richtmyer–Meshkov instabilities at all density ratios. *Laser Part. Beams* 21, 327.
- Kelvin, Lord, 1871. Hydrokinetic solutions and observations. *Phil. Mag.* 42, 362.
- Keiter, P.A., Trantham, M., Malamud, G., Klein, S.R., Davis, J., VanDervort, R., Shvarts, D., Drake, R.P., Stone, J.M., Fraenkel, M., Frank, Y., 2017. Design of laboratory experiments to study radiation-driven implosions. *High Energy Density Phys.* 22, 37.
- Kendrew, S., Simpson, R., Bressert, E., Povich, M.S., Sherman, R., Lintott, C.J., Robitaille, T.P., Schawinski, K., Wolf-Chase, G., 2012. The Milky Way Project: A statistical study of massive star formation associated with infrared bubbles. *Astrophys. J.* 755, 71.
- Kennard, E.H., 1938. Kinetic Theory of Gases. McGraw-Hill, New York.
- Kerr, R.M., 1988. Simulation of Rayleigh–Taylor flows using vortex blobs. *J. Comput. Phys.* 76, 48.
- Keskinen, M.J., Szuszczewicz, E.P., Ossakow, S.L., Holmes, J.C., 1981. Nonlinear theory and experimental observations of the local collisional Rayleigh–Taylor instability in a descending equatorial spread F ionosphere. *J. Geophys. Res.* 86, 5785.
- Khokhlov, A.M., 1995. Propagation of turbulent flames in supernovae. *Astrophys. J.* 449, 695.
- Khokhlov, A.M., Oran, E.S., Chtchelkanova, A.Yu., Wheeler, J.C., 1999a. Interaction of a shock with a sinusoidally perturbed flame. *Combust. Flame* 117, 99.
- Khokhlov, A.M., Oran, E.S., Thomas, G.O., 1999b. Numerical simulation of deflagration-to-detonation transition: The role of shock–flame interactions in turbulent flames. *Combust. Flame* 117, 323.
- Kida, S., Orszag, S.A., 1990. Energy and spectral dynamics in forced compressible turbulence. *J. Sci. Comput.* 5, 85.
- Kifonidis, K., Plewa, T., Janka, H.-Th., Muller, E., 2000. Nucleosynthesis and clump formation in a core-collapse supernova. *Astrophys. J. Lett.* 531, L123.
- Kifonidis, K., Plewa, T., Janka, H.-Th., Muller, E., 2003. Non-spherical core collapse supernovae. I. Neutrino-driven convection, Rayleigh–Taylor instability, and the formation and propagation of metal clumps. *Astron. Astrophys.* 408, 621.
- Kifonidis, K., Plewa, T., Scheck, L., Janka, H.-Th., Muller, E., 2006. Non-spherical core collapse supernovae, II. The late-time evolution of globally anisotropic neutrino-driven explosions and their implications for SN 1987A. *Astron. Astrophys.* 453, 661.
- Kilkenny, J.D., Glendinning, S.G., Haan, S.W., Hammel, B.A., Lindl, J.D., Munro, D., Remington, B.A., Weber, S.V., Knauer, J.P., Verdon, C.P., 1994. A review of the ablative stabilization of the Rayleigh–Taylor instability in regimes relevant to inertial confinement fusion. *Phys. Plasmas* 1, 1379.
- Klein, S.R., Deininger, M., Gillespie, R.S., Di Stefano, C.A., MacDonald, M.J., Manuel, M.J.E., Young, R.P., Kuranz, C.C., Keiter, P.A., Drake, R.P., 2016. Novel target fabrication using 3D printing developed at University of Michigan. *J. Phys.: Conf. Ser.* 713, 012004.
- Kolmogorov, A.N., 1941. The local structure of turbulence in incompressible viscous fluid for very large Reynolds number. *Dokl. Akad. Nauk SSSR* 30, 301.
- Kotelnikov, A.D., Ray, J., Zabusky, N.J., 2000. Vortex morphologies on reaccelerated interfaces: Visualization, quantification and modeling of one- and two-mode compressible and incompressible environments. *Phys. Fluids* 12, 3245.
- Kraichnan, R.H., 1959. Structure of isotropic turbulence at very large Reynolds number. *J. Fluid Mech.* 5, 497.
- Kraichnan, R.H., 1963. Direct-interaction approximation for a system of several interacting shear waves. *Phys. Fluids* 6, 1603.
- Kraichnan, R.H., 1964. Direct-interaction approximation for shear and thermally driven turbulence. *Phys. Fluids* 7, 1048.
- Kraichnan, R.H., 1965. Inertial range spectrum of hydromagnetic turbulence. *Phys. Fluids* 8, 1385.
- Kraichnan, R.H., 1967. Inertial ranges in two dimensional turbulence. *Phys. Fluids* 10, 1417.
- Kraichnan, R.H., 1971. Inertial-range transfer in two- and three-dimensional turbulence. *J. Fluid Mech.* 47, 525.
- Kraichnan, R.H., 1976. Eddy viscosity in two and three dimensions. *J. Atmos. Sci.* 33, 1521.
- Kraichnan, R., Montgomery, D., 1980. Two-dimensional turbulence. *Rep. Progr. Phys.* 43, 547.
- Kramer, R.M.J., Pullin, D.L., Meiron, D.I., Pantano, C., 2010. Shock-resolved Navier–Stokes simulation of the Richtmyer–Meshkov instability start-up at a light-heavy interface. *J. Fluid Mech.* 642, 421.
- Krasny, R., 1986. Desingularization of periodic vortex sheet roll-up. *J. Comput. Phys.* 65, 292.
- Krechetnikov, R., 2009. Rayleigh–Taylor and Richtmyer–Meshkov instabilities of flat and curved interfaces. *J. Fluid Mech.* 625, 387.
- Kritcher, A.L., Döppner, T., Swift, D., Hawrelak, J., Collins, G., Nilsen, J., Bachmann, B., et al., 2014. Probing matter at Gbar pressures at the NIF. *High Energy Density Phys.* 10, 27.
- Krivets, V.V., Ferguson, K.J., Jacobs, J.W., 2017. Turbulent mixing induced by Richtmyer–Meshkov instability. *AIP Conf. Proc.* 1793, 150003.
- Kucherenko, Yu.A., Shibarshov, L.I., Chitaikin, V.I., Balabin, S.I., Pylaev, A.P., 1991. Experimental study of the gravitational turbulent mixing self-similar mode. In: Dautray, R. (Ed.), Proceedings of the Third International Workshop on Physics Compressible Turbulent Mixing. Commissariat Energie Atomique. Cesta, France, p. 427.
- Kuchugov, P., Zmitrenko, N., Rozanov, V., Yanilkin, Yu., Sin'kova, O., Statsenko, V., Chernyshova, O., 2012. The evolution model of the Rayleigh–Taylor instability development. *J. Russ. Laser Res.* 33, 517.
- Kuchugov, P., Rozanov, V.B., Zmitrenko, N.V., 2014. The differences in the development of Rayleigh–Taylor instability in 2D and 3D geometries. *Plasma Phys. Rep.* 40, 451.

- Kuhl, A.L., 1996. Spherical mixing layers in explosions. In: Bowen, J.R. (Ed.), *Dynamics of Exothermicity*. Gordon and Breach, Amsterdam, Netherlands, p. 291.
- Kuhl, A.L., 2015. On the structure of self-similar detonation waves in TNT charges. *Combust. Explosion Shock Waves* 511, 72.
- Kuhl, A.L., Bell, J.B., Beckner, V.E., Reichenbach, H., 2011. Gasdynamic model of turbulent combustion in TNT explosions. *Proc. Combust. Inst.* 33, 2177.
- Kuhl, A.L., Bell, J.B., Beckner, V.E., Balakrishnan, K., Aspden, A.J., 2013. Spherical combustion clouds in explosions. *Shock Waves* 23, 233.
- Kull, H.J., 1989. Incompressible description of Rayleigh–Taylor instabilities in laser-ablated plasmas. *Phys. Fluids B* 1, 170.
- Kull, H.J., 1991. Theory of the Rayleigh–Taylor instability. *Phys. Rep.* 206, 197.
- Kuramitsu, Y., Chu, H.H., Hau, L.N., Chen, S.H., Liu, Y.L., Hsieh, C.Y., Sakawa, Y., Hideaki, T., Wang, J., 2015. Relativistic plasma astrophysics with intense lasers. *High Energy Density Phys.* 17, 198.
- Kuramitsu, Y., Nakani, N., Kondo, K., Sakawa, Y., Mori, Y., Miura, E., Tsuji, K., Kimura, K., Fukumochi, S., Kashihara, M., Tanimoto, T., 2011a. Model experiment of cosmic ray acceleration due to an incoherent wakefield induced by an intense laser pulse. *Phys. Plasmas* 18, 010701.
- Kuramitsu, Y., Nakani, N., Kondo, K., Sakawa, Y., Mori, Y., Miura, E., Tsuji, K., Kimura, K., Fukumochi, S., Kashihara, M., Tanimoto, T., 2011b. Experimental evidence of nonthermal acceleration of relativistic electrons by an intensive laser pulse. *Phys. Rev. E* 83, 026401.
- Kuramitsu, Y., Ohnishi, N., Sakawa, Y., Morita, T., Tanji, H., Ide, T., Nishio, K., et al., 2016. Model experiment of magnetic field amplification in laser-produced plasmas via the Richtmyer–Meshkov instability. *Phys. Plasmas* 23, 032126.
- Kuramitsu, Y., Sakawa, Y., Waugh, J.N., Gregory, C.D., Morita, T., Dono, S., Aoki, H., Tanji, H., Loupias, B., Koenig, M., Woolsey, N., 2009. Jet formation in counterstreaming collisionless plasmas. *Astrophys. J. Lett.* 707, L137.
- Kuranz, C.C., Drake, R.P., Leibrandt, D.R., Harding, E.C., Robey, H.F., Miles, A.R., Blue, B.E., Hansen, J.F., Louis, H., Bono, M., Knauer, J., Arnett, D., Meakin, C.A., 2005. Progress toward the study of laboratory scale, astrophysically relevant, turbulent plasmas. *Astrophys. Space Sci.* 298, 9.
- Kuranz, C.C., Drake, R.P., Harding, E.C., Grosskopf, M.J., Robey, H.F., Remington, B.A., Edwards, M.J., Miles, A.R., Perry, T.S., Plewa, T., Hearn, N.C., Knauer, J.P., Arnett, D., Leibrandt, D.R., 2009a. Two-dimensional blast-wave-driven Rayleigh–Taylor instability: experiment and simulation. *Astrophys. J.* 696, 749.
- Kuranz, C.C., Drake, R.P., Grosskopf, M.J., Budde, A., Krauland, C., Marion, D.C., Visco, A.J., Ditmar, J.R., Robey, H.F., Remington, B.A., Miles, A.R., Cooper, A.B.R., Sorce, C., Plewa, T., Hearn, N.C., Killibrew, K.L., Knauer, J.P., Arnett, D., Donajkowski, T., 2009b. Three-dimensional blast-wave-driven Rayleigh–Taylor instability and the effects of long-wavelength modes. *Phys. Plasmas* 16, 156310.
- Kuranz, C.C., Park, H.-S., Remington, B.A., Drake, R.P., Miles, A.R., Robey, H.F., Kilkenny, J.D., Keane, C.J., Kalantar, D.H., Huntington, C.M., Krauland, C.M., Harding, E.C., Grosskopf, M.J., Marion, D.C., Doss, F.W., Myra, E., Maddox, B., Young, B., Kline, J.L., Kyrala, G., Plewa, T., Wheeler, J.C., Arnett, W.D., Wallace, R.J., Giraldez, E., Nikroo, A., 2011. Astrophysically relevant radiation hydrodynamics experiment at the National Ignition Facility. *Astrophys. Space Sci.* 336, 207.
- Lamb, H., 1932. *Hydrodynamics*. Dover, New York.
- Landau, L.D., Lifshitz, E.M., 1987. *Fluid Mechanics*. Pergamon, Oxford.
- Lanier, N.E., Barnes, C.W., Batha, S.H., Day, R.D., Magelssen, G.R., Scott, J.M., Dunne, A.M., Parker, K.W., Rothman, S.D., 2003. Multimode seeded Richtmyer–Meshkov mixing in a convergent, compressible, miscible plasma system. *Phys. Plasmas* 10, 1616.
- Latini, M., 2007. Simulations and Analysis of Two- and Three-Dimensional Single-Mode Richtmyer–Meshkov instability Using Weighted Essentially Non-Oscillatory and Vortex Methods (Ph.D. thesis). California Institute of Technology.
- Latini, M., Schilling, O., Don, W.S., 2007a. High-resolution simulations and modeling of reshocked single-mode Richtmyer–Meshkov instability: comparison to experimental data an to amplitude growth model predictions. *Phys. Fluids* 19, 024104.
- Latini, M., Schilling, O., Don, W.S., 2007b. Effects of WENO flux reconstruction order and spatial resolution on reshocked two-dimensional Richtmyer–Meshkov instability. *J. Comput. Phys.* 221 805, 805.
- Lawrence, G.A., Broadw, F.K., Redekopp, L.G., 1991. The instability of a sheared density interface. *Phys. Fluids A* 3, 2360.
- Lawrie, A.G.W., 2009. On Rayleigh–Taylor Mixing: Confinement by Stratification and Geometry (Ph.D. dissertation). University of Cambridge, Cambridge, UK.
- Lawrie, A.G.W., Dalziel, S.B., 2011a. Turbulent diffusion in tall tubes. I. Models for Rayleigh–Taylor instability. *Phys. Fluids* 23, 085109.
- Lawrie, A.G.W., Dalziel, S.B., 2011b. Turbulent diffusion in tall tubes. II. Confinement by stratification. *Phys. Fluids* 23, 085110.
- Layes, G., Le Métayer, O., 2007. Quantitative numerical and experimental studies of the shock accelerated heterogeneous bubbles motion. *Phys. Fluids* 19, 042105.
- Layes, G., Jourdan, G., Houas, L., 2003. Distortion of a spherical gaseous interface accelerated by a plane shock wave. *Phys. Rev. Lett.* 91, 174502.
- Layes, G., Jourdan, G., Houas, L., 2005. Experimental investigation of the shock wave interaction with a spherical gas inhomogeneity. *Phys. Fluids* 17, 028103.
- Layes, G., Jourdan, G., Houas, L., 2009. Experimental study on a plane shock wave accelerating a gas bubble. *Phys. Fluids* 21, 074102.
- Layzer, D., 1955. On the instability of superposed fluids in a gravitational field. *Astrophys. J.* 122, 1.
- Lebedev, S.V., Beg, F.N., Bland, S.N., Chittenden, J.P., Dangor, A.E., Haines, M.G., Kwek, K.H., Pikuz, S.A., Shelkovenko, T.A., 2001. Effect of discrete wires on the implosion dynamics of wire array Z pinches. *Phys. Plasmas* 8, 3734.
- Lebedev, S.V., Ampleford, D.J., Bland, S.N., Bott, S.C., Chittenden, J.P., Goyer, J., Jennings, C., et al., 2005. Physics of wire array Z-pinch implosions: experiments at Imperial College. *Plasma Phys. Control. Fusion* 47, A91.
- Lee, H.G., Kim, J., 2013. Numerical simulation of the three-dimensional Rayleigh–Taylor instability. *Comput. Math. Appl.* 66, 1466.
- Lee, H.G., Kim, K., Kim, J., 2011. On the long time simulation of the Rayleigh–Taylor instability. *Internat. J. Numer. Methods Engrg.* 85, 1633.
- Leith, C.E., 1968. Diffusion approximation for two-dimensional turbulence. *Phys. Fluids* 11, 671.
- Leith, C.E., 1990. Stochastic backscatter in a subgrid-scale model: plane shear mixing layer. *Phys. Fluids A* 2, 297.
- LeLievre, R., Lasher, G.J., Bjorklund, F., 1955. Effect of a density gradient on Taylor instability (No. UCRL-4459). Radiation Lab., Univ. of Calif., Livermore.
- Lemaigre, L., Budroni, M.A., Riolfi, L.A., Grosfils, P., De Wit, A., 2013. Asymmetric Rayleigh–Taylor and double-diffusive fingers in reactive systems. *Phys. Fluids* 25, 014103.
- Lesieur, M., 1990. *Turbulence in Fluids*. Kluwer, Dordrecht.
- Leslie, D.C., 1973. *Developments in the Theory of Turbulence*. Clarendon, Oxford, UK.
- Lewis, D.J., 1950. The instability of liquid surfaces when accelerated in a direction perpendicular to their planes II. *Proc. R. Soc. Lond. Ser. A Math. Phys. Eng. Sci.* 202, 81.
- Li, B., Zhao, F.P., Wu, H.A., Luo, S.N., 2014. Microstructure effects on shock-induced surface jetting. *J. Appl. Phys.* 115, 073504.
- Li, C., Kailasanath, K., Book, D.L., 1991. Mixing enhancement by expansion waves in supersonic flows of different densities. *Phys. Fluids A* 3, 1369.
- Li, J.W., Pei, W.B., He, X.T., Li, J.H., Zheng, W.D., Zhu, S.P., Kang, W., 2013. Preheat of radiative shock in double-shell ignition targets. *Phys. Plasmas* 20, 082707.
- Li, M., Zhu, Q., Li, G., 2016. Effect of surface tension and viscosity on bubble growth of single mode Rayleigh–Taylor instability. *Appl. Math. Mech.* 37, 1607.
- Li, X., Chu, V.H., 2007. Rayleigh–Taylor Instabilities by overturning experiments. *J. Hydrodynamics Ser. B* 19, 303.
- Li, X.L., Zhang, Q., 1997. A comparative numerical study of the Richtmyer–Meshkov instability with nonlinear analysis in two and three dimensions. *Phys. Fluids* 9, 3069.
- Li, Y., Luo, X., 2014. Theoretical analysis of effects of viscosity, surface tension, and magnetic field on the bubble evolution of Rayleigh–Taylor instability. *Acta Phys. Sin.* 63, 85203.

- Liang, H., Shi, B.C., Guo, Z.L., Chai, Z.H., 2014. Phase-field-based multiple-relaxation-time lattice Boltzmann model for incompressible multiphase flows. *Phys. Rev. E* 89, 053320.
- Liang, H., Li, Q.X., Shi, B.C., Chai, Z.H., 2016. Lattice Boltzmann simulation of three-dimensional Rayleigh–Taylor instability. *Phys. Rev. E* 93, 033113.
- Libby, S.B., Van Bibber, K.A. (Eds.), 2010. Edward Teller Centennial Symposium: Modern Physics and the Scientific Legacy of Edward Teller: Livermore, CA, USA, 28 May 2008. World Scientific.
- Likhachev, O.A., Jacobs, J.W., 2005. A vortex model for Richtmyer–Meshkov instability accounting for finite Atwood number. *Phys. Fluids* 17, 031704.
- Lin, H., Storey, B.D., Szeri, A.J., 2002. Rayleigh–Taylor instability of violently collapsing bubbles. *Phys. Fluids* 14, 2925.
- Linden, P.F., Redondo, J.M., Youngs, D.L., 1994. Molecular mixing in Rayleigh–Taylor instability. *J. Fluid Mech.* 265, 97.
- Lindl, J.D., 1995. Development of the indirectdrive approach to inertial confinement fusion and the target physics basis for ignition and gain. *Phys. Plasmas* 2, 3933.
- Lindl, J.D., 1998. Inertial Confinement Fusion. Springer.
- Lindl, J.D., Amendt, P., Berger, R.L., Glendinning, S.G., Glenzer, S.H., Haan, S.W., Kauffman, R.L., Landen, O.L., Suter, L.J., 2004. The physics basis for ignition using indirect-drive targets on the National Ignition Facility. *Phys. Plasmas* 11, 339.
- Liu, H., Xiao, Z.-L., 2016. Scale-to-scale energy transfer in mixing flow induced by the Richtmyer–Meshkov instability. *Phys. Rev. E* 93, 053112.
- Liu, W.H., Wang, L.F., Ye, W.H., He, X.T., 2012. Nonlinear saturation amplitudes in classical Rayleigh–Taylor instability at arbitrary Atwood numbers. *Phys. Plasmas* 19, 042705.
- Liu, W.H., Wang, L.F., Ye, W.H., He, X.T., 2013. Temporal evolution of bubble tip velocity in classical Rayleigh–Taylor instability at arbitrary Atwood numbers. *Phys. Plasmas* 20, 062101.
- Liu, Y., Grieves, B., 2014. Ejecta production and transport from a shocked Sn coupon. *ASME J. Fluids Eng.* 136, 091202.
- Livescu, D., 2013. Numerical simulations of two-fluid turbulent mixing at large density ratios and applications to the Rayleigh–Taylor instability. *Philos. Trans. R. Soc. Lond. Ser. A Math. Phys. Eng. Sci.* 371, 20120185.
- Livescu, D., Ristorcelli, J.R., 2007. Buoyancy-driven variable-density turbulence. *J. Fluid Mech.* 591, 43.
- Livescu, D., Ristorcelli, J.R., Petersen, M.R., Gore, R.A., 2010. New phenomena in variable-density Rayleigh–Taylor turbulence. *Phys. Scr. T* 142, 014015.
- Livescu, D., Wei, T., Petersen, M.R., 2011. Direct numerical simulations of Rayleigh–Taylor instability. *J. Phys.: Conf. Ser.* 318, 082007.
- Livescu, S., Roy, R.V., Schwartz, L.W., 2011. Leveling of thixotropic liquids. *J. Non-Newton. Fluid Mech.* 166, 395.
- Llor, A., 2003. Bulk turbulent transport and structure in Rayleigh–Taylor, Richtmyer–Meshkov and variable acceleration instabilities. *Laser Part. Beams* 21, 305.
- Llor, A., 2006. Invariants of free turbulent decay. [arXiv:physics/0612220](https://arxiv.org/abs/physics/0612220).
- LOBACHEV, V., Betti, R., 2000. Ablative stabilization of the deceleration phase Rayleigh–Taylor instability. *Phys. Rev. Lett.* 85, 4522.
- Lombardini, M., Pullin, D.I., 2009. Startup process in the Richtmyer–Meshkov instability. *Phys. Fluids* 21, 044104.
- Lombardini, M., Hill, D.J., Pullin, D.I., Meiron, D.I., 2011. Atwood ratio dependence of Richtmyer–Meshkov flows under reshock conditions using large-eddy simulations. *J. Fluid Mech.* 670, 439.
- Lombardini, M., Pullin, D.I., Meiron, D.I., 2012. Transition to turbulence in shock-driven mixing: a Mach number study. *J. Fluid Mech.* 690, 203.
- Lombardini, M., Pullin, D.I., Meiron, D.I., 2014a. Turbulent mixing driven by spherical implosions. Part 1. Flow description and mixing-layer growth. *J. Fluid Mech.* 748, 85.
- Lombardini, M., Pullin, D.I., Meiron, D.I., 2014b. Turbulent mixing driven by spherical implosions. Part 2. Turbulence statistics. *J. Fluid Mech.* 748, 113.
- Long, C.C., Krivets, V.V., Greenough, J.A., Jacobs, J.W., 2009. Shock tube experiments and numerical simulation of the single-mode, three-dimensional Richtmyer–Meshkov instability. *Phys. Fluids* 21, 114104.
- López Cela, J.J., Piriz, A.R., Temporal, M., Tahir, N.A., Moreno, M.C.S., 2005. Elastoplastic effects on the Rayleigh–Taylor instability in an accelerated solid slab. *Eur. Phys. J. Appl. Phys.* 29, 247.
- López Cela, J.J., Piriz, A.R., Moreno, M.C.S., Tahir, N.A., 2006. Numerical simulations of Rayleigh–Taylor instability in elastic solids. *Laser Part. Beams* 24, 427.
- López Ortega, A., Lombardini, M., Pullin, D.I., Meiron, D.I., 2014. Numerical simulations of the Richtmyer–Meshkov instability in solid–vacuum interfaces using calibrated plasticity laws. *Phys. Rev. E* 89, 033018.
- Lugomer, S., 2007. Micro-fluid dynamics via laser–matter interactions: Vortex filament structures, helical instability, reconnection, merging, and undulation. *Phys. Lett. A* 361, 87.
- Lugomer, S., 2016a. Laser–matter interactions: Inhomogeneous Richtmyer–Meshkov and Rayleigh–Taylor instabilities. *Laser Part. Beams* 34, 123.
- Lugomer, S., 2016b. Laser generated Richtmyer–Meshkov instability and nonlinear wave paradigm in turbulent mixing: I. Central region of Gaussian spot. *Laser Part. Beams* 34, 687.
- Lund, H.M., Dalziel, S.B., 2014. Bursting water balloons. *J. Fluid Mech.* 756, 771.
- Luo, X., Wang, X., Si, T., 2013. The Richtmyer–Meshkov instability of a three-dimensional air/SF₆ interface with a minimum-surface feature. *J. Fluid Mech.* 722, R2.
- Luo, X., Guan, B., Si, T., Zhai, Z., Wang, X., 2016a. Richtmyer–Meshkov instability of a three-dimensional SF₆–air interface with a minimum-surface feature. *Phys. Rev. E* 93, 013101.
- Luo, X., Guan, B., Zhai, Z., Si, T., 2016b. Principal curvature effects on the early evolution of three-dimensional single-mode Richtmyer–Meshkov instabilities. *Phys. Rev. E* 93, 023110.
- Ma, T., Patel, P.K., Izumi, N., Springer, P.T., Key, M.H., Atherton, L.J., Benedetti, L.R., Bradley, D.K., Callahan, D.A., Celliers, P.M., Cerjan, C.J., Clark, D.S., Dewald, E.L., Dixit, S.N., Doppner, T., Edgell, D.H., Epstein, R., Glenn, S., Grim, G., Haan, S.W., Hammel, B.A., Hicks, D., Hsing, W.W., Jones, O.S., Khan, S.F., Kilkenny, J.D., Kline, J.L., Kyrala, G.A., Landen, O.L., Le Pape, S., MacGowan, B.J., Mackinnon, A.J., MacPhee, A.G., Meezan, N.B., Moody, J.D., Pak, A., Parham, T., Park, H.-S., Ralph, J.E., Regan, S.P., Remington, B.A., Robey, H.F., Ross, J.S., Spears, B.K., Smalyuk, V., Suter, L.J., Tommasini, R., Town, R.P., Weber, S.V., Lindl, J.D., Edwards, M.J., Glenzer, S.H., Moses, E.I., 2013. Onset of hydrodynamic mix in high-velocity, highly compressed inertial confinement fusion implosions. *Phys. Rev. Lett.* 111, 085004.
- Ma, T., Patel, P.K., Izumi, N., Springer, P.T., Key, M.H., Atherton, L.J., Barrios, M.A., et al., 2017. The role of hot spot mix in the low-foot and high-foot implosions on the NIF. *Phys. Plasmas* 24, 056311.
- Ma, X., Delamere, P.A., Otto, A., 2016. Plasma transport driven by the Rayleigh–Taylor instability. *J. Geophys. Res.: Space Phys.* 121, 5260.
- MacNeice, P., Olson, K.M., Moberly, C., De Fainchtein, R., Packer, C., 2000. PARAMESH: A parallel adaptive mesh refinement community toolkit. *Comput. Phys. Comm.* 126, 330.
- Mahalov, A., 2014. Multiscale modeling and nested simulations of three-dimensional ionospheric plasmas: Rayleigh–Taylor turbulence and nonequilibrium layer dynamics at fine scales. *Phys. Scr.* 89, 098001.
- Mahalov, A., Moustakou, M., 2014. Multiscale nested simulations of Rayleigh–Taylor instabilities in ionospheric flows. *ASME J. Fluids Eng.* 136, 060908.
- Maimouni, I., Goyon, J., Lac, E., Pringuet, T., Boujlel, J., Chateau, X., Coussot, P., 2016. Rayleigh–Taylor instability in elastoplastic solids: A local catastrophic process. *Phys. Rev. Lett.* 116, 154502.
- Malamud, G., Grosskopf, M.J., Drake, R.P., 2013. Conceptual design of a Rayleigh–Taylor experiment to study bubble merger in two dimensions on NIF. *High Energy Density Phys.* 11, 17.
- Mandelbrot, B.B., 1967. How long is the coast of Britain. *Science* 156, 636.

- Marati, N., Casciola, C.M., Piva, R., 2004. Energy cascade and spatial fluxes in wall turbulence. *J. Fluids Mech.* 521, 191.
- Marble, F.E., Hendricks, G.J., Zukoski, E.E., 1987. Progress toward shock enhancement of supersonic combustion processes, AIAA paper 87-1880.
- Margolin, L.G., Rider, W.J., 2002. A rationale for implicit turbulence modeling. *Int. J. Numer. Methods Fluids* 39, 821.
- Margolin, L.G., Rider, W.J., 2005. The design and construction of implicit LES models. *Internat. J. Numer. Methods Fluids* 47, 1173.
- Margolin, L.G., Smolarkiewicz, P.K., Wyszogrodzki, A.A., 2002. Implicit turbulence modeling for high Reynolds number flows. *ASME J. Fluids Eng.* 124, 862.
- Mariani, C., Vandenoevergaerde, M., Jourdan, G., Souffland, D., Houas, L., 2008. Investigation of the Richtmyer–Meshkov instability with stereolithographed interfaces. *Phys. Rev Lett.* 100, 254503.
- Marinak, M.M., Tipton, R.E., Landen, O.L., Murphy, T.J., Amendt, P., Haan, S.W., Hatchet, S.P., Keane, C.J., McEachern, R., Wallace, R., 1996. Three-dimensional simulations of Nova high growth factor capsule implosion experiments. *Phys. Plasmas* 3, 2070.
- Markstein, G.H., 1957a. Flow disturbances induced near a slightly wavy contact surface, or flame front traversed by a shock wave. *J. Aerosol Sci.* 24, 238.
- Markstein, G.H., 1957b. A shock tube study of flame front-pressure wave interactions. In: 6th intl Symp. Comb. Reinhold, New York, pp. 387–398.
- Marmottant, P., Villermaux, E., 2004. On spray formation. *J. Fluid Mech.* 498, 73.
- Marocchino, A., Atzeni, S., Schiavi, A., 2010. Numerical study of the ablative Richtmyer–Meshkov instability of laser-irradiated deuterium and deuterium–tritium targets. *Phys. Plasmas* 17, 112703.
- Marsh, B.D., 1979. Island Arc development: Some observations, experiments and speculations. *J. Geol.* 87, 687.
- Martinez, D.O., Chen, S., Doolen, G.D., Kraichnan, R.H., Wang, L.-P., Zhou, Y., 1997. Energy spectrum in the dissipation range of fluid turbulence. *J. Plasma Phys.* 57, 195.
- Massa, L., Jha, P., 2012. Linear analysis of the Richtmyer–Meshkov instability in shock-flame interactions. *Phys. Fluids* 24, 056101.
- Matsumoto, J., Masada, Y., 2013. Two-dimensional numerical study for Rayleigh–Taylor and Richtmyer–Meshkov instabilities in relativistic jets. *Astrophys. J. Lett.* 772, 1.
- Matsumoto, Y., Hoshino, M., 2004. Onset of turbulence induced by a Kelvin–Helmholtz vortex. *Geophys. Res. Lett.* 31, L02807.
- Matsumoto, T., 2009. Anomalous scaling of three-dimensional Rayleigh–Taylor turbulence. *Phys. Rev. E* 79, 055301(R).
- Matsuoka, C., 2009. Vortex sheet motion in incompressible Richtmyer–Meshkov and Rayleigh–Taylor instabilities with surface tension. *Phys. Fluids* 21, 092107.
- Matsuoka, C., Nishihara, K., 2006. Vortex core dynamics and singularity formations in incompressible Richtmyer–Meshkov instability. *Phys. Rev. E* 73, 026304; Erratum: Vortex core dynamics and singularity formations in incompressible Richtmyer–Meshkov instability; Matsuoka, C., Nishihara, K., 2006. *Phys. Rev. E* 74, 049902.
- Matsuoka, C., Nishihara, K., Fukuda, Y., 2003. Nonlinear evolution of an interface in the Richtmyer–Meshkov instability. *Phys. Rev. E* 67, 036301; Erratum: Nonlinear evolution of an interface in the Richtmyer–Meshkov instability; Matsuoka, C., Nishihara, K., Fukuda, Y., 2003. *Phys. Rev. E* 68, 029902.
- Matthaeus, W.H., Zhou, Y., 1989. Extended inertial range phenomenology of magnetohydrodynamic turbulence. *Phys. Fluids* B 1, 1929.
- Matzen, M.K., 1997. Z pinches as intense x-ray sources for high-energy density physics applications. *Phys. Plasmas* 4, 1519.
- Mazariegos, R.A., Andrews, M.J., Russell, J.E., 1996. Modeling the evolution of salt structure using nonlinear rocksalt flow laws. *Tectonophysics* 256, 129.
- McCray, R., 1998. Supernova 1987A revisited. *Annu. Rev. Astron. Astrophys.* 31, 175.
- McCrory, R.L., 2004. Recent progress in inertial confinement fusion in the United States. *Nucl. Fusion* 44, S123.
- McQueen, R.G., Marsh, S.P., Taylor, J.W., Fritz, J.N., Carter, W.J., 1970. The equation of state of solids from shock wave studies. In: Kinslow, R. (Ed.), *High Velocity Impact Phenomena*. Academic Press, New York, p. 293.
- McWilliams, J.C., 1984. The emergence of isolated coherent vortices in turbulent flow. *J. Fluid Mech.* 146, 21.
- Meinecke, J., Tzeferacos, P., Bell, A., Bingham, R., Clarke, R., Churazov, E., Crowston, R., et al., 2015. Developed turbulence and nonlinear amplification of magnetic fields in laboratory and astrophysical plasmas. *Proc. Natl. Acad. Sci.* 112, 8211.
- Menikoff, R., Plohr, B.J., 1989. The Riemann problem for fluid flow of real materials. *Rev. Modern Phys.* 61, 75.
- Menikoff, R., Zemach, C., 1983. Rayleigh–Taylor instability and the use of conformal maps for ideal fluids flow. *J. Comput. Phys.* 51, 28.
- Menikoff, R., Mjolsness, R.C., Sharp, D.H., Zemach, C., 1977. Unstable normal mode for Rayleigh–Taylor instability in viscous fluids. *Phys. Fluids* 20, 2000.
- Menikoff, R., Mjolsness, R.C., Sharp, D.H., Zemach, C., 1978. Initial value problem for Rayleigh–Taylor instability of viscous fluids. *Phys. Fluids* 21, 1674.
- Menon, S., Lal, M., 1998. On the dynamics and instability of bubbles formed during underwater explosions. *Exp. Thermal Fluid Sci.* 16, 305.
- Merritt, E.C., Doss, F.W., Loomis, E.N., Flippo, K.A., Kline, J.L., 2015. Modifying mixing and instability growth through the adjustment of initial conditions in a high-energy-density counter-propagating shear experiment on OMEGA. *Phys. Plasmas* 22, 062306.
- Meshkov, E.E., 1969. Instability of the interface of two gases accelerated by a shock wave. *Sov. Fluid Dyn.* 4, 101.
- Meshkov, E.E., 1970. Instability of a shock wave accelerated interface between two gases. *NASA Tech. Trans. F-13*, 074.
- Meshkov, E.E., 1992. Instability of shock-accelerated interface between two media. In: Dannevik, W., Buckingham, A., Leith, C. (Eds.), *Advances in Compressible Turbulent Mixing*, p. 473.
- Meshkov, E.E., 1995. One approach to the experimental study of hydrodynamic instabilities: creation of a gas-gas interface using the dynamic technique. In: Young, R., Glimm, J., Boston, B. (Eds.), *Proc. 5th international Workshop on the Physics of Compressible Turbulent Mixing*. Stony Brook, NY, USA, p. 237.
- Meshkov, E.E., 2013. Some peculiar features of hydrodynamic instability development. *Philos. Trans. R. Soc. Lond. Ser. A Math. Phys. Eng. Sci.* 371, 20120288.
- Meyer, K.A., Blewett, P.J., 1972. Numerical investigation of the stability of a shock accelerated interface between two fluids. *Phys. Fluids* 15, 753.
- Mikaelian, K.O., 1986. Approximate treatment of density gradients in Rayleigh–Taylor instabilities. *Phys. Rev. A* 33, 1216.
- Mikaelian, K.O., 1989. Turbulent mixing generated by Rayleigh–Taylor and Richtmyer–Meshkov instabilities. *Physica D* 36, 343.
- Mikaelian, K.O., 1990. Rayleigh–Taylor and Richtmyer–Meshkov instabilities in multilayer fluids with surface tension. *Phys. Rev. A* 42, 7211.
- Mikaelian, K.O., 1991. Density gradient stabilization of the Richtmyer–Meshkov instability. *Phys. Fluids A* 3, 2638.
- Mikaelian, K.O., 1993. Effect of viscosity on Rayleigh–Taylor and Richtmyer–Meshkov instabilities. *Phys. Rev. E* 47, 375.
- Mikaelian, K.O., 1994a. Freeze-out and the effect of compressibility in the Richtmyer–Meshkov instability. *Phys. Fluids* 6, 356.
- Mikaelian, K.O., 1994b. Oblique shocks and the combined Rayleigh–Taylor, Kelvin–Helmholtz, and Richtmyer–Meshkov instabilities. *Phys. Fluids* 6, 1943.
- Mikaelian, K.O., 1996a. Rayleigh–Taylor instability in finite-thickness fluids with viscosity and surface tension. *Phys. Rev. E* 54, 3676.
- Mikaelian, K.O., 1996b. Connection between the Rayleigh and the Schroedinger equations. *Phys. Rev. E* 53, 3551.
- Mikaelian, K.O., 1998. Analytical approach to non-linear RT and RM instability. *Phys. Rev. Lett.* 80, 508.
- Mikaelian, K.O., 2003. Explicit expressions for the evolution of single-mode Rayleigh–Taylor and Richtmyer–Meshkov instabilities at arbitrary Atwood numbers. *Phys. Rev. E* 67, 026319.
- Mikaelian, K.O., 2005. Richtmyer–Meshkov instability of arbitrary shapes. *Phys. Fluids* 17, 034101.
- Mikaelian, K.O., 2008. Limitations and failures of the Layzer model for hydrodynamic instabilities. *Phys. Rev. E* 78, 015303.
- Mikaelian, K.O., 2009a. Reshocks, rarefactions, and the generalized Layzer model for hydrodynamic instabilities. *Phys. Fluids* 21, 024103.
- Mikaelian, K.O., 2009b. Nonlinear hydrodynamic interface instabilities driven by time-dependent accelerations. *Phys. Rev. E* 79, 065303.
- Mikaelian, K.O., 2010. Analytic approach to nonlinear hydrodynamic instabilities driven by time-dependent accelerations. *Phys. Rev. E* 81, 016325.
- Mikaelian, K.O., 2013. Shock-induced interface instability in viscous fluids and metals. *Phys. Rev. E* 87, 031003.
- Mikaelian, K.O., 2014a. Solution to Rayleigh–Taylor instabilities: Bubbles, spikes, and their scalings. *Phys. Rev. E* 89, 053009.

- Mikaelian, K.O., 2014b. Boussinesq approximation for Rayleigh–Taylor and Richtmyer–Meshkov instabilities. *Phys. Fluids* 26, 054103.
- Mikaelian, K.O., 2014c. Comment on “The effect of viscosity, surface tension and non-linearity on Richtmyer–Meshkov instability”. *Eur. J. Mech. B Fluids* 21, 511–526.
- Mikaelian, K.O., 2015. Testing an analytic model for Richtmyer–Meshkov turbulent mixing widths. *Shock Waves* 25, 35.
- Mikaelian, K.O., 2016. Oscillations of a standing shock wave generated by the Richtmyer–Meshkov instability. *Phys. Rev. Fluids* 1, 033601.
- Miller, G.H., Moses, E.I., Wuest, C.R., 2004a. The National Ignition Facility. *Opt. Eng.* 43, 2841.
- Miller, G.H., Moses, E.I., Wuest, C.R., 2004b. The National Ignition Facility: enabling fusion ignition for the 21st century. *Nucl. Fusion* 44, S228.
- Miller, P.L., Dimotakis, P.E., 1991. Reynolds number dependence of scalar fluctuations in a high Schmidt number turbulent jet. *Phys. Fluids A* 1156.
- Mima, K., 2004. Present status and future prospects of IFE and high power laser research in Asia. *Nucl. Fusion* 44, S129.
- Misra, A., Pullin, D.I., 1997. A vortex-based model for large-eddy simulation. *Phys. Fluids* 9, 2443.
- Mitchell, I.H., Bayley, J.M., Chittenden, J.P., Worley, J.F., Dangor, A.E., Haines, M.G., Choi, P., 1996. A high impedance mega-ampere generator for fiber Z-pinch experiments. *Rev. Sci. Instrum.* 67, 1533.
- Modestov, M., Bychkov, V., Marklund, M., 2009. The Rayleigh–Taylor instability in quantum magnetized plasma with para- and ferromagnetic properties. *Phys. Plasmas* 16, 032106.
- Mohseni, F., Mendoza, M., Succi, S., Herrmann, H.J., 2014. Relativistic effects on the Richtmyer–Meshkov instability. *Phys. Rev. D* 90, 125028.
- Moin, P., Mahesh, K., 1998. Direct numerical simulation: A tool in turbulence research. *Annu. Rev. Fluid Mech.* 30, 539.
- Momeni, M., 2013. Linear study of Rayleigh–Taylor instability in a diffusive quantum plasma. *Phys. Plasmas* 20, 082108.
- Monfared, S.K., Buttler, W.T., Frayer, D.K., Grover, M., LaLone, B.M., Stevens, G.D., Stone, J.B., Turley, W.D., Schauer, M.M., 2015. Ejected particle size measurement using Mie scattering in high explosive driven shockwave experiments. *J. Appl. Phys.* 117, 223105.
- Monin, A.S., Yaglom, A.M., 1975. Statistical Fluid Mechanics. MIT Press, Cambridge, MA.
- Mons, V., Cambon, C., Sagaut, P., 2016. A spectral model for homogeneous shear-driven anisotropic turbulence in terms of spherically averaged descriptors. *J. Fluid Mech.* 788, 147.
- Moretto, L.G., Tso, K., Colonna, N., Wozniak, G.J., 1992. New Rayleigh–Taylor-like surface instability and nuclear multifragmentation. *Phys. Rev. Lett.* 69, 1884.
- Morgan, R.V., Aure, R., Stockero, J.D., Greenough, J.A., Cabot, W., Likhachev, O.A., Jacobs, J.W., 2012. On the late-time growth of the two-dimensional Richtmyer–Meshkov instability in shock tube experiments. *J. Fluid Mech.* 712, 354.
- Morgan, R.V., Likhachev, O.A., Jacobs, J.W., 2016. Rarefaction-driven Rayleigh–Taylor instability. Part 1. Diffuse-interface linear stability measurements and theory. *J. Fluid Mech.* 791, 34.
- Moses, E.I., Wuest, C.R., 2003. The National Ignition Facility: Status and plans for laser fusion and high-energy-density experimental studies. *Fusion Sci. Technol.* 43, 420.
- Moses, E.I., Boyd, R.N., Remington, B.A., Keane, C.J., Al-Ayat, R., 2009. The National Ignition Facility: ushering in a new age for high energy density science. *Phys. Plasmas* 16, 041006.
- Motl, B., Oakley, J., Ranjan, D., Weber, C., Anderson, M., Bonazza, R., 2009. Experimental validation of a Richtmyer–Meshkov scaling law over large density ratio and shock strength ranges. *Phys. Fluids* 21, 126102.
- Movahed, P., Johnsen, E., 2013. A solution-adaptive method for efficient compressible multifluid simulations, with application to the Richtmyer–Meshkov instability. *J. Comput. Phys.* 239, 166.
- Mueschke, N.J., Schilling, O., 2009a. Investigation of Rayleigh–Taylor turbulence and mixing using direct numerical simulations with experimentally measured initial conditions. I. Comparison to experimental data. *Phys. Fluids* 21, 014106.
- Mueschke, N.J., Schilling, O., 2009b. Investigation of Rayleigh–Taylor turbulence and mixing using direct numerical simulation with experimentally measured initial conditions. II. Dynamics of transitional flow and mixing statistics. *Phys. Fluids* 21, 014107.
- Müller, B., Janka, H.-Th., 2015. Non-radial instabilities and progenitor asphericities in core-collapse supernovae. *Mon. Not. R. Astron. Soc.* 448, 2141.
- Müller, B., Melson, T., Heger, A., Janka, H.-Th., 2017. Supernova simulations from a 3D progenitor model –Impact of perturbations and evolution of explosion properties. *Mon. Not. R. Astron. Soc.* 472, 491.
- Müller, E., Fryxell, B., Arnett, D., 1991. Instability and clumping in SN 1987A. *Astron. Astrophys.* 251, 505.
- Mullin, T., 2011. Experimental studies of transition to turbulence in a pipe. *Annu. Rev. Fluid Mech.* 43, 1.
- Munro, D.H., 1988. Analytical solution for Rayleigh–Taylor growth rate in smooth density gradients. *Phys. Rev. A* 38, 1433.
- Murakami, M., Iida, S., 2002. Scaling laws for hydrodynamically similar implosions with heat conduction. *Phys. Plasmas* 9, 2745.
- Murdin, P., Murdin, L., 1985. Supernovae. Cambridge University Press, Cambridge, UK.
- Nagel, S.R., Haan, S.W., Rygg, J.R., Barrios, M., Benedetti, L.R., Bradley, D.K., Field, J.E., Hammel, B.A., Izumi, N., Jones, O.S., Khan, S.F., Ma, T., Pak, A.E., Tommasini, R., Town, R.P.J., 2015. Effect of the mounting membrane on shape in inertial confinement fusion implosions. *Phys. Plasmas* 22, 022704.
- Nakai, S., Takabe, H., 1996. Principles of inertial confinement fusion-physics of implosion and the concept of inertial fusion energy. *Rep. Progr. Phys.* 59, 1071.
- Nayfeh, A.H., 1969. On the nonlinear Lamb–Taylor instability. *J. Fluid Mech.* 38, 619.
- Nayfeh, A.H., 1973. Perturbation Methods. Wiley, New York.
- Nelkin, M., 1994. Universality and scaling in fully developed turbulence. *Adv. Phys.* 43, 143.
- Neuvazhaev, V.E., Yakovlev, V.G., 1976a. Turbulent mixing of an interface in a numerical gasdynamic calculation. *Zh. Vychisl. Mat. Fiz.* 16, 154.
- Neuvazhaev, V.E., Yakovlev, V.G., 1976b. Theory of turbulent mixing at the interface of fluids in a gravity field. *J. Appl. Mech. Tech. Phys.* 17, 513.
- Ngan, K., Straub, D.N., Bartello, P., 2005. Aspect ratio effects in quasi-two-dimensional turbulence. *Phys. Fluids* 17, 125102.
- Niederhaus, C.E., Jacobs, J.W., 2003. Experimental study of the Richtmyer–Meshkov instability of incompressible fluids. *J. Fluid Mech.* 485, 243.
- Niederhaus, J.H.J., Greenough, J.A., Oakley, J.G., Bonazza, R., 2008a. Vorticity evolution in two- and three-dimensional simulations for shock-bubble interactions. *Phys. Scr. T.* 132, 014019.
- Niederhaus, J.H.J., Greenough, J.A., Oakley, J.G., Ranjan, D., Anderson, M., Bonazza, R., 2008b. A computational parameter study for the three-dimensional shock–bubble interaction. *J. Fluid Mech.* 594, 85.
- Nishihara, K., Ikegawa, T., 1999. Weakly nonlinear theory of Rayleigh–Taylor instability. *J. Plasma Fusion Res. Series* 2, 536.
- Nishihara, K., Wouchuk, J.G., Matsuoka, C., Ishizaki, R., Zhakhovsky, V.V., 2010. Richtmyer–Meshkov instability: theory of linear and nonlinear evolution. *Phil. Trans. R. Soc. A* 368, 1769.
- Nittmann, J., Falle, S.A.E.G., Gaskell, P.H., 1982. The dynamical destruction of shocked gas clouds. *Mon. Not. R. Astron. Soc.* 201, 833.
- Nobile, A., Nikroo, A., Cook, R.C., Cooley, J.C., Alexander, D.J., Hackenberg, R.E., Necker, C.T., Dickerson, R.M., Kilkenny, J.L., Bernat, T.P., Chen, K.C., Xu, H., Stephens, R.B., Huang, H., Haan, S.W., Forsman, A.C., Atherton, L.J., Letts, S.A., Bono, M.J., Wilson, D.C., 2006. Status of the development of ignition capsules in the U.S. effort to achieve thermonuclear ignition on the National Ignition Facility. *Laser Part. Beams* 24, 567.
- Novak, G.S., Ostriker, J.P., Ciotti, L., 2011. Feedback from central black holes in elliptical galaxies: two-dimensional models compared to one-dimensional models. *Astrophys. J.* 737, 26.
- Nuckolls, J., Wood, L., Thiessen, A., Zimmerman, G., 1972. Laser compression of matter to super-high density: Thermonuclear (CTR) applications. *Nature* 239, 139.

- Obenschain, S.P., Bodner, S.E., Colombant, D., Gerber, K., Lehmberg, R.H., McLean, E.A., Mostovych, A.N., et al., 1996. The Nike KrF laser facility: Performance and initial target experiments. *Phys. Plasmas* 3, 2098.
- Oertel, M., Hempel, M., Klähn, T., Typel, S., 2017. Equations of state for supernovae and compact stars. *Rev. Modern Phys.* 89, 015007.
- Ofer, O., Alon, U., Shvarts, D., McCrory, R.L., Verdon, C.P., 1996. Modal model for the nonlinear multimode Rayleigh–Taylor instability. *Phys. Plasmas* 3, 3073.
- Oggian, T., Drikakis, D., Youngs, D.L., Williams, R.J.R., 2015. Computing multi-mode shock-induced compressible turbulent mixing at late times. *J. Fluid Mech.* 779, 411.
- Ohkitani, K., Kida, S., 1992. Triad interactions in a forced turbulence. *Phys. Fluids A* 4, 794.
- Olson, B.J., Greenough, J.A., 2014. Large eddy simulation requirements for the Richtmyer–Meshkov Instability. *Phys. Fluids* 26, 044103.
- Olson, D.H., Jacobs, J.W., 2009. Experimental study of Rayleigh–Taylor instability with complex initial perturbation. *Phys. Fluids* 21, 034103.
- Olver, P.J., 1993. Applications of Lie Groups to Differential Equations. Springer, Berlin.
- Oparin, A.M., Inogamov, N.A., Dem'yanov, A.Yu., 2000. On the spectral and statistical properties of Rayleigh–Taylor mixing. *JETP Lett.* 72, 490.
- Oron, D., Arazi, L., Kartoon, D., Rikanati, A., Alon, A., Shvarts, D., 2001. Dimensionality dependence of Rayleigh–Taylor and Richtmyer–Meshkov instability late time scaling laws. *Phys. Plasmas* 8, 2883.
- Orszag, S.A., 1970. Analytical theories of turbulence. *J. Fluid Mech.* 41, 363.
- Orszag, S.A., 1977. In: Balian, R., Peube, J.L. (Eds.), *Fluid Dynamics: Les Houches 1973*. Gordon & Breach, NY.
- Ott, E., 1972. Nonlinear evolution of the Rayleigh–Taylor instability of a thin layer. *Phys. Rev. Lett.* 20, 1429.
- Pacitto, G., Flament, C., Bacri, J.-C., Widom, M., 2000. Rayleigh–Taylor instability with magnetic fluids: Experiment and theory. *Phys. Rev. E* 62, 7941.
- Palmer, C.A.J., Schreiber, J., Nagel, S.R., Dover, N.P., Bellei, C., Beg, F.N., Bott, S., et al., 2012. Rayleigh–Taylor instability of an ultrathin foil accelerated by the radiation pressure of an intense laser. *Phys. Rev. Lett.* 108, 225002.
- Pandian, A., Swisher, N.C., Abarzhi, S.I., 2017. Deterministic and stochastic dynamics of Rayleigh–Taylor mixing with a power-law time-dependent acceleration. *Phys. Scr.* 92, 014002.
- Park, H.-S., Hurricane, O.A., Callahan, D.A., Casey, D.T., Dewald, E.L., Dittrich, T.R., Döppner, T., Hinkel, D.E., Berzak Hopkins, L.F., Le Pape, S., Ma, T., Patel, P.K., Remington, B.A., Robey, H.F., Salmonson, J.D., Kline, J.L., 2014. High-adiabat, high-foot inertial confinement fusion implosion experiments on the National Ignition Facility. *Phys. Rev. Lett.* 112, 055001.
- Peltier, W.R., Caulfield, C.R., 2003. Mixing efficiency in stratified shear flows. *Annu. Rev. Fluid Mech.* 35, 135.
- Peng, G., Zabusky, N.J., Zhang, S., 2003. Vortex-accelerated secondary baroclinic vorticity deposition and late-intermediate time dynamics of a two-dimensional Richtmyer–Meshkov interface. *Phys. Fluids* 15, 3730.
- Penney, W.G., Price, A.T., 1942. On the changing form of a nearly spherical submarine bubble. In: Hartmann, G.K., Hill, E.G. (Eds.), *British Report SW-27* (1942). In: Underwater Explosion Research, Vol. II, Office of Naval Research, Washington, D.C., p. 145.
- Perlmutter, S., Gabi, S., Goldhaber, G., Goobar, A., Groom, D.E., Hook, I.M., Kim, A.G., et al., 1997. Measurements of the cosmological parameters omega and lambda from the first seven supernovae at $Z \geq 0.35$. *Astrophys. J.* 483, 565.
- Perlmutter, S., Aldering, G., Goldhaber, G., Knop, R., Nugent, P., Castro, P., Deustua, S., Fabbro, S., Goobar, A., Groom, D., Hook, I., Kim, A., Kim, M., Lee, J., Nunes, N., Pain, R., Pennypacker, C., Quimby, R., Lidman, C., Ellis, R., Irwin, M., McMahon, R., Ruiz-Lapuente, P., Walton, N., Schaefer, B., Boyle, B., Filippenko, A., Matheson, T., Fruchter, A., Panagia, N., Newberg, H., Couch, W., 1999. (Supernova Cosmology Project), Measurements of Ω and Λ from 42 high-redshift supernovae. *Astrophys. J.* 517, 565.
- Petchenko, A., Bychkov, V., Vyacheslav, A., Eriksson, L.-E., 2006. Violent folding of a flame front in a flame-acoustic resonance. *Phys. Rev. Lett.* 97, 164501.
- Peterson, D.L., Bowers, R.L., Brownell, J.H., Greene, A.E., McLenithan, K.D., Oliphant, T.A., Roderick, N.F., Scannapieco, A.J., 1996. Two-dimensional modeling of magnetically driven Rayleigh–Taylor instabilities in cylindrical Z pinches. *Phys. Plasmas* 3, 368.
- Petraso, R.D., 1994. Rayleigh's challenge endures. *Nature* 367, 217.
- Pham, T., Meiron, D.I., 1993. A numerical study of Richtmyer–Meshkov instability in continuously stratified fluids. *Phys. Fluids A* 5, 344.
- Picone, J.M., Boris, J.P., 1986. Vorticity generation by shock propagation through bubbles in air. In: NRL Memorandum Rep. 5884. Naval Research Laboratory, Washington, D.C.
- Picone, J.M., Boris, J.P., Greig, J.R., Raleigh, M., Fernsler, R.F., 1981. Convective cooling of lightning channels. *J. Atmos. Sci.* 38, 2056.
- Picone, J.M., Oran, E.S., Boris, J.P., Young, T.R., 1985. Dynamics of Shock Waves Explosions and Detonations. American Institute of Aeronautics and Astronautics, New York, p. 429.
- Picone, J.M., Boris, J.P., Oran, E.S., Ahearne, R., 1986. Rotational motion generated by shock propagation through a nonuniform gas. In: Bershadier, D., Hanson, R. (Eds.), Proc. 15th Int'l Symp. on Shock Waves and Shock Tubes. Stanford University Press Stanford, Calif., pp. 523–529.
- Piriz, A.R., López Cela, J.J., Cortazar, O.D., Tahir, N.A., Hoffmann, D.H.H., 2005. Rayleigh–Taylor instability in elastic solids. *Phys. Rev. E* 72, 056313.
- Piriz, A.R., López Cela, J.J., Tahir, N.A., Hoffmann, D.H.H., 2006. Richtmyer–Meshkov flow in elastic solids. *Phys. Rev. E* 74, 037301.
- Piriz, A.R., López Cela, J.J., Serna Moreno, M.C., Cortázar, O.D., Tahir, N.A., Hoffmann, D.H.H., 2007. A new approach to Rayleigh–Taylor instability: Application to accelerated elastic solids. *Nucl. Instrum. Methods Phys. Res. A* 577, 250.
- Piriz, A.R., López Cela, J.J., Tahir, N.A., Hoffmann, D.H.H., 2008. Richtmyer–Meshkov instability in elastic–plastic media. *Phys. Rev. E* 78, 056401.
- Piriz, A.R., Lopez Cela, J.J., Tahir, N.A., 2009. Richtmyer–Meshkov instability as a tool for evaluating material strength under extreme conditions. *Nucl. Instrum. Methods Phys. Res. A* 606, 139.
- Piriz, A.R., Sun, Y.B., Tahir, N.A., 2015a. Hydrodynamic instability of elastic–plastic solid plates at the early stage of acceleration. *Phys. Rev. E* 91, 033007.
- Piriz, A.R., Sun, Y.B., Tahir, N.A., 2015b. Analytic model for the dynamic Z-pinch. *Phys. Plasmas* 22, 062704.
- Plag, H.-P., Jüttner, H.-U., 1995. Rayleigh–Taylor instabilities of a self-gravitating Earth. *J. Geodyn.* 20, 267.
- Plessset, M.S., Whipple, C.G., 1974. Viscous effects in Rayleigh–Taylor instability. *Phys. Fluids* 17, 1.
- Plewa, T., 2007. Detonating failed deflagration model of thermonuclear supernovae. I. Explosion dynamics. *Astrophys. J.* 657, 942.
- Plohr, J.N., Plohr, B.J., 2005. Linearized analysis of Richtmyer–Meshkov flow for elastic materials. *J. Fluid Mech.* 537, 55.
- Podladchikov, Yu.Yu., Talbot, C., Poliakov, A.N.B., 1993. Numerical models of complex diaps. *Tectonophysics* 228, 349.
- Pons, J., Oudin, C., Valero, J., 1992. Kinematics of large syn-orogenic intrusions: example of the lower proterozoic saraya batholith (eastern Senegal). *Geol. Rund.* 81, 473.
- Pope, S.B., 2004. Ten questions concerning the large Eddy simulation of turbulent flows. *New J. Phys.* 6, 35.
- Popil, R., Curzon, F.L., 1979. Production of reproducible Rayleigh–Taylor instabilities. *Rev. Sci. Instrum.* 50, 1291.
- Popil, R., Curzon, F.L., 1980. Climbing water films in experiments on Rayleigh–Taylor instabilities. *Phys. Fluids* 23, 1718.
- Poujade, O., 2006. Rayleigh–Taylor turbulence is nothing like Kolmogorov turbulence in the self-similar regime. *Phys. Rev. Lett.* 97, 185002.
- Poujade, O., Peybernes, M., 2010. Growth rate of Rayleigh–Taylor turbulent mixing layers from first principles. *Phys. Rev. E* 81, 016316.
- Pouquet, A., Frisch, U., Leorat, J., 1976. Strong MHD helical turbulence and the nonlinear dynamo effect. *J. Fluid Mech.* 77, 321.
- Pozzi, A., 1994. Applications of Padé Approximation Theory in Fluid Dynamics. World Scientific, Singapore.
- Prasad, J.K., Rasheed, A., Kumar, S., Sturtevant, B., 2000. The late-time development of the Richtmyer–Meshkov instability. *Phys. Fluids* 12, 2108.
- Prestridge, K., Vorobieff, P., Rightley, P.M., Benjamin, R.F., 2000a. Validation of an instability growth model using particle image velocimetry measurements. *Phys. Rev. Lett.* 84, 4353.

- Prestridge, K., Rightley, P.M., Vorobieff, P., Benjamin, R.F., Kurnit, N.A., 2000b. Simultaneous density-field visualization and PIV of a shock-accelerated gas curtain. *Exp. Fluids* 29, 339.
- Prime, M.B., Vaughan, D.E., Preston, D.L., Buttler, W.T., Chen, S.R., Oró, D.M., Pack, C., 2014. Using growth and arrest of Richtmyer–Meshkov instabilities and Lagrangian simulations to study high-rate material strength. *J. Phys.: Conf. Ser.* 500, 112051.
- Prime, M.B., Buttler, W.T., Buechler, M.A., Denissen, N.A., Kenamond, M.A., Mariam, F.G., Martinez, J.I., Oró, D.M., Schmidt, D.W., Stone, J.B., Tupa, D., Vogan-McNeil, W., 2017. Estimation of metal strength at very high rates using free-surface Richtmyer–Meshkov instabilities. *J. Dyn. Behav. Mater.* 3, 189.
- Probyn, M.G., Thornber, B., Drikakis, D., Youngs, D., Williams, R., 2014. An investigation into non-linear growth rate of 2D and 3D single-mode Richtmyer–Meshkov instability. *ASME J. Fluids Eng.* 136, 091208.
- Pullin, D.I., 2000. A vortex-based model for the subgrid flux of a passive scalar. *Phys. Fluids* 12, 2311.
- Puranik, P.B., Oakley, J.G., Anderson, M.H., Bonazza, R., 2004. Experimental study of the Richtmyer–Meshkov instability induced by a Mach 3 shock wave. *Shock Waves* 13, 413.
- Qiu, X., Liu, Y.-L., Zhou, Q., 2014. Local dissipation scales in two-dimensional Rayleigh–Taylor turbulence. *Phys. Rev. E* 90, 043012.
- Qiu, Z., Wu, Z., Cao, J., Li, D., 2008. Effects of transverse magnetic field and viscosity on the Richtmyer–Meshkov instability. *Phys. Plasmas* 15, 042305.
- Radha, P.B., Delettrez, J., Epstein, R., Glebov, V.Yu., Keck, R., McCrory, R.L., McKenty, P., Meyerhofer, D.D., Marshall, F., Regan, S.P., Roberts, S., Sangster, T.C., Seka, W., Skupsky, S., Smalyuk, V., Sorce, C., Stoeckl, C., Soures, J., Town, R.P.J., Yaakobi, B., 2002. Inference of mix in direct-drive implosions on OMEGA. *Phys. Plasmas* 9, 2208.
- Raman, K.S., Smalyuk, V.A., Casey, D.T., Haan, S.W., Hoover, D.E., Hurricane, O.A., Kroll, J.J., Nikroo, A., Peterson, J.L., Remington, B.A., Robey, H.F., Clark, D.S., Hammel, B.A., Landen, O.L., Marinak, M.M., Munro, D.H., Peterson, K.J., Salmonson, J., 2014. An in-flight radiography platform to measure hydrodynamic instability growth in inertial confinement fusion capsules at the National Ignition Facility. *Phys. Plasmas* 21, 072710.
- Ramaprabhu, P., Andrews, M.J., 2004. Experimental investigation of Rayleigh–Taylor mixing at small Atwood number. *J. Fluid Mech.* 502, 233.
- Ramaprabhu, P., Dimonte, G., 2005. Single-mode dynamics of the Rayleigh–Taylor instability at any density ratio. *Phys. Rev. E* 71, 036314.
- Ramaprabhu, P., Dimonte, G., Andrews, M.J., 2005. A numerical study of the influence of initial perturbations on the turbulent Rayleigh–Taylor instability. *J. Fluid Mech.* 536, 285.
- Ramaprabhu, P., Dimonte, G., Young, Y.-Y., Calder, A.C., Fryxwell, B., 2006. Limits of the potential flow approach to the single-mode Rayleigh–Taylor problem. *Phys. Rev. E* 74, 066308.
- Ramaprabhu, P., Dimonte, G., Woodward, P., Fryer, C., Rockefeller, G., Muthuraman, K., Lin, P.-H., Jayaraj, J., 2012. The late-time dynamics of the single-mode Rayleigh–Taylor instability. *Phys. Fluids* 24, 074107.
- Ramaprabhu, P., Karkhanis, V., Lawrie, A.G.W., 2013. The Rayleigh–Taylor instability driven by an accel-decel-accel profile. *Phys. Fluids* 25, 115104.
- Ramaprabhu, P., Karkhanis, V., Banerjee, R., Varshochi, H., Khan, M., Lawrie, A.G.W., 2016. Evolution of the single-mode Rayleigh–Taylor instability under the influence of time-dependent accelerations. *Phys. Rev. E* 93, 013118.
- Ramshaw, J.D., 1998. Simple model for linear and nonlinear mixing at unstable fluid interfaces with variable acceleration. *Phys. Rev. E* 58, 5834.
- Ranjan, D., Anderson, M., Oakley, J., Bonazza, R., 2005. Experimental investigation of a strongly shocked gas bubble. *Phys. Rev. Lett.* 94, 184507.
- Ranjan, D., Niederhaus, J., Motl, B., Anderson, M., Oakley, J., Bonazza, R., 2007. Experimental investigation of primary and secondary features in high-Mach-number shock-bubble interaction. *Phys. Rev. Lett.* 98, 024502.
- Ranjan, D., Niederhaus, J.H.J., Oakley, J.G., Anderson, M.H., Bonazza, R., Greenough, J.A., 2008a. Shock-bubble interactions: Features of divergent shock-refraction geometry observed in experiments and simulations. *Phys. Fluids* 20, 036101.
- Ranjan, D., Niederhaus, J.H.J., Oakley, J.G., Anderson, M.H., Greenough, J.A., Bonazza, R., 2008b. Experimental and numerical investigation of shock-induced distortion of a spherical gas inhomogeneity. *Phys. Scr. T* 132, 014020.
- Ranjan, D., Oakley, J., Bonazza, R., 2011. Shock-bubble interactions. *Annu. Rev. Fluid Mech.* 43, 117.
- Rao, P., Caulfield, C.P., Gibbon, J.D., 2017. Nonlinear effects in buoyancy-driven variable density turbulence. *J. Fluid Mech.* 810, 362.
- Rasthofer, U., Burton, G.C., Wall, W.A., Gravemeier, V., 2014a. Multifractal subgrid-scale modeling within a variational multiscale method for large-eddy simulation of passive-scalar mixing in turbulent flow at low and high Schmidt numbers. *Phys. Fluids* 26, 055108.
- Rasthofer, U., Burton, G.C., Wall, W.A., Gravemeier, V., 2014b. An algebraic variational multiscale-multigrid-multifractal method for large-eddy simulation of turbulent variable-density flow at low Mach number. *Internat. J. Numer. Methods Fluids* 76, 416.
- Ratafia, M., 1973. Experimental investigation of Rayleigh–Taylor instability. *Phys. Fluids* 16, 1207.
- Rayleigh, Lord, 1883. Investigation of the character of the equilibrium of an incompressible heavy fluid of variable density. *Proc. Lond. Math. Soc.* 14, 170–177.
- Rayleigh, Lord, 1900. *Scientific Papers Vol. II*. Cambridge Univ. Press, Cambridge, England, p. 200.
- Read, K.I., 1984. Experimental investigation of turbulent mixing by Rayleigh–Taylor instability. *Physica D* 12, 45.
- Read, K.I., Youngs, D.L., 1983. Experimental investigation of turbulent mixing by Rayleigh–Taylor instability. *Atomic Weapons Research Establishment Report 011/83*.
- Regan, S.P., Epstein, R., Hammel, B.A., Suter, L.J., Ralph, J., Scott, H., Barrios, M.A., Bradley, D.K., Callahan, D.A., Cerjan, C., Collins, G.W., Dixit, S.N., Doeppner, T., Edwards, M.J., Farley, D.R., Glenn, S., Glenzer, S.H., Golovkin, I.E., Haan, S.W., Hamza, A., Hicks, D.G., Izumi, N., Kilkenny, J.D., Kline, J.L., Kyrala, G.A., Landen, O.L., Ma, T., MacFarlane, J.J., Mancini, R.C., McCrory, R.L., Meezan, N.B., Meyerhofer, D.D., Nikroo, A., Peterson, K.J., Sangster, T.C., Springer, P., Town, R.P.J., 2012. Hot-spot mix in ignition-scale implosions on the NIF. *Phys. Plasmas* 19, 056307.
- Reid, W.H., 1961. The effect of surface tension and viscosity on the stability of two superposed fluids. *Proc. Camb. Philos. Soc.* 57, 415.
- Reinaud, J., Joly, L., Chassaing, P., 2000. The baroclinic secondary instability of the two-dimensional shear layer. *Phys. Fluids* 12, 2489.
- Reinecke, M., Hillebrandt, W., Niemeyer, J.C., 2002. Three-dimensional simulations of type Ia supernovae. *Astron. Astrophys.* 391, 1167.
- Remington, B.A., Weber, S.V., Marinak, M.M., Haan, S.W., Kilkenny, J.D., Wallace, R.J., Dimonte, G., 1995. Single-mode and multimode Rayleigh–Taylor experiments on Nova. *Phys. Plasmas* 2, 241.
- Remington, B.A., Kane, J., Drake, R.P., Glendinning, S.G., Estabrook, K., London, R., Castor, J., Wallace, R.J., Arnett, D., Liang, E., McCray, R., Rubenchik, A., Fryxell, B., 1997. Supernova hydrodynamics experiments on the Nova laser. *Phys. Plasmas* 4, 1994.
- Remington, B.A., Arnett, D., Drake, R.P., Takabe, H., 1999. Modeling astrophysical phenomena in the laboratory with intense lasers. *Science* 284, 1488.
- Remington, B.A., Drake, R.P., Ryutov, D.D., 2000. A review of astrophysics experiments on intense lasers. *Phys. Plasmas* 7, 1641.
- Remington, B.A., Drake, R.P., Ryutov, D.D., 2006. Experimental astrophysics with high power lasers and Z pinches. *Rev. Mod. Phys.* 78, 755.
- Remington, B.A., Rudd, R.E., Wark, J.S., 2015. From microjoules to megajoules and kilobars to gigabars: Probing matter at extreme states of deformation. *Phys. Plasmas* 22, 090501.
- Ren, G., Chen, Y., Tang, T., Li, Q., 2014. Ejecta production from shocked Pb surface via molecular dynamics. *J. Appl. Phys.* 116, 133507.
- Ren, G., Yan, J., Liu, J., Lan, K., Chen, Y.H., Huo, W.Y., Fan, Z., Zhang, X., Zheng, J., Chen, Z., Jiang, W., Chen, L., Tang, Q., Yuan, Z., Wang, F., Jiang, S., Ding, Y., Zhang, W., He, X.T., 2017. Neutron generation by laser-driven spherically convergent plasma fusion. *Phys. Rev. Lett.* 118, 165001.
- Renoult, M.-C., Petschek, R.G., Rosenblatt, C., Carlès, P., 2011. Deforming static fluid interfaces with magnetic fields: application to the Rayleigh–Taylor instability. *Exp. Fluids* 51, 1073.
- Renoult, M.-C., Carles, P., Ferjani, S., Rosenblatt, C., 2013. 2D Rayleigh–Taylor instability: interfacial arc-length vs deformation amplitude. *Europhys. Lett.* 101, 54001.

- Renoult, M.-C., Rosenblatt, C., Carles, P., 2015. Nodal analysis of nonlinear behavior of the instability at a fluid interface. *Phys. Rev. Lett.* 114, 114503.
- Reynolds, S.P., 2008. Supernova remnants at high energy. *Annu. Rev. Astron. Astrophys.* 46, 89.
- Riccobelli, D., Ciarletta, P., 2017. Rayleigh–Taylor instability in soft elastic layers. *Phil. Trans. R. Soc. A A375*, 20160421.
- Richtmyer, R.D., 1960. Taylor instability in shock acceleration of compressible fluids. *Commun. Pure Appl. Math.* 13, 297.
- Riess, A.G., Filippenko, A.V., Challis, P., Clocchiatti, A., Diercks, A., Garnavich, P.M., Gilliland, R.L., Hogan, C., Jha, S., Kirshner, R., Leibundgut, B., Phillips, M., Reiss, D., Schmidt, B., Schommer, R., Smith, R., Spyromilio, J., Stubbs, C., Suntzeff, N., Tonry, J. (High-Z Supernova Search), 1998. Observational evidence from supernovae for an accelerating universe and a cosmological constant. *Astron. J.* 116, 1009.
- Rightley, P.M., Vorobieff, R., Martin, R., Benjamin, R.F., 1999. Experimental observations of the mixing transition in a shock-accelerated gas curtain. *Phys. Fluids* 11, 186.
- Rikanati, A., Alon, U., Shvarts, D., 1998. Vortex model for the nonlinear evolution of the multimode Richtmyer–Meshkov instability at low Atwood numbers. *Phys. Rev. E* 58, 7410.
- Rikanati, A., Oron, D., Alon, U., Shvarts, D., 2000. Statistical mechanics merger model for hydrodynamic instabilities. *Astrophys. J. Suppl. Ser.* 127, 451.
- Rikanati, A., Oron, D., Sadot, O., Shvarts, D., 2003. High initial amplitude and high Mach number effects on the evolution of the single-mode Richtmyer–Meshkov instability. *Phys. Rev. E* 67, 026307.
- Ristorcelli, J.R., Clark, T.T., 2004. Rayleigh–Taylor turbulence: self-similar analysis and direct numerical simulations. *J. Fluid Mech.* 507, 213.
- Roberts, J.K., Miller, A.R., 1954. Heat and Thermodynamics, Vol. 4. Interscience Publishers.
- Roberts, M.S., Jacobs, J.W., 2016. The effects of forced small-wavelength, finite-bandwidth initial perturbations and miscibility on the turbulent Rayleigh–Taylor instability. *J. Fluid Mech.* 787, 50.
- Roberts, P.D., Rose, S.J., Thompson, P.C., Wright, R.J., 1980. The stability of multiple shell ICF targets. *J. Phys. D: Appl. Phys.* 13, 1957.
- Robey, H.F., 2004. Effects of viscosity and mass diffusion in hydrodynamically unstable plasma flows. *Phys. Plasmas* 11, 4123.
- Robey, H.F., Kane, J.O., Remington, B.A., Drake, R.P., Hurricane, O.A., Louis, H., Wallace, R.J., Knauer, J., Keiter, P., Arnett, D., Ryutov, D.D., 2001. An experimental testbed for the study of hydrodynamic issues in supernovae. *Phys. Plasmas* 8, 2446.
- Robey, H.F., Zhou, Y., Buckingham, A.C., Keiter, P., Remington, B.A., Drake, R.P., 2003. The time scale for the transition to turbulence in a high Reynolds number, accelerated flow. *Phys. Plasmas* 10, 614.
- Robinson, K., Dursi, L.J., Raicker, P.M., Rosner, R., Calder, A.C., Zingale, M., Truran, J.W., Linde, T., Caceres, A., Fryxell, B., Olson, K., Riley, K., Siegel, A., Vladimirova, N., 2004. Morphology of rising hydrodynamic and magnetohydrodynamic bubbles from numerical simulations. *Astrophys. J.* 601, 621.
- Rodriguez Azara, J.L., Emanuel, G., 1988. Compressible rotational flows generated by the substitution principle. *Phys. Fluids* 31, 1058.
- Rogallo, R.S., Moin, P., 1984. Numerical simulation of turbulent flows. *Annu. Rev. Fluid Mech.* 16, 99.
- Rollin, B., Andrews, M.J., 2013. On generating initial conditions for turbulence models: the case of Rayleigh–Taylor instability turbulent mixing. *J. Turbul.* 14, 77.
- Rosen, P.A., Wilde, B.H., Williams, R.J.R., Foster, J.M., Keiter, P.A., Coker, R.F., Perry, T.S., Taylor, M.J., Khokhlov, A.M., Drake, R.P., Bennett, G.R., Sinars, D.B., Campbell, R.B., 2005. Recent experimental results and modelling of high-Mach-number jets and the transition to turbulence. *Astrophys. Space Sci.* 298, 121.
- Rosslowe, C.K., Crowther, P.A., 2015. Spatial distribution of Galactic Wolf–Rayet stars and implications for the global population. *Mon. Not. R. Astron. Soc.* 447, 2322.
- Rott, N., 1956. Diffraction of a weak shock with vortex generation. *J. Fluid Mech.* 1, 111.
- Rott, N., 1992. Lord Rayleigh and hydrodynamic similarity. *Phys. Fluids A* 4, 2595.
- Roy, S., Mandal, L.K., Khan, M., Gupta, M.R., 2014. Combined effect of viscosity, surface tension and compressibility on Rayleigh–Taylor bubble growth between two fluids. *ASME J. Fluids Eng.* 136, 091101.
- Ruderman, M.S., 2017. Compressibility effect on the Rayleigh–Taylor instability with sheared magnetic fields. *Solar Phys.* 292, 47.
- Rudinger, G., 1958. Shock wave and flame interactions. In: Thring, M.W. (Ed.), Combustions and Propulsion: Third AGARD Colloquium. Pergamon, New York, pp. 153–182.
- Rudinger, G., Somers, L., 1960. Behaviour of small regions of different gases carried in accelerated gas flows. *J. Fluid Mech.* 7, 161.
- Ruev, G.A., Fedorov, A.V., Fomin, V.M., 2004. Evolution of the diffusion mixing layer of two gases upon interaction with shock waves. *J. Appl. Mech. Tech. Phys.* 45, 328.
- Ruev, G.A., Fedorov, A.V., Fomin, V.M., 2005. Development of the Richtmyer–Meshkov instability upon interaction of diffusion mixing layer of two gases with shock waves. *J. Appl. Mech. Tech. Phys.* 46, 307.
- Ruev, G.A., Fedorov, A.V., Fomin, V.M., 2006. Development of the Rayleigh–Taylor instability due to interaction of a diffusion mixing layer of two gases with compression waves. *Shock Waves* 16, 65.
- Ruszkowski, R., Enblin, T.A., Brüggen, M., Heinz, S., Pfrommer, C., 2007. Impact of tangled magnetic fields on fossil radio bubbles. *Mon. Not. Astron. Soc.* 378, 662.
- Ryutov, D.D., Remington, B.A., 2002. Scaling astrophysical phenomena to high-energy-density laboratory experiments. *Plasma Phys. Control. Fusion* 44, B407.
- Ryutov, D.D., Remington, B.A., 2003. A ‘perfect’ hydrodynamic similarity and effect of the Reynolds number on the global scale motion. *Phys. Plasmas* 10, 2629.
- Ryutov, D.D., Drake, R.P., Kane, J., Liang, E., Remington, B.A., Wood-Vasey, W.M., 1999. Similarity criteria for the laboratory simulation of supernova hydrodynamics. *Astrophys. J.* 518, 821.
- Ryutov, D.D., Derzon, M.S., Matzen, M.K., 2000. The Physics of fast Z pinches. *Rev. Mod. Phys.* 72, 167.
- Saddoughi, S.G., Veeravalli, S.V., 1994. Local isotropy in turbulent boundary layers at high Reynolds number. *J. Fluid Mech.* 268, 333.
- Sadot, O., Erez, L., Alon, U., Oron, D., Levin, L.A., Erez, G., Ben-Dor, G., Shvarts, D., 1998. Study of nonlinear evolution of single-mode and two-bubble interaction under Richtmyer–Meshkov instability. *Phys. Rev. Lett.* 80, 1654.
- Sadot, O., Rikanati, A., Oron, D., Ben-Dor, G., Shvarts, D., 2003. An experimental study of the high Mach number and high initial-amplitude effects on the evolution of the single-mode Richtmyer–Meshkov instability. *Laser Part. Beams* 21, 341.
- Saffman, P.G., 1967. The large-scale structure of homogeneous turbulence. *J. Fluid Mech.* 27, 581.
- Saffman, P.G., 1992. Vortex Dynamics. Cambridge University Press, Cambridge, p. 141.
- Saffman, P.G., Meiron, D.I., 1989. Kinetic energy generated by the incompressible Richtmyer–Meshkov instability in a continuously stratified fluid. *Phys. Fluids A* 1, 1767.
- Sagaut, P., 2006. Large Eddy Simulation for incompressible Flows, 3rd ed. Springer, Berlin.
- Sagaut, P., Cambon, C., 2008. Homogeneous Turbulence Dynamics. Cambridge University Press.
- Sager, I., Howell, J., Staber, A., Strother, T., Colbry, D., Bauer, W., 2015. Knudsen-number dependence of two-dimensional single-mode Rayleigh–Taylor fluid instabilities. *Phys. Rev. E* 92, 013009.
- Samtaney, R., Zabusky, N.J., 1998. Baroclinic circulation generation on shock accelerated slow/fast gas interfaces. *Phys. Fluids* 10, 1217.
- Samulyak, R., Prykarpatsky, Y., 2004. Richtmyer–Meshkov instability in liquid metal flows: influence of cavitation and magnetic fields. *Mathematics and Computers in Simulations* 65, 431.

- Sano, T., Nishihara, K., Matsuoka, C., Inoue, T., 2012. Magnetic field amplification associated with the Richtmyer–Meshkov instability. *Astrophys. J.* 758, 126.
- Saric, W.S., Reed, H.L., White, E.B., 2003. Stability and transition of three-dimensional boundary layers. *Annu. Rev. Fluid Mech.* 35, 413.
- Saurel, R., Huber, G., Jourdan, G., Lapébie, E., Munier, L., 2012. Modelling spherical explosions with turbulent mixing and post-detonation. *Phys. Fluids* 24, 115101.
- Sazonov, S.V., 1991. Dissipative structures in the F-region of the equatorial ionosphere generated by Rayleigh–Taylor instability. *Planet. Space Sci.* 39, 1667.
- Scannapieco, E., Brüggen, M., 2008. Subgrid modeling of AGN-driven turbulence in galaxy clusters. *Astrophys. J.* 686, 927.
- Schauer, M.M., Buttler, W.T., Frayer, D.K., Grover, M., Lalone, B.M., Monfared, S.K., Sorenson, D.S., Stevens, G.D., Turley, W.D., 2017. Ejected particle size distributions from shocked metal surfaces. *J. Dyn. Behav. Mater.* 3, 217.
- Schill, W., Wasem, J.V., Owen, J.M., 2017. Modelling and simulation of cratering and ejecta production during high velocity impacts. *J. Dyn. Behav. Mater.* 3, 180.
- Schilling, O., Mueschke, N.J., 2010. Analysis of turbulent transport and mixing in transitional Rayleigh–Taylor unstable flow using direct numerical simulation data. *Phys. Fluids* 22, 105102.
- Schilling, O., Zhou, Y., 2002. Analysis of spectral eddy viscosity and backscatter in incompressible, isotropic turbulence using statistical closure theory. *Phys. Fluids* 14, 1244.
- Schneider, M., Dimonte, G., Remington, B., 1998. Large and small scale structure in Rayleigh–Taylor mixing. *Phys. Rev. Lett.* 80, 3507.
- Schranner, F.S., Domaradzki, J.A., Hickel, S., Adams, N.A., 2015. Assessing the numerical dissipation rate and viscosity in numerical simulations of fluid flows. *Comput. & Fluids* 114, 84.
- Schultz, D.M., Kanak, K.M., Straka, J.M., Trapp, R.J., Gordon, B.A., Zrnic, D.S., Bryan, G.H., Durant, A.J., Garrett, T.J., Klein, P.M., Lilly, D.K., 2006. The mysteries of mammatus clouds: Observations and formation mechanisms. *J. Atmos. Sci.* 63, 2409.
- Schumann, U., 1975. Subgrid-scale model for finite-difference simulations of turbulence in plane channels and annuli. *J. Comput. Phys.* 18, 376.
- Schwartzschild, M., 1965. *Structure and Evolution of The Stars*. Dover, NY.
- Scorer, R.S., 1957. Experiments on convection of isolated masses of buoyant fluid. *J. Fluid Mech.* 2, 583.
- Seager, S., Kuchner, M., Hier-Majumder, C.A., Militzer, B., 2007. Mass–radius relationships for solid exoplanets. *Astrophys. J.* 669, 1279.
- Sedov, L.I., 1997. *Mechanics of Continuous Media*. World Scientific, Singapore.
- Selig, F., Wermund, E.G., 1966. Families of salt domes in the gulf coastal province. *Geophysics* 31, 726.
- Sen, S., Fukuyama, A., Honary, F., 2010. Rayleigh Taylor instability in a dusty plasma. *J. Atmos. Sol.-Terr. Phys.* 72, 938.
- Serra, S., Toutant, A., Bataille, F., Zhou, Y., 2012a. Turbulent kinetic energy spectrum in very anisothermal flows. *Phys. Lett. A* 376, 3177.
- Serra, S., Toutant, A., Bataille, F., Zhou, Y., 2012b. High-temperature gradient effect on a turbulent channel flow using thermal large-eddy simulation in physical and spectral spaces. *J. Turbul.* 13, 1.
- Shadloo, M.S., Zainali, A., Yıldız, M., 2013. Simulation of single mode Rayleigh–Taylor instability by SPH method. *Comput. Mech.* 51, 699.
- Shao, J.-L., Wang, P., He, A.-M., Duan, S.-Q., Qin, C.-S., 2013. Atomistic simulations of shock-induced microjet from a grooved aluminium surface. *J. Appl. Phys.* 113, 153501.
- Shao, J.-L., Wang, P., He, A.-M., 2014. Microjetting from a grooved Al surface under supported and unsupported shocks. *J. Appl. Phys.* 116, 073501.
- Sharp, D.H., 1984. An overview of Rayleigh–Taylor instability. *Physica D* 12, 3.
- Sharp, D.H., Wheeler, J.A., 1961. Late Stage of Rayleigh–Taylor instability, institute for Defense Analysis, Report AD-A009 943. Distributed by National Technical Information Service, U. S. Department of Commerce.
- Shen, X.F., Qiao, B., Zhang, H., Kar, S., Zhou, C.T., Chang, H.X., Borghesi, M., He, X.T., 2017. Achieving stable radiation pressure acceleration of heavy ions via successive electron replenishment from ionization of a High-Z material coating. *Phys. Rev. Lett.* 118, 204802.
- Shetty, R., Ostriker, E.C., 2008. Cloud and star formation in disk galaxy models with feedback. *Astrophys. J.* 684, 978.
- Shigeyama, T., Nomoto, K., 1990. Theoretical light curve of SN 1987A and mixing of hydrogen and nickel in the ejecta. *Astrophys. J.* 360, 242.
- Shigeyama, T., Nomoto, K., Hashimoto, M., 1988. Hydrodynamical models and the light curve of Supernova 1987A in the Large Magellanic Cloud. *Astron. Astrophys.* 196, 141.
- Shirkey, R.C., 1978. The radio dynamical evolution of young supernova remnants. *Astrophys. J.* 224, 477.
- Shu, C.-W., 1999. High order ENO and WENO schemes for computational fluid dynamics. In: Barth, T.J., Deconinck, H. (Eds.), *High-Order Methods for Computational Physics*. Springer-Verlag, New York, p. 439.
- Shu, C.-W., Osher, S., 1988. Efficient implementation of essentially non-oscillatory shock-capturing schemes. *J. Comput. Phys.* 77, 439.
- Shu, H., Fu, S., Huang, X., Wu, J., Xie, Z., Zhang, F., Ye, J., Jia, G., Zhou, H., 2014. Measuring preheat in laser-drive aluminum using velocity interferometer system for any reflector: Experiment. *Phys. Plasmas* 21, 082708.
- Shvarts, D., Alon, U., Ofer, O., McCrory, R.L., Verdon, C.P., 1995. Nonlinear evolution of multimode Rayleigh–Taylor instability in two and three dimensions. *Phys. Plasmas* 2, 2465.
- Shvarts, D., Oron, D., Kartoon, D., Rikanati, A., Sadot, O., Srebro, Y., Yedvab, Y., Ofer, D., Levin, A., Sarid, E., Ben-Dor, G., Erez, L., Erez, G., Yosef-Hai, A., Alon, U., Arazi, L., 2000. Scaling laws of nonlinear Rayleigh–Taylor and Richtmyer–Meshkov instabilities in two and three dimensions. *C. R. Acad. Sci. Paris, Série IV* 1, 719.
- Si, T., Zhai, Z., Yang, J., Luo, X., 2012. Experimental investigation of reshocked spherical gas interfaces. *Phys. Fluids* 24, 054101.
- Simakov, A.N., Wilson, D.C., Yi, S.A., Kline, J.L., Clark, D.S., Milovich, J.L., Salmonson, J.D., Batha, S.H., 2014. Optimized beryllium target design for indirectly driven inertial confinement fusion experiments on the National Ignition Facility. *Phys. Plasmas* 21, 022701.
- Siqueiros, D.A., Collective suicide. Museum of Modern Art, New York, http://www.moma.org/collection/object.php?object_id=79146.
- Skinner, M.A., Burrows, A., Dolence, J.C., 2016. Should one use the ray-by-ray approximation in core-collapse supernova simulations? *Astrophys. J.* 831, 81.
- Skrbek, L., Stalp, S.R., 2000. On the decay of homogeneous isotropic turbulence. *Phys. Fluids* 12, 1997.
- Slutz, S.A., Herrmann, M.C., Vesey, R.A., Sefkow, A.B., Sinars, D.B., Rovang, D.C., Peterson, K.J., Cuneo, M.E., 2010. Pulsed-power-driven cylindrical liner implosions of laser preheated fuel magnetized with an axial field. *Phys. Plasmas* 17, 056303.
- Smagorinsky, J., 1963. General circulation experiments with the primitive equations: I. The basic experiment. *Mon. Weather Rev.* 91, 99.
- Smalyuk, V.A., 2012. Experimental techniques for measuring Raleigh–Taylor instability in inertial confinement fusion. *Phys. Scr.* 86, 058204.
- Smalyuk, V.A., Boehly, T.R., Bradley, D.K., Goncharov, V.N., Delettrez, J.A., Knauer, J.P., Meyerhofer, D.D., Oron, D., Shvarts, D., 1998. Saturation of the Rayleigh–Taylor growth of broad-bandwidth laser-imposed nonuniformities in planar targets. *Phys. Rev. Lett.* 81, 5342.
- Smalyuk, V.A., Boehly, T.R., Bradley, D.K., Goncharov, V.N., Delettrez, J.A., Knauer, J.P.D., Meyerhofer, D., Oron, D., Shvarts, D., Srebro, Y., Town, R.P.J., 1999. Nonlinear evolution of broad-bandwidth, laser-imprinted nonuniformities in planar targets accelerated by 351-nm laser light. *Phys. Plasmas* 6, 4022.
- Smalyuk, V.A., Delettrez, J.A., Goncharov, V.N., Marshall, F.J., Meyerhofer, D.D., Regan, S.P., Sangster, T.C., Town, R.P.J., Yaakobi, B., 2002. Rayleigh–Taylor instability in the deceleration phase of spherical implosion experiments. *Phys. Plasmas* 9, 2738.
- Smalyuk, V.A., Sadot, O., Delettrez, J.A., Meyerhofer, D.D., Regan, S.P., Sangster, T.C., 2005. Fourier-space nonlinear Rayleigh–Taylor growth measurements of 3D laser-imprinted modulations in planar targets. *Phys. Rev. Lett.* 95, 215001.
- Smalyuk, V.A., Sadot, O., Betti, R., Goncharov, V.N., Delettrez, J.A., Meyerhofer, D.D., Regan, S.P., Sangster, T.C., Shvarts, D., 2006. Rayleigh–Taylor growth measurements of three-dimensional modulations in a nonlinear regime. *Phys. Plasmas* 13, 056312.

- Smalyuk, V.A., Tipton, R.E., Pino, J.E., Casey, D.T., Grim, G.P., Remington, B.A., Rowley, D.P., Weber, S.V., Barrios, M., Benedetti, L.R., Bleuel, D.L., Bradley, D.K., Caggiano, J.A., Callahan, D.A., Cerjan, C.J., Clark, D.S., Edgell, D.H., Edwards, M.J., Frenje, J.A., Gatu-Johnson, M., Glebov, V.Y., Glenn, S., Haan, S.W., Hamza, A., Hatarik, R., Hsing, W.W., Izumi, N., Khan, S., Kilkenny, J.D., Kline, J., Knauer, J., Landen, O.L., Ma, T., McNamey, J.M., Mintz, M., Moore, A., Nikroo, A., Pak, A., Parham, T., Petrasco, R., Sayre, D.B., Schneider, M.B., Tommasini, R., Town, R.P., Widmann, K., Wilson, D.C., Yeamans, C.B., 2014a. Measurements of an ablator-gas atomic mix in indirectly driven implosions at the National Ignition Facility. *Phys. Rev. Lett.* 112, 025002.
- Smalyuk, V.A., Casey, D.T., Clark, D.S., Edwards, M.J., Haan, S.W., Hamza, A., Hoover, D.E., Hsing, W.W., Hurricane Kilkenny, J.D., Kroll, J., Landen, O., Moore, A., Nikroo, A., Peterson, L., Raman, K., Remington, B.A., Robey, H.F., Weber, S.V., Widmann, K., 2014b. First measurements of hydrodynamic instability growth in indirectly driven implosions at ignition-relevant conditions on the National Ignition Facility. *Phys. Rev. Lett.* 112, 185003.
- Smalyuk, V.A., Weber, C.R., Robey, H.F., Casey, D.T., Chen, K.-C., Clark, D.S., Farrell, M., Felker, S., Field, J.E., Haan, S.W., Hammel, B.A., Hamza, A.V., Hoover, D., Kroll, J.J., Landen, O.L., MacPhee, A.G., Martinez, D., Nikroo, A., Rice, N., 2017. Hydrodynamic instability growth of three-dimensional modulations in radiation-driven implosions with “low-foot” and “high-foot” drives at the National Ignition Facility. *Phys. Plasmas* 24, 042706.
- Smarr, L., 2009. Progenitors of core-collapse supernovae. *Annu. Rev. Astron. Astrophys.* 47, 63.
- Smarr, L., Wilson, J.R., Barton, R.T., Bowers, R.L., 1981. Rayleigh–Taylor overturn in supernova core collapse. *Astrophys. J.* 246, 515.
- Smeeton, V.S., Youngs, D.L., 1987. Experimental investigation of turbulent mixing by Rayleigh–Taylor instability, III, AWE Report N.O 35/87.
- Snider, D.M., Andrews, M.J., 1994. Rayleigh–Taylor and shear driven with an unstable thermal stratification. *Phys. Fluids* 6, 3324.
- Sohn, S.-I., 2003. Simple potential-flow model of Rayleigh–Taylor and Richtmyer–Meshkov instabilities for all density ratios. *Phys. Rev. E* 67, 026301.
- Sohn, S.-I., 2004. Vortex model and simulations for Rayleigh–Taylor and Richtmyer–Meshkov instabilities. *Phys. Rev. E* 69, 036703.
- Sohn, S.-I., 2007. Bubble interaction model for hydrodynamic unstable mixing. *Phys. Rev. E* 75, 066312.
- Sohn, S.-I., 2008. Quantitative modeling of bubble competition in Richtmyer–Meshkov instability. *Phys. Rev. E* 78, 017302.
- Sohn, S.-I., 2009. Effects of surface tension and viscosity on the growth rates of Rayleigh–Taylor and Richtmyer–Meshkov instabilities. *Phys. Rev. E* 80, 055302(R).
- Sohn, S.-I., 2016. Self-similar roll-up of a vortex sheet driven by a shear flow: Hyperbolic double spiral. *Phys. Fluids* 28, 064104.
- Sohn, S.-I., Baek, S., 2017. Bubble merger and scaling law of the Rayleigh–Taylor instability with surface tension. *Phys. Lett. A* 381, 3812.
- Sohn, S.-I., Zhang, Q., 2001. Late time behavior of bubbles at unstable interfaces in two dimensions. *Phys. Fluids* 13, 3493–3495.
- Sorenson, D.S., Capelle, G.A., Grover, M., Johnson, R.P., Kaufman, M.I., LaLone, B.M., Malone, R.M., et al., 2017. Measurements of Sn ejecta particle-size distributions using ultraviolet in-line Fraunhofer holography. *J. Dyn. Behav. Mater.* 3, 233.
- Soulard, O., 2012. Implications of the Monin–Yaglom relation for Rayleigh–Taylor turbulence. *Phys. Rev. Lett.* 109, 254501.
- Soulard, O., Griffond, J., 2012. Inertial range anisotropy in Rayleigh–Taylor turbulence. *Phys. Fluids* 24, 025101.
- Soulard, O., Griffond, J., Gréa, B.-J., 2014. Large-scale analysis of self-similar unstably stratified homogeneous turbulence. *Phys. Fluids* 26, 015110.
- Soulard, O., Griffond, J., Gréa, B.-J., 2015. Large-scale analysis of unconfined self-similar Rayleigh–Taylor turbulence. *Phys. Fluids* 27, 095103.
- Spielman, R.B., Deeney, C., Chandler, G.A., Douglas, M.R., Fehl, D.L., Matzen, M.K., McDaniel, D.H., et al., 1998. Tungsten wire-array Z-pinch experiments at 200 TW and 2 MJ. *Phys. Plasmas* 5, 2105.
- Spindloe, C., Wyatt, D., Haddock, D., East, I., Cross, J.E., Danson, C.N., Falize, E., Foster, J.M., Koenig, M., Gregori, G., 2015. Target fabrication for the POLAR experiment on the Orion laser facility. *High Power Laser Sci. Eng.* 3, e8.
- Statsenko, V.P., Yanilkin, Yu.V., Zhmaylo, V.Z., 2013. Direct numerical simulation of turbulent mixing. *Phil. Trans. R. Soc. A* 371, 20120216.
- Stixrude, L., 2012. Structure of Iron to 1 Gbar and 40000 K. *Phys. Rev. Lett.* 108, 055505.
- Stokes, G.G., 1851. On the effect of the internal friction of fluids on the motion of pendulums. *Cambr. Phil. Trans. IX*, 8.
- Sturtevant, B., Kulkarni, V.A., 1976. The focusing of weak shock waves. *J. Fluid Mech.* 73, 651.
- Subramaniam, A., Ghaisas, N., Lele, S., 2017. High-order Eulerian simulations of multi-material elastic-plastic Flow. *ASME. J. Fluids Eng.* <http://dx.doi.org/10.1115/1.4038399>.
- Sultan, P.J., 1996. Linear theory and modeling of the Rayleigh–Taylor instability leading to the occurrence of equatorial spread F. *J. Geophys. Res.* 101, 26875.
- Swegle, J.W., Robinson, A.C., 1989. Acceleration instability in elastic–plastic solids I. Numerical simulations of plate acceleration. *J. Appl. Phys.* 66, 2838.
- Takabe, H., 2001. Astrophysics with intense and ultra-intense lasers “laser astrophysics”. *Prog. Theoret. Phys. Suppl.* 143, 202.
- Takabe, H., 2004. A historical perspective of developments in hydrodynamic instabilities, integrated codes and laboratory astrophysics. *Nucl. Fusion* 44, S149.
- Takabe, H., Montierth, L., Morse, R.L., 1983. Self-consistent eigenvalue analysis of Rayleigh–Taylor instability in an ablating plasma. *Phys. Fluids* 26, 2299.
- Takabe, H., Mima, K., Montierth, L., Morse, R.L., 1985. Self-consistent growth rate of the Rayleigh–Taylor instability in an ablatively accelerating plasma. *Phys. Fluids* 28, 3676.
- Takabe, H., Yamanaka, M., Mima, K., Yamanaka, C., Azechi, H., Miyanaga, N., Nakatsuka, M., Jitsuno, T., Norimatsu, T., Takagi, M., Nishimura, H., Nakai, M., Yabe, T., Sasaki, T., Yoshida, K., Nishihara, K., Kato, Y., Izawa, Y., Yamanaka, T., Nakai, S., 1988. Scalings of implosion experiments for high neutron yield. *Phys. Fluids* 31, 2884.
- Takabe, H.A., Kato, T.N., Sakawa, Y., Kuramitsu, Y., Morita, T., Kadono, T., Shigemori, K., Otani, K., Nagatomo, H., Norimatsu, T., Dono, S., 2008. High-Mach number collisionless shock and photo-ionized non-LTE plasma for laboratory astrophysics with intense lasers. *Plasma Phys. Contr. Fusion* 50, 124057.
- Tang, W., Mahalov, A., 2013. Stochastic Lagrangian dynamics for charged flows in the E–F regions of ionosphere. *Phys. Plasmas* 20, 032305.
- Tanveer, S., 1993. Singularities in the classical Rayleigh–Taylor flow: formation and subsequent motion. *Proc. R. Soc. Lond. Ser. A Math. Phys. Eng. Sci.* 441, 501.
- Tassart, J., 2004. Overview of inertial fusion and high-intensity laser plasma research in Europe. *Nucl. Fusion* 44, S134.
- Taylor, G.I., 1950. The instability of liquid surfaces when accelerated in a direction perpendicular to their plane. *Proc. R. Soc. Lond. Ser. A Math. Phys. Eng. Sci.* 201, 192.
- Taylor, G.I., 1974. The interaction between experiment and theory in fluid mechanics. *Annu. Rev. Fluid Mech.* 6, 1.
- Tennekes, H., Lumley, J.L., 1972. *First Course in Turbulence*. MIT Press, Cambridge, MA.
- Terrones, G., 2005. Fastest growing linear Rayleigh–Taylor modes at solid/fluid and solid/solid interfaces. *Phys. Rev. E* 71, 036306.
- Thomas, G.O., 2003. The aerodynamic breakup of ligaments. *Atom. Sprays* 13, 117.
- Thomas, V.A., Kares, R.J., 2012. Drive asymmetry and the origin of turbulence in an ICF implosion. *Phys. Rev. Lett.* 109, 075004.
- Thormann, A., Meneveau, C., 2014. Decay of homogeneous, nearly isotropic turbulence behind active fractal grids. *Phys. Fluids* 26, 025112.
- Thornber, B., 2016. Impact of domain size and statistical errors in simulations of homogeneous decaying turbulence and the Richtmyer–Meshkov instability. *Phys. Fluids* 28, 045106.
- Thornber, B., Drikakis, D., 2007. Large-eddy simulation of shock-wave-induced turbulent mixing. *ASME J. Fluids Eng.* 129, 1504.
- Thornber, B., Zhou, Y., 2012. Energy transfer in the Richtmyer–Meshkov instability. *Phys. Rev. E* 86, 056302.
- Thornber, B., Mosedale, A., Drikakis, D., Youngs, D.L., Williams, R.J.R., 2008a. An improved reconstruction method for compressible flows with low Mach number features. *J. Comput. Phys.* 227, 4873.
- Thornber, B., Drikakis, D., Williams, R., Youngs, D., 2008b. On Entropy generation and dissipation of kinetic energy in high-resolution shock-capturing schemes. *J. Comput. Phys.* 227, 4853.

- Thornber, B., Drikakis, D., Youngs, D.L., Williams, R.J.R., 2010. The influence of initial conditions on turbulent mixing due to Richtmyer–Meshkov instability. *J. Fluid Mech.* 654, 99.
- Thornber, B., Bilger, R.W., Masri, A.R., Hawkes, E.R., 2011a. An algorithm for LES of premixed compressible flows using the conditional moment closure model. *J. Comput. Phys.* 230, 7687.
- Thornber, B., Drikakis, D., Youngs, D.L., Williams, R.J.R., 2011b. Growth of a Richtmyer–Meshkov turbulent layer after reshock. *Phys. Fluids* 23, 095107.
- Thoroddsen, S.T., van Atta, C.W., Yampolsky, J.S., 1998. Experiments on homogeneous turbulence in an unstably stratified fluid. *Phys. Fluids* 10, 3155.
- Tian, B.-L., Zhang, X.-T., Qi, J., Wang, S.-H., 2011a. Effects of a premixed layer on the Richtmyer–Meshkov instability. *Chin. Phys. Lett.* 28, 114701.
- Tian, B.-L., Shen, W.-D., Jiang, S., Wang, S.-H., Yan, L., 2011b. A global arbitrary Lagrangian–Eulerian method for stratified Richtmyer–Meshkov instability. *Comput. & Fluids* 46, 113.
- Tian, L., Russell, A., 2014. Phase field study of interfacial diffusion-driven spheroidization in a composite comprised of two mutually insoluble phases. *J. Chem. Phys.* 140, 124706.
- Tomasini, R., Field, J.E., Hammel, B.A., Landen, O.L., Haan, S.W., Aracne-Ruddle, C., Benedetti, L.R., Bradley, D.K., Callahan, D.A., Dewald, E.L., Doeppner, T., 2015. Tent-induced perturbations on areal density of implosions at the National Ignition Facility. *Phys. Plasmas* 22, 056315.
- Townsend, A.A., 1976. Structure of Turbulent Shear Flow. Cambridge Univ. Press, Cambridge, UK.
- Trimble, V., 1968. Motions and structure of the filamentary envelope of the Crab Nebula. *Astron. J.* 73, 535.
- Tritschler, V.K., Hickel, S., Hu, X.Y., Adams, N.A., 2013a. On the Kolmogorov inertial subrange developing from Richtmyer–Meshkov instability. *Phys. Fluids* 25, 071701.
- Tritschler, V.K., Hu, X.Y., Hickel, S., Adams, N.A., 2013b. Numerical simulation of a Richtmyer–Meshkov instability with an adaptive central-upwind sixth-order WENO scheme. *Phys. Scr. T* 155, 014016.
- Tritschler, V.K., Olson, B.J., Lele, S.K., Hickel, S., Hu, X.Y., Adam, N.A., 2014a. On the Richtmyer–Meshkov instability evolving from a deterministic multimode planar interface. *J. Fluid Mech.* 755, 429.
- Tritschler, V.K., Zubel, M., Hickel, S., Adams, N.A., 2014b. Evolution of length scales and statistics of Richtmyer–Meshkov instability from direct numerical simulations. *Phys. Rev. E* 90, 063001.
- Tryggvason, G., 1988. Numerical simulations of the Rayleigh–Taylor instability. *J. Comput. Phys.* 75, 253.
- Tryggvason, G., Unverdi, S.O., 1990. Computations of three-dimensional Rayleigh–Taylor instability. *Phys. Fluids A* 2, 656.
- Tsiklashvili, V., Romero Colio, P.E., Likhachev, O.A., Jacobs, J.W., 2012. An experimental study of small Atwood number Rayleigh–Taylor instability using the magnetic levitation of paramagnetic fluids. *Phys. Fluids* 24, 052106.
- Turner, J.S., 1973. Buoyancy Effects in Fluids. Cambridge Univ. Press, London.
- Uchiyama, Y., Aharonian, F.A., 2008. Fast variability of nonthermal X-ray emission in Cassiopeia A: probing electron acceleration in reverse-shocked ejecta. *Astrophys. J. Lett.* 677, L105.
- Uchiyama, Y., Aharonian, F.A., Tanaka, T., Takahashi, T., Maeda, Y., 2007. Extremely fast acceleration of cosmic rays in a supernova remnant. *Nature* 449, 576.
- Unverdi, S.O., Tryggvason, G., 1992. Computations of multi-fluid flows. *Physica D* 60, 70.
- Vandenboomgaerde, M., 2003. Nonlinear analytic growth rate of a single-mode Richtmyer–Meshkov instability. *Laser Part. Beams* 21, 317.
- Vandenboomgaerde, M., Lafitte, O., 2004. Analytic model for the single-mode Richtmyer–Meshkov instability from the linear to the nonlinear regime. In: Dalziel, S. (Ed.), Proceedings of 9th International Workshop on The Physics of Compressible Turbulent Mixing. Cambridge, UK.
- Vandenboomgaerde, M., Mügler, C., Gauthier, S., 1998. Impulsive model for the Richtmyer–Meshkov instability. *Phys. Rev. E* 58, 1874.
- Vandenboomgaerde, M., Gauthier, S., Mügler, C., 2002. Nonlinear regime of a multimode Richtmyer–Meshkov instability: A simplified perturbation theory. *Phys. Fluids* 14, 1111.
- Vandenboomgaerde, M., Cherfils, C., Galmiche, D., Gauthier, S., Raviart, P.A., 2003. Efficient perturbation methods for Richtmyer–Meshkov and Rayleigh–Taylor instabilities: Weakly nonlinear stage and beyond. *Laser Part. Beams* 21, 321.
- Vandenboomgaerde, M., Souffland, D., Mariani, C., Biamino, L., Jourdan, G., Houas, L., 2014. An experimental and numerical investigation of the dependency on the initial conditions of the Richtmyer–Meshkov instability. *Phys. Fluids* 26, 024109.
- Vanden-Broeck, J.-M., 1984. Bubbles rising in a tube and jets falling from a nozzle. *Phys. Fluids* 27, 1090.
- Vandervoort, P.O., 1961. The character of the equilibrium of a compressible, inviscid fluid of varying density. *Astrophys. J.* 134, 699.
- Vassilenco, A.M., Buryakov, O.V., Kuropatenko, V.F., Olkhovskaya, V.I., Ratnikov, V.P., Jakovlev, V.G., 1992. Experimental research of gravitational instability and turbulization of flow at the noble gases interface. In: Dannevik, W.P., Buckingham, A.C., Leith, C.E. (Eds.), Advances in Compressible Turbulent Mixing, First Intl Workshop on the Physics of Compressible Turbulent Mixing, p. 581.
- Veerasha, B.M., Das, A., Sen, A., 2005. Rayleigh–Taylor instability driven nonlinear vortices in dusty plasmas. *Phys. Plasmas* 12, 044506.
- Velikovich, A.L., 1996. Analytic theory of Richtmyer–Meshkov instability for the case of reflected rarefaction wave. *Phys. Fluids* 8, 1666.
- Velikovich, A.L., Dimonte, G., 1996. Nonlinear perturbation theory of the incompressible Richtmyer–Meshkov instability. *Phys. Rev. Lett.* 76, 3112.
- Velikovich, A.L., Cochran, F.L., Davis, J., 1996. Suppression of Rayleigh–Taylor instability in Z-pinch loads with tailored density profiles. *Phys. Rev. Lett.* 77, 853.
- Velikovich, A.L., Dahlburg, J.P., Schmitt, A.J., Gardner, J.H., Phillips, L., Cochran, F.L., Chong, Y.K., Dimonte, G., Metzler, N., 2000. Richtmyer–Meshkov-like instabilities and early-time perturbation growth in laser targets and Z-pinch loads. *Phys. Plasmas* 7, 1662.
- Velikovich, A.L., Herrmann, M., Abarzhi, S.I., 2014. Perturbation theory and numerical modeling of weakly and moderately nonlinear dynamics of the incompressible Richtmyer–Meshkov instability. *J. Fluid Mech.* 751, 432.
- Verdon, C.P., McCrory, R.L., Morse, R.L., Baker, G.R., Meiron, D.I., Orszag, S.A., 1982. Nonlinear effects of multifrequency hydrodynamic instabilities on ablatively accelerated thin shells. *Phys. Fluids* 25, 1653.
- Versluis, M., Schmitz, B., von der Heydt, A., Lohse, D., 2000. How snapping shrimp snap: Through cavitating bubbles. *Science* 289, 2114.
- Vetter, M., Sturtevant, B., 1995. Experiments on the Richtmyer–Meshkov instability of an air/SF₆ interface. *Shock Waves* 4, 247.
- Veynante, D., Vervisch, L., 2002. Turbulent combustion modeling. *Prog. Energy Combustion Sci.* 28, 193–266.
- Veynante, D., Trouvé, A., Bray, K.N.C., Mantel, T., 1997. Gradient counter-gradient scalar transport in turbulent premixed flames. *J. Fluid Mech.* 332, 263.
- Vishniac, E.T., 1983. The dynamic and gravitational instabilities of spherical shocks. *Astrophys. J.* 274, 152.
- Vladimirova, N., Chertkov, M., 2009. Self-similarity and universality in Rayleigh–Taylor, Boussinesq turbulence. *Phys. Fluids* 21, 015102.
- Vlasov, Y.A., Gerasimov, S.I., Gubkov, E.V., Dudin, V.I., Kopyshev, V.P., Meshkov, E.E., Nikulin, A.A., Ryabov, V.P., Tilkunov, V.A., 1996. Shock tube with GEM-driver. Preprint 47–96, RFNC-VNIIEF.
- Vreman, A.M., 2004. An eddy-viscosity subgrid-scale model for turbulent shear flow: Algebraic theory and applications. *Phys. Fluids* 16, 3670.
- Waddell, J.T., Niederhaus, C.E., Jacobs, J.W., 2001. Experimental study of Rayleigh–Taylor instability: Low Atwood number liquid systems with single-mode initial perturbations. *Phys. Fluids* 13, 1263.
- Waitz, I.A., Marble, F., Zukoski, E.E., 1993. Investigation of a contoured wall injector for hypervelocity mixing augmentation. *AIAA J.* 31, 1014.
- Walchli, B., Thornber, B., 2017. Reynolds number effects on the single-mode Richtmyer–Meshkov instability. *Phys. Rev. E* 95, 013104.
- Wang, C.-Y., Chevalier, R.A., 2001. Instabilities and clumping in type Ia supernova remnants. *Astrophys. J.* 549, 1119.

- Wang, J., Smith, R.F., Eggert, J.H., Braun, D.G., Boehly, T.R., Patterson, J.R., Celliers, P.M., Jeanloz, R., Collins, G.W., Duffy, T.S., 2013. Ramp compression of iron to 273 GPa. *J. Appl. Phys.* 114, 023513.
- Wang, L., Li, J., 2005. Fluid mixing due to Rayleigh–Taylor instability in a time-dependent acceleration field. *Commun. Nonlinear Sci. Numer. Simul.* 10, 571.
- Wang, L., Li, J., Xie, Z., 2002. Large-eddy simulation of 3-dimensional Rayleigh–Taylor instability in incompressible fluids. *Sci. China A* 45, 95.
- Wang, L.F., Ye, W.H., Fan, Z.F., Li, Y.J., He, X.T., Yu, M.Y., 2009a. Weakly nonlinear analysis on the Kelvin–Helmholtz instability. *Europhys. Lett.* 86, 15002.
- Wang, L.F., Xue, C., Ye, W.H., Li, Y.J., 2009b. Destabilizing effect of density gradient on the Kelvin–Helmholtz instability. *Phys. Plasmas* 16, 112104.
- Wang, L.F., Ye, W.H., Li, Y.J., 2010a. Interface width effect on the classical Rayleigh–Taylor instability in the weakly nonlinear regime. *Phys. Plasmas* 17, 052305.
- Wang, L.F., Ye, W.H., Fan, Z.F., Li, Y.J., 2010b. Nonlinear saturation amplitude in the Rayleigh–Taylor instability at arbitrary Atwood numbers with continuous profiles. *Europhys. Lett.* 90, 15001.
- Wang, L.F., Ye, W.H., Sheng, Z.M., Don, W.-S., Li, Y.J., He, X.T., 2010c. Preheating ablation effects on the Rayleigh–Taylor instability in the weakly nonlinear regime. *Phys. Plasmas* 17, 122706.
- Wang, T., Tao, G., Bai, J.S., Li, P., Wang, B., 2015. Numerical comparative analysis of Richtmyer–Meshkov instability simulated by different SGS. *Can. J. Phys.* 93, 519.
- Wang, T., Bai, J.S., Li, P., Wang, B., Du, L., Tao, G., 2016. Large-eddy simulations of the multi-mode Richtmyer–Meshkov instability and turbulent mixing under reshock. *High Energy Density Phys.* 19, 65.
- Wang, W.-M., Nepveu, M., 1983. A numerical study of the nonlinear Rayleigh–Taylor instability, with application to accreting X-ray sources. *Astron. Astrophys.* 118, 267.
- Wang, W.-M., Nepveu, M., Robertson, J.A., 1984. Further numerical studies of the Rayleigh–Taylor instability in the context of accreting X-ray sources. *Astron. Astrophys.* 135, 66.
- Wang, X.-L., Itoh, M., Shi, H.-H., Kishimoto, M., 2001. Experimental study of Rayleigh–Taylor instability in a shock tube accompanying cavity formation. *Jpn. J. Appl. Phys.* 40, 6668.
- Ward, G.M., Pullin, D.I., 2010. A hybrid, center-difference, limiter method for simulations of compressible multicomponent flows with Mie–Grüneisen equation of state. *J. Comput. Phys.* 229, 2999.
- Ward, G.M., Pullin, D.I., 2011. A study of planar Richtmyer–Meshkov instability in fluids with Mie–Grüneisen equations of state. *Phys. Fluids* 23, 076101.
- Watt, R.G., Duke, J., Fontes, C.J., Gobby, P.L., Hollis, R.V., Kopp, R.A., Mason, R.J., Wilson, D.C., Verdon, C.P., Boehly, T.R., Knauer, J.P., Meyerhofer, D.D., Smalyuk, V., Town, R.P.J., Iwase, A., Willi, O., 1998. Laser imprint reduction using a low-density foam buffer as a thermal smoothing layer at 351-nm wavelength. *Phys. Rev. Lett.* 81, 4644.
- Weber, C.R., Haehn, N.S., Oakley, J.G., Rothamer, D.A., Bonazza, R., 2012. Turbulent measurements in the Richtmyer–Meshkov instability. *Phys. Fluids* 24, 074105.
- Weber, C.R., Cook, A.W., Bonazza, R., 2013. Growth rate of a shocked mixing layer with known initial perturbations. *J. Fluid Mech.* 725, 372.
- Weber, C.R., Clark, D.S., Cook, A.W., Busby, L.E., Robey, H.F., 2014a. Inhibition of turbulence in inertial-confinement-fusion hot spots by viscous dissipation. *Phys. Rev. E* 89, 053106.
- Weber, C.R., Haehn, N.S., Oakley, J.G., Rothamer, D.A., Bonazza, R., 2014b. An experimental investigation of the turbulent mixing transition in the Richtmyer–Meshkov instability. *J. Fluid Mech.* 748, 457.
- Wei, T., Livescu, D., 2012. Late-time quadratic growth in single-mode Rayleigh–Taylor instability. *Phys. Rev. E* 86, 046405.
- Welser-Sherrill, L., Mancini, R.C., Haynes, D.A., Haan, S.W., Golovkin, I.E., MacFarlane, J.J., Radha, P.B., Delettrez, J.A., Regan, S.P., Koch, J.A., Izumi, N., Tommasini, R., Smalyuk, V.A., 2007. Development of two mix model postprocessors for the investigation of shell mix in indirect drive implosion core. *Phys. Plasmas* 14, 072705.
- Welser-Sherrill, L., Cooley, J.H., Haynes, D.A., Wilson, D.C., Sherrill, M.E., Mancini, R.C., Tommasini, R., 2008. Application of fall-line mix models to understand degraded yield. *Phys. Plasmas* 15, 072702.
- Welser-Sherrill, L., Fincke, J., Doss, F., Loomis, E., Flippo, K., Offermann, D., Keiter, P., Haines, B., Grinstein, F., 2013. Two laser-driven mix experiments to study reshock and shear. *High Energy Density Phys.* 9, 496.
- Wheeler, J.C., Harkness, R.P., 1990. Type I supernovae. *Pep. Prog. Phys.* 53, 1467.
- White, D.A., 2009. Siqueiros: Biography of A Revolutionary Artist. BookSurge Publishing.
- White, J., Oakley, J., Anderson, M., Bonazza, R., 2010. Experimental measurements of the nonlinear Rayleigh–Taylor instability using a magnetorheological fluid. *Phys. Rev. E* 81, 026303.
- Whitehead, J.A., Luther, D.S., 1975. Dynamics of laboratory diapir and plume models. *J. Geophys. Res.* 80, 705.
- Wilcock, W.S.D., Whitehead, J.A., 1991. The Rayleigh–Taylor instability of an embedded layer of low-viscosity fluid. *J. Geophys. Res.* 96, 12193.
- Willkinson, J.P., Jacobs, J.W., 2007. Experimental study of the single-mode three-dimensional Rayleigh–Taylor instability. *Phys. Fluids* 19, 124102.
- Williams, R.J.R., 2016. The late time structure of high density contrast, single mode Richtmyer–Meshkov flow. *Phys. Fluids* 28, 074108.
- Williams, R.J.R., 2017. Sub-grid properties and artificial viscous stresses in staggered-mesh schemes (submitted for publication).
- Williams, R.J.R., Grapes, C.C., 2017. Simulation of double-shock ejecta production. *J. Dyn. Behav. Mater.* 3, 291.
- Wilson, B.M., Mejia-Alvarez, R., Prestridge, K.P., 2016. Single-interface Richtmyer–Meshkov turbulent mixing at the Los Alamos vertical shock tube. *ASME J. Fluids Eng.* 138, 071201.
- Wilson, D.C., Scannapieco, A.J., Cranfill, C.W., Clover, M.R., Hoffman, N.M., Collins, J., 2003. Degradation of radiatively driven inertial confinement fusion capsule implosions by multifluid interpenetration mixing. *Phys. Plasmas* 10, 4427.
- Wilson, D.C., Cranfill, C.W., Christensen, C., Forster, R.A., Peterson, R.R., Hoffman, N.M., Pollak, G.D., Li, C.K., Seguin, F.H., Frenje, J.A., Petrasso, R.D., McKenty, P.W., Marshall, F.J., Glebov, V.Y., Stoeckl, C., Schmid, G.J., Izumi, N., Amendt, P., 2004. Multifluid interpenetration mixing in directly driven inertial confinement fusion capsule implosions. *Phys. Plasmas* 11, 2723.
- Woltjer, L., 1972. Supernova remnants. *Annu. Rev. Astron. Astrophys.* 10, 129.
- Wongwathanarat, A., Mueller, E., Janka, H.-Th., 2015. Three-dimensional simulations of core-collapse supernovae: from shock revival to shock breakout. *Astron. Astrophys.* 577, A48.
- Wood, W.M., Buttler, W.T., Thomas, V.A., Turley, W.D., Stevens, G.D., Grover, M., Schmidt, D.W., Martinez, J.I., 2017. Ejecta directions and size information from recent “sweeper wave” data in Sn. *J. Dynamic Behavior Mater.* 3, 240.
- Woods, J.D., 1968. Wave-induced shear instability in the summer thermocline. *J. Fluid Mech.* 32, 791.
- Wood-Vasey, W.M., Budil, K.S., Remington, B.A., Glendinning, S.G., Rubenchik, A.M., Berning, M., Kane, J.O., Larsen, J.T., 2000. Computational modeling of classical and ablative Rayleigh–Taylor instabilities. *Laser Part. Beams* 18, 583.
- Woodward, P.R., et al., 2010. The piecewise-parabolic Boltzmann Advection Scheme (PPB) Applied to Multifluid Hydrodynamics, Los Alamos National Laboratory Report No. LAUR-10-01823.
- Woosley, S.E., Weaver, T.A., 1986. The physics of supernova explosion. *Annu. Rev. Astron. Astrophys.* 24, 205.
- Wouchuk, J.G., 2001a. Growth rate of the linear Richtmyer–Meshkov instability when a shock is reflected. *Phys. Rev. E* 63, 056303.
- Wouchuk, J.G., 2001b. Growth rate of the Richtmyer–Meshkov instability when a rarefaction is reflected. *Phys. Plasmas* 8, 2890.
- Wouchuk, J.G., Cobos Campos, F., 2017. Linear theory of Richtmyer–Meshkov like flows. *Plasma Phys. Control. Fusion* 59, 014033.

- Wouchuk, J.G., Nishihara, K., 1996. Linear perturbation growth at a shocked interface. *Phys. Plasmas* 3, 3761.
- Wouchuk, J.G., Nishihara, K., 1997. Asymptotic growth in the linear Richtmyer–Meshkov instability. *Phys. Plasmas* 4, 1028.
- Wu, C.C., 2000. Shock wave interaction with magnetopause. *J. Geophys. Res.* 105, 7533.
- Wu, C.C., Roberts, P.H., 1999. Richtmyer–Meshkov instability and the dynamics of the magnetosphere. *Geophys. Res. Lett.* 26, 655.
- Wu, J.F., Miao, W.Y., Wang, L.F., Yuan, Y.T., Cao, Z.R., Ye, W.H., Fan, Z.F., et al., 2014. Indirect-drive ablative Rayleigh–Taylor growth experiments on the Shenguang-II laser facility. *Phys. Plasmas* 21, 042707.
- Wunsch, C., Ferrari, R., 2004. Vertical mixing energy and the general circulation of oceans. *Annu. Rev. Fluid Mech.* 36, 281–314.
- Xia, T.J., Dong, Y.Q., Cao, Y.G., 2013. Effects of surface tension on Rayleigh–Taylor instability. *Acta Phys. Sin.* 62, 214702.
- Xia, T.J., Wang, H.L., Dong, Y.Q., Guo, H.Z., Cao, Y.G., 2015. Effects of head loss on the growth of the Rayleigh–Taylor and the Richtmyer–Meshkov instabilities. *Int. J. Heat Mass Transfer* 84, 158.
- Xie, C.-Y., Tao, J.J., Sun, Z.L., Li, J., 2017a. Retarding viscous Rayleigh–Taylor mixing by an optimized additional mode. *Phys. Rev. E* 95, 023109.
- Xie, C.-Y., Tao, J.-J., Li, J., 2017b. Viscous Rayleigh–Taylor instability with and without diffusion effect. *Appl. Math. Mech.* 38, 263.
- Xie, X.-F., Li, Z.-C., Li, S.-W., Huang, Y.-B., Jing, L.-F., Yang, D., Huo, W.-Y., et al., 2016. Radiation flux study of spherical hohlraums at the SGIII prototype facility. *Phys. Plasmas* 23, 112701.
- Yaakobi, B., Pelah, I., Hoose, J., 1976. Preheat by fast electrons in laser-fusion experiments. *Phys. Rev. Lett.* 37, 836.
- Yabe, T., Hoshino, H., Tsuchiya, T., 1991. Two- and three-dimensional behavior of Rayleigh–Taylor and Kelvin–Helmholtz instabilities. *Phys. Rev. A* 44, 2756.
- Yaglom, A.M., 1949. On the local structure of a temperature field in a turbulent flow. *Dokl. Akad. Nauk SSSR* 69, 743.
- Yakovenko, S.N., 2014. The effects of density difference and surface tension on the development of Rayleigh–Taylor instability of an interface between fluid media. *Fluid Dyn.* 49, 748.
- Yang, J., Kubota, T., Zukoski, E.E., 1993. Applications of shock-induced mixing in supersonic combustion. *AIAA J.* 31, 854.
- Yang, Q., Chang, J., Bao, W., 2014. Richtmyer–Meshkov instability induced mixing enhancement in the scramjet combustor with a central strut. *Adv. Mech. Eng.* 6, 614189.
- Yang, Y., Zhang, Q., Sharp, D.H., 1994. Small amplitude theory of Richtmyer–Meshkov instability. *Phys. Fluids* 6, 1856.
- Yanillkin, Yu.V., Shanin, A.A., et al., 1993. EGAK codes for computing 2-D flows in multicomponent media. *VANT Ser. Mat. Modelir. Fiz. Proc. N.4* 69, (in Russian).
- Ye, W.H., Zhang, W., He, X.T., 2002. Stabilization of ablative Rayleigh–Taylor instability due to change of the Atwood number. *Phys. Rev. E* 65, 057401.
- Yeung, P.K., Brasseur, J.G., 1991. The response of isotropic turbulence to isotropic and anisotropic forcing at large scales. *Phys. Fluids A* 3, 884.
- Yeung, P.K., Zhou, Y., 1997. Universality of the Kolmogorov constant in numerical simulations of turbulence. *Phys. Rev. E* 56, 1746.
- Yih, C.-S., 1960. A transformation for non-homentropic flows, with an application to large-amplitude motion in the atmosphere. *J. Fluid Mech.* 9, 68.
- Yin, J.-W., Pan, H., Wu, Z.-H., Hao, P.-C., 2017. A growth study of the Richtmyer–Meshkov flow in the elastoplastic solids under explosive loading. *Acta Phys. Sin.* 66, 074701.
- Yosef-Hai, A., Sadot, O., Kartoon, D., Oron, D., Levin, L., Sarid, E., Elbaz, Y., Ben-Dor, G., Shvarts, D., 2003. Late-time growth of the Richtmyer–Meshkov instability for different Atwood numbers and different dimensionalities. *Laser Part. Beams* 21, 363.
- Young, R.P., Kuranz, C.C., Drake, R.P., Hartigan, P., 2017. Accretion shocks in the laboratory: Design of an experiment to study star formation. *High Energy Density Phys.* 23, 1.
- Young, Y.-N., Ham, F.E., 2006. Surface tension in incompressible Rayleigh–Taylor mixing flow. *J. Turbul.* 7, 71.
- Young, Y.-N., Tufo, H., Dubey, A., Rosner, R., 2001. On the miscible Rayleigh–Taylor instability: Two and three dimensions. *J. Fluid Mech.* 447, 377.
- Youngs, D.L., 1984. Numerical simulation of turbulent mixing by Rayleigh–Taylor instability. *Physica D* 12, 32.
- Youngs, D.L., 1989. Modeling turbulent mixing by Rayleigh–Taylor instability. *Physica D* 37, 270.
- Youngs, D.L., 1991. Three-dimensional numerical simulation of turbulent mixing by Rayleigh–Taylor instability. *Phys. Fluids A* 3, 1312.
- Youngs, D.L., 1992. Experimental investigation of turbulent mixing by Rayleigh–Taylor instability. In: Dannevick, W.P., Buckingham, A.C., Leith, C.E. (Eds.), *Advances in Compressible Turbulent Mixing*, Proceeding of the 1st International Workshop on the Physics of Compressible Turbulent Mixing, Princeton Univ., p. 607.
- Youngs, D.L., 1994. Numerical simulation of mixing by Rayleigh–Taylor and Richtmyer–Meshkov instabilities. *Laser Part. Beams* 12, 725.
- Youngs, D.L., 1997. Variable acceleration Rayleigh–Taylor mixing. In: Jourdan, G., Houas, L. (Eds.), *Proceedings of the 6th International Workshop on the Physics of Compressible Turbulent Mixing*. Provence University Press, Marseille, France, p. 534.
- Youngs, D.L., 2003. Application of MILES to Rayleigh–Taylor and Richtmyer–Meshkov mixing, AIAA paper 2003-4102.
- Youngs, D.L., 2004. Effect of initial conditions on self-similar turbulent mixing. In: *Proceedings of the International Workshop on the Physics of Compressible Turbulent Mixing*, 9, Available online at: <http://www.iwptcm.org/>.
- Youngs, D.L., 2013. The density ratio dependence of self-similar Rayleigh–Taylor mixing. *Phil. Trans. R. Soc. A* 371, 20120173.
- Youngs, D.L., 2017. Rayleigh–Taylor mixing: direct numerical simulation and implicit large eddy simulation. *Phys. Scr.* 92, 074006.
- Yuan, Y., Tu, S., Miao, W., Wu, J., Wang, L., Yin, C., Hao, Y., Ye, W., Ding, Y., Jiang, S., 2016. A new data processing technique for Rayleigh–Taylor instability growth experiments. *AIP Advances* 6, 065207.
- Zabusky, N.J., 1999. Vortex Paradigm for accelerated inhomogeneous flows: Visiometrics for the Rayleigh–Taylor and Richtmyer–Meshkov environments. *Annu. Rev. Fluid Mech.* 31, 495.
- Zabusky, N.J., Zeng, S.M., 1998. Shock cavity implosion morphologies and vortical projectile generation in axisymmetric shock–spherical fast/slow bubble interactions. *J. Fluid Mech.* 362, 327.
- Zabusky, N., Ray, J., Samtaney, R.S., 1995. Vortex models for Richtmyer–Meshkov fast/slow environments: scaling laws for interface growth rates. In: Young, R., Glimm, J., Boyton, B. (Eds.), *Proceedings of the 5th International Workshop on Compressible Turbulent Mixing*. World Scientific, Singapore.
- Zabusky, N.J., Lugomer, S., Zhang, S., 2005. Micro-fluid dynamics via laser metal surface interactions: Wave-vortex interpretation of emerging multiscale coherent structures. *Fluid Dyn. Res.* 36, 291.
- Zaitsev, S.G., Lebo, I.G., Rozanov, V.B., Titov, S.N., Chebotareva, E.I., 1991. Hydrodynamic instability of the contact zone between accelerated gases. *Fluid Dyn.* 26, 806.
- Zaitsev, S.G., Titov, S.N., Chebotareva, E.I., 1994. Evolution of the continuous interface between gases of different density during the passage of a shock wave. *Fluid Dyn.* 29, 171.
- Zaitsev, S.G., Krivets, V.V., Mazilin, I.M., Titov, S.N., Chebotareva, E.I., Nikishin, V.V., Tishkin, V.F., Bouquet, S., Haas, J.-F., 2003. Evolution of the Rayleigh–Taylor instability in the mixing zone between gases of different densities in a field of variable acceleration. *Laser Part. Beams* 21, 393.
- Zeldovich, Y.B., Raizer, Y.P., 1966. *Physics of Shock Waves and High-Temperature Hydrodynamic Phenomena*. Academic, New York.
- Zellner, M.B., Buttler, W.T., 2008. Exploring Richtmyer–Meshkov instability phenomena and ejecta cloud physics. *Appl. Phys. Lett.* 93, 114102.
- Zellner, M.B., Grover, M., Hammerberg, J.E., Hixson, R.S., Iverson, A.J., Macrum, G.S., Morley, K.B., Obst, A.W., Olson, R.T., Payton, J.R., Rigg, P.A., 2007. Effects of shock-breakout pressure on ejection of micron-scale material from shocked tin surfaces. *J. Appl. Phys.* 102, 013522.
- Zetina, S., Godinez, F.A., Zenit, R., 2015. A hydrodynamic instability is used to create aesthetically appealing patterns in painting. *PLOS ONE* 10, 1.
- Zhai, Z., Si, T., Luo, X., Yang, J., 2011. On the evolution of spherical gas interfaces accelerated by a planar shock wave. *Phys. Fluids* 23, 084104.
- Zhang, Q., 1990. Validation of the chaotic mixing renormalization group fixed point. *Phys. Lett. A* 151, 18.

- Zhang, Q., 1998. Analytical solutions of Layzer-type approach to unstable interfacial fluid mixing. *Phys. Rev. Lett.* 81, 3391.
- Zhang, Q., Guo, W., 2016. Universality of finger growth in two-dimensional Rayleigh–Taylor and Richtmyer–Meshkov instabilities with all density ratios. *J. Fluid Mech.* 786, 47.
- Zhang, Q., Sohn, S.-I., 1996. An analytical nonlinear theory of Richtmyer–Meshkov instability. *Phys. Lett. A* 212, 149.
- Zhang, Q., Sohn, S.-I., 1997a. Non-linear theory of unstable fluid mixing driven by shock wave. *Phys. Fluids* 9, 1106.
- Zhang, Q., Sohn, S.-I., 1997b. Padé approximation for an interfacial fluid mixing problem. *Appl. Math. Lett.* 10, 121.
- Zhang, Q., Sohn, S.-I., 1999. Quantitative theory of Richtmyer–Meshkov instability in three dimensions. *Z. Angew. Math. Phys.* 50, 1.
- Zhang, Q., Deng, S., Guo, W., 2016. An accurate close-form theory for the growth rate of Richtmyer–Meshkov instability in compressible fluids with all density ratios, 15th International Workshop on the Physics of Compressible Turbulent Mixing, Sydney, Australia.
- Zhang, Q., Deng, S., Guo, W., 2017. A quantitative theory for compressible Richtmyer–Meshkov instability at all density ratios (submitted for publication).
- Zhang, K., Zhong, J.Y., Wang, J.Q., Pei, X.X., Wei, H.G., Yuan, D.W., Yang, Z.W., Wang, C., Li, F., Han, B., Yin, C.L., 2015. Modeling the interaction of solar wind with a dipole magnetic field with Shenguang II intense lasers. *High Energy Density Phys.* 17, 32.
- Zhang, X., 2013. Single-mode bubble evolution simulations of Rayleigh–Taylor instability with spectral element method and a viscous model. *Comput. & Fluids* 88, 813.
- Zhang, Y.S., He, Z.W., Li, X.L., Tian, B.L., 2015. The realization of non-reflecting boundaries for compressible Rayleigh–Taylor flows with variable acceleration histories. *Proc. Eng.* 126, 118.
- Zhang, Y.-T., Shi, J., Shu, C.-W., Zhou, Y., 2003. Numerical viscosity and resolution of high-order weighted essentially nonoscillatory schemes for compressible flows with high Reynolds numbers. *Phys. Rev. E* 68, 046709.
- Zhang, Y.-T., Shu, C.-W., Zhou, Y., 2006. Effects of shock waves on Rayleigh–Taylor instability. *Phys. Plasmas* 13, 062705.
- Zhigalin, A.S., Rousskikh, A.G., Baksht, R.B., Chaikovsky, S.A., Labetskaya, N.A., Oreshkin, V.I., 2015. Suppression of Rayleigh–Taylor instabilities in Z-pinchers. *Tech. Phys. Lett.* 41, 554.
- Zhong, J., Li, Y., Wang, X., Wang, J., Dong, Q., Xiao, C., Wang, S., Liu, X., Zhang, L., An, L., Wang, F., 2010. Modelling loop-top X-ray source and reconnection outflows in solar flares with intense lasers. *Nature Phys.* 6, 984.
- Zhou, Q., 2013. Temporal evolution and scaling of mixing in two-dimensional Rayleigh–Taylor turbulence. *Phys. Fluids* 25, 085107.
- Zhou, Q., Huang, Y.X., Lu, Z.M., Liu, Y.L., Ni, R., 2016. Scale-to-scale energy and enstrophy transport in two-dimensional Rayleigh–Taylor turbulence. *J. Fluid Mech.* 786, 294.
- Zhou, Q., Jiang, L.F., 2016. Kinetic and thermal energy dissipation rates in two-dimensional Rayleigh–Taylor turbulence. *Phys. Fluids* 28, 045109.
- Zhou, Y., 1991. Eddy damping backscatter and subgrid stresses in subgrid modeling of turbulence. *Phys. Rev. A* 43, 7049.
- Zhou, Y., 1993a. Degree of locality of energy transfer in the inertial range. *Phys. Fluids A* 5, 1092.
- Zhou, Y., 1993b. Interacting scales and energy transfer in isotropic turbulence. *Phys. Fluids A* 5, 2511.
- Zhou, Y., 1995. A phenomenological treatment of rotating turbulence. *Phys. Fluids* 7, 2092.
- Zhou, Y., 2001. A scaling analysis of turbulent flows driven by Rayleigh–Taylor and Richtmyer–Meshkov instabilities. *Phys. Fluids* 13, 538.
- Zhou, Y., 2007. Unification and extension of the concepts of similarity criteria and mixing transition for studying astrophysics using high energy density laboratory experiments or numerical simulations. *Phys. Plasmas* 14, 082701.
- Zhou, Y., 2010. Renormalization group theory for fluid and plasma turbulence. *Phys. Reports* 488, 1.
- Zhou, Y., 2017. Rayleigh–Taylor and Richtmyer–Meshkov instability induced flow, turbulence, and mixing. II. *Phys. Reports* 723–725, 1.
- Zhou, Y., Matthaeus, W.H., 1990. Models of inertial range spectra of interplanetary magnetohydrodynamic turbulence. *J. Geophys. Res.* 95, 14881.
- Zhou, Y., Oughton, S., 2011. Nonlocality and the critical Reynolds numbers of the minimum state magnetohydrodynamic turbulence. *Phys. Plasmas* 18, 072304.
- Zhou, Y., Speziale, C.G., 1998. Advances in the fundamental aspects of turbulence: Energy transfer, interacting scales, and self-preservation in isotropic decay. *ASME Appl. Mech. Rev.* 51, 267.
- Zhou, Y., Thornber, B., 2016. A comparison of three approaches to compute the effective Reynolds number of the implicit large-eddy simulations. *ASME J. Fluids Eng.* 138, 071205.
- Zhou, Y., Vahala, G., 1993. Reformulation of recursive-renormalization-group based subgrid modeling of turbulence. *Phys. Rev. E* 47, 2503.
- Zhou, Y., Vahala, G., Hossain, M., 1988. Renormalization-group theory for the eddy viscosity in subgrid modeling. *Phys. Rev. A* 37, 2590.
- Zhou, Y., Hossain, M., Vahala, G., 1989a. A critical look at the use of filters in large eddy simulations. *Phys. Lett. A* 139, 330.
- Zhou, Y., Vahala, G., Hossain, M., 1989b. Renormalized eddy viscosity and Kolmogorov's constant in forced Navier–Stokes turbulence. *Phys. Rev. A* 40, 5865.
- Zhou, Y., Yeung, P.K., Brasseur, J.G., 1996. Scale disparity and spectral transfer in anisotropic numerical turbulence. *Phys. Rev. E* 53, 1261.
- Zhou, Y., Schilling, O., Ghosh, S., 2002. Subgrid scale and backscatter model for magnetohydrodynamic turbulence based on closure theory: Theoretical formulation. *Phys. Rev. E* 66, 026309.
- Zhou, Y., Robey, H.F., Buckingham, A.C., 2003a. Onset of turbulence in accelerated high-Reynolds-number flow. *Phys. Rev. E* 67, 056305.
- Zhou, Y., Remington, B.A., Robey, H.F., Cook, A.W., Glendinning, S.G., Dimits, A., Buckingham, A.C., Zimmerman, G.B., Burke, E.W., Peyser, T.A., Cabot, W., Eliason, D., 2003b. Progress in understanding turbulent mixing induced by Rayleigh–Taylor and Richtmyer–Meshkov instabilities. *Phys. Plasmas* 10, 1883.
- Zhou, Y., Matthaeus, W.H., Dmitruk, P., 2004. Colloquium: Magnetohydrodynamic turbulence and time scales in astrophysical and space plasma. *Rev. Modern Phys.* 76, 1015.
- Zhou, Y., Buckingham, A.C., Bataille, F., Mathelin, L., 2009. Minimum state for high Reynolds and Péclet number turbulent flows. *Phys. Lett. A* 373, 2746.
- Zhou, Y., Grinstein, F.F., Wachtor, A.J., Haines, B.M., 2014. Estimating the effective Reynolds number in implicit large eddy simulation. *Phys. Rev. E* 89, 013303.
- Zhou, Y., Cabot, W.H., Thornber, B., 2016. Asymptotic behavior of the mixed mass in Rayleigh–Taylor and Richtmyer–Meshkov instability induced flows. *Phys. Plasmas* 23, 052712.
- Zingale, M., Woosley, S.E., Rendleman, C.A., Day, M.S., Bell, J.B., 2005a. Three-dimensional numerical simulations of Rayleigh–Taylor unstable flames in Type Ia supernovae. *Astrophys. J.* 632, 1021.
- Zingale, M., Woosley, S.E., Bell, J.B., Day, M.S., Rendleman, C.A., 2005b. The physics of flames in type Ia supernovae. *J. Phys. Conf.* 16, 405.
- Zou, L.-Y., Liu, J.-H., Liao, S.-F., Zheng, X.-X., Zhai, Z.-G., Luo, X.-S., 2017. Richtmyer–Meshkov instability of a flat interface subjected to a rippled shock wave. *Phys. Rev. E* 95, 013107.
- Zufiria, J.A., 1988a. Bubble competition in Rayleigh–Taylor instability. *Phys. Fluids* 31, 440.
- Zufiria, J.A., 1988b. Vortex-in-cell simulation of bubble competition in a Rayleigh–Taylor instability. *Phys. Fluids* 31, 3199.
- Zweibel, E., 1991. Spinning a tangled web. *Nature* 352, 755.